Energy Transfer and Excitonic Interactions in Conjugated Chromophore Arrangements of Bodipys and Pyrenes and Squaraines

Dissertation zur Erlangung
des naturwissenschaftlichen Doktorgrades der
Julius-Maximilians-Universität Würzburg

vorgelegt von
Nina A. Auerhammer

aus Rothenburg o. d. T.

Würzburg 2018

Eingereicht bei der Fakultät für Chemie und Pharmazie am

_____

Gutachter der schriftlichen Arbeit

1. Gutachter: _____

2. Gutachter: _____

Prüfer des öffentlichen Promotionskolloquiums

1. Prüfer: _____

2. Prüfer: _____

3. Prüfer: _____

Datum des öffentlichen Promotionskolloquiums

_____

Doktorurkunde ausgehändigt am

_____

Die vorliegende Arbeit wurde in der Zeit von Mai 2014 bis April 2018 am Institut für Organische Chemie der Universität Würzburg angefertigt.

Mein besonderer Dank gilt

Herrn Prof. Dr. Christoph Lambert

für die Überlassung dieser äußerst vielseitigen und interessanten Themen und das mit vielen Anregungen verbundene Interesse an dieser Arbeit

Copyright

The following thesis contributed to this work:

1. Synthese und Charakterisierung von Farbstofftrimeren, A. Schulz, Bachelor Thesis, Julius-Maximilians-Universität (Würzburg), **2015**.

2. Synthese und spektroskopische Charakterisierung von Farbstoffoligomeren, N. J. S. Jordan, Bachelor Thesis, Julius-Maximilians-Universität (Würzburg), **2017**.

3. Synthese und spektroskopische Charakterisierung eines starr-verbrückten *trans*-Squarains, S. Ricker, Bachelor Thesis, Julius-Maximilians-Universität (Würzburg), **2017**.

Contents

Abbreviations

bodipy	4-bora-3a,4a-diaza-*s*-indacene
CI	configuration interaction
DADS	decay associated difference spectra
dba	dibenzylideneacetone
DBU	1,8-diazabicyclo[5.4.0]undec-7-ene
DCTB	(*trans*-2-[3-(4-*tert*-butylphenyl)-2-methyl-2-propenyl-idene]malononitrile)
DSSC	dye sensitised sollar cell
DIPA	*N*,*N*-diisopropylamine (IUPAC: *N*-isopropylpropan-2-amine)
DNA	deoxyribonucleic acid
dppf	1,1’-bis(diphenylphosphanyl)ferrocene
dtbpy	4,4′-di-*tert*-butyl-2,2′-dipyridyl
EADS	evolution associated difference spectrum
EI	electron ionisation
ESA	excited state absorption
ESI	electronspray ionisation
FLUC	fluorescence-upconversion spectroscopy
FCWD	Franck-Condon weighted density of states
fwhm	full width at half maximum
GPC	gel permeation chromatography
GSB	ground state bleach
HAB	hexaarylbenzene
HOMO	highest occupied molecular orbital
IRF	instrument response function
LUMO	lowest unoccupied molecular orbital
MALDI-TOF	matrix assisted laser desorption/ionisation-time of flight
MW	mircowave

Abbreviations

NIR	near-infrared
NMR	nuclear magnetic resonance
NOPA	noncollinear optical parametric amplifier
RuPhos	2-dicyclohexylphosphino-2′,6′-diisopropoxybiphenyl
SADS	species associated difference spectra
SE	stimulated emission
TA	transient absorption
TBAF	tetrabutylammonium fluorid
TCSPC	time-correlated single photon counting
TD-DFT	time-dependent density functional theory
TEA	triethylamine
TFA	trifluoroacetic acid
TMS	trimethylsilyl
TMSA	trimethylsilylacetylene
XPhos	2-dicyclohexylphosphino-2′,4′,6′-triisopropylbiphenyl

1 Introduction

Energy transfer in organic molecules is one of the most studied processes in photophysics and this predominant research interest is due to its fundamental nature. Energy transfer processes play an important role in photosynthesis, but can also be utilised for several applications in the field of optoelectronic devices such as organic light emitting diodes (OLEDs), field effect transistors (FETs) and solar cells.[1-8] In order to optimise the performance of such applications, it must be assured that the energy transfer is rapid to compete with other deactivation pathways, such as fluorescence or triplet formation.[9] Therefore an indepth understanding of the underlying mechanisms is of great importance.

Depending on the coupling strength of the chromophores with each other, different mechanisms and hence molecular and structural properties become more important.

Generally, three different cases are distinguished: (a) strong coupling, (b) weak coupling and (c) very weak coupling.

In case of a very weak coupling between the donor and the acceptor *Förster* resonance energy transfer theory[10] may be used to describe the system. In a situation that can be descirbed by this theorie, the interacting molecules retain their individual properties and energy is transferred from the donor to the acceptor. An extention of *Försters* approach was accomplished by *Dexter*[11] to incorporate forbidden transitions.[12, 13]

Strong coupling between the molecules leads to mixing of the electronic states and therefore delocalisation, so hence the discussion of energy transfer from donor to acceptor is irrelevant.[12, 13] This situation is best described by the exciton coupling theory and energy transfer between the constituents can be viewed as an internal conversion process. [3, 14-20]

The description of the energy transfer process for the weak coupling case is more difficult as energy transfer takes place before relaxation of the excited state, but the coupling is not strong enough to form an excitonic state.[12, 13] As the accurate description of these coupling cases is more complex and the theories are beyond the research of this work, this will not be discussed any further.

The strong and very weak coupling cases will be discussed in more detail in the following chapter as their knowledge is necessary for the studies discussed in this thesis.

2 Theory

2.1 Interaction Between Light and Molecules

When a molecule interacts with the electric field of electromagnetic radiation, it can be excited and changes its electronic configuration by promoting an electron to a level higher in energy.

The excitation of a molecule is characterised by the transition-dipole moment, that can be described by a classically oscillating field induced by the interaction with light:[21]

$$\mu = \mu_0 \cos(2\pi\upsilon t) \quad (1)$$

With μ_0 being the maximum value that the transition-dipole moment μ can adopt, t the time and υ the frequency of the oscillation. This dipole causes an oscillating electric field itself that can interact with molecules nearby. A reasonable interaction of the electric oscillating field is only given if the other transitions are strongly allowed, hence have a strong oscillator strength and posses large transition dipoles.[21]

Depending on the transition dipoles multiple pathways are possible for the molecule to relax back to its ground state. An overview of these processes can be seen in the *Jablonski* diagram in Figure 1.

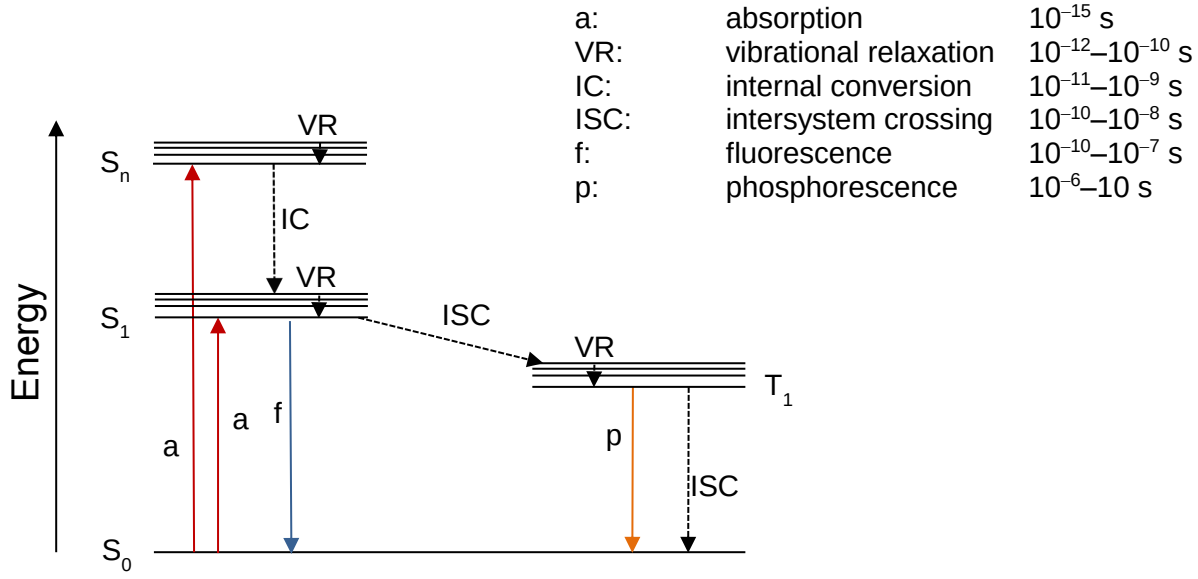

Figure 1 *Jablonski* diagram showing possible deactivation pathways of an excited organic molecule. According time constants for the processes are given on the right.[22]

The transition probability of the excitation and relaxation can be calculated by *Fermis* Golden Rule which results from time-dependent pertubation theory:[20]

$$k \propto \sum_{\mathrm{f}} |\langle \mathrm{f}|\hat{\mu} \cdot e|\mathrm{g}\rangle|^2 \delta(E_{\mathrm{f}} - E_{\mathrm{g}} - \hbar\omega) \qquad (2)$$

Here $\hat{\mu}$ is the dipole operator of the molecule, e the polarisation vector of the electromagnetic wave, $|\mathrm{g}\rangle$ the initial ground state with the energy E_{g} and $|\mathrm{f}\rangle$ the excited state with the energy E_{f}. The δ-function ensures energy conservation, as the transition is only possible if the incident light is resonant with a transition of the molecule.[23]

The matrix element $\langle \mathrm{f}|\hat{\mu} \cdot e|\mathrm{g}\rangle$ describes the resulting oscillation of the molecule due to the interaction with the electromagnetic field. Strong oscillations result in a strong interaction and hence a fast transfer rate.[21]

If the molecules come in sufficiently close proximity during the lifetime of their excited states energy transfer becomes a possible deactivation process. This process is only efficient if the transfer is faster than the competing processes, shown in the *Jablonski* diagramm above (see Figure 1).

2.2 Energy Transfer in Different Coupling Regimes

Energy transfer describes the process of an excited donor transfering its energy onto an acceptor molecule.

The coupling between the molecules is distinguished into three categories according to the interaction strength, hence the rate of the transfer in comparison to the vibrational relaxation:[24] strong, weak and very weak.

One speaks of strong coupling if the electronic interaction between the molecules is much greater than the electronic and nuclear motions in the single chromophore. The energy transfer is then faster than the nuclear vibrations and vibrational localisation, and therefore the excitation energy is delocalised over the molecules. The excited state is never centered at one molecule, but a superposition of states of multiple molecules is necessary to account for an appropriate description of the system.[22]

Very weak coupling is characterised by interactions in the single molecules that are larger than the coupling between donor and acceptor, and therefore vibrational motions proceed on a much faster timescale than the energy transfer.[25]

If the solvent relaxation is on the same timescale as the energy transfer and the states of donor and acceptor are already slightly mixed, the interactions are in the weak coupling range.[12]

2.2.1 Energy Transfer in Very Weakly Coupled Systems

In very weak coupled systems, incoherent energy transfer takes place on a much slower timescale than vibrational relaxation. Therefore the transfer is occuring from vibrational relaxed states.[24]

To describe the energy transfer in very weakly coupled systems accuratly, different mechanisms have to be applied depending on the distance between the interacting molecules. If the molecules are closley spaced, orbital overlap is possible and energy can be transferred by an electron exchange (see Figure 2, blue arrows). Energy transfer through-space, which is based on interactions of oscillating dipoles, is possible at short distances as well as for further separated molecules (see Figure 2, red arrows).[21]

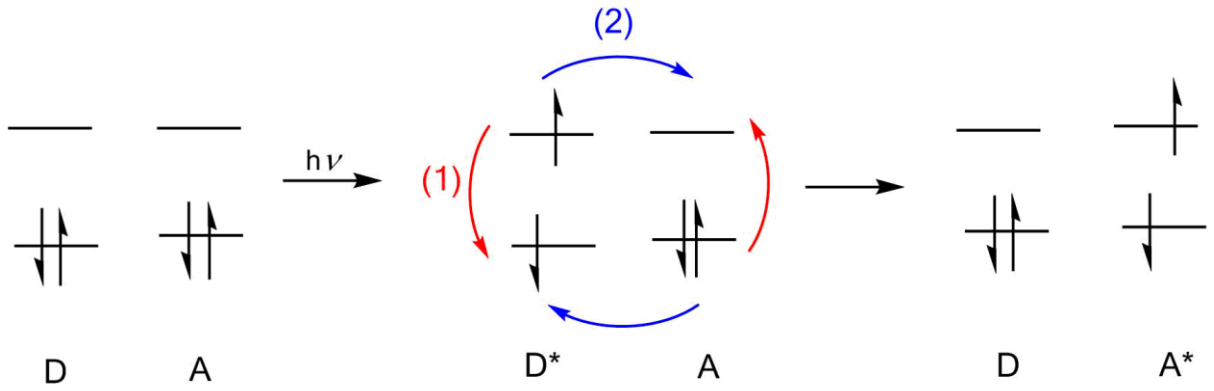

Figure 2 Schematic representation of energy transfer pathways in an acceptor (A) and donor (D) pair. The asterisk * denotes the excited state. (1) shows the Coulomb interaction (red arrows) and (2) the exchange interaction (blue arrows).

The simplest system where energy transfer is possible is a dimer where the resulting Hamiltonian is given by:[26]

$$\hat{H} = \hat{H}_1 + \hat{H}_2 + \hat{H}_{21} \tag{3}$$

And the antisymmetric wavefunction of the initial and final state Ψ_i and Ψ_f of the two interacting molecules may be written as:

$$\Psi_\mathrm{i} = \frac{1}{\sqrt{2}} [\varphi_{1^*}(1)\chi_{1^*}(1)\varphi_2(2)\chi_2(2) - \varphi_{1^*}(2)\chi_{1^*}(2)\varphi_2(1)\chi_2(1)] \tag{4a}$$

and

$$\Psi_\mathrm{f} = \frac{1}{\sqrt{2}} [\varphi_1(1)\chi_1(1)\varphi_{2^*}(2)\chi_{2^*}(2) - \varphi_1(2)\chi_1(2)\varphi_{2^*}(1)\chi_{2^*}(1)] \tag{4b}$$

Where φ denotes the spatial wavefunctions of molecule 1 or 2 and χ the corresponding spin wavefunction. The asterisk * denotes the excited state.

When these two molecules interact, in addition to their ground state energy $(H_1 + H_2)$ an interaction term results that is defined as:

$$H_{21} = \langle \psi_f | \hat{H}_{21} | \psi_i \rangle \tag{5a}$$

with

$$H_{21}^{\text{Coulomb}} = \langle \varphi_1(1)\varphi_{2^*}(2) | \hat{H}_{21} | \varphi_{1^*}(1)\varphi_2(2) \rangle \langle \chi_1(1) | \chi_{1^*}(1) \rangle \langle \chi_{2^*}(2) | \chi_2(2) \rangle$$

$$= \langle \varphi_1(1)\varphi_{2^*}(2) \left| \frac{1}{r_{21}} \right| \varphi_{1^*}(1)\varphi_2(2) \rangle \langle \chi_1(1) | \chi_{1^*}(1) \rangle \langle \chi_{2^*}(2) | \chi_2(2) \rangle \tag{5b}$$

and

$$H_{21}^{\text{exchange}} = -\langle \varphi_1(2)\varphi_{2^*}(1) | \hat{H}_{21} | \varphi_{1^*}(1)\varphi_2(2) \rangle \langle \chi_{2^*}(1) | \chi_{1^*}(1) \rangle \langle \chi_1(2) | \chi_2(2) \rangle$$

$$= -\langle \varphi_1(2)\varphi_{2^*}(1) \left| \frac{1}{r_{21}} \right| \varphi_{1^*}(1)\varphi_2(2) \rangle \langle \chi_{2^*}(1) | \chi_{1^*}(1) \rangle \langle \chi_1(2) | \chi_2(2) \rangle \tag{5c}$$

The Coulomb term describes the situation were one electron at the donor relaxes from the excited state to the ground state while a second electron at the acceptor is simultaneously excited to a higher state by dipole-dipole interaction. In the exchange term the electrons at the donor and the acceptor are transferred from one molecule to the other.[22] The exchange term arises from the antisymmetry conditions of the wavefuntion and is of purely quantum mechanical origin.[22]

To make electron exchange possible, direct orbital overlap of the interacting molecules is required and therefore it is only important at short distances.[22] Even in closely spaced systems, the Coulombic interaction is dominant for all allowed transitions, as long as the transition-dipole strength is reasonably high, while the orbital overlap is the main reason for energy transfer processes in forbidden transitions.[22, 26]

The overall rate constant of the energy transfer is proportional to the electron exchange and the Coulomb integral:[21]

$$k_{\text{EnT}}(\text{total}) \propto \left[\alpha \langle \psi(\text{D}^*)\psi(\text{A}) | \hat{H}_{\text{dd}} | \psi(\text{D})\psi(\text{A}^*) \rangle^2 \right] + \left[\beta \langle \psi(\text{D}^*)\psi(\text{A}) | \hat{H}_{\text{ex}} | \psi(\text{D})\psi(\text{A}^*) \rangle^2 \right] \tag{6}$$

Where $\psi(\text{D})$ and $\psi(\text{A})$ are the eigenfunctions of the donor and the acceptor and * denotes the excited state. α and β are prefactors to account for the weighting of the interaction terms. Descriptions of the two energy transfer mechanisms based on Coulombic interactions or exchange interactions were firstly derived by *Förster*[27] and *Dexter,*[11] after whom the theories, which will be discussed in the following sections, are named.

2.2.2 *Förster* Transfer

Derivation

In *Försters* dipole-dipole energy transfer mechanism the exchange interaction is neglected as this term is only of considerable size if orbital overlapp is ensures and therefore only possible at very short distances. The interaction Hamiltonian of the Coulomb potential can be interpreted as the influence of the electromagnetic field, induced by the transition dipole of molecule 1, on the transition moment of molecule 2.[26] The transition dipole of the donor has an oscillating electric field that interacts with the acceptor and induces an oscillating electric field, so that the donor simiultaneously realxes to its ground state while the acceptor gets excited.[21]

The derivation of *Försters* energy transfer rate is based on *Fermis* Golden Rule:

$$k_{\mathrm{EnT}}=\frac{2\pi}{\hbar}|\langle\psi_{\mathrm{i}}|V|\psi_{\mathrm{f}}\rangle|^2\,\delta(E_{\mathrm{i}}\text{-}E_{\mathrm{f}}) \tag{7}$$

Where ψ_{i} and ψ_{f} denote the wavefunctions of the initial and the final state of the system, V is the pertubation operator and E_{i} and E_{f} are the energies of the initial and final state.

The wavefunctions ψ_{i} and ψ_{f} can be described as:

$$\psi_{\mathrm{i}}=\varphi_{\mathrm{i}}\chi_{\mathrm{iv}'}\ and\ \psi_{\mathrm{f}}=\varphi_{\mathrm{f}}\chi_{\mathrm{fv}''} \tag{8}$$

With φ_{i} and φ_{f} are the electronic wavefunctions and $\chi_{\mathrm{iv}'}$ and $\chi_{\mathrm{fv}''}$ denote the nuclear wavefunctions with vibrational states v' and v''. Because the vibrational relaxation is faster than the energy transfer, a weigthed average of all accessible vibrational levels has to be taken into account.[28]

$$k_{\mathrm{EnT}}=\frac{2\pi}{\hbar}|\langle\varphi_{\mathrm{i}}|V|\varphi_{\mathrm{f}}\rangle|^2\sum_{\mathrm{v}'}\sum_{\mathrm{v}''}P_{\mathrm{iv}'}|\langle\chi_{\mathrm{iv}'}|\chi_{\mathrm{fv}''}\rangle|^2\delta(E_{\mathrm{iv}'}-E_{\mathrm{fv}''}) \tag{9}$$

With P_{i} being the initial distribution of the thermally accessible modes described by the *Boltzmann* distribution, E_{i} and E_{f} are the energies of the initial and final state in the vibrational state v' and $\mathrm{v}''$and $\hbar$ is Planck's constant devided by 2π. The nuclear wavefunctions can be written as a product over all possible normal modes j of the coordinates q:[29]

$$\langle\chi_{\mathrm{iv}'}|\chi_{\mathrm{fv}''}\rangle=\prod_{\mathrm{j}}\left\langle\sigma_{\mathrm{iv}_{\mathrm{j}}'}(q_{\mathrm{j}}')\middle|\sigma_{\mathrm{fv}_{\mathrm{j}}''}(q_{\mathrm{j}}'')\right\rangle \tag{10}$$

Because the interaction of the two molecules is due to electronic oscillations the pertubation operator can be described as dipole-dipole interaction.

Hence the Coulomb term can be expanded into a sum of multipole-multipole interactions, but mostly only dipole-dipole interactions are dominant and therefore are the only ones considered:

$$\langle\varphi_{\mathrm{i}}|V|\varphi_{\mathrm{f}}\rangle = \left\langle\varphi_{\mathrm{D}^*}\varphi_{\mathrm{A}}\middle|\widehat{H}_{\mathrm{dd}}\middle|\varphi_{\mathrm{D}}\varphi_{\mathrm{A}^*}\right\rangle = H_{\mathrm{dd}} = \frac{M_{\mathrm{D}}\cdot M_{\mathrm{A}}}{R^3} - 3\frac{(M_{\mathrm{D}}\cdot R)(M_{\mathrm{A}}\cdot R)}{R^5} \qquad (11a)$$

Where R denotes the distance between the donor and the acceptor and $\widehat{\mathrm{H}}_{\mathrm{dd}}$ is the Coulomb operator.

With the transition-dipole moments

$$M_{\mathrm{D}} = \sqrt{2}\langle\varphi_{\mathrm{D}}|er_{\mathrm{D}}|\varphi_{\mathrm{D}^*}\rangle \qquad (11b)$$

$$M_{\mathrm{A}} = \sqrt{2}\langle\varphi_{\mathrm{A}}|er_{\mathrm{A}}|\varphi_{\mathrm{A}^*}\rangle \qquad (11c)$$

r_{D} and r_{A} are the vectors of the dipole moment of the donor and the acceptor and φ_{D} and φ_{A} are the spatial wavefunctions of the donor and the acceptor in the excited (*) or ground state, respectively.[30]

From this equation of the electrostatic interaction energy, it is obvious that the transfer rate depends on the size of the transition-dipole moments and the distance of the molecules.[21] As the dipole approximation is used in this description, it is only valid for distances between the interacting molecules that are much larger than the dimension of the molecules.[22] For large dipole moments or small distances methodes that implement a more accurate description of the electron density such as the transition monopole approximation (TMA)[31] or the more complex transition density cube methode (TDC)[32] must be applied to get reliable results.

If the dipole approximation of the Coulomb term is incorporated into *Fermis* Golden Rule the transfer rate becomes:[28, 33, 34]

$$k_{\mathrm{EnT}} = \frac{2\pi}{\hbar}\left[\frac{M_{\mathrm{D}}M_{\mathrm{A}}}{nR^3}\kappa(\theta_{\mathrm{D}},\theta_{\mathrm{A}})\right]^2 \sum_{\mathrm{v}'}\sum_{\mathrm{v}''} P_{\mathrm{iv}'}\left\{\prod_{\mathrm{j}}\left|\left\langle\sigma_{\mathrm{iv}_{\mathrm{j}}'}\middle|\sigma_{\mathrm{fv}_{\mathrm{j}}''}\right\rangle\right|\right\}^2 \delta(E_{\mathrm{iv}'} - E_{\mathrm{fv}''}) \qquad (12a)$$

with the orientation factor

$$\kappa = (\cos\theta_{\mathrm{AD}} - 3\cos\theta_{\mathrm{D}}\cos\theta_{\mathrm{A}})^2 \qquad (12b)$$

and the refractive index of the medium is n.

Resonant vibronic transitions of donor and acceptor molecules ensure energy conversion and are hence crucial for efficient energy transfer. This important condition is implemented in the equation by the δ-function.

As the energy conversion in solution is reflected by vibrational motions, it can be interpreted as vibrational Franck-Condon weighted density of states (FCWD) for the electronic transition and one can write:[23]

$$k_{\mathrm{EnT}} = \frac{2\pi}{\hbar}\left[\frac{\kappa(\theta_{\mathrm{D}},\theta_{\mathrm{A}})}{nR^3}\right]^2 \int S_{\mathrm{D}}(\upsilon) S_{\mathrm{A}}(\upsilon) d\upsilon \qquad (13a)$$

with

$$S_{\mathrm{D}}(\upsilon) = M_{\mathrm{D}}^2 \sum_{\mathrm{v}'} \sum_{\mathrm{v}''} P_{\mathrm{iv}'} \left\{\prod_{\mathrm{j}} \left|\left\langle \sigma_{\mathrm{iv}_{\mathrm{j}}'} \middle| \sigma_{\mathrm{fv}_{\mathrm{j}}''} \right\rangle\right|\right\}^2 \delta\left(\omega - \omega_{\mathrm{iv}',\mathrm{fv}''}^{\mathrm{D}}\right) \qquad (13b)$$

$$S_{\mathrm{A}}(\upsilon) = M_{\mathrm{A}}^2 \sum_{\mathrm{v}'} \sum_{\mathrm{v}''} P_{\mathrm{iv}'} \left\{\prod_{\mathrm{j}} \left|\left\langle \sigma_{\mathrm{iv}_{\mathrm{j}}'} \middle| \sigma_{\mathrm{fv}_{\mathrm{j}}''} \right\rangle\right|\right\}^2 \delta\left(\omega - \omega_{\mathrm{iv}',\mathrm{fv}''}^{\mathrm{A}}\right) \qquad (13c)$$

$\omega_{\mathrm{iv}',\mathrm{fv}''}^{\mathrm{D}}$ and $\omega_{\mathrm{iv}',\mathrm{fv}''}^{\mathrm{A}}$ denote the energy difference between the initial and the final state of the donor or the acceptor.

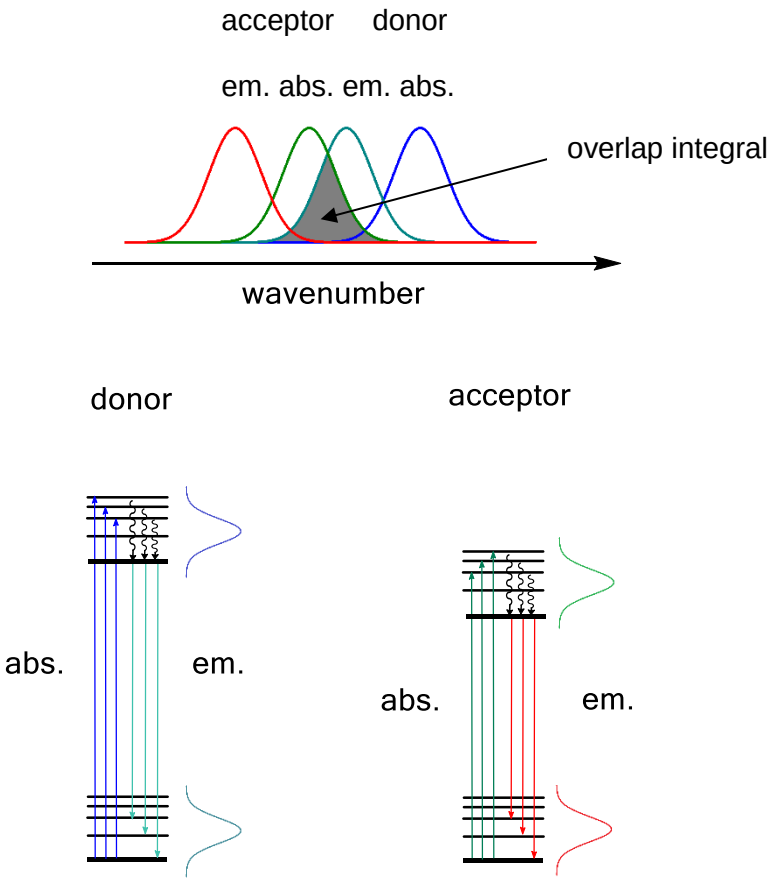

Figure 3 Schematic representation of resonant energy transfer in a donor acceptor system with several vibrational levels. The spectral overlap integral that ensures energy conversion, is depicted above.

The integral describes the overlap between the absorption spectrum of the acceptor and the emission spectrum of the donor (see Figure 3) and hence are closely related to the emission spectrum $f_{\mathrm{D}}(\nu)$ of the donor and the absorption spectrum $\varepsilon_{\mathrm{A}}(\nu)$ of the acceptor

$$\varepsilon_{\mathrm{A}}(\nu) = \frac{4\pi^2 \nu N_{\mathrm{AV}}}{3000(\ln 10) n \hbar c} S_{\mathrm{A}}(\upsilon) \tag{14}$$

$$f_{\mathrm{D}}(\nu) = \frac{32\pi^3 n \tau_{\mathrm{D}} \nu^3}{3\hbar c^3 Q_{\mathrm{D}}} S_{\mathrm{D}}(\upsilon) \tag{15}$$

Where τ_{D} and Q_{D} are the lifetime and the quantum yield of the donor in abscence of the acceptor, c is the speed of the light and N_{AV} is the Avogadro constant.[34]

If eq. (14) and eq. (15) are implemented into eq. (13a) and frequency is changed to wavenumber with $\tilde{\upsilon} = \frac{\upsilon}{c}$, the resulting standard *Förster* formulation is:[30, 33, 34]

$$k_{\mathrm{EnT}}^{\mathrm{dd}} = \frac{9000(\ln 10)\kappa^2 Q_{\mathrm{D}} J_{\mathrm{C}}}{128\pi^5 n^4 N_{\mathrm{AV}} R^6 \tau_{\mathrm{D}}} \tag{16}$$

Rate and Efficiency Dependency

The energy transfer rate is strongly distance dependent with R^{-6} and hence is regularly used for measuring distances in molecular biological systems.[35-40] For this purpose, a distance dependent formulation of the rate constant is of advantage.

If two molecules are separated by the *Förster* distance the rate of energy transfer is exactly the inverse decay time of the donor in the absence of the acceptor:[41-43]

$$k_{\mathrm{EnT}}^{\mathrm{dd}} = \frac{1}{\tau_{\mathrm{D}}} \left(\frac{R_0}{R}\right)^6 \tag{17}$$

Where τ_{D} is the lifetime of the donor in the absence of the acceptor, R_0 is the *Förster* distance and R is the distance between donor and acceptor. The *Förster* distance is defined as:[33]

$$R_0^6 = \frac{9000(\ln 10)\kappa^2 Q_{\mathrm{D}} J_{\mathrm{C}}}{128\pi^5 n^4 N_{\mathrm{AV}}} \tag{18}$$

With Q_{D} being the quantum yield of the donor in the absence of the acceptor, n is the refractive index of the medium, N_{AV} is *Avogadro's* constant, κ^2 the orientation factor and J_C the overlap integral.

The overlap integral in wavenumber form is given by:[33, 42]

$$J_{\mathrm{C}} = \int_0^{\infty} \frac{f_{\mathrm{D}}(\tilde{\nu})\varepsilon_{\mathrm{A}}(\tilde{\nu})}{\tilde{\nu}^4} d\tilde{\nu} \tag{19a}$$

with $f_{\mathrm{D}}(\tilde{\nu})$ being the normalised fluorescence:

$$f_{\mathrm{D}}(\tilde{\nu}) = \frac{F_{\mathrm{D}}(\tilde{\nu})}{\int_0^{\infty} F_{\mathrm{D}}(\tilde{\nu}) d\tilde{\nu}} \tag{19b}$$

The overlap integral of donor fluorescence and acceptor absorption summarises a number of complicated relations in one simple measurable value. It incorporates line shapes and hence temperature dependency, energy relaxation *via* the *Stokes* shift and nuclear overlap factors in the form of the Franck-Condon overlap.[12] As convenient as this simplification is, the spectral overlap integral assumes that the vibrational relaxation of donor and acceptor are independent of each other, which becomes incorrect in the intermediate coupling range.[44] Therefore the Förster Theory is only applicable if the systems are coupled by very week interactions so that the spectroscopic characteristica remain unchanged in relation to the constituents.

Besides the overlap integral another important influence on the energy transfer rate is the alignment of the transition-dipole moments, and with that the orientation factor *κ* that can be calculated by the following relationship:

$$\kappa^2 = (\cos\theta_{\mathrm{AD}} - 3\cos\theta_{\mathrm{D}}\cos\theta_{\mathrm{A}})^2 \tag{20}$$

θ_{D} and θ_{A} define the angle between the transition-dipole moment and the connecting vector from the center of the donor to the center of the acceptor and θ_{AD} is the angle between the two transition-dipole moments

The orientation of the transition-dipole moments relative to each other dictates the strength of the interaction, as can be seen in Figure 4 on the right. If the transition moments are in-line the maximum value of 4 for κ^2 is reached, while a perpendicular orientation leads to no coupling and hence no energy transfer. In many cases the orientation of the transition moments is not fixed but the molecules can rotate and have a distribution of orientations. If the rotation is much faster than the relaxation rate of the donor, an average value of $\kappa^2 = \frac{2}{3}$ can be assumed.[22, 33]

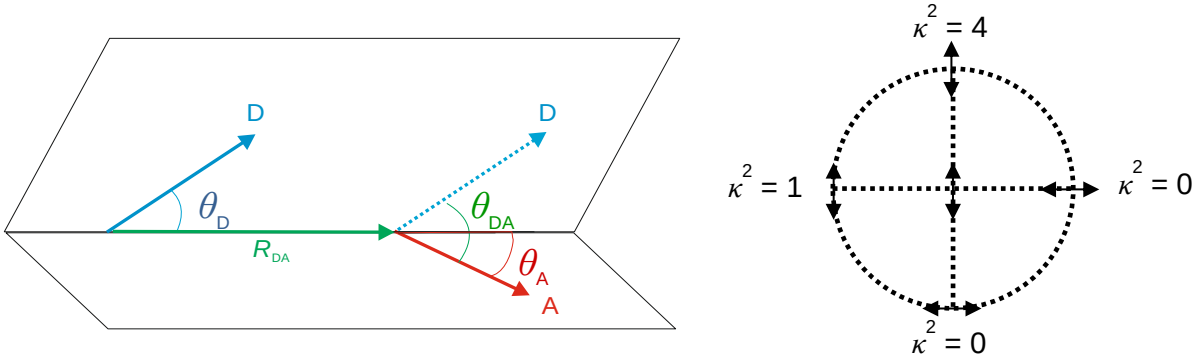

Figure 4 Illustration of the transition-dipole moments of acceptor and donor and the projection of the latter. θ_D and θ_A define the angle between the transition-dipole moments, and R_{DA} the connecting vector from the center of the donor to the center of the acceptor and θ_{AD} the angle between the two transition-dipole moments. (left). The orientation factor κ dependent on the orientation of the transition-dipole moments is depicted on the right.

In order for energy transfer to occur efficiently, not only the energy transfer rate but also the competing deactivation pathways have to be accounted for and can be expressed as:

$$E = \frac{k_{EnT}}{k_{EnT}+k_D+k_{Di}} \tag{21}$$

With k_{EnT} as the rate constant of the energy transfer, k_D is the radiative decay constant and k_{Di} is the radiationless decay constant. The transfer efficiency E can be determined by measuring the fluorescence quantum yield of the donor in the absence and in the presence of the acceptor:

$$E = 1 - \frac{Q_{DA}}{Q_D} \tag{22a}$$

$$Q_{DA} = \frac{k_{EnT}}{k_{EnT}+k_D+k_{Di}} \tag{22b}$$

$$Q_D = \frac{k_D}{k_D+k_{Di}} \tag{22c}$$

To obtain a distance dependent energy transfer efficiency, eq. (17) is incorporated in eq. (21) and this leads to:

$$E = \frac{R_0^6}{R_0^6+R^6} \tag{23}$$

From this formulation, the definition of the *Förster* radius can be deduced as the distance where the energy transfer efficiency is 50 %.[33]

Considering all these properties derived from the formulation of the dipole-dipole interaction mechanism, *Förster* enegy transfer is most efficient if the following criteria are fulfilled:

- A large spectral overlap between acceptor absorption and donor fluorescence
- A large radiative rate constant of the donor, meaning a large oscillator strength for the transition from the excited state to the ground state
- The extinction coefficient ε_A of the acceptor is high in the spectral overlap region of donor and acceptor
- Donor and acceptor are closer than the *Förster* radius
- A favourable orientation of the transition dipoles of donor and acceptor is given.[21]

If the interacting molecules come too close, the dipole-dipole approximation breaks down, which is one of the basic asumptions of *Förster's* theory, and other theories are necessary to describe energy transfer in such systems accuratly.[26]

2.2.3 *Dexter* Transfer

The original derivation of the *Dexter* mechanism is based on the assumption of a parallel two-electron transfer from the donor to the acceptor and vice verca, meaning excitation energy is transfered (see Figure 2, red arrows).[11, 45] Here, in contrast to *Försters* theory, spin wavefunctions not necessarly need to be constant which makes energy transfer to triplet states possible as well. This can be seen when looking at equation (5b), where the product of the spin functions of the Coulomb term vanishes if the spin wavefuntions of the molecules are different.[26]

As already mentioned in Chapter 2.2.1, the exchange integral is dominant for the *Dexter* mechanism and applying *Fermis* Golden Rule the rate can be formulated similar to *Försters*:[30]

$$k_{\mathrm{EnT}}^{\mathrm{ex}} = \frac{2\pi}{\hbar} H_{\mathrm{ex}}^2 \sum_{\mathrm{v}'} \sum_{\mathrm{v}''} P_{\mathrm{i}} \left| \prod_{\mathrm{j}} \left\langle \sigma_{\mathrm{iv}_{\mathrm{j}}'} \middle| \sigma_{\mathrm{fv}_{\mathrm{j}}''} \right\rangle \right|^2 \delta(E_{\mathrm{i}} - E_{\mathrm{f}}) \tag{24a}$$

with

$$H_{\mathrm{ex}} = \langle \varphi_{\mathrm{D}^*}(1) \varphi_{\mathrm{A}}(2) \left| \frac{1}{r_{21}} \right| \varphi_{\mathrm{D}}(2) \varphi_{\mathrm{A}^*}(1) \rangle \tag{24b}$$

With H_{ex} as the exchange integral and P_{i} as the initial distribution of the vibrational accessible states. As the overlap of the orbitals defines the efficiency of the exchange interaction, the distance dependency with which the orbital overlap becomes smaller also defines the rate constant of the energy transfer.

Assuming hydrogen like orbitals, the common *Dexter* formulation is:[30]

$$k_{\mathrm{EnT}}^{\mathrm{ex}} = \frac{2\pi}{\hbar} K J_{\mathrm{ex}} e^{(-2R/L)} \tag{25a}$$

Here L is an average *van der Waals* radius, K is a constant that cannot directly be derived from spectroscopic features and the integral overlap J_{ex} is defined as: [22]

$$J_{\mathrm{ex}} = \int_0^{\infty} f_{\mathrm{D}}(\tilde{\nu}) \varepsilon_{\mathrm{A}}(\tilde{\nu}) d\tilde{\nu} \tag{25b}$$

with the normalisation condition:

$$\int_0^{\infty} f_{\mathrm{D}}(\tilde{\nu}) d\tilde{\nu} = \int_{\infty}^{0} \varepsilon_{\mathrm{A}}(\tilde{\nu}) d\tilde{\nu} = 1 \tag{25c}$$

This normalisation entails that the overlap integral does not depend on the extinction coefficient. This is important in comparison with the *Förster* transfer, where the intensity of the absoprtion in the overlap area is important for a fast transfer rate. For the *Dexter* transfer

the overlap integral can be thought of as density of degenerated states that couple the donor and the acceptor, as only the shape and not the size of the band is important.[21, 30]

The exponential distance dependency leads to a fast decrease of the energy transfer rate of the exchange mechanism. The difference of the distance dependency of *Förster* and *Dexter* energy transfer is the best way of distinguishing between the two mechanisms. Coulombic interactions can lead to an efficient energy transfer up to distances of 30–40 Å, while the orbital overlap already diminishes at distances larger than 10 Å.[21]

2.3 Excitons: Strongly Coupled Systems

2.3.1 Exciton Theory

If the energy transfer rate in a molecular aggregate is much faster than vibrational relaxation, the excitation energy gets delocalised over the whole molecule, and the interaction of the molecules can be expressed in a new wavefuntion that is a superposition of the individual molecules. This coherent interaction between the excited states produces a wavepacket that extends over the whole molecule and can be described by exciton theory.[3, 15-19, 24] The exciton theory is based on the description by *Frenkel*[14] of localised electron hole pairs, called excitons. The simplest system that can show excitonic interaction is a dimer.

The Iocated molecules have two eigenstates described by:[18]

$$\hat{H}_{\mathrm{n}}\varphi_{\mathrm{n}}^{(\mathrm{i})} = \varepsilon_{\mathrm{n}}^{(\mathrm{i})}\varphi_{\mathrm{n}}^{(\mathrm{i})} \tag{26}$$

Where n denotes the molecule 1 or 2 and i the excited (e) or the ground state (g)

The electronic ground state of the dimer can be denoted as:

$$\psi_{\mathrm{g}} = \varphi_1^{\mathrm{g}}\varphi_2^{\mathrm{g}} \tag{27}$$

This formulation is possible since the interaction can be seen as weak and described as a pertubation, and therefore the eigenfunctions of the dimer can be written as superpositions of the product of molecular eigenfunctions. In this description, electronic exchange is neglected, hence the wavefunction is not antisymmetric.[18]

To describe the two molecules apart from the Hamiltonians $\hat{H}_1$ and $\hat{H}_2$ for the individual molecules, a third operator $\hat{V}$ has to be incorporated to account for the interaction between the molecules.

This leads to the describtion of the electronic ground state energy as follows:

$$E_{\mathrm{g}} = \left\langle \varphi_1^{(\mathrm{g})} \varphi_2^{(\mathrm{g})} \middle| \hat{H}_1 + \hat{H}_2 + \hat{V} \middle| \varphi_1^{(\mathrm{g})} \varphi_2^{(\mathrm{g})} \right\rangle$$

$$= \left\langle \varphi_1^{(\mathrm{g})} \middle| \hat{H}_1 \middle| \varphi_1^{(\mathrm{g})} \right\rangle + \left\langle \varphi_2^{(\mathrm{g})} \middle| \hat{H}_2 \middle| \varphi_2^{(\mathrm{g})} \right\rangle + \left\langle \varphi_1^{(\mathrm{g})} \varphi_2^{(\mathrm{g})} \middle| \hat{V} \middle| \varphi_1^{(\mathrm{g})} \varphi_2^{(\mathrm{g})} \right\rangle = \varepsilon_1^{(\mathrm{g})} + \varepsilon_2^{(\mathrm{g})} + V_{\mathrm{gg}} \quad (28)$$

Here V_{gg} is the stabilisation energy of the ground state that originates from the interaction of the molecules and can be described in terms of a Coulombic potential.[46]

The electronic excited state can be written as linear combination of the excitation being localised at one or the other molecule:

$$\psi_{\mathrm{e}} = c_{\mathrm{e}1} \varphi_1^{(\mathrm{e})} \varphi_2^{(\mathrm{g})} + c_{\mathrm{e}2} \varphi_1^{(\mathrm{g})} \varphi_2^{(\mathrm{e})} = c_{\mathrm{e}1} \Psi_1 + c_{\mathrm{e}2} \Psi_2 \quad (29)$$

The eigenstates have to be normalised and orthogonal, therefore the coefficients have to fulfil the following condition:

$$|c_{\mathrm{e}1}|^2 + |c_{\mathrm{e}2}|^2 = 1 \quad (30)$$

To calculate the eigenenergies of the excited state the stationary *Schrödinger* equation has to be solved:[18]

$$\left(\hat{H}_1 + \hat{H}_2 + V\right) \psi_{\mathrm{e}} = E_{\mathrm{e}} \psi_{\mathrm{e}} \quad (31)$$

Considering that $\langle \Psi_{\mathrm{i}} | \Psi_{\mathrm{j}} \rangle = 0$ if i≠j, two eigenfunctions and two eigenenergies are resulting:[26]

$$\psi_{\mathrm{B}^+} = \sqrt{\frac{(1+s)}{2}} \psi_1 + \sqrt{\frac{(1-s)}{2}} \psi_2 \; ; E_{\mathrm{B}^+} = E_0 + \frac{1}{2} \sqrt{\delta^2 + 4H_{12}^2}; \quad (32a)$$

$$\psi_{\mathrm{B}^-} = \sqrt{\frac{(1-s)}{2}} \psi_1 - \sqrt{\frac{(1+s)}{2}} \psi_2 \; ; E_{\mathrm{B}^-} = E_0 - \frac{1}{2} \sqrt{\delta^2 + 4H_{12}^2}; \quad (32b)$$

with

$$s = \frac{\delta}{\sqrt{\delta^2 + 4H_{12}^2}} \quad (32c)$$

$$\delta = H_{11} - H_{22} \quad (32d)$$

and

$$E_0 = \frac{(H_{11} + H_{22})}{2} \quad (32e)$$

Hereby ψ_{B^+} and E_{B^+} denote the wavefunction or energy describing the upper excitonic state and ψ_{B^-} and E_{B^-} characterise the excitonic state lower in energy. δ stands for the energy difference between the non-interacting monomers. H_{11}, H_{22} and H_{12} are defined as follows:

$$H_{11} = \langle \varphi_1^* \varphi_2 | \hat{H}_1 + \hat{H}_{12} | \varphi_1^* \varphi_2 \rangle = E_1 + \langle \varphi_1^* \varphi_2 | \hat{H}_{12} | \varphi_1^* \varphi_2 \rangle \quad (33a)$$

$$H_{22} = \langle \varphi_1 \varphi_2^* | \hat{H}_2 + \hat{H}_{12} | \varphi_1 \varphi_2^* \rangle = E_2 + \langle \varphi_1 \varphi_2^* | \hat{H}_{12} | \varphi_1 \varphi_2^* \rangle \quad (33b)$$

$$H_{12} = H_{21} = \langle \varphi_1^* \varphi_2 | \hat{H}_{12} | \varphi_1 \varphi_2^* \rangle = \langle \varphi_1 \varphi_2^* | \hat{H}_{21} | \varphi_1^* \varphi_2 \rangle \quad (33c)$$

If the two molecules are significantly different in energy and $|\delta| \gg |H_{12}|$, this leads to:

$$\psi_{B^+} \rightarrow \psi_1 \, ; E_{B^+} = H_{11} \quad (34a)$$

$$\psi_{B^-} \rightarrow \psi_2 ; E_{B^-} = H_{22} \quad (34b)$$

In this case, the lower excited state has mostly the spectroscopic character of molecule 2 whereas the higher energetic state is more similar to molecule 1. The mixing is not very strong and the molecules retain most of their individual properties (see Figure 5, left).

On the contrary, if the two molecules are very similar in energy $|\delta| \ll |H_{12}|$ the following relations for eigenfunctions and eigenenergies become:

$$\psi_{B^+} = 2^{-1/2}(\psi_1 + \psi_2); E_{B^+} = E_0 + H_{21}; \quad (35a)$$

$$\psi_{B^-} = 2^{-1/2}(\psi_1 - \psi_2); E_{B^-} = E_0 - H_{21}; \quad (35b)$$

The states are completely mixed and a large splitting occurs which leads to a distinct lowering of the E_{B^-} state and raise of the upper state (see Figure 5, right).[26, 47]

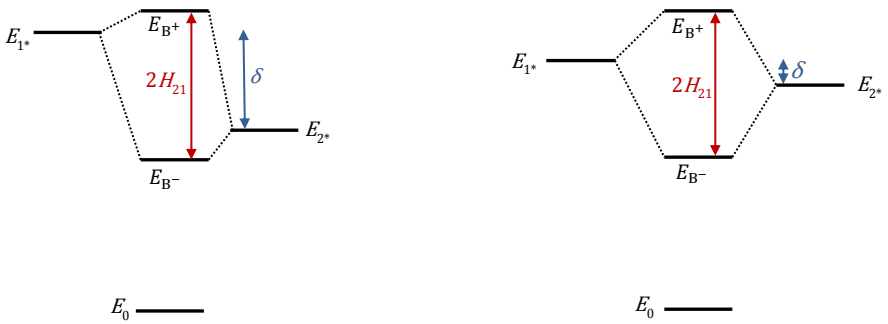

Figure 5 Splitting of the excitonic states depending on the energy difference of the interacting molecules.

2.3.2 Transition-Dipole Moments and Orientation Dependency

The energetic splitting of the excitonic states (see Chapter 2.3.1) can be observed in the absorption spectrum and serves as a reference for the coupling strength of the molecules. The dimer has two separated absorption bands from which the oscillator strength can be deduced from the transition-dipole moments:

$$\mu_{\mathrm{eg}^{\pm}} = \langle \psi_{\mathrm{e}^{\pm}} | \mu_1 + \mu_2 | \psi_{\mathrm{g}} \rangle = \left\langle C_{1(\mathrm{e}^{\pm})} \varphi_1^* \varphi_2 + C_{2(\mathrm{e}^{\pm})} \varphi_1 \varphi_2^* \middle| \mu_1 + \mu_2 \middle| \varphi_1 \varphi_2 \right\rangle$$

$$= C_{1(\mathrm{e}^{\pm})} \langle \varphi_1^* | \hat{\mu}_1 | \varphi_1 \rangle + C_{2(\mathrm{e}^{\pm})} \langle \varphi_2^* | \hat{\mu}_2 | \varphi_2 \rangle = C_{1(\mathrm{e}^{\pm})} \mu_1 + C_{2(\mathrm{e}^{\pm})} \mu_2 \qquad (36a)$$

and

$$D_{\mathrm{eg}^{\pm}} = \left(C_{1(\mathrm{e}^{\pm})} \mu_1 + C_{2(\mathrm{e}^{\pm})} \mu_2 \right) \left(C_{1(\mathrm{e}^{\pm})} \mu_1 + C_{2(\mathrm{e}^{\pm})} \mu_2 \right)$$

$$= C_{1(\mathrm{e}^{\pm})}^2 D_{\mathrm{eg}(1)} + C_{2(\mathrm{e}^{\pm})}^2 D_{\mathrm{eg}(2)} + 2 C_{1(\mathrm{e}^{\pm})} C_{2(\mathrm{e}^{\pm})} \mu_1 \mu_2 \qquad (36b)$$

Where μ_1 and μ_2 are the transition-dipole moment vectors of the individual molecules, $D_{\mathrm{eg}(1)}$ and $D_{\mathrm{eg}(2)}$ are the dipole strengths of the individual molecules and $C_{1(\mathrm{e}^{\pm})}^2$ and $C_{2(\mathrm{e}^{\pm})}^2$ are the coefficients of the excited states. The asterisk denotes the excited state. The coefficients account for the distribution of the dipole strength between the two absorption bands. The maximum value of oscillator strength that one absorption band can account for is $2D_{\mathrm{eg}}$, which leaves the second band with zero oscillator strength. If fluorescence occurs from such an exclusively allowed state, it is called superradiance or cooperative spontaneous emission.[20] Following the sum rule for excitonic bands, the sum of the dipole strength of all bands of the excitonic spectrum must be equal to the sum of the monomeric dipole strengths.[26]

If we consider the case of a homodimer with $\delta = 0$, $D_{\mathrm{eg}(1)} = D_{\mathrm{eg}(2)}$ and the coefficients known from solving the *Schrödinger* equation:[18]

$$C_{1(\mathrm{e}^+)} = \frac{1}{\sqrt{2}};\ C_{1(\mathrm{e}^-)} = \frac{1}{\sqrt{2}};\ C_{2(\mathrm{e}^+)} = \frac{1}{\sqrt{2}};\ C_{2(\mathrm{e}^-)} = -\frac{1}{\sqrt{2}}; \tag{37}$$

we get to the following simplification of the description of dipole moments and oscillator strengths:

$$\mu_{\mathrm{eg}^+} = \frac{1}{\sqrt{2}}(\mu_1 + \mu_2) \tag{38a}$$

$$\mu_{\mathrm{eg}^-} = \frac{1}{\sqrt{2}}(\mu_1 - \mu_2) \tag{38b}$$

$$D_{\mathrm{eg}^+} = C_{1(\mathrm{e}^+)}^2 D_{\mathrm{eg}} + C_{2(\mathrm{e}^+)}^2 D_{\mathrm{eg}} + 2C_{1(\mathrm{e}^+)}C_{2(\mathrm{e}^+)}\mu_1\mu_2 = \frac{1}{2}D_{\mathrm{eg}} + \frac{1}{2}D_{\mathrm{eg}} + D_{eg}cos\theta$$

$$= D_{\mathrm{eg}} + D_{\mathrm{eg}}\cos\theta = D_{\mathrm{eg}}(1 + \cos\theta) \tag{38c}$$

$$D_{\mathrm{eg}^-} = C_{1(\mathrm{e}^-)}^2 D_{\mathrm{eg}(1)} + C_{2(\mathrm{e}^-)}^2 D_{\mathrm{eg}(2)} + 2C_{1(\mathrm{e}^-)}C_{2(\mathrm{e}^-)}\mu_1\mu_2 = \frac{1}{2}D_{\mathrm{eg}} + \frac{1}{2}D_{\mathrm{eg}} - D_{eg}cos\theta$$

$$= D_{\mathrm{eg}} - D_{\mathrm{eg}}\cos\theta = D_{\mathrm{eg}}(1 - \cos\theta) \tag{38d}$$

From eq. (38a), eq. (38b), eq. (38c) and eq. (38d) it can be concluded that the transition dipole of the excitonic state is proportional to the vector sum of the transition-dipole moments of the monomers. The dipole strength of the bands depends on the angle θ between the transition moments and can range from 0 to $2D_{\mathrm{eg}}$.[26] The angle θ between the transition moments does not only influence the dipole strength of a transition, but is also important for the Coulomb interaction H_{21}. The transition moments influence the sign of the coupling element and hence the fact if the allowed transition is higher or lower in energy (see Figure 6).[18, 47] Starting from an in-line dimer, where $\theta = 0°$ and all dipole strength is combined in the lower transition, the transition higher in energy is forbidden. Moving the molecules in a way that the transition moments relative to each other vary, but stay in the same plane, the splitting gets smaller until no distinction between the states can be seen at an angle of $\theta = 54.7°$. When the transition moments are moved further a splitting reappears until a maximum is reached at $\theta = 90°$ where the transition moments are parallel to each other. Contrary to the extreme case of the in-line-dimer, the parallel dimer has a forbidden transition at low energies and the upper state combines all dipole strength. The change of the allowed state is due to the dipole interaction of the molecules. For an in-line dimer the parallel arrangement leads to attraction, implying a negative sign in the Coulomb interaction and therefore the energy of the state is lowered relative to the excited monomer state. For the parallel dimer in an arrangement were both transition moments have the same direction,

repulsion is the consequence and the state is raised above the energy level of the monomer state.[26] The lowering or raise of the allowed transitions lead to distinct shifts in the spectrum compared to the monomer. The parallel alignment of the transition-dipole moments, also called H-aggregates,[48] leads to a blue-shift of the absorption band relative to the monomer and quenching of the fluorescence. Molecules where the transition-dipole moments are oriented in-line are also refered to as J-aggregates[49] and are characterised by a shift to lower wavenumbers and enhanced fluorescence. Furthermore, the band splitting of the in-line dimer is more pronounced than for the parallel dimer. This is due to the angle dependency which results from the dipole approximation:[18, 46]

$$\Delta\varepsilon = \frac{2|\mu|^2}{r_{12}^3}\,(1 - 3\cos^2\theta) \tag{39}$$

Where $\Delta\varepsilon$ denotes the band splitting, μ the transition moment of the monomer, r_{12} the distance between the two molecules and θ the angle between the transition-dipole moments of the connecting vector of the two transition-dipole moments.

This angle dependency explains the difference in the energy splitting of H- and-J aggregates, (see Figure 6) as for a parallel allignement ($\theta = 90° \rightarrow \cos(90°) = 0$) a smaller value of 1 and for an in-line arrangement ($\theta = 0° \rightarrow \cos(0°) = 1$) a larger value of -2 is obtained from the trigonometric function for the term in brackets in eq. (39). Hence the splitting for a J-aggregate is twice the sice than the one in a H-aggregate. Furthermore, the angle θ, were no exciton splitting occurs, can be derived as $\theta = \arccos\frac{1}{\sqrt{3}} = 54.7°$.

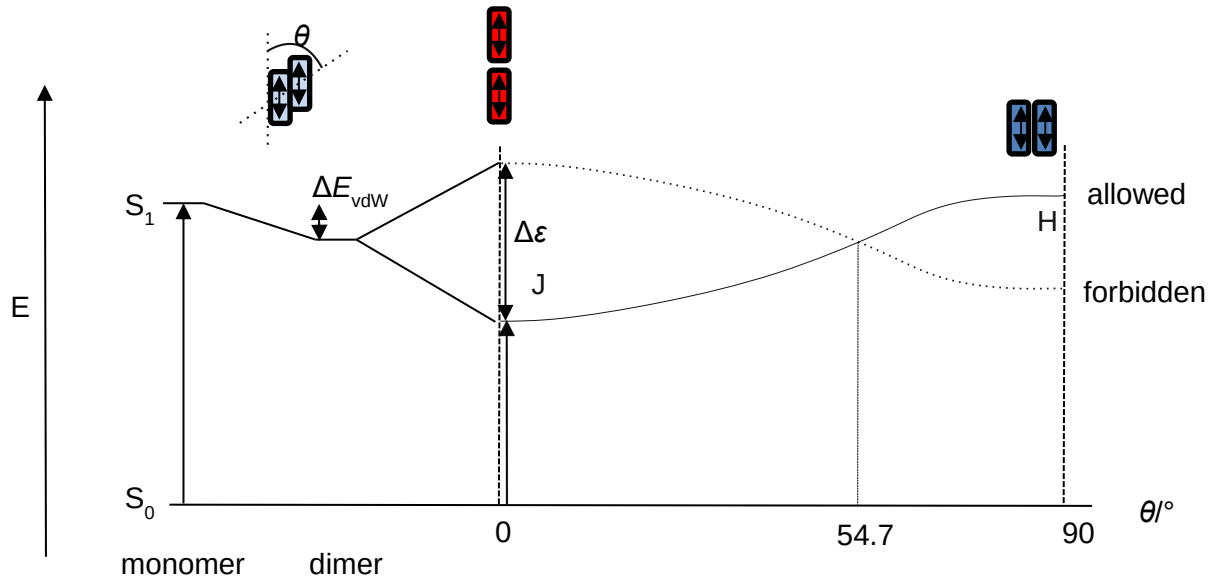

Figure 6 Dependency of excitonic transitions on the angle θ in a coplanar dimer.

So far, only the influence of the orientation of the transition-dipole moments arranged in the same plane with a relative angle θ to each other on the exciton band splitting was considered. If the tilting out of plane is incorporated a new relation of the exciton band energy depending on the two angles α and θ arises:

$$\Delta\varepsilon = \frac{2|\mu|^2}{r_{12}^3}(\cos\alpha + 3\cos^2\theta) \qquad (40)$$

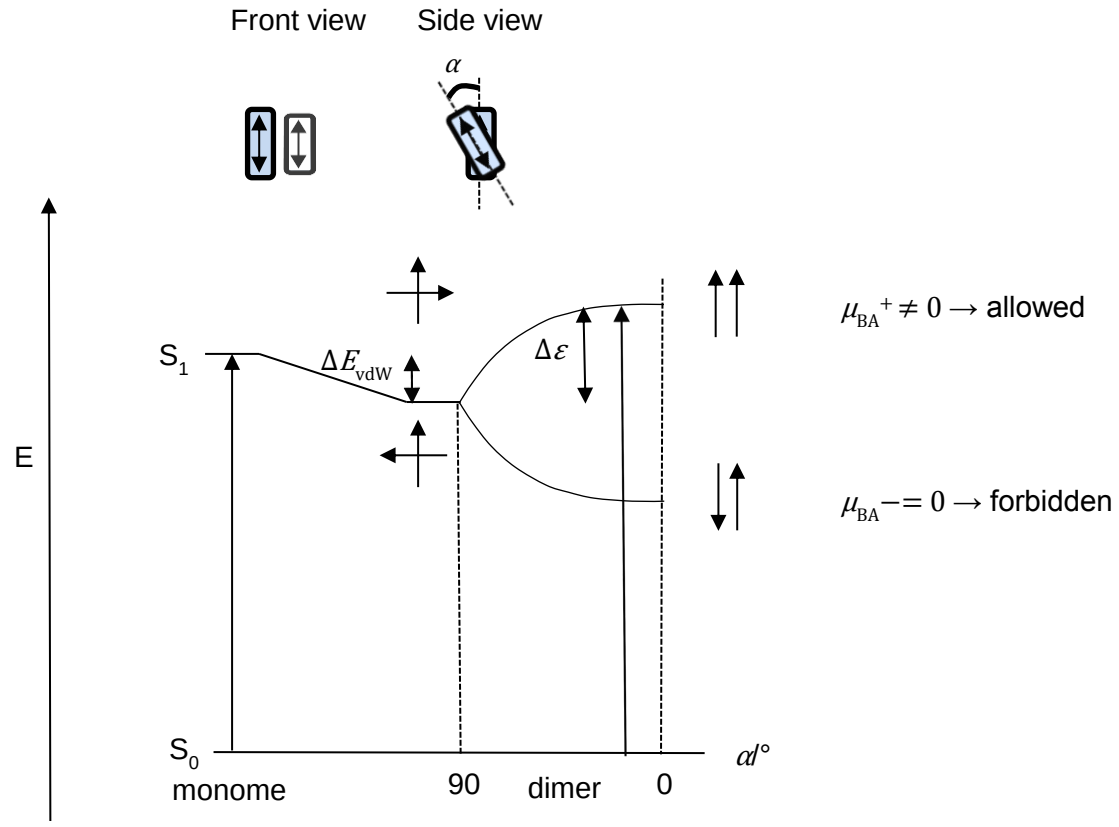

Figure 7 The influence of the angle α in a non-coplanar dimer and the resulting transition moments of the states.

For a non-coplanar dimer no band splitting is observed for $\alpha = 90°$, as the coupling strength is zero. Maximum splitting is found at $0°$ (see Figure 7) and at $180°$ (not depicted). Just as described for the coplanar dimer, the allowed and forbidden transitions interchange depending on the angle α. At an orientation of $0°$ the transition at higher energies is allowed while the low-energy transition is forbidden. At $180°$ this is vice versa.

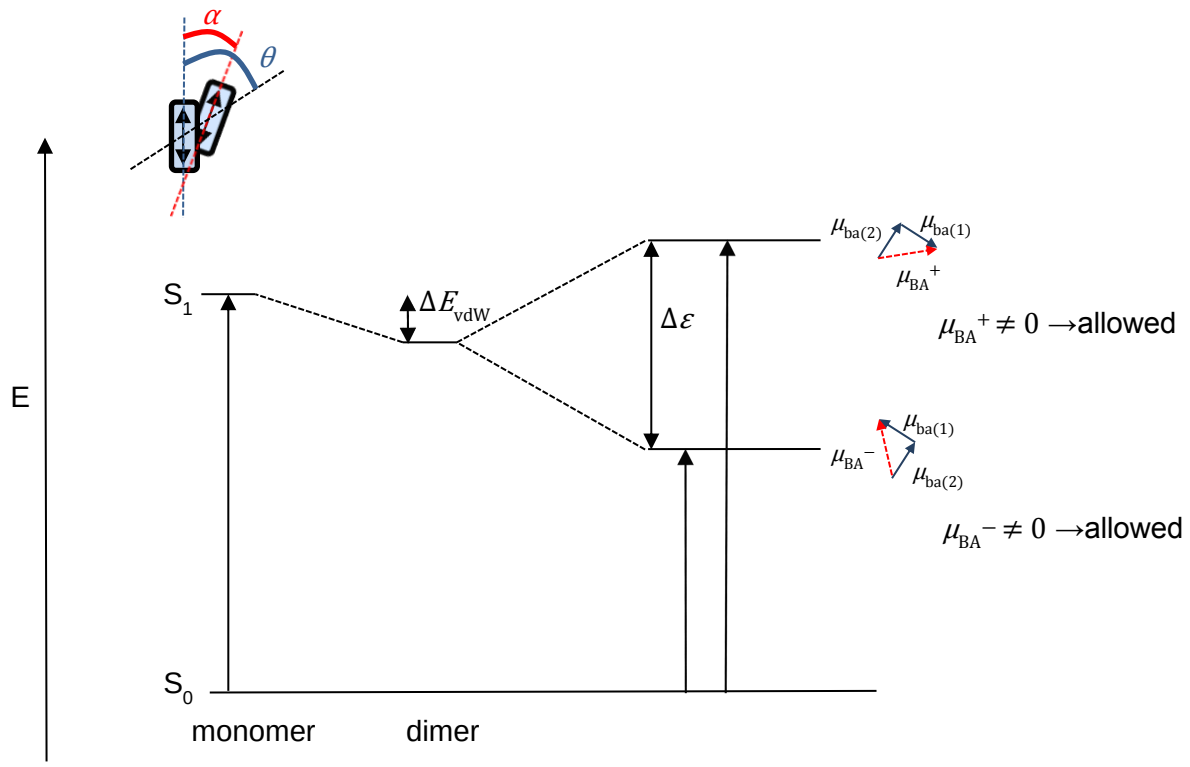

Figure 8 Band splitting of a dimer with the angle α and θ between the transition-dipole moments.

In the case of oblique orientation of the transition-dipole moments, the dipole strength is shared between both transitions and no transition-dipole moment is canceled (see Figure 8). As a consequence, a band splitting can be observed in the spectrum, in which the band ratio depends on the dipole strength of the states. This can be calculated using equation (40).

2.3.3 Solvent Interaction and Exchange Narrowing

After excitation, molecules are normaly in a hot state and relax by interactions with their surroundings. This leads to inhomogenous broadening of bands. For excitons the interaction with the solvent becomes weaker with larger delocalisation, and as a consequence, the spectral bands are narrowed compared to the monomer. If we consider a homodimer in solution, both molecules have equal electronic energies, but are slightly shifted on the solvent coordinate (see Figure 9) as the surrounding is not exactly equal. The excitonic interaction is large in comparison to the interaction with the solvent, and two states, one lower than the individual molecules and one higher, are formed. The excitonic states are represented by a lower curvature of the parabola which accounts for the smaller *Stokes* shift of the dimer in comparison to the monomer. If the dimer is excited into higher vibrational

levels and relaxes, it is not localised on one of the molecules. This delocalisation leads to a band narrowing in the spectrum by a factor of $\sqrt{2}$ of the single molecule band width. This so called exchange narrowing can be explained by the delocalisation averaging over the inhomogenous linewidth of the individual molecules. This leads to a cancelling of larger deviations and hence to a band narrowing.[20, 50]

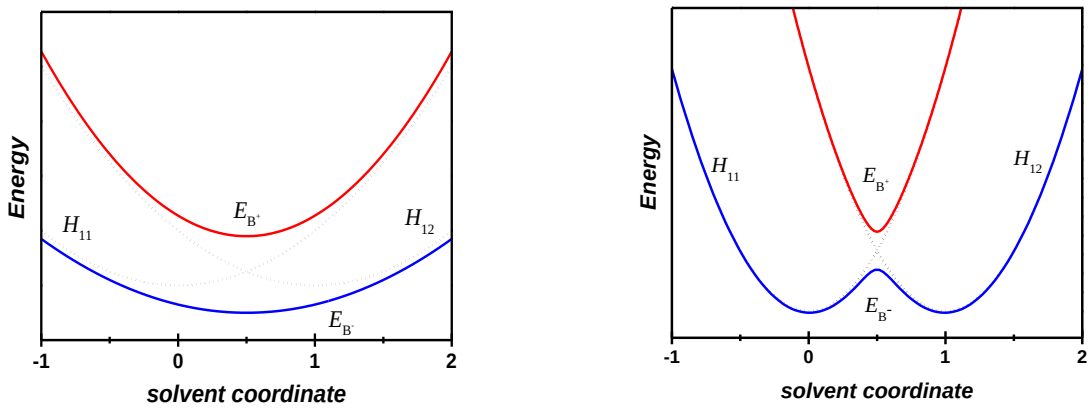

Figure 9 Influence of different coupling strength on the shape of the excited state potential of the exciton. H_{11} and H_{22} (dashed lines) are the potentials of the individual molecules and E_{B^+} (red) and E_{B^-} (blue) are the excitonic potentials.

If the interaction of the two molecules is small in comparison with the stabilisation through the solvent, two minima E_{B^-} result, which are in close proximity to the minima of the individual molecules. Therefore, after relaxation, the excitation becomes more localised on one of the individual molecules, and two absorption bands arise in the spectrum at a similar frequency compared the monomers.[26]

3 State of the Art

3.1 Pyrene-Containing HABs in Energy Transfer

In a hexaarylbenzene (HAB) six π-molecules are arranged in a ring-like fashion around the central benzene ring. In this alignment the C_2 axes of the central ring form a 60° angle to one another and the arene planes are tilted round about 60° out of the benzene plane. Because of this propeller-like arrangement, interactions *via* the central benzene ring can be neglected but the electronic coupling through-space is possible (see Figure 10). Therefore they are suitable modell compounds to study π-interactions between the arene molecules.[51, 52]

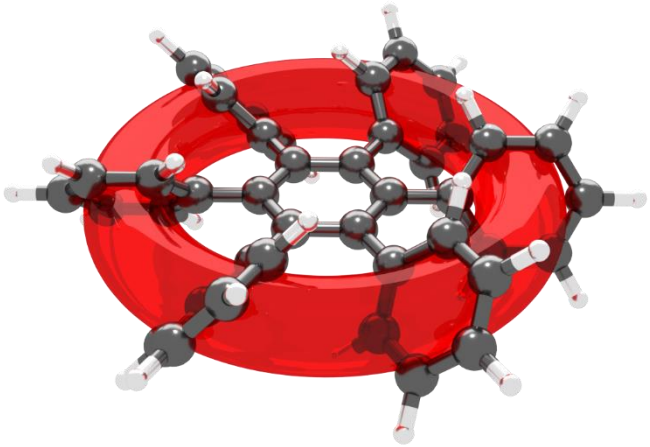

Figure 10 Toridorial delocalisation of charge in a hexaarylbenzene.

The ring-like HAB scaffold mimics the assembly of the chromophores in natural light harvesting complexes of LHI and LHII. Therefore it plays an important part in the investigation of the light harvesting mechanism as well as the construction of artifical light harvesting systems to learn more about the electronic and geometric requirements of the energy transfer.[9, 53-57]

Chromophores that find application in these systems have to be choosen regarding the requirement of suitable photophysical properties. One chromophore meeting these criteria is pyrene. It absorbs in the UV/Vis spectral region, forms excimers at higher concentrations[58] and owns a long fluorescence lifetime,[59, 60] which qualifies it as a chromophore to study spacial electronic coupling in a HAB. Nevertheless there are only a few examples of HABs that include pyrene in the system (see Figure 11). Especially interesting in this regard is the 2,7-substitution pattern, where the nodal plane of the HOMO and the LUMO orbital runs through. The lack of orbital coefficients at these positions leads to decoupling of the system as could be shown by several literature reports using DFT calculations as well as experimentally.[61-63] Therefore interaction between pyrene chromophores connected *via*

the 2- and 7-position is only possible through-space and thus through-bond interactions can be neglected.

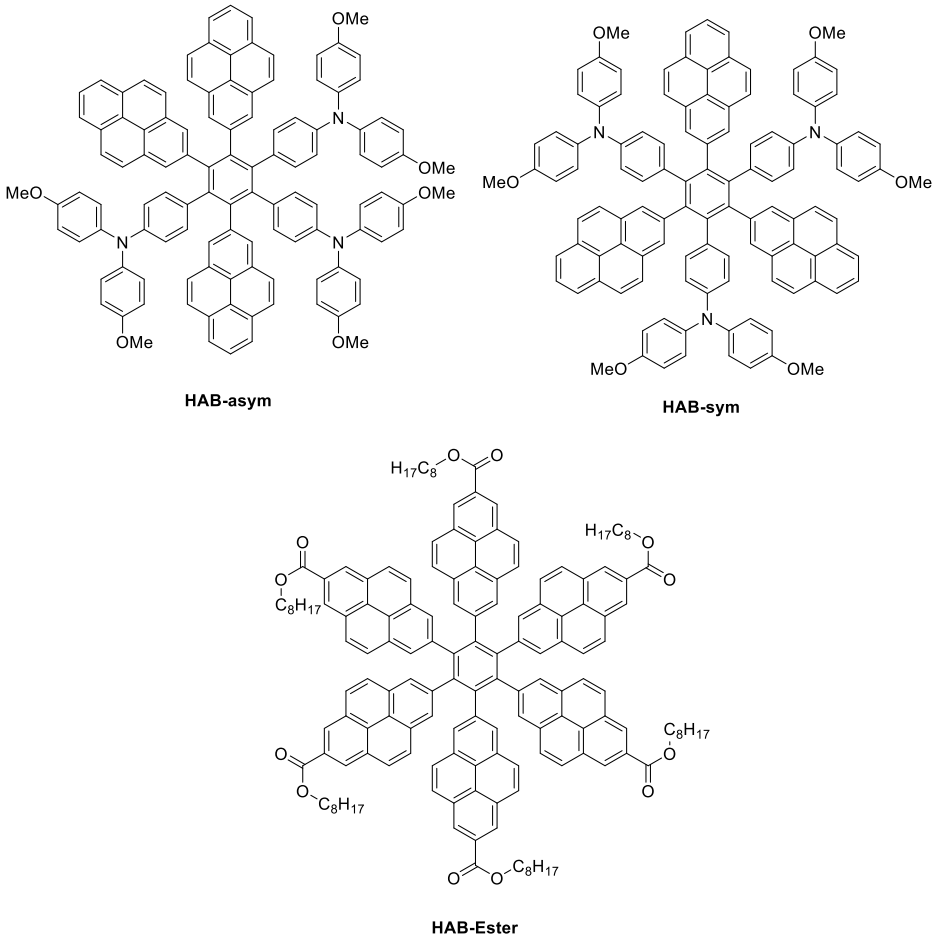

Figure 11 HABs containing one or more pyrene ligands.[59, 64, 65]

Lambert et al. studied the optical properties of HABs with pyrene chromophores incorporated into the scaffold. Two HABs that bear triarylamine moieties as a donor and pyrene chromophores as the acceptor were investigated.[59] The absorption spectra of both compounds feature besides the localised pyrene and triarylamine excitations a broad structurless band at around 25000 cm^{-1} (400 nm) that was assigned to a charge transfer state. Unlike the localised bands, the broad absorption band showed a positiv solvatochromism which confirmes the assumption of a charge-transfer origin. The same solvent influences can be seen in the fluorescence spectra, where the emission band is shifted to lower energies by up to 5700 cm^{-1} from cyclohexane to acetonitril. By use of excitation anisotropy spectroscopy a red-edge excitation effect for **HAB-asym** and **HAB-sym** was revealed which is often found in such chromophores due to energy transfer and symmetry breaking. In the same research group the interaction in a HAB containing only pyrene molecules functionalised by ester groups was investigated (see Figure 11).[64] The absorption spectrum shows the typical vibrational progression of pyrene, but in addition a

structurless band at lower energies. This broad absorption band appears at an energy lower than the $S_1 \leftarrow S_0$ transition, and shows a smaller oscillator strength and less vibrational structure than the pyrene monomer. This could be due to intramolecular exciton formation, which is supported by the fact that no such band is present in the absorption spectrum of the monomer. A similar broad and red shifted band in comparison to the monomer fluorescence is also visible in the emission spectrum of the HAB. Aggregation between different molecules could be excluded, as the spectrum proved to be concentration-independent. The origin of this unresolved bands in fluorescence and absorption spectra could not be proved so far, but excitonic interaction in the HAB could be an explanation of the absorption and fluorescence properties.

3.2 Alkyne-Bridged Chromophores in Energy Transfer

3.2.1 Different Topologies in Energy Transfer Systems

In recent years the development of new techniques made it possible to gain deep insight into the photosynthetic processes in nature. Several different topologies of molecular arrays for energy transfer have been studied and this rises the question of which alignment to choose for an artificial system. As already discussed in Chapter 2.2.1 the orientation of the transition-dipole moments and hence the molecules is important for the efficiency of the process, but there are further reasons why choosing the right topology is important. Usually more than one energy harvesting molecule is needed to absorb the sunlight in the necessary range (12500–33300 cm^{-1} (300–800 nm)) to be useful for optical applications so the construction of an array of chromophores is a requirement.[56]

Such architectures have to fulfil several important properties. The energy transfer has to be highly uni-directional to get high efficiencies.[66] The single transfer steps have to be fast to minimise unwanted side reactions such as fluorescence and non-radiative decay, the chosen chromophores should be photostable and the synthesis reasonably simple. Between the molecules a barrier is necessary to ensure that they don't act as a superchromophore and form an extended excited state. This can already be achieved by twisting the molecules relative to each other so that they are non-coplanar. However this twist should be kept modest, otherwise non-radiative decay processes could be favoured over through-bond energy transfer.[67] For high efficiencies a defined geometric arrangement and well defined bonds are necessary.[68] Often these arrays are built mimicking natural examples, so that a vast majority are cyclic or wheel-shape formed.[69-73] Another clearly nature-inspired way of building artificial energy transfer arrays is using a biological scaffold, mostly DNA[54, 72, 74-79] or protein-based arrays to position the chromophores in the desired fashion.[72, 80-82]

Dyes that absorb in the NIR region sometimes entail the disadvantage of being planar, and hence these π-delocalised aromates favour aggregation over energy transfer due to their flate structure. To utilise these chromophores in energy transfer systems, arrangements that prevent aggregation such as dendritic structures[55, 72, 83-88] are one option to circumvent this inconvenience. A drawback of dendrimers is the lack of directionality of the energy transport, which is a fact in long linear molecular arrangements, so called molecular wires.[72, 89, 90] These wires often have the advantage of showing broad absorption spectras and hence being able to cover a large area of the sun spectrum for photon absorption. To study through-space energy transfer solely and inhibit through-bond interaction spiro-like arrays serve best due to the incorporation of an orthogonal non-conjugated spacer.[72] Overall it is often difficult to synthesise large conjugated arrays with distinct energy transfer properties, so that supramoleculare assemblies formed *via* self-aggregation seem an easy solution.[72, 91-93] These can be used as energy transfer arrays as well, but it has to be considered that the interaction forces have to be strong enough to create a stable architecture. Because more and more complicated systems could be constructed, the utility of linear arrangements is often challenged as the damage of one of the chromophores leads to failure of the whole system. Apart from that, easy synthesizeable systems did help in the past to study the underlying interaction mechanism. The investigation of basic concepts such as appropriate bridges[68, 94] for energy transfer is best tested in linear systems where no specific interactions due to the spacial structure can influence the efficency of the process. For further applications zig-zag arrangements and V-shaped arrays[95] seem more suitable, as they are not as sensitive to damage as the linear ones and also do not feature the disadvantage of dendric structures that are less uni-directional.

The choice of the bridging unit between the chromophores is especially important if not only through-space but also through-bond transfer is considered, as in this case the bridge influences the energy transfer greatly. Furthermore alkyne bridges are known to ensure good electronical communication[96] and imply a fixed distance between the entities but still make rotation possible but planarisation and superchromophoric behaviour is more unlikely.[97]

Therefore the alkyne bridge is one of the most used connectors between chromophores to study energy transfer.[9, 68, 72, 98, 99]

This bridge was for example applied by *Odobel et al.* who investigated a tri- and a bichromophore for their suitability of incorporation into dye-sensitised solar cells (see Figure 12). The end-positioned squaraine is chosen due to the low lying excited state

that makes it a suitable acceptor. Furthermore squaraines are known as good sensitisers in solar cells as electron injectors. The triad as well as the bichromophore showed a red shift of the squaraine band in comparison to the monomer absorption due to the extended π-system. As energy transfer between squaraine and bodipy proofed to be ineffective in their system due to low spectral overlap the porphyrin was necessary to enable energy migration from bodipy to squaraine. By using this bridging chromophore energy transfer efficiencies of over 98 % could be achieved and fluorescence stemmed only from the squaraine.[100]

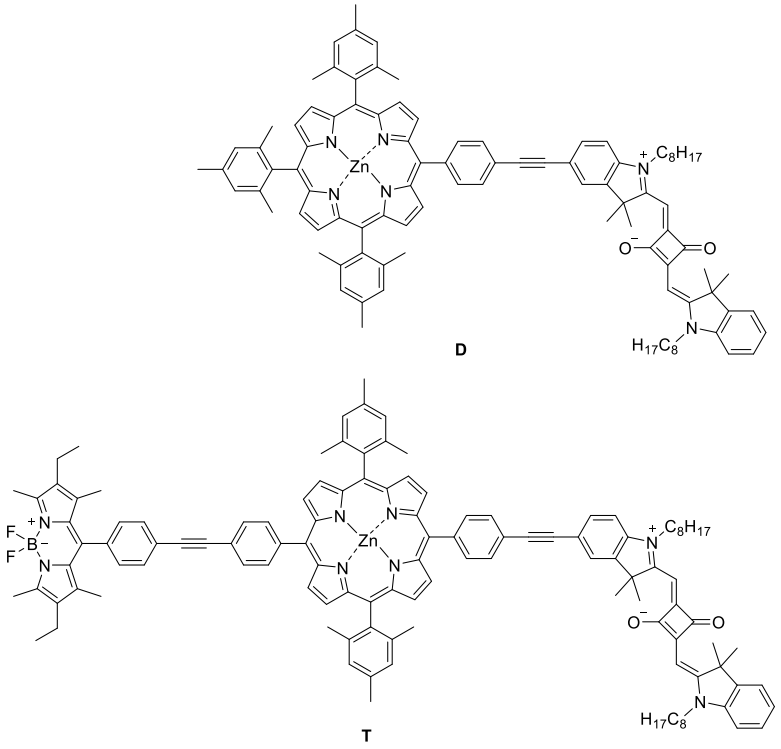

Figure 12 Squaraine-containing tri- and bichromophore for DSSC application.[100]

Lambert et al. synthesised two heterochromophores consisting of bodipy and *trans*-indolenine squaraine where lack of spectral overlap was not an issue (see Figure 13). The interaction between the chromophores was strong and excitonic behaviour of the compounds instead of energy transfer was the consequence. The head-to-tail arrangement leads to formation of J-aggregates and a strongly allowed low energetic transition which has mostly squaraine character was the main feature in the absorption and fluorescence spectra. The quantum yield of 57 % for the monomer was improved to 83 % for the **B_2SQA** triad but was lowered to 53 % for **$(SQA)_2$B**. While the higher quantum yield of the **B_2SQA** chromophore can be explained by intensity borrowing from bodipy, the lowering of the **$(SQA)_2$B** conjugate must have its origin elsewhere. This observation was ascribed to different geometries that can be adopted, so that three state have an allowed transition if a *cis*-conformation is adopted. The upper exciton state in **$(SQA)_2$B** was too weak for transient absorption measurements but the time-dependent anisotropy was studied by FLUC measurements. The

triad showed very low initial anisotropy values, which the authors assigned to an ultrafast energy transfer from bodipy to squaraine, which they were unable to resolve due to the time resolution of their set up.[97]

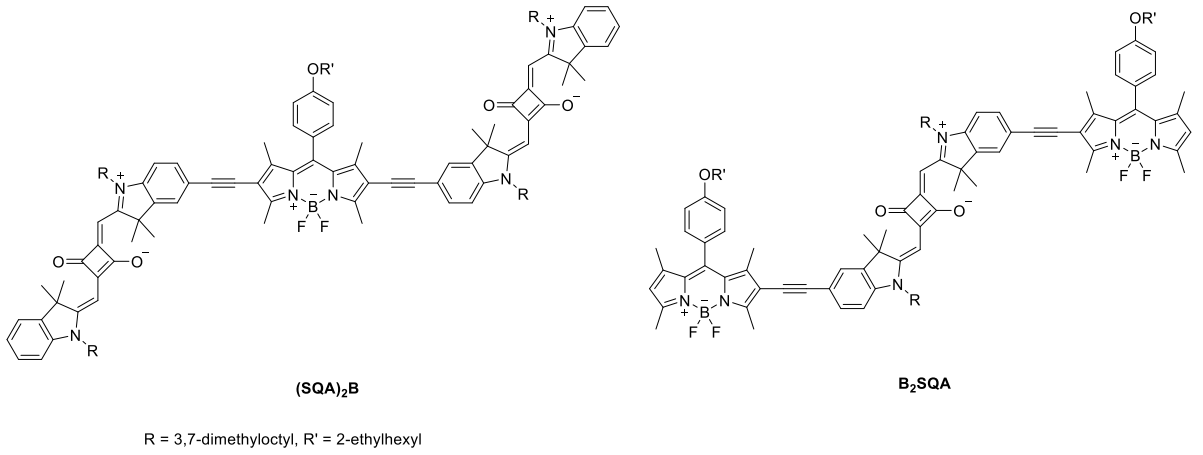

Figure 13 Coupled heterochromophores synthesised by *Lambert et al*.[97]

3.2.2 Bodipy-Pyrene – A Popular Combination in Energy Transfer

Due to its outstanding spectroscopic properties bodipy (see Figure 14) is a quite common fluorophore used in energy transfer studies. Various combinations of pyrene and bodipy have been investigated regarding their spectroscopic properties.[66, 67, 72, 95, 96, 101-108] The broad variation of the structural motif in the connection of these chromophores makes it impossible to give a short overview of all bodipy conjugates investigated for their energy transfer properties. Therefore the focus of this recap will be on ethynyl bridged energy transfer arrays incorporating both, bodipy and pyrene. A varity of studies are focusing on intramolecular energy transfer in bodipy-pyrene conjugates, but in all cases the pyrene molecule is connected at the 1-position.

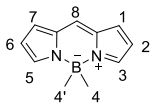

Figure 14 Numbering scheme used for the 4-bora-3a,4a-diaza-*s*-indacene (bodipy) core.

The most widley used substitution pattern for connecting pyrene to bodipy is the substitution at the boron-center. *Harriman et al.* synthesised two simple triads, one consisting of only bodipy with two pyrenes as substituents connected *via* alkyne-groups at the 4- and 4'-position and a mixed triad with pyrene and perylene as energy donors (see Figure 15). The conjugates behave quite similar, leading to bodipy fluorescence with small *Stokes* shifts, high

quantum yields of 90 % and a monoexponential decay with a lifetime of 6.5 ns. All these observed features fit nicely with the photophysical properties of the bodipy monomer. Time-resolved fluorescence studies revealed lifetimes for the polycycles of about 50 ps which explaines the missing residual fluorescence. The energy transfer from the perylene unit could be followed by ultrafast spectroscopy, but unfortunately the range where the excited state of pyrene would have been expected could not be probed. Nevertheless, due to the similarity of the compounds, it was assumed that energy transfer for pyrene should be in a comparable range as perylene.[96]

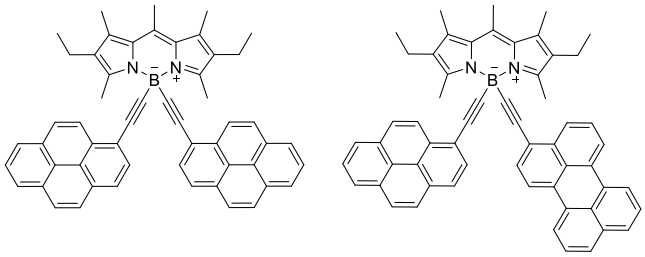

Figure 15 Chromophores for energy transfer that contain perylene, pyrene and bodipy with substitution at the boron center.[96]

A comparison of the bodipy substituted by two pyrenes with a system where only one pyrene is connected to the bodipy core *via* the boron-center and an ethynyl or trimethylsilyl-ethynyl group as second substituent was performed in the group of *Ziessel et al.*[101, 109] The lack of one pyrene molecule did not influence the energy transfer properties greatly and so for all three compounds high quantum yields of 80–90 % and energy transfer efficiencies of over 90 % were found.

Another unsymmetrical energy transfer array was prepared by *Harriman et al.*[66] that also incorporated pyrene and perylene, but in addition to that a fluorenyl unit was attached to the pyrene core (see Figure 16). The problem in all molecules consisting of pyrene and perylene is the overlap of the absorption spectra. Therefore it is not possible to excite pyrene solely as either perylene or bodipy show slight absorption in similar regions. The main fluorescence band stems from the bodipy and shows all typical spectroscopic properties already discussed above. In addition to that, residual fluorescence from the polycycles is visible. Compared to the monomer with a time constant of 21 ns, the lifetime of pyrene in the system is with 55 ps drastically reduced, but similar to the previous results of *Harriman et al.*[96]

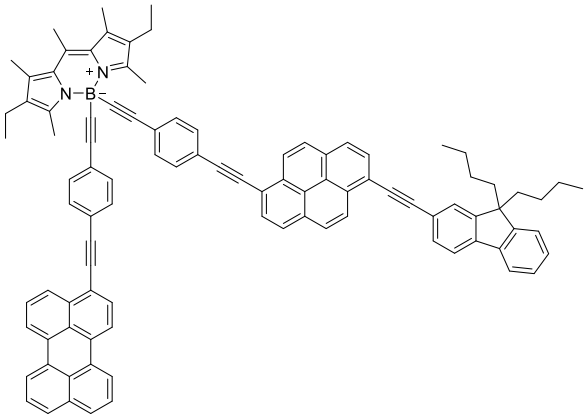

Figure 16 Unsymmetrical cascade for energy transfer with substitution at the boron-center of bodipy.[66]

Two branched, larger arrays incorporating multiple bodipys, where at the end of the branches pyrene chromophores serve as energy donors, have been investigated by *Ziessel et al.* (see Figure 17).[95, 104] In both cases an efficient energy transfer from pyrene to the centered bodipy was observed, but no residual pyrene fluorescence could be detected. In contrast to that, in both systems the bodipys in the branches showed small quantum yields of 3–7 %. The main fluorescence band could always be ascribed to the terminal bodipy and was much more intense than emissions from the bridging chromophores. This intense emission resembles the typical spectral properties known from the monomer, that is high quantum yields and monoexponential decays in the ns regime. In the **PMEX** array the residual fluorescence of the bodipys is due to exciton migration in the system. The excitation is not directly transported from the bodipy in the branches to the terminal bodipy but can hop *via* through-space energy transfer from branch to branch and additional back energy transfer is occuring on a considerable short timescale. Escpecially the final step in the **PMEX** array shows a slow energy transfer rate due to this fluctuation of energy but still an efficiency of 90 % can be gathered. The slow energy transfer can be observed by time correlated single photon counting as a grow-in time of bodipy fluorescence with a time constant of 150 ps followed by a decay of 6 ns. The pyrene to bodipy transfer on the other hand is extremly fast and shows no back transfer so that no residual pyrene fluorescence can be detected.[95] For a smaller system, with only one bridging bodipy between pyrene and the terminal accepting bodipy the excitation energy at the pyrene absorption wavenumber was varried. At lower excitation energies the pyrene transfers energy to the middle bodipy and from there further energy transfer to the terminal bodipy occurs. On the contrary, at higher excitation energy the middle bodipy is excluded and direct energy transfer from pyrene to the terminal bodipy is favoured. This also leads to a lack of residual fluorescence of the middle bodipy.[104]

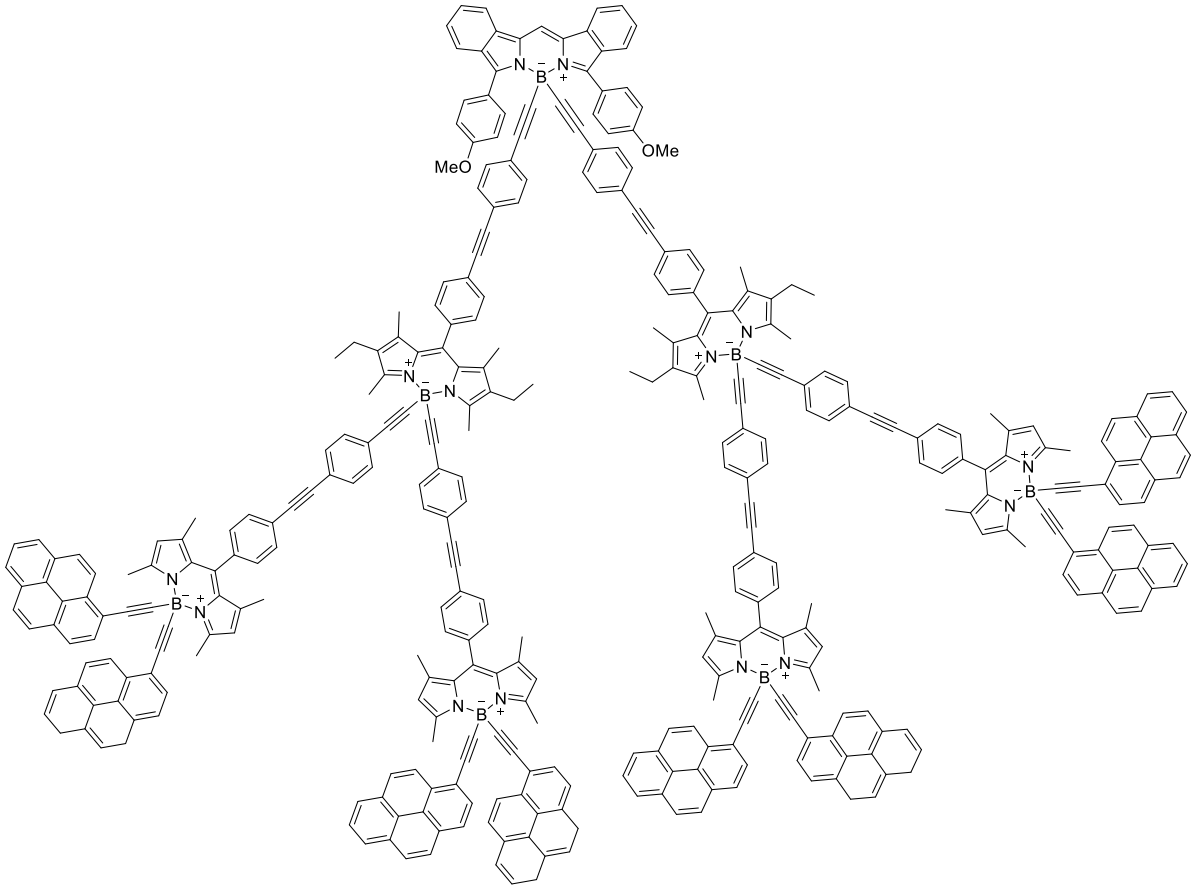

Figure 17 Multichromophore array for energy transfer directed to one final bodipy acceptor.[95]

A lot less common is the substitution of bodipy in 8-position at the methylene bridge between the two pyrrol rings. A study of the energy transfer properties with this pattern was done by *Ziessel et al.*[67] Three different compounds with different bridge lengths and numbers of pyrene units were compared (see Figure 18). All showed well distinguishable peaks in the absorption spectra, that could be assigned to bodipy or pyrene origin. While the directly coupled molecule **BPy-1** showed typical bodipy quantum yields and lifetimes, the phenyl-ethynyl spacer lead to a decrease of quantum yield and lifetime due to an increase of the non-radiant decay. Fluorescence following excitation into the pyrene absorption stems from bodipy in all three chromophore arrays. In case of **BPy-2** and **BPy-3** additional to the main bodipy fluorescence a small residual band was visible, that could be assigned to pyrene. The comparison of excitation and absorption spectra supports the assumption of an effective energy transfer of over 90 % from pyrene to bodipy. To evaluate whether the two pyrene units in compound **BPy-3** act as one single chromophore or are electronically coupled quantum chemical calculations were done. The results not only showed the electronical coupling of the pyrenes but also showed that in all three compounds no strong electronical communication between pyrene and bodipy was present as they are oriented orthogonal to

each other. The calculated energy transfer rate for **BPy-1** shows fast energy transfer due to good spectral overlap. The overlap of **BPy-2** and **BPy-3** is reduced due to a shift introduced by the ethynyl substituent and hence the energy transfer rate decreases. This might then lead to the residual fluorescence of pyrene which has a calculated lifetime of 27 ps, but could not be confirmed by measurements because of the temporal resolution of the instruments. The fact that the two pyrene units in **BPy-3** act as one chromophore increases the distance between donor and acceptor and leads to a further decrease of the energy transfer rate.

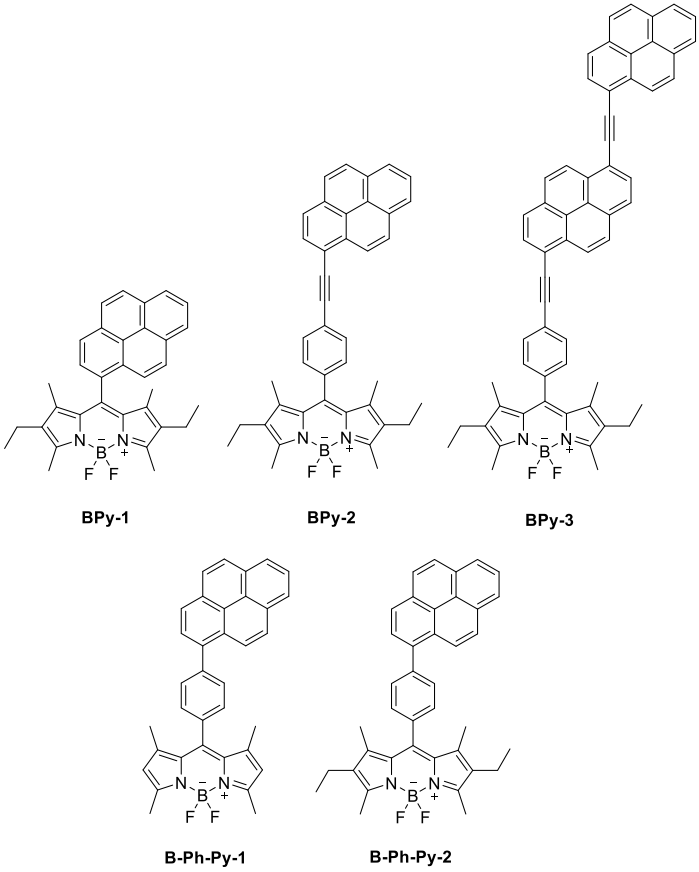

Figure 18 Substitution between the two pyrrole units of the bodipy at different separation lengths.[67, 110]

Molecules where pyrene is used as substituent not only at 4,4'-positions but in addition to that at the methylene bridge between the pyrrols were also investigated by *Ziessel et al*.[102] For **B3Py-1** pyrene was directly attached to the bodipy scaffold whereas in **B3Py-2** a phenylethynyl spacer was inserted between the two constituents (see Figure 19). Electronical delocalisation could be excluded as the absorption spectrum looks like a superposition of the monomers. High energy transfer efficiencies of 97 % for the closely spaced dyad and 99 % for the dyes connected *via* spacer were found. A similar conjugate was investigated by *Vauthey et al.*[110], where pyrene is directly linked to bodipy *via* the benzene ring without an additional alkyne bridge (see Figure 18). They found efficient energy

transfer from pyrene to bodipy on a time scale of 0.3–0.5 ps. As the overlap between the S_1 state of bodipy with pyrene fluorescence is almost negligtible while the S_2 shows a distinct integral this state should be responsible for energy transfer, which was reported in literature several times.[67, 106]

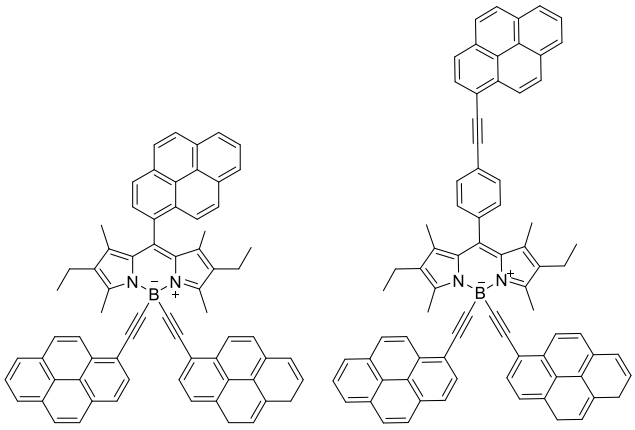

Figure 19 Bodipy-pyrene arrays with multiple substitution positions.[102]

Pyrene substitution at the 2-position of the bodipy core is rarely described in literature. One example of such an array was prepared by *Ziessel et al*. (see Figure 20).[105] While the substitution at the boron-center yielded 99 % quantum yield for direct bodipy excitation, the substitution in 2-position of the bodipy leads to a drastic reduction of the quantum yield to 20 %. Furthermore the almost quantitative energy transfer of the boron-substituted compound **B2Py2TME** cannot be reproduced for **BPy** but is very weak with additional residual fluorescence of 2 % originating from pyrene. This is in contrast to the results of *Burgess et al.*[111] where the energy transfer of heterodimers consisting of bodipy and anthracene depending on substitution postitions were studied. They found efficient energy transfer in all compounds, but the energy transfer rate was much faster when the anthracene was attached at the 2-position of the bodipy.

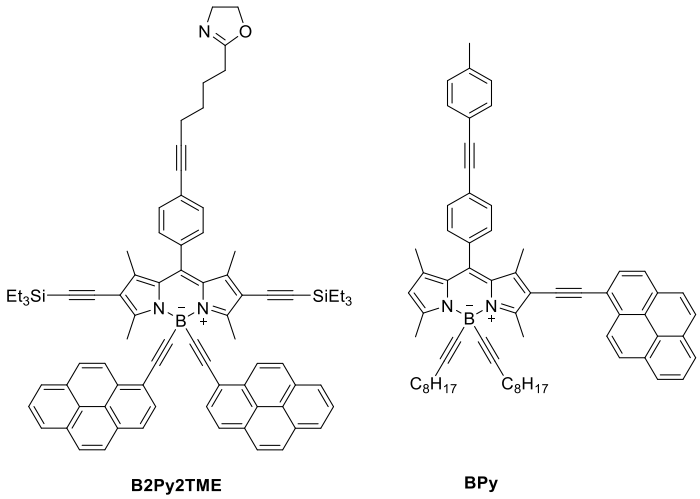

Figure 20 Substitution of pyrene to the pyrrole ring of bodipy.[105]

3.1 Linear Bridged Indolenine Squaraines

A common procedure to influence the properties of dyes and modify their spectroscopic properties is the extension of the π-system, especially with the goal of shifting the absorption and fluorescence spectra into the NIR region.[112] The spectral changes are based on the interaction between the connected dyes. Hence the way of connection can influence the interaction. *Geiger et al.* studied the influence of different bridging units on the properties of squaraine dyes (see Figure 21).[113] Independent of the bridge all compounds showed a red shift of the absorption band, but no influence of the electronic nature of the bridge itself on the spectra. The strongest red shift was found for the planar bridge **(SQ)V**, due to the lack of distortion that reduces interaction in the more flexible dyes.

Furthermore *Geiger et al*. used the same planar bridging unit to couple two different squaraines and observed again a bathochromic shift. Due to the coupling of the subunits also two absorption bands were observed in the spectra.[114] In order to get an even stronger red shift they used an anthracene bridge instead of the naphthalene one in **(SQ)V** but suprisingly the absorption spectra hardly differ. Therefore they synthesised an even more rigid squaraine **(SQ)VI** which showed a strong red shift but also a smaller extinction coefficient. Whereas the squaraines with naphthalene and anthracene bridges seemed to show slight coupling, the more rigid one acts as a single dye leading to the small extinction coefficient.[115]

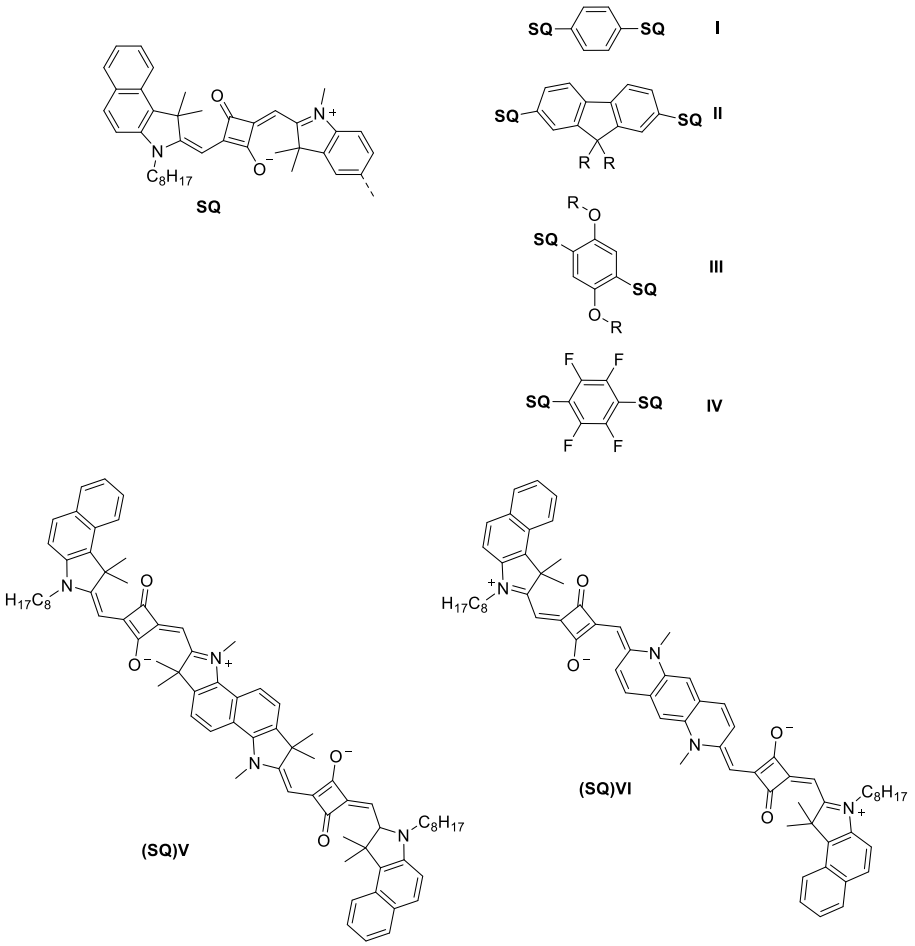

Figure 21 Monomeric squaraine **SQ** and the bridging units **I-IV**. For **(SQ)V** a planar bridge was introduced and **(SQ)VI** is additionally rigidified.[113-115]

More flexibly linked squaraines were investigated by *Lambert et al.*[116] They studied the optical properties of *cis*- and *trans*-squaraine monomers, dimers and trimers (see Figure 22). The absorption spectra of the oligomers can be explained by exciton coupling theory. Several peaks with different intensities where present with the main absorption band at lower energies. Exciton theory predicts three transitions where the lowest one is strongly allowed. Due to the flexibility of the oligomers different conformations are possible and hence the selection rules are less strict, leading to several peaks in the absorption spectra. The fluorescence spectra obtained after excitation at the lowest energetic absorption band lead to the typical narrow intense fluorescence band between 13500–14000 cm^{-1} (714–741 nm) for the *trans*-indolenine squaraines and 12500–13300 cm^{-1} (752–800 nm) for the *cis*-indolenine squaraines. All of these oligomers show an increasing transition-dipole moment when going from the monomer to the oligomers but no additivity. Hence a microscopic superradiant effect seems to be present.

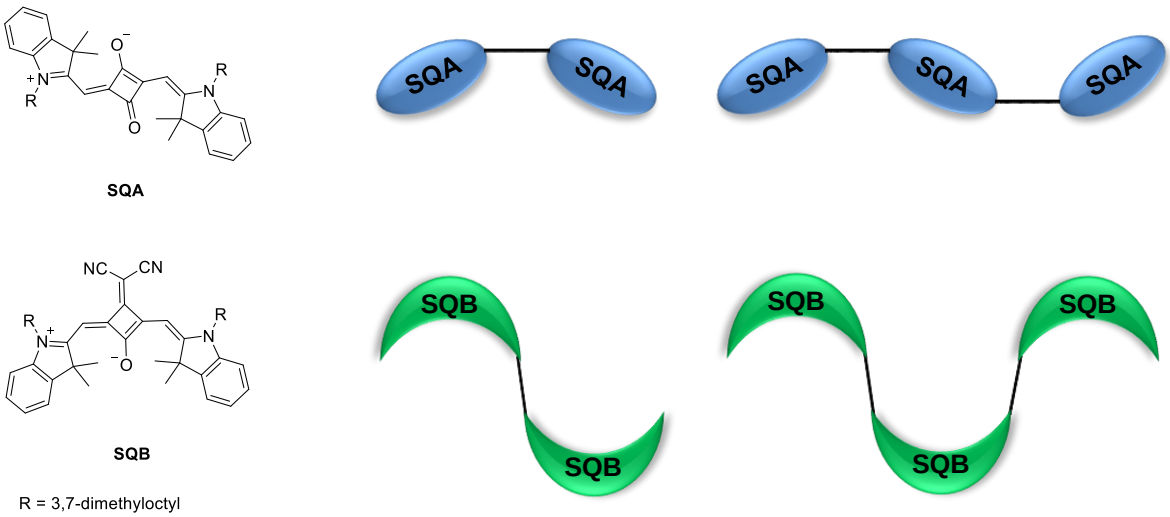

Figure 22 Linearly connected indolenine squaraines.[116]

4 Scope of the Work

In this work energy transfer of coupled chromophores in different spacial arrangements are studied. A HAB is used to mimic the scaffold of the chromophores in natural light harvesting systems whereas the conjugated chromophores arranged in a linear fashion should enable the investigation of basic influences on the energy transfer efficiency. Furthermore stronger coupling between dye conjugates, rather explainable by exciton theory, with focus on the influence of the bridging unit onto the coupling phenomena will be explored in the third part.

4.1 Hexaarylbenzenes

This part is based on the HAB synthesised by *Lambert et al.*, which consists of six pyrene units substituted with an ester group at the 7-position. Unfortunately the pyrene molecule seemed to interact with the ester function, making investigation of mere pyrene properties impossible.[64] In this work a six-fold pyrene substituted HAB with an alkyl chain instead of the ester function is chosen as the target molecule to minimise the influence of the substituent on the spectroscopic properties (see Figure 23).

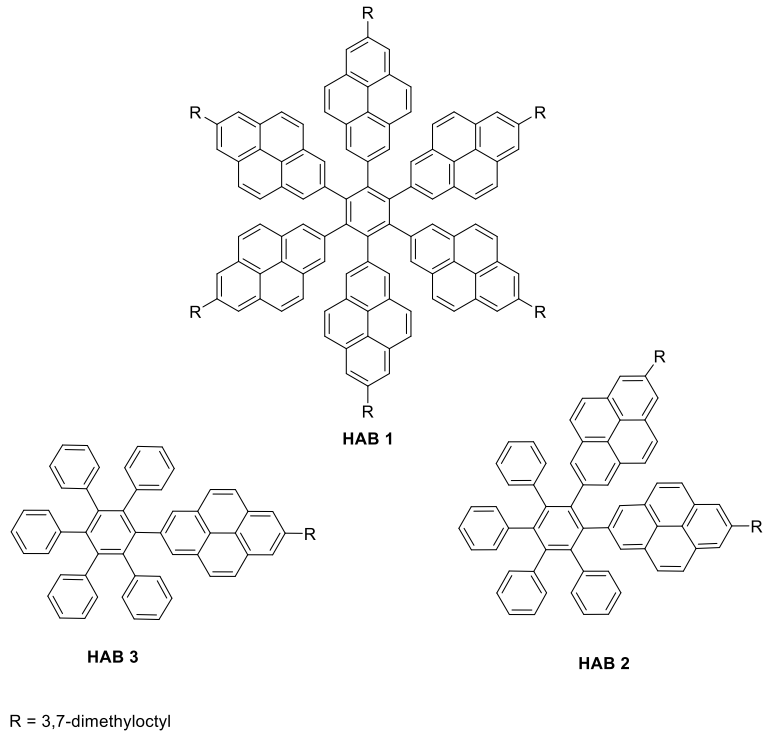

Figure 23 Target compound **HAB 1** and the model compounds **HAB 2** and **HAB 3**.

Pyrene as substituent is implemented owing to the fact that its photophysical properties were intensively studied and showed several interesting properties, including a long fluorescence lifetime,[60, 117] excimer formation[58] and a high sensitivity to solvent polarity concerning the

vibrational peak ratios.[118, 119] These properties can be explained by taking a look at the orbitals and the corresponding transition-dipole moments involved in the photophysics of pyrene. The $S_1 \leftarrow S_0$ transition, which is perpendicular polarised to the long axis of the molecule is very weak, so that the main absorption band belongs to the $S_2 \leftarrow S_0$ transition which is polarised horizontaly to the long axis. The orbitals which are involved in the last mentioned transition are the HOMO and the LUMO, and posses a nodal plane through the 2,7-position (see Figure 24).[120, 121]

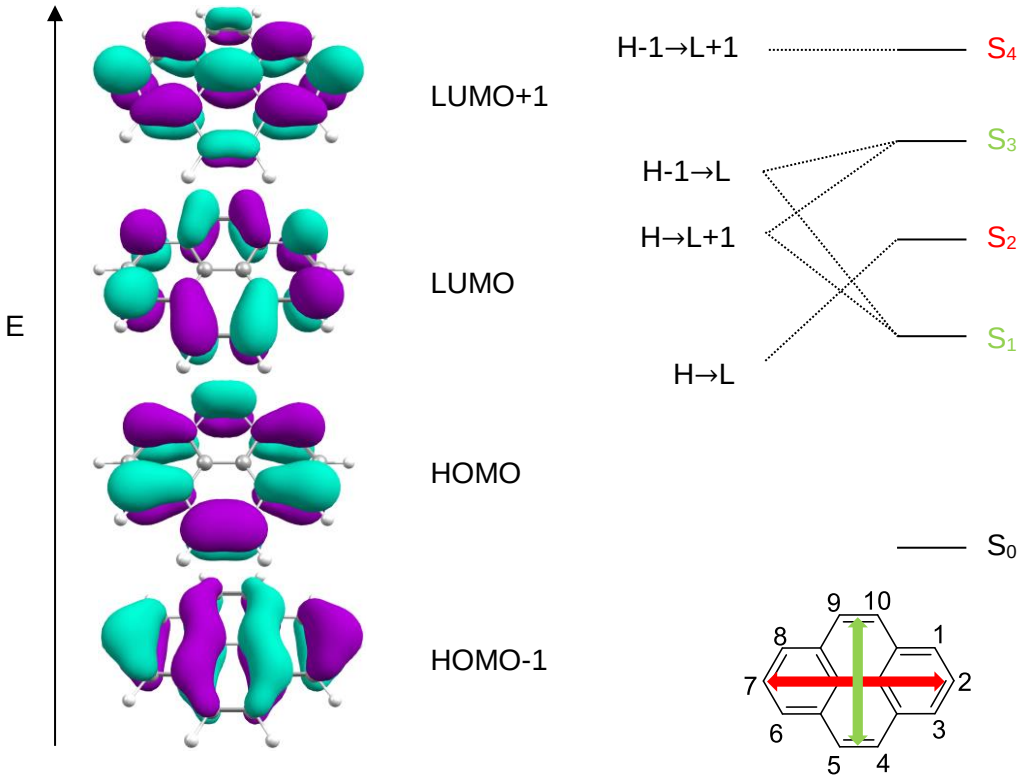

Figure 24 Frontier orbitals of pyrene (left) and the optical transition with the corresponding orbital contribution (right). The Orbitals were calculated using DFT computations at B3LYP/6-31G* level of theory and were executed by Dr. Marco Holzapfel. The typical numbering scheme of a pyrene molecule and the transition-dipole moments are depicted on the bottom of the right side.

The lack of electron density at the 2,7-position and the alkyl chain as substituent should lead to spectral features of the HAB that originate from the pyrene chromophore only. Therefore this system should make investigations of the interaction between the pyrene units without substituent influences possible. Additional to the six-fold pyrene HAB two further HABs carrying only one or two pyrene units as substituents should be synthesised for comparison.

4.2 Linear Multichromophore Systems

In the second part of this thesis electronic interactions in hetero-dye conjugates are investigated. For this study the chromophores are aligned in a linear fashion and connected *via* an ethynylene bridge. This linker is choosen as it reduces flexibility and keeps the chromophores at a fixed distance to each other, while rotational freedom is still enabled.[97] This rotational freedom is crucial, as a planar spacial arrangement of the chromophores relative to each other favours superchromophoric behaviour due to excitonic coupling instead of energy transfer.[67] Furthermore the alkyne bridge is known as a linker that enables highly efficient energy transfer.[96] This work partly follows the dye conjugates investigated by *Lambert et al*.,[97] who synthesised symmetrical triads consisting of bodipy and *trans*-indolenine squaraine (see Figure 25), which showed fluorescence enhancement through excitonic coupling.

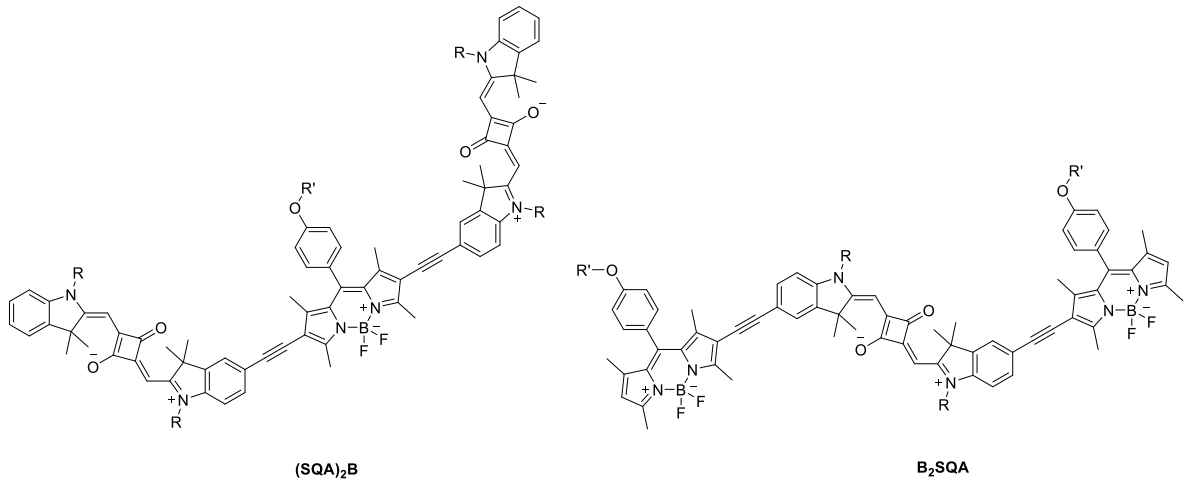

Figure 25 Hetero-dye conjugates synthesised by *Lambert et al*.[97]

The chosen chromophores, namely bodipy[98] and the *trans*-indolenine squaraine,[116, 122] (see Figure 26) have an intense and narrow absorption band and high to medium fluorescence quantum yields. In contrast to the previous work, here the *trans*-indolenine is exchanged by the red-shifted *cis*-indolenine squaraine.[116, 122-124] The substitution with a chromophore with a lower excited state should influence the excitonic coupling in several ways: First of all the lowest excitonic state will be lower in energy than for the literature known **$(SQA)_2B$** and **B_2SQA** due to the energetic difference between the squaraine monomers. The greater energy difference between the two coupling dyes should lead to smaller energetic shifts, even if the coupling strength is the same. Furthermore the *cis*-squaraine is c-shaped while the *trans*-squaraine represents a more s-shaped geometry. Therefore, in the triads with *cis*-squaraine a different orientation of the transition-dipole moments and hence distribution of

the oscillator strength is the consequence. The investigation of these influences with special interest in the sequence of the chromophores is the focus of this research.

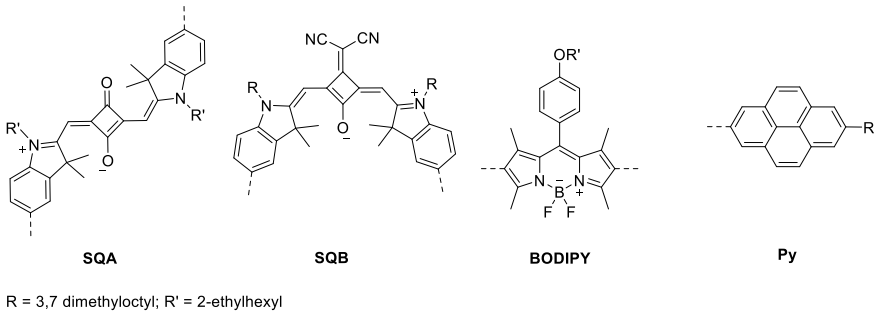

Figure 26 Monomers that are used to synthesise triads and pentads.

Additionally all three chromophores, bodipy, *cis*- and *trans*-squaraine are also implemented into triads with a third chromophore which absorbs at high energies. As discussed before, the orientation of the transition moments greatly influences the coupling strength and hence exciton theory or energy transfer are more appropriate to describe the photophysical properties of the system. In this context, the 2,7-substituted pyrenes are suitable as they should prohibit through-bond energy transfer due to the nodal plane and possess two transition-dipole moments that are orthogonal to each other. Additionally, the main absorption band in pyrene is ascribed to the $S_2 \leftarrow S_0$ transition followed by an ultrafast (75–85 fs)[125, 126] internal conversion to S_1. The transition from the S_1 state to the ground state is almost forbidden[59, 121] and long lifetimes of hundreds of nanoseconds are the consequence. This leads to a population accumulation in the S_1 state, which makes pyrene a well suited chromophore for non-radiant energy transfer. With the absorption lying in the UV/Vis region pyrene serves as the high energy chromophore, providing its energy after excitation to another, energy accepting, chromophore. The other chosen chromophores, bodipy[98] and the *cis*- and *trans*-indolenine squaraine,[116, 122] (see Figure 26) all have a distinctly lower excitation energy than pyrene. Especially the bodipy scaffold is an ideal building block in energy transfer arrays from synthetic as well as photophysical point of view. Therefore it is extensively used in energy transfer research due to being easily chemical variable and having a high absorption coefficient in the visible as well as a good fluorescence quantum yield and a very low triplet quantum yield.[72, 95, 127-130] Squaraines on the other hand are used in numerous applications due to their outstanding properties such as high extinction coefficient, fluorescence in the NIR-region, structural diversity and good photostability.[47, 131-133]

At first, symmetrical triads following the structural architecture of the triads presented in *Lambert et al.*[97] will be synthesised. The symmetric conjugates are appropriate compounds to study the photophysical interaction between the chosen monomers and the efficiency of

the energy transfer. Owing to the different geometric structure of the chromophore in the center position, different orientations of the transition-dipole moments relative to each other are the consequence. For the symmetrical triads containing the *trans*-squaraine one can find that the spectral overlap between the fluorescence spectrum of pyrene and the absorption of the squaraine is nearly zero. This should lead to no through-space energy transfer where the overlap integral is one key influence on the efficiency. The through-bond energy transfer does not dependent on the size of the overlapping area of the spectra but only on the form of the overlapping bands and could hence be possible.[21, 30] Nevertheless no orbital coefficients are located at the 2,7-positions of pyrenes, preventing an effective exchange coupling between the chromophores. Hence no energy transfer should occur in the system.

In addition to the symmetric conjugates, unsymmetric triads and pentads are synthesised consisting of the above mentioned monomers. Here a stepwise energy transfer should take place. To make this process possible, each single energy transfer step has not only to be highly efficient, but also fast to minimise side reactions such as triplet formation or fluorescence.[9, 72] These unsymmetric triads and pentads can cover a broad spectral range and a different sequence of the chromophores lead to a change in the spacial arrangement to each other due to the individual geometric structure of the chromophores. Assuming that the through-bond energy transfer from pyrene is negligible due to the nodal plane through the 2,7-position, the through-space mechanism is the only possible dissipation for the energy after pyrene was excited. Due to the different orientations of the bodipy and pyrene chromophore relative to each other and hence the transition-dipole moments, different energy transfer efficiencies should result (see Figure 27).

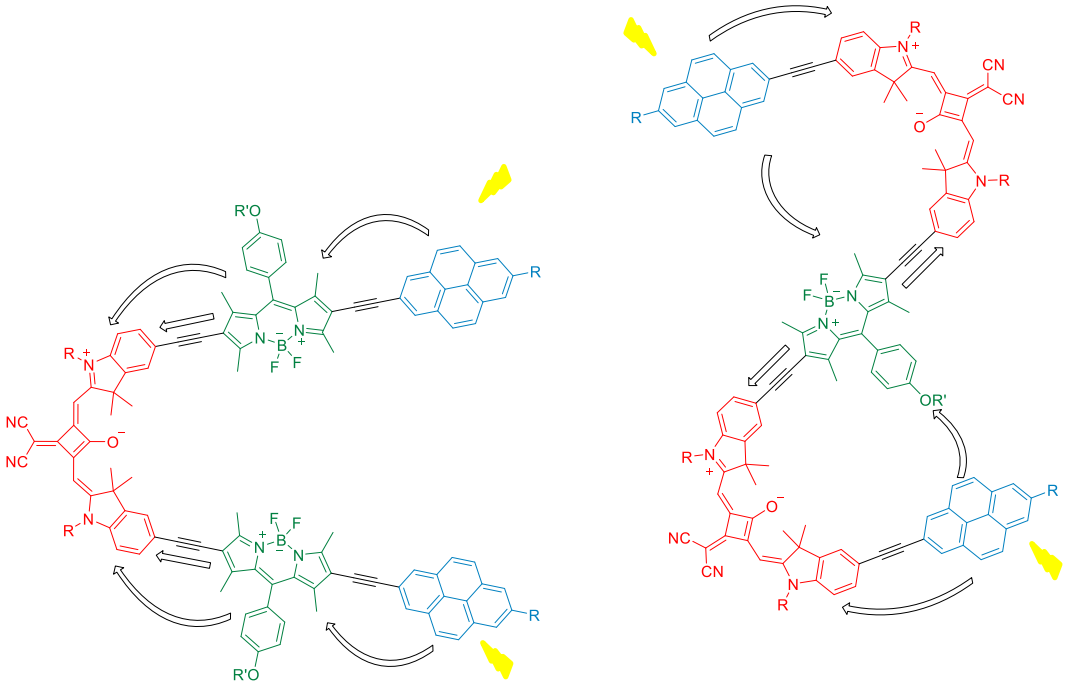

Figure 27 Possible energy transfer pathways in two alkyne-bridged pentads, where bent arrows mark through-space energy transfer and straight arrows mark through-bond energy transfer.

4.3 Rigidly Bridged *Trans*-Squaraines

The third part of this thesis will focus on the interaction of squaraine dimers due to excitonic coupling and is based on the work of *Ceymann et al.*[134] Herein a homodimer and homotrimer composed of *trans*-indolenine squaraines were synthesised (see Figure 28), where the monomeric building blocks were flexibly connected over a biaryl axis. The elongation of the π-system leads to a red shifted, broadened absorption spectrum and additional bands due to excitonic coupling. Due to rotational freedom, different conformers can be adopted, which leads to a difference in the excitionic coupling strength and therefore several absorption bands are visible in the spectrum. To exclude rotational conformers, a squaraine dimer connected through a ridgid, non-conjugated linker is synthesised (see Figure 28). This should lead to a narrow absorption band with an extinction coefficient twice the intensity of the monomer. Only one absorption and fluorescence band should be present in the spectrum and high quantum yields shall be achieved.

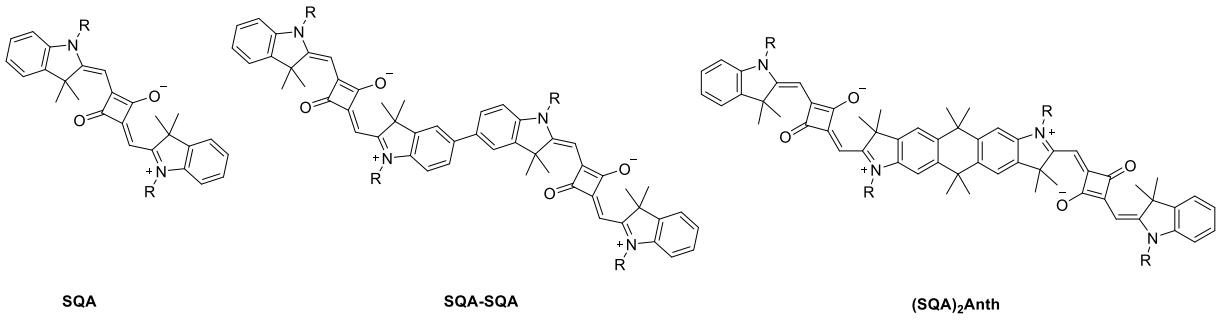

Figure 28 Monomeric squaraine **SQA** and the dimers **SQA-SQA** and **(SQA)$_2$Anth**.

5 Results and Discussion

5.1 Hexaarylbenzenes

To achieve substitution at the 2- and 7-position of pyrene, the well established iridium-catalysed borylation was applied.[135] Starting from pyrene boronic acid derivatives that are feasible coupling partners in *Sonogashira* reactions can be synthesised by standard functionalisation reactions. *Sonogashira* reaction then leads to the desired tolans, serving as starting material in the *Diels-Alder* reaction or the cobalt-catalysed trimerisation to get to the HABs.

5.1.1 Synthesis

The complete optimised synthetic pathway can be found in Scheme 1. Parts of this synthesis were carried out in an earlier work,[136] where the optimisation of the first steps till the alkylation (**Py-4**) were discussed in detail.

The synthesis starts from commercially available pyrene **Py-1** using the iridium-catalysed borylation to get access to the 2-substituted pyrene **Py-2**. The selective substitution of pyrene in 2-position is possible due to the steric demanding iridium-catalyst. This feature is assigned to the crowded nature of the five-coordinated *fac*-tris(boryl) species, [Ir(bpy)$(Bpin)_3$], present in the rate limiting step.[137] To reduce the amount of symmetrical substituted pyrene, additionally to the nonpolar solvent, which favours the formation of mono substituted pyrene, the dilution principle was applied.[138] This leads to good yields of 61 % of **Py-2**. The functionalised pyrene can then be brominated by using $CuBr_2$ in a mixture of water and methanol. The first two steps are very similar to the known literature procedure,[135] with only slight variations for the bromination in temperature and reaction time. The alkylation of **Py-3** was successfully performed under *Suzuki-Miyaura* conditions, adapted from literature as well[139] and leads to high yields of **Py-4**.

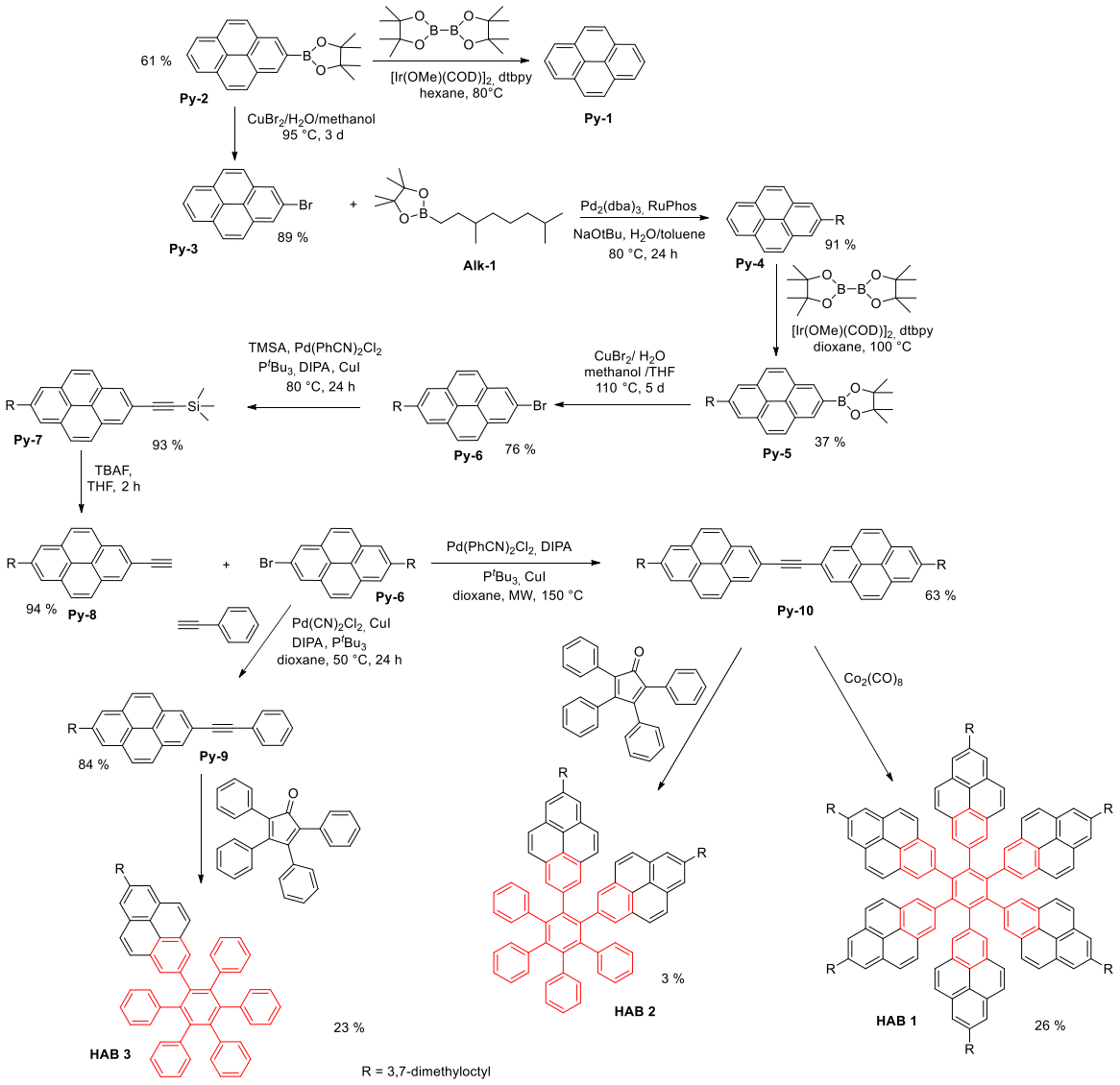

Scheme 1 Synthesis of hexaarylbenzenes **HAB 1**, **HAB 2** and **HAB 3**.

For this alkylation the borylated alkyl chain **Alk-1** is needed, which was obtained through conversion of 1-iodo-3,7-dimethyloctyl with 4,4,4',4',5,5,5',5'-octamethyl-2,2'-bi(1,3,2-dioxaborolane) (**Alk-2**) and CuI as catalyst (see Scheme 2).[139]

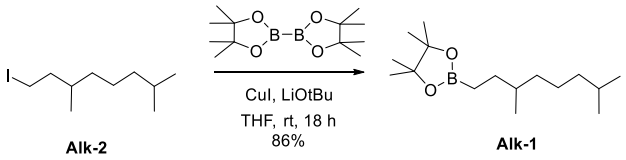

Scheme 2 Borylation of 1-iodo-3,7-dimethyloctyl.

For the substitution in the 7-position the same steps and very similar reaction conditions as for the functionalisation in 2-position were applied as it can be assumed that the alkyl chain doesn't hinder these reactions significantly. In both steps the procedures for diborylation and dibromination of pyrene were followed,[135] as they lead to a distinct improvement of the yields compared to the conditions for the mono functionalisation.

For the alkynylation and deprotection of **Py-6** the procedure of *Lambert et al*.[64] was applied successfully by using a $Pd(C_6H_5CN)_2Cl_2$-catalyst and tri-*tert*-butylphosphine as ligand, followed by cleavage of the TMS group with tetrabutylammonium fluoride.

Two different tolanes are needed for the cyclisation to the different hexaarylbenzenes. One symmetrical one, containg only alkyl-substituted pyrene as a ligand and one with a pyrene and a phenyl ligand.

To synthesis these tolanes the *Sonogashira* coupling conditions that yielded **Py-6** were tested first. These conditions lead to very good yields for the coupling of phenylacetylene with pyrene **Py-6**, but in the attempt to couple the two pyrenes **Py-6** and **Py-8** with each other, no product could be isolated in dioxane or DMF as solvent (see Table 1, conditions I and II).

A screening in a previous work in this group, where pyrene was coupled to triarylamines, proved that the conditions shown in Scheme 3 yielded the best results.[120]

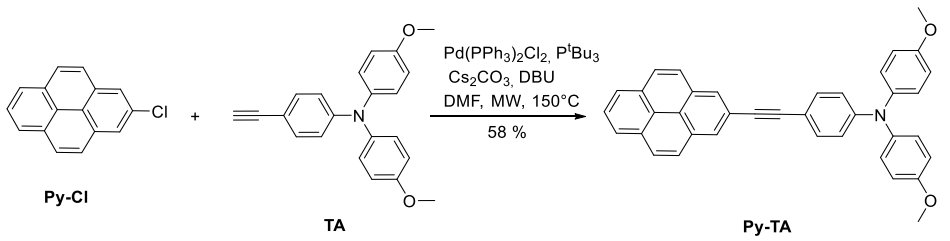

Scheme 3 Optimised coupling conditions of pyrene with a triarylamine.

Table 1 Reaction conditions tested for *Sonogashira* coupling between two pyrene molecules.

	coupling agent	reaction condition	yield [%]
I[120]	$Pd(C_6H_5CN)_2Cl_2$, P(^{t}Bu)$_3$, CuI, DIPA	DMF, 80 °C, 24 h	-
II[64]	$Pd(C_6H_5CN)_2Cl_2$, P(^{t}Bu)$_3$, CuI, DIPA	dioxane, 50 °C, 24 h	-
III[120, 140]	$Pd(PPh_3)_2Cl_2$, P(^{t}Bu)$_3$, Cs_2CO_3, DBU	DMF, 150 °C, 10 min, MW	37
IV[120, 140]	$Pd(C_6H_5CN)_2Cl_2$, P(^{t}Bu)$_3$, CuI, DIPA	DMF, 150 °C, 20 min, MW	63

These conditions only lead to acceptable yields of 37 % for the pyrene-pyrene coupling (Table 1, condition III). In a second attempt with the $Pd(C_6H_5CN)_2Cl_2$-catalyst and tri-*tert*-butylphosphine under microwave irradiation with DMF as solvent (see Table 1, condition IV) the desired product **Py-10** could be isolated in 63 % yield.

Py-9 and **Py-10** were both cyclised in a *Diels-Alder* reaction with 2,3,4,5-tetraphenylcyclopenta-2,4-dienone.[141] As for these reactions temperatures up to 300 °C and higher are needed, the range of solvents is limited. For both cases diphenylether was used as it has a boiling point of 260 °C. For **HAB 3** reasonable yields of 23 % could be achieved while for the **HAB 2** only 3 % of pure product could be isolated. This drop of the yield may be explained by the higher steric demand of **Py-10** in the cyclisation compared to **Py-9**.

Lastly to get to the desired **HAB 1** the cobalt-catalysed trimerisation was applied, which resulted in 26 % yield of the desired compound (see Scheme 1).[64]

For purification of the three HABs, thin Layer Chromatography (TLC) was successfully performed.

5.1.2 Absorption Spectroscopy

To investigate the interactions between the pyrene chromophores in the HAB, steady-state absorption spectra of **HAB 1** were measured and **Py-7** was applied as reference compound.

Py-7 was used for comparison, as it shows the typical pyrene absorption spectrum,[60] that is a well resolved vibrational $S_0 \leftarrow S_2$ transition with a six-fold maximum extinction coefficient of 300000 M^{-1} cm^{-1} at 29500 cm^{-1} (339 nm) in cyclohexane and 250000 M^{-1} cm^{-1} at 29200 cm^{-1} (342 nm) in toluene (see Figure 29). Although for the monomer an influence on the band ratio by solvent polarity can be seen, the band at the low-energy side is always highest in intensity.

The absorption properties of **HAB 1** were investigated in cyclohexane, toluene and DMF.

Comparison of **HAB 1** with the corresponding monomer (see Figure 29) shows that the extinction coefficient of the **HAB 1** is not six-time the value of the monomer **Py-7**, but the transition-dipole moments μ^2_{abs} show an increase of 27 % for **HAB 1** compared to the six-fold value of **Py-7** in toluene (μ^2_{abs}(**HAB 1**): 126.6 D^2, μ^2_{abs}(**Py-7**): 16.6 D^2) and 39 % in cyclohexane (μ^2_{abs}(**HAB 1**): 130.9 D^2, μ^2_{abs}(**Py-7**):15.7 D^2). The spectrum of **HAB 1** is dominated by two intense peaks at 28600 cm^{-1} (349 nm) and 30100 cm^{-1} (332 nm), which belong to the same electronic transition and are a vibrational progression. This assignment is based on the energy difference of the two peaks in comparison with the pyrene monomer, which both show a spacing between the first two bands of about 1400 cm^{-1} in toluene. The band ratio of the **HAB 1** resembles the absorption spectrum of the monomer, even if it is broadened and the intensities of the vibrational bands realtive to the 0-0 transition are less different (see Figure 29b). In contrast, in DMF and cyclohexane the band ratio is reversed, that is, the 0,1 band is more intense (see Figure 30). This behaviour is not observed for the pyrene monomer, where no influence on the band ratios due to solvent polarity can be seen. Additionally in cyclohexane and toluene a profound red shift of the absorption of the **HAB 1** compared to the monomer is observable.

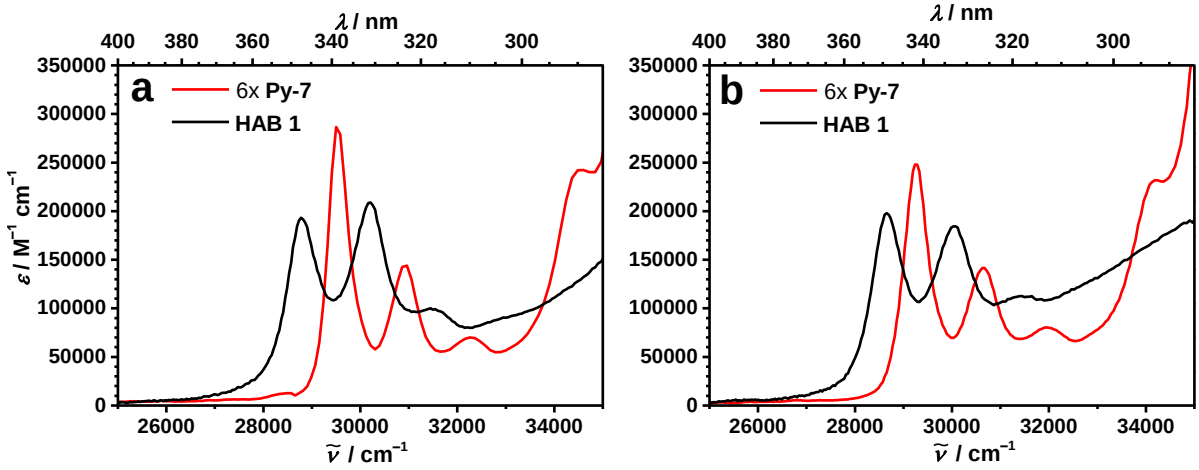

Figure 29 Comparison of **HAB 1** with the monomer **Py-7** in cyclohexane (**a**) and toluene (**b**) at rt.

The influence of the solvent polarity on the vibratonal band intensities is well known for pyrene and can be explained by the Ham effect.[142, 143] This effect describes the increase in intensity of absorption and fluorescence bands due to interaction with the surrounding solvent. The interaction of the molecule with the solvent leads to a coupling of the S_1 and S_2 state and hence symmetry breaking is the consequence. This pertubation leads to a higher intensity of forbidden transitions with vibrational components. The effect gets even more pronounced in polar solvents as additionally to dispersion interactions electrostatic interactions play a role in the solvent-solute interaction. Most remarkably in that context is the

enhancement of the 0-0 band, the energetic lowest transition in pyrene.[118] Applying this theory to **HAB 1**, the 0-0 transition should be most intense in DMF and undergo a distinct decrease in intensity in cyclohexane. However, no such trend can be observed in the spectra of **HAB 1** and additionally the monomer shows no solvent-dependent change of band intensities. Therefore, the Ham effect can not serve as an explanation for the spectral behaviour of the **HAB 1**.

The change in intensity of the band structur relative to each other along with the red shift is often a sign that indicates preassociation in pyrene containing systems.[144] Pyrene does not form aggregates in standard organic solvents but only in polymeric solutions[145] and aqueous media.[146] Additionally to that, the branched alkyl chain should hamper intermolecular aggregation by hindering the molecules from approaching one another. Such observations were already made for hexa-*peri*-hexabenzocoronen[147] and phenylacetylene macrocycles.[148] All this leads to the conclusion that intramolecular interactions should be responsible for the spectroscopic features of **HAB 1**. To study if this assumption is true, concentration-dependent absorption spectra were measured.

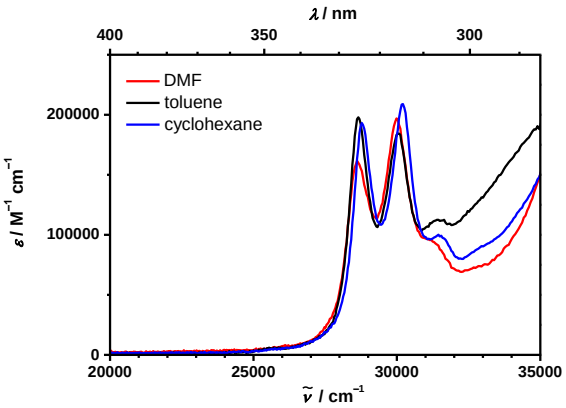

Figure 30 Absorption spectrum of **HAB 1** in different solvents at rt.

Therefore the stock solution of the dye was successivly diluted in the measuring cuvette to prepare concentrations from 10^{-5}–10^{-8} M, but no spectral changes were observed in any solvent.

Hence, the spectral features of **HAB 1** must be caused by intramolecular interactions and there are two possible explanations for these interactions. The centred benzene ring could influence the $S_2 \leftarrow S_0$ transition more than expected from the nodal plain of the involved orbitals of mere pyrene. This could lead to an energetic shift and intensity change of the band ratios. However no such shift is reported for either 2-phenylethynylpyrene or pyrenyl-2[4-(methylbenzonate)] and their absorption spectra resemble the typical band structure of pyrene with a maximum at around (29400 cm^{-1} (340 nm).[60] On the other hand, **HAB-ester** shows a profound red-shift of the $S_2 \leftarrow S_0$ absorption band to 28800 cm^{-1} (347 nm) which is in

a comparable range as for **HAB 1**.[64] Nevertheless no change of the band intensities can be observed in the spectra of **HAB-ester**. The absence of any shifts in the spectra of 2-phenylethynylpyrene or pyrenyl-2[4-(methylbenzonate)] lead to the assumption that the spectral profil of **HAB 1** is not caused by the interaction to the benzene ring, but more likely due to an intramolecular excitonic interaction of the pyrene entities in the HAB, similar to the ones observed for **HAB-ester**.

For a true excitonic interaction a band splitting would be expected and the coupling strength can be exctracted from the measured spectra by comparing the splitting of the band intensities.[97] The coupling element is dependent on the number of interacting chromophores and hence cannot be deduced from the spectra of **HAB 1**. It cannot be concluded from the observed spectra if a complete delocalised system incorporating all six chromophores or just partly delocalisation is dictating the photophysical properties of **HAB 1**, so no exact calculation of the exciton coupling *J* can be performed. Furthermore only one excitonic band ((28600 cm^{-1} (349 nm) in toluene) is observed, as the other bands can be accounted to a vibrational progression. Nevertheless, the red shift can be accounted to a dipole-dipole interaction between the chromophores, leading to a splitting and stabilisation of the state lowest in energy. (see Figure 31). This interaction leads principally to a red shift of the absoprtion spectra independent of the amount of coupled chromophores. For cyclohexane a shift of 780 cm^{-1} and for toluene of 580 cm^{-1} is resulting. This suggests that the interaction strength is influenced by the solvent, though the coupling strength is of similar magnitude.

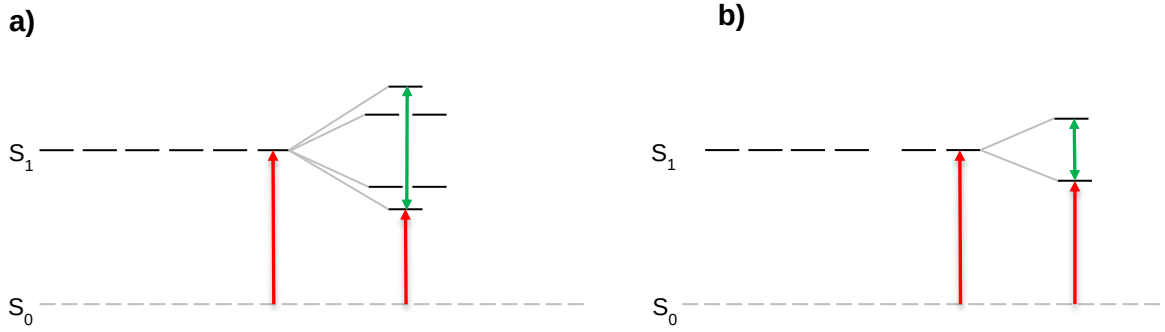

Figure 31 Exciton eigenstates formed by exciton interaction in case of **HAB 1** (C_6-symmertry). The state energies are arbitrary and depend on the coupling *J*. Red arrows indicate the transition from the groundstate to the lowest excited state, green arrows indicate the splitting of the lowest and highest excitonic state. In a) the excitonic coupling for a complet delocalised system and hence interaction of all six chromophores is depicted, while b) represents the case where only two chromophores of the HAB are interacting.

These findings support the assumption that intramolecular interactions are present in all solvents but due to the different band ratios must discern in some way. This difference could be caused by unlike interaction strengths, a different amount of coupled chromophores or a change of orientation of the coupled chromophores relative to each other. Added to that, the interaction observed in **HAB-ester** (see Figure 11) is quite different with the strong enhancement of the $S_1 \leftarrow S_0$ transition but no influence on the higher $S_2 \leftarrow S_0$ transition. The strong electron acceptor properties of the oxygen should lead to stronger intramoleuclar coupling due to electrostatic interactions,[148] making this compound more prone for excitonic interactions as **HAB 1**. Hence additional influences have to play a role in the interaction process to explain the spectral differences between **HAB 1** and **HAB-ester**.

It has already been mentioned, that no concentration-dependency could be observed after dilution of the stock solution in the measuring cuvette. However, dilution experiments that were performed in volumetric flasks lead to concentration effects, but no clear trend was emerging, so that this was not proceeded any further. By using only silylated glass ware, interactions with the glass surface leading to additional spectral changes can be excluded. Futhermore some kinetic studies were executed to evaluate if the aggregation process of **HAB 1** is time-dependent but no definit conculsion could be drawn from these experiments as reproducibility was a constant issue.

5.1.3 Fluorescence Spectroscopy

The interaction of the pyrene chromophores cannot only be studied in the absorption spectra, but is also influencing the fluorescence as inter- and intramolecular interaction lead to different emission properties compared to a non-interacting species.

The emission properties of the **HAB 1** were investigated in different solvents to get a complete picture of the possible interacting species in **HAB 1** and **Py-7** served as modell compound.

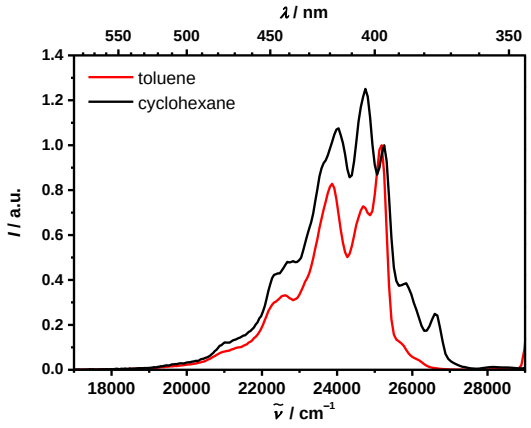

Figure 32 Fluorescence of **Py-7** in toluene (red) and cyclohexane (black) at rt.

The fluorescence of **Py-7** extends the wavenumber range between 27000 cm^{-1} (370 nm) and 19000 cm^{-1} (526 nm) and shows several vibrational bands (see Figure 32), as it is typical for pyrene fluorescence.[118] The band intensities vary with the polarity of the solvent due to the Ham effect, which was discussed in the previous chapter.

Excitation of **HAB 1** at 28600 cm^{-1} (348 nm) in toluene and cyclohexane (see Figure 33a and 33b), leads to two fluorescence peaks. One broad structurless band between 15000 cm^{-1} (667 nm) and 23000 cm^{-1} (435 nm) typical of pyrene aggregates or excimers[58, 144] and a second band at higher energies. The latter band is observed in the range of 23000 cm^{-1} (435 nm) to 27000 cm^{-1} (370 nm) and similar to the pyrene monomer fluorescence.[118] In cyclohexane this pyrene-like band is more structured than in toluene and hence more similar to the parent chromophore **Py-7**. Nevertheless the high energy band shows a broadened spectral profil in comparison with the monomer in both solvents.

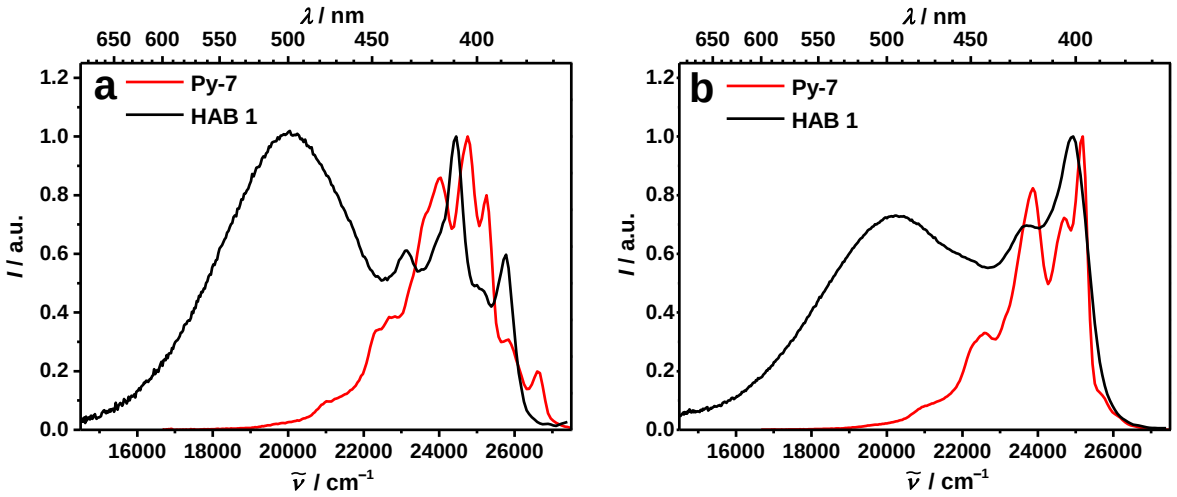

Figure 33 Comparison of the fluorescence spectra of **HAB 1** in cyclohexane (**a**) and toluene (**b**) with its parent compound **Py-7** at rt.

The fluorescence of **HAB 1** is compared in polar, nonpolar and aromatic solvents, more precisely DMF, cyclohexane and toluene. Excitation of the chromophore was always ensued in the lowest energetic absorption band. In all three solvents two peaks, one unresolved, low energy band and a structured fluorescence at higher energies is present (see Figure 34). In the three solvents the most vibrationally-resolved fluorescence can be seen in cyclohexane, whereas in DMF only one maximum at 25300 cm^{-1} (395 nm) with a shoulder at the low energy side is visible. While for the broad band no shift due to solvent polarity can be observed, the high energy band shows an influence on the maximum fluorescence being shifted to lower wavenumbers in cyclohexane. Furthermore the ratio between the two bands is solvent-dependent. The broad band shows highest intensity in DMF and cyclohexane and lower intensity in toluene. This difference in emission intensity of the broad fluorescence band fits well with the observation from the absorption spectra, where the behaviour in toluene is different from DMF and cyclohexane.

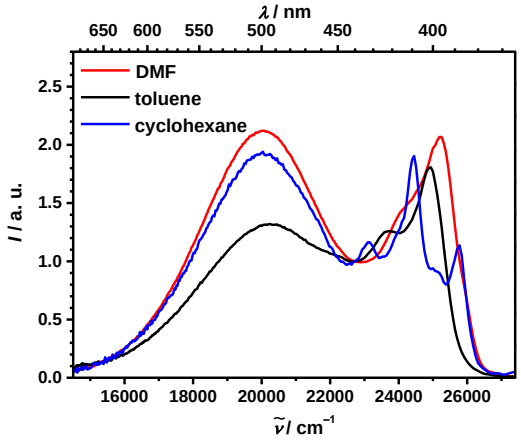

Figure 34 Fluorescence spectrum of **HAB 1** in different solvents at rt.

Due to the similar spectral features of an excimer and an excited intramolecular aggregate that is allready present in the ground state, a distinction based on fluorescence spectra is not possible.[144] But as intermolecular excimer fluorescence is a concentration dependent phenomenon, emission spectra at different optical densities were recorded. The procedure of dilution was the same as described for the measurement of the absorption spectra. No influence of concentration could be found, hence excimer formation between different molecules can be excluded but still intramolecular excimers cannot be ruled out. Furthermore it is not clear whether the monomer fluorescence stems from a true non-interacting monomer or a trapped localised fluorescence from an intramolecular excitonic ensemble. However systems that show localised and delocalised exciton fluorescence have been investigated.[149] It has to be stressed that these molecules are in no way structurally comparable to the here discussed **HAB 1**, but the observed spectral features show some similarities. These star shaped squaraine superchromophores show complex fluorescence spectra with two maxima. The excitation spectra showed that monitoring the fluorescence at different wavelength lead to completely different spectra, of which only the one measured at the low energy side fits with the absorption spectrum. The authors concluded that excitonically decoupling and hence fluorescence stemming from a localised squaraine chromophore and the excitonic manifold defined the spectral properties. A similar spectral profile that shows some similarities to **HAB 1** was observed for **HAB-ester** (see Figure 11). An unresolved shoulder was observed on the low energy side of the monomeric fluorescence. The broad band was assigned to fluorescence from the excitonic manifold of one HAB molecule, as no concentration dependency was observed and excimer formation could be excluded.[64] Such a localised decoupled fluorescence in addition to intramolecularly coupled entities could explain the monomer band additional to the structurless band at lower energies.

To test this assumption excitation spectra at different emisson wavenumbers where recorded to investigate whether the broad fluorescence band stems from intramolecular excimers or intramolecular interactions already present in the ground state.

The excimer can either be formed through the encounter of an excited pyrene monomer and a ground state monomer or a radical anion and a radical kation, but either way the formation takes place on an excited potential energy surface.[150] If the excited ground state aggregate is deactivated, e.g. through fluorescence, it leads to a bound ground state, where as the excimer leads to a dissociative ground state (see Figure 35). For the excimer an excitation spectrum similar to the monomer spectrum should result as no corresponding ground state dimer is accessible. A red-shiftet excitation spectrum is expected if interacting species are already present in the ground state, leading to a relative stabilisation and a minimum on the potential energy surface.[151] In the case of pyrene these ground state aggregates are typicaly arranged in a sandwich type structure, but such an orientation is impossible in the constrained geometry of the **HAB 1**.

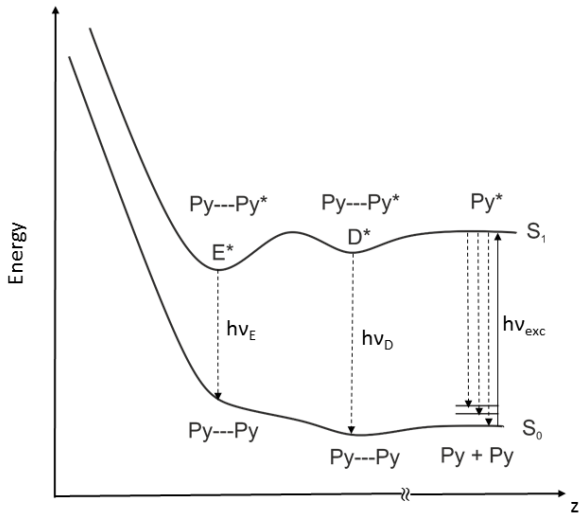

Figure 35 Schematic potential energy diagram for pyrene excimer and excited ground state aggregates.

The excitation spectra will be disscussed for the case of DMF, as the results are similar for cyclohexane and toluene and do not differ in their basic spectral features. The excitation spectra recorded in toluene and cyclohexane can be found in the appendix.

All spectra that where recorded at emission wavenumber of the high energy emission band show the typical vibrational structured monomer bands, which do not fit the absorption spectrum in DMF, but are reminiscent of **Py-7**. Whereas if the emission wavenumber of the low energy band is monitored the typical red shifted absorption spectrum with inverse band intensities of interacting pyrene chromophores is detected (see Figure 36). Therefore the

formation of additional excimers in a considerable amount on the excited state surface can be excluded and the low energy fluorescence stems from intramolecular interacting species already present in the ground state.

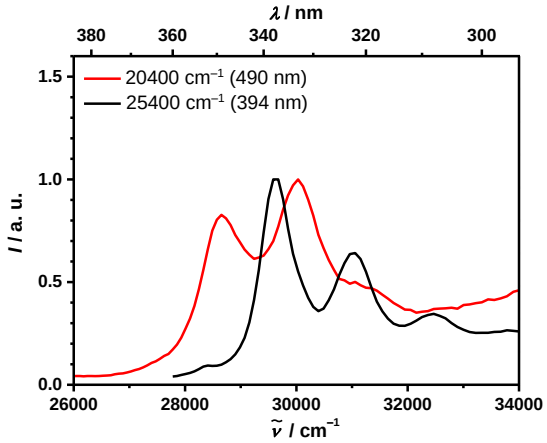

Figure 36 Excitation spectra of **HAB 1** at different emission wavenumbers in DMF at rt.

Due to the difference between the excitation spectra at different wavelength the contribution of at least two different excited species to the spectral features could be confirmed. The distinct difference between the absoprtion spectra and the excitation spectra at high energy wavenumbers leads to the conclusion that a similar situation as decribed for the excitonic squaraine stars is present in **HAB 1**. Hence the emission properties can be accounted to symmetry breaking, possible evoked by solvent interactions, that leads to structured fluorescence of a decoupled pyrene chromophore along with broad low energy fluorescence from a state resulting from intramolecular interaction of two or more pyrenes within one **HAB 1**.

Just as already mentioned for the absorption spectra, additional dilution experiments were also performed in volumetric flasks for the emission spectra. Again this different preperation methode of the diluted samples lead to concentration effects but no clear trend was emerging, so that this study was not proceeded any more. Furthermore these concentration-dependent spectra showed differences in the emission spectra depending on the chosen excitation wavenumber, which made any interpretation impossible. It can not be excluded that kinetic effects play a role in the emission spectra of these experiments as reproducibility was again an issue that could not be solved.

5.1.4 Conclusion

A general synthetic protocol for pyrene alkylation and *Sonogashira* coupling in 2- and 7-position was established. This synthetic route opens a broad varity of new molecules that include a decoupled aromatic system due to the nodal plane through the connecting axis. The synthesis of the hexaarylbenzenes **HAB 1**, **HAB 2** and **HAB 3** worked quite well, even if the yield of the *Diels-Alder* reaction leading to **HAB 2** was quite low.

Absorption and fluorescence spectra reveal strong intramolecular interactions between the pyrene molecules in the **HAB 1**. The absorption bands of the vibrationally resolved $S_2 \leftarrow S_0$ transition are broadened and red shifted. According to this, a broad unresolved blue emission band in the typical emission region of pyrene ground state aggregates or excimers is present in the fluorescence spectra. This blue emission is accompanied by a more structured high energy band similar to pyrene monomer fluorescence. While the lack of concentration dependence proved the presence of intramolecular interactions, the electronic structure seems to vary with the solvent. In DMF and cyclohexane similar electronic interaction lead to comparable spectra, while toluene showed different band ratios in absorption as well as fluorescence spectra. Emission in toluene shows a smaller ratio of the low energy to monomer emission additional to a slightly more resolved vibrational structure of the monomer fluorescence. In all solvents a high energy fluorescence that can be accounted to a state similar to the monomer **Py-7** is present and suggests electronical decoupling in the excited state.

Due to the strong electronic coupling and hence intramolecular interaction being already present in the ground state of the molecule, no energy transfer could be studied. The six pyrene units cannot be seen as separate spectroscopic entities between which energy could be transferred.

5.2 Symmetrical Triads

As in Chapter 4.2 already discussed, the symmetric conjugates are ideal to study the efficiency of energy transfer or the coupling in excitonic states between covalently bound chromophores.

Using ethynyl as a bridging unit makes all symmetric triads easy accessible *via Sonogashira* reactions.

The synthesis of the four chromophores (see Figure 26) needed to built up the conjugates, is literature known or has been established in this work beforehand, hence to work out suitable *Sonogashira* coupling conditions was the focus of this synthetic research. All chromophores were tested in the coupling process with either an alkyne function or in halogenated form. For pyrene and bodipy the synthesis of both starting molecules is literature known. Since the alkynylated form of the indolenine squaraines has not been reported, a procedure was established. In case where the bodipy chromophore was subjected to a *Sonogashira* coupling the iodinated derivative was used, whereas for pyrene and squaraine the brominated analogues were implemented first. To expand the reaction scheme a halogen exchange was tried to substitute the bromo-substituted chromophores by the iodo-analogues which should be more reactive in *Sonogashira* couplings.

5.2.1 Pyrene-containing Triads[1]

Synthesis

Synthesis of **Py_2B**

Bodipy is a well known coupling partner in *Sonogashira* reactions and one can find coupling reactions with 2,6-iodo-[152-158] as well as alkyne-[154, 156] substituted bodipy in literature.

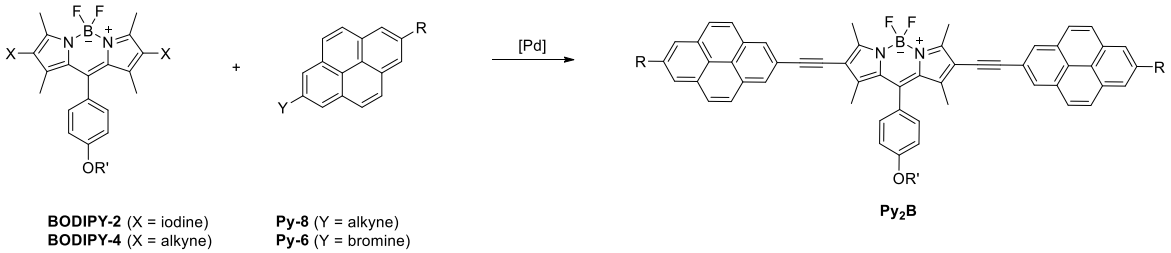

BODIPY-2 (X = iodine)
BODIPY-4 (X = alkyne)

Py-8 (Y = alkyne)
Py-6 (Y = bromine)

Py_2B

R = 3,7-dimethyloctyl; R' = 2-ethylhexyl

Scheme 4 Coupling of differently substituted monomers to the final triad **Py_2B**.

To test both of these substitution patterns in the *Sonogashira* coupling, the iodinated and the alkynylated bodipy were synthesised following literature procedures (see Scheme 3).[154]

To synthesise the bodipy core 4-(2'-ethyl)hexyloxybenzaldehyde was condensated with 2,4-dimethylpyrrole and subsequently oxidised with DDQ to yield the dipyrromethene (see Scheme 5). Complexation of the dipyrromethene with trifluoroborane dietherate led to the desired chromophore **BODIPY-1**. The functionalisation succeded with the use of *N*-iodosuccinimide in 78 % yield. To get to the alkynylated bodipy **BODIPY-4** another two steps were necessary, including a *Sonogashira* reaction with TMSA, followed by deprotection of the trimethylsilyl-group.

[1]Parts of this chapter have been investigated in a Bachelor thesis under the supervision of N. Auerhammer: A. Schulz, Bachelor Thesis, Julius-Maximilians-Universität (Würzburg), 2015.

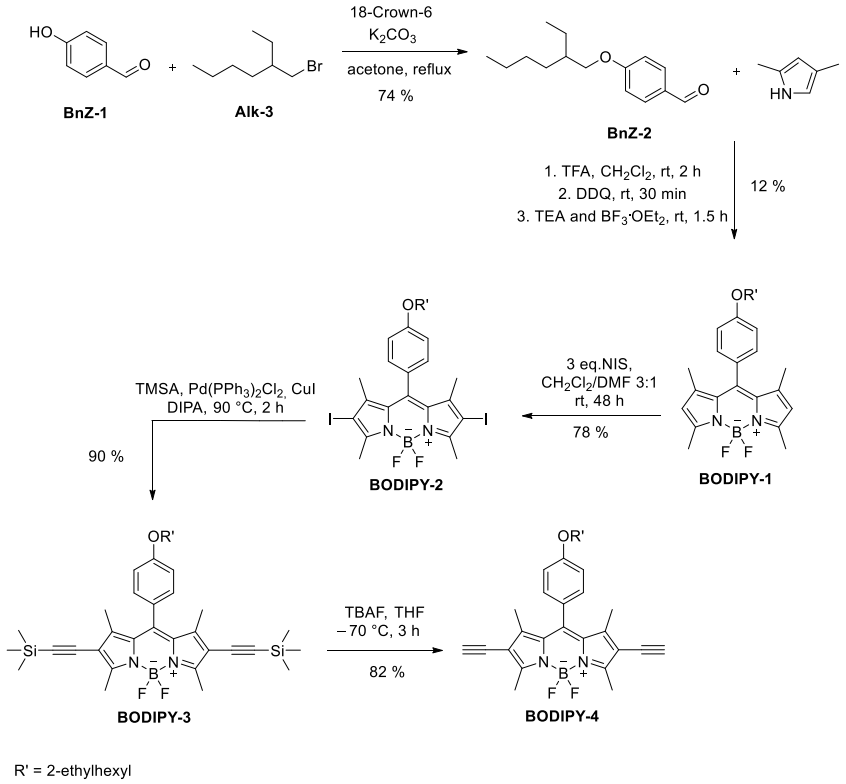

Scheme 5 Synthesis of symmetric bodipy monomers.

The synthesis of the two pyrene compounds used in the coupling reactions follows the pathway described in Chapter 5.1.1.

For the coupling of the bodipy chromophore to pyrene different *Sonogashira* reaction conditions were tested which are summarised in Table 2. The first attempted synthesis follows the procedure of *Thayumanavan et al.*,[154] who used a $Pd(PPh_3)_4$ catalyst to synthesise a bodipy-containing co-polymer (see Table 2, condition I). Unfortunately the yield of the isolated triad, was very low, which is due to the high amount of homo coupled bodipy formed during the reaction. This problem can be due to the CuI co-catalyst or to oxygen present in the solution.[159-161] Considering that the homo coupled bodipy was a problem in an earlier work in this group[162] when using **BODIPY-4**, it is assumed that the homo coupling is often favoured in case of less reactive coupling partners. This assumption is supported by mass spectrometry analysis. Under condition I the di- or tri-homo conjugates subsequently coupled to pyrene leading to heterotetrads and heteropentads. Therefore a less reactive catalytic system consisting of $Pd(C_6H_5CN)_2Cl_2/P^tBu_3$, which was already successfully applied in *Sonogashira* reactions involving pyrene[120, 140] (see also Chapter 5.1.1) was chosen next to surpress the multiple homo coupling of the bodipy chromophore (see Table 2, condition II). Unfortunatly with **BODIPY-4** no product was formed when the reaction was carried out in dioxane.

As formation of homo coupled pyrene was never an issue in *Sonogashira* couplings of **Py-6** to **Py-8** and iodinated bodipy should be more reactive than brominated pyrene, the substituents of the coupling partners were changed. In the coupling of **Py-8** and **BODIPY-2** the conditions from *Hundertmark et al*.[140] were tried again, only the solvent was changed to DMF (see Table 2, condition III). Under these conditions only 10 % of the desired triad could be isolated. The reason to change the solvent was, that due to the higher polarity of DMF compared to dioxane, the stabilisation of the transition state formed during the reaction might be improved. This effect has already been observed in copper-free *Sonogashira* reactions.[163]

In a last attempt, to improve the yield, conditions from *Ziessel et al*.[158] were tried (see Table 2, condition IV). They coupled an unsymmetrically substituted bis(difluoroboron)-1,2-bis{(1*H*-pyrrol-2-yl)methylene}hydrazine (BOPHY) to a perylene molecule with $Pd(dppf)Cl_2 \cdot CH_2Cl_2$ under ligand free conditions at room temperature. As their system is quite similar to the bodipy-pyrene one used in this study, the conditions should work equally well here. As the reaction did not seem to proceed after four days, the temperature was raised to 50 °C. The product could be isolated in 50 % yield, even though surprisingly also a small amount of homo coupled pyrene was formed.

Table 2 Coupling conditions to yield the symmetric triad **Py_2B** (for X and Y compare Scheme 4).

	X	Y	catalyst/ligand [mol%]	base	solvent	CuI [mol%]	T/t	yield [%]
I[152, 154]	alkyne	Br	$Pd(PPh_3)_4$/- (7)	TEA	toluene	14	60 °C/24 h	3
II[120, 140]	alkyne	Br	$Pd(C_6H_5CN)_2Cl_2$/ P^tBu_3 (3/65)	DIPA	dioxane	2	55 °C/10 min	-
III[120, 140]	I	alkyne	$Pd(C_6H_5CN)_2Cl_2$/ P^tBu_3 (3/65)	DIPA	DMF	2	50 °C/3 d	10[a]
IV[158]	I	alkyne	$Pd(dppf)Cl_2 \cdot CH_2Cl_2$/- (6)	TEA	THF	12	rt → 50 °C/4 d	50

[a] not purified completely.

Synthesis of **Py_2SQB**

As for the synthesis of the symmetric triad an excess of the terminal pyrene is used, homo coupling can be a competing reaction when the alkynylated pyrene **Py-8** is used, as could be seen in the synthesis of **Py_2B**. To exclude this problem, the *Sonogashira* coupling for synthesising **Py_2SQB** was tried using alkynylated squaraine and brominated pyrene **Py-6**

The pyrene synthesis follows the reaction scheme from Chapter 5.1.1.

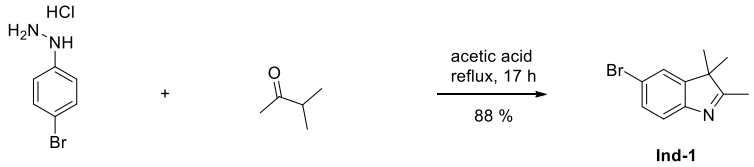

Scheme 6 Synthesis of the bromo-substituted indolenine scaffold.

The synthesis of the symmetrical *cis*-squaraine starts with the *Fischer-Indol*-reaction of *p*-bromophenylhydrazine hydrochloride with isopropylmethyl ketone (see Scheme 6). The yielded indolenine derivative 5-bromo-2,3,3-trimethyl-3*H*-indole (**Ind-1**) was alkylated by refluxing in nitromethane with 1-iodo-3,7-dimethyloctyl (**Alk-2**) (see Scheme 7).[134]

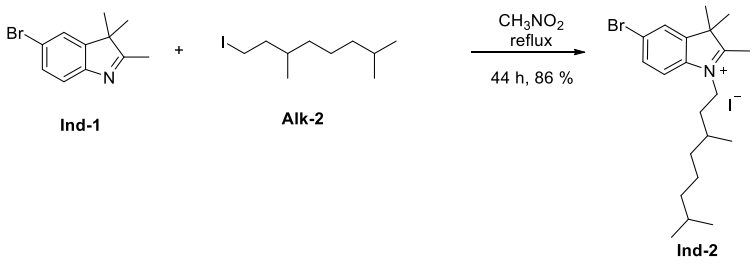

Scheme 7 Alkylation of brominated indole.

The quaternary salt 5-bromo-1-(3,7-dimethyloctyl)-2,3,3-trimethyl-3*H*-indole-1-ium iodine (**Ind-2**) was converted to the cisoid squaraine in a one pot reaction with a yield of 86 % (see Scheme 8). In this reaction the first step is the deprotonation of the methyl group, leading to the highly nucleophilic methylene base, which subsequently undergoes a condensation with triethylammonium 2-butoxy-3-(dicyanomethylene)-4-oxocyclobut-1-enolate.[134] The later was synthesised according to literature procedure from 3,4-dibutoxy-3-cyclobutene-1,2-dione and malonitrile.[164]

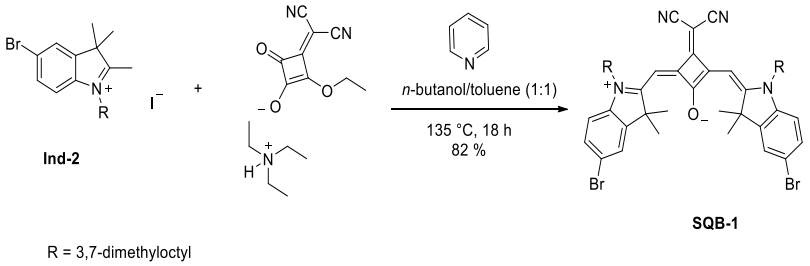

Scheme 8 Synthesis of symmetric *cis*-squaraine **SQB-1**.

For the alkynylation of the *cis*-squaraine **SQB-1** the already established conditions for pyrene (see Chapter 5.1.1) were successfully applied, leading to 77 % yield. The squaraine **SQB-2** was stirred with TBAF for 2 h to cleave the trimethylsilylgroup and get the free alkyne **SQB-3** in 87 % yield (see Scheme 9).

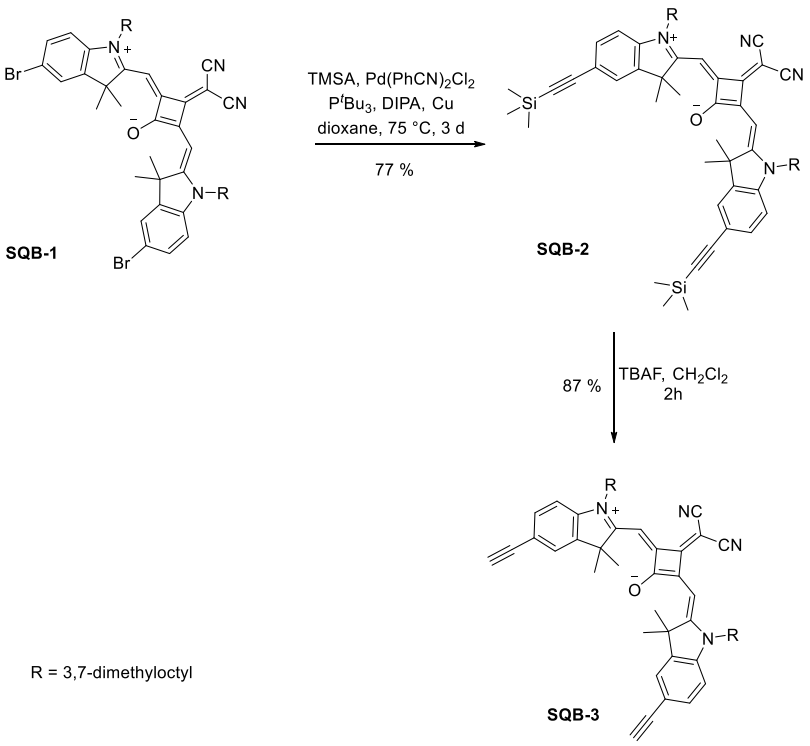

Scheme 9 Alkynylation and cleavage of the TMS-group of *cis*-squaraine **SQB-1**.

Table 3 Tested conditions for the synthesis of **Py_2SQB**.

	catalyst./ligand [mol%]	base	solvent	CuI [mol%]	T/t	yield
I[120, 165, 166]	$Pd(PPh_3)_2Cl_2/P^tBu_3$ (2/4)	DBU	DMF	-	150 °C/10 min; MW	-
II[167]	$Pd_2(dba)_3$/P(*o*-tol) (10/100)	DIPA	THF	0.17	45 °C/3 h	-
III[120, 140]	$Pd(C_6H_5CN)_2Cl_2/P^tBu_3$ (10/13)	DIPA	DMF	0.08	75 °C/3 d	15 %
IV[120, 140]	$Pd(C_6H_5CN)_2Cl_2/P^tBu_3$ (20/26)	DIPA	dioxane	0.08	75 °C/3 d	11 %

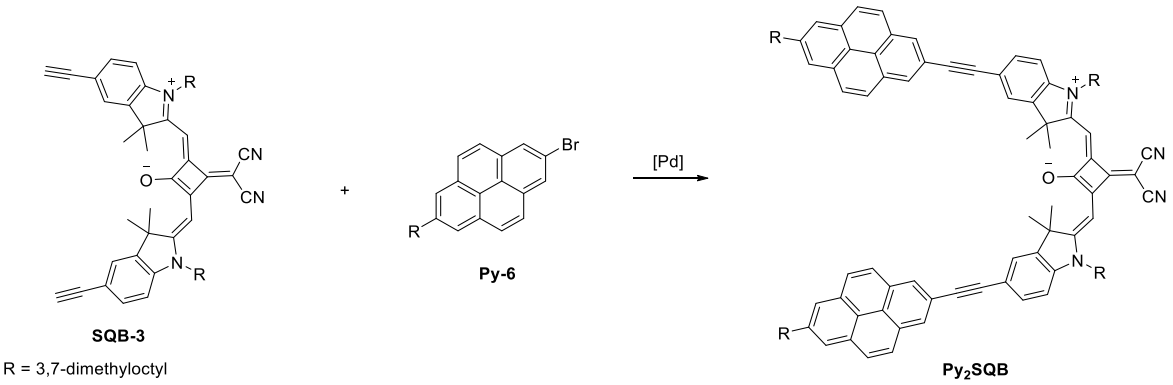

Scheme 10 Coupling of the alkynylated *cis*-squaraine **SQB-3** with bromo substituted pyrene **Py-6** to yield the **Py_2(SQB)** triad.

The tested *Sonogashira* conditions for the **Py_2SQB** triad (see Scheme 10) are summarised in Table 3. Only few *Sonogashira* reactions involving indolenine squaraines are reported in literature. The few that were found mostly made use of the brominated squaraine[168] or at least a halogenated squaraine[100, 167] as coupling partner, but this should be avoided to exclude homo coupling of **Py-8**. Nevertheless these conditions could serve as a starting point for the synthesis.

First a microwave reaction which proved to be successful for pyrene couplings before (see Chapter 5.1.1) was tried using $Pd(PPh_3)_2Cl_2$ as catalyst and P^tBu_3 as ligand[120, 166] (see Table 3, condition I), but the alkynylated squaraine seemed to decompose as only pyrene could be isolated afterwards. Next a $Pd_2(dba)_3$ catalyst was tested,[167] but again no product formation could be observed (see Table 3, conditions II). Instead homo coupled squaraine and mono coupled product was detected. Lastly the $Pd(C_6H_5CN)_2Cl_2$ catalyst with P^tBu_3 as ligand[120, 140] was tested and led to the desired triad in DMF as well as in dioxane after 3 d at 75 °C (see Table 3, conditions III and IV). In both cases the yield was pretty low, but no side products

could be identified, therefore it is assumed that decomposition of squaraine could be a problem, as this seemed to happen under conditions I as well.

Synthesis of **Py_2SQA**

For the synthesis of **Py_2SQA** three squaraines with different substituents were synthesised to test their performance in the coupling reactions in order to get higher yields than for the *cis*-analogue.

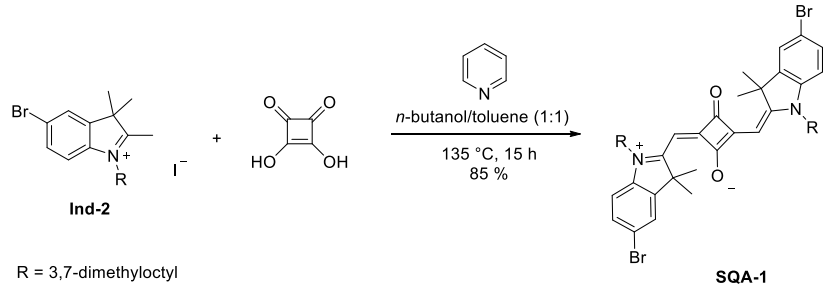

Scheme 11 Synthesis of symmetric *trans*-squaraine **SQA-1**.

First **SQA-1** was synthesised in a one pot reaction by condensation of 5-bromo-1-(3,7-dimethyloctyl)-2,3,3-trimethyl-3*H*-indole-1-ium iodide (**Ind-2**) with squaric acid (see Scheme 11).[169]

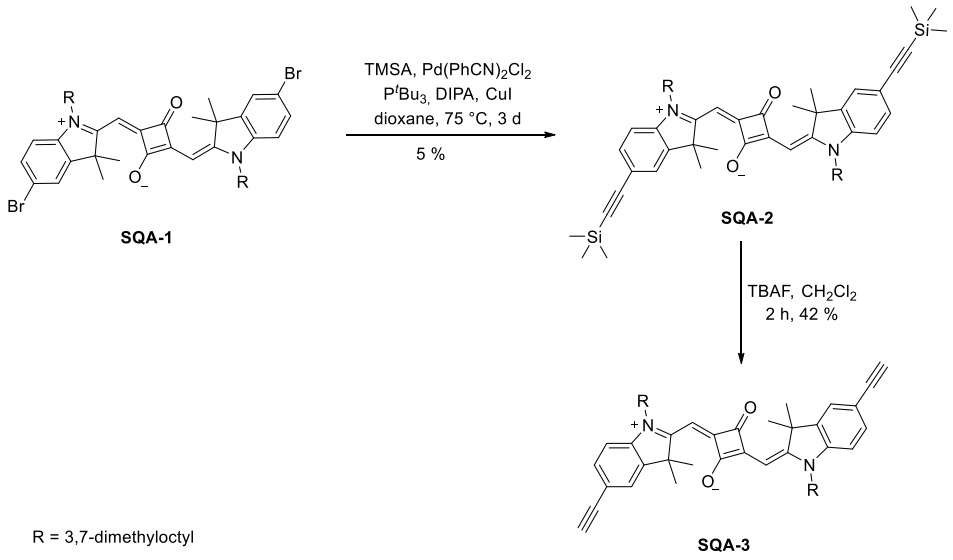

Scheme 12 Alkynylation and deprotection of *trans*-squaraine **SQA-2**.

The symmetric transoid squaraine **SQA-1** was then converted with TMSA in a *Sonogashira* reaction to the alkynylated squaraine **SQA-2**, which was deprotected by stirring in CH_2Cl_2 with an excess of TBAF (see Scheme 12). To try another substituent in the *Sonogashira* coupling a halogen exchange reaction with the symmetrical transoid indolenine squaraine **SQA-1** was carried out which yielded the iodinated *trans*-squaraine derivative **SQA-4** in 89 %

yield (see Scheme 13).[170, 171] This aromatic *Finkelstein* reaction depends on the equilibrium, which is shifted by a high amount of NaI added, to yield the desired **SQA-4**.

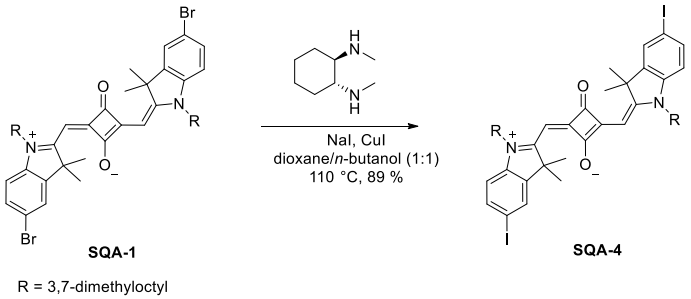

Scheme 13 Synthesis of symmetric substituted iodo *trans*-squaraine **SQA-4**.

The *Sonogashira* couplings were tested with the three different symmetric squaraines **SQA-1**, **SQA-3** and **SQA-4** and the appropriate pyrene on such a small scale, that no yield could be determined and product analysis was accomplished by mass spectroscopy. All findings from these test reactions are summarised in Table 4.

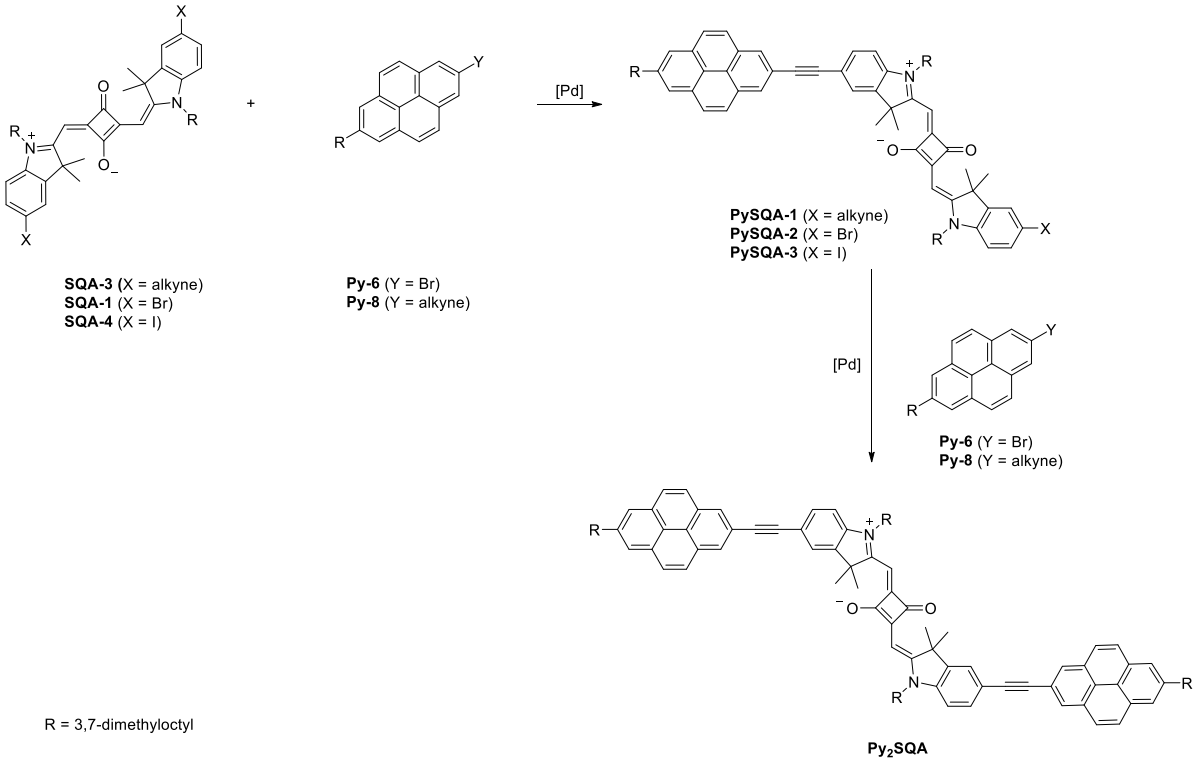

Scheme 14 *Sonogashira* coupling to yield **Py$_2$SQA** in a two step synthesis.

For the alkynylated squaraine **SQA-3** the $Pd(C_6H_5CN)_2Cl_2$ catalyst with P^{t}Bu$_3$ as ligand was tested for the coupling with **Py-6** in DMF and dioxane as solvents (see Table 4, conditions II and III).[120, 140] Unfortunately only the second condition showed any conversion, but the reaction stopped at the mono coupled product **PySQA-1**.

With $Pd(PPh_3)_2Cl_2$ as catalyst[172] no product formation whatsoever could be detected (see Table 4, condition I).

When changing the applied squaraine from **SQA-3** to **SQA-1** the catalytic system $Pd(PhCN)_2Cl_2/P^tBu_3$[120, 140] was tested again as it worked best in the coupling of the alkynylated *cis*-squaraine with pyrene. However it only led to the half coupling product **PySQA-2**, with a lot of starting material still present in the reaction mixture (see Table 4, condition V).

Since using $Pd(PPh_3)_4$ as catalyst in THF[152] was not successful as well (see Table 4, condition VII), a different protocol was followed which led to efficient coupling with the same indolenine squaraine as used in this synthesis.[97] Under these copper-free coupling conditions only traces of the mono coupled product could be isolated (see Table 4, condition IV).

Lastly the $Pd(MeCN)_2Cl_2$ catalyst with a sterically demanding biarylphosphine ligand was tested,[173] which yielded a mixture of **Py_2SQA** and **PySQA-2**, that was impossible to separate (Table 4, condition VI).

After all, these *Sonogashira* reactions involve several problems. Some catalytic systems were not reactive enough to lead to coupling of the monomers but the dehalogenation as competing reaction was the main issue. Therefore a lot of debrominated mono coupled product and starting material was always present in the reaction mixture. To overcome this obstacle the iodinated squaraine **SQA-4** was synthesised, as the higher reactivity could lead to a faster coupling and thus overcome dehalogenation.

Several small test reactions were run to evaluate the performance of **SQA-4** in the *Sonogashira* coupling. Therefore, the most promising conditions from the previously tried couplings were tested first. In this case the $Pd(MeCN)_2Cl_2$ catalyst showed the worst performance by resulting in only mono coupled product **PySQA-3** (see Table 4, condition X). However the $Pd(PPh_3)_4$ catalyst, which did not lead to product formation with brominated squaraine **SQA-1**, showed promising results when the iodinated squaraine **SQA-4** was used (see Table 4, condition XI).

In the case of the $Pd(C_6H_5CN)_2Cl_2$ catalyst the influence of changing the base from DIPA (see Table 4, condition VIII) to the sterically less demanding TEA (see Table 4, condition IX) was studied. There was no big difference in the product conversion, just a marginally better mono coupled to bi coupled product ratio when TEA as base was used.

Table 4 Tested conditions for the synthesis of **Py_2SQA** (for X and Y compare Scheme 14).

	X	Y	catalyst/ligand	base	solvent	T/t	conversion
I[172]	alkyne	Br	$Pd(PPh_3)_2Cl_2$	TEA	THF	60 °C/5 d	-
II[120, 140]	alkyne	Br	$Pd(C_6H_5CN)_2Cl_2$/ P^tBu_3	DIPA	DMF	75 °C/7 d	-
III[120, 140]	alkyne	Br	$Pd(C_6H_5CN)_2Cl_2$/ P^tBu_3	DIPA	dioxane	60 °C/3 d	**PySQA-1**
IV[97]	Br	alkyne	$Pd_2(dba)_3$/ P(*o*-tol)	TEA	toluene	90° C/7 d	traces of **PySQA-2**
V[140]	Br	alkyne	$Pd(C_6H_5CN)_2Cl_2$/ P^tBu_3	DIPA	dioxane	75 °C/11 d	**PySQA-2**
VI[173]	Br	alkyne	$Pd(MeCN)_2Cl_2$/ XPhos	DIPA	dioxane	90 °C/6d	**PySQA-2**, **Py_2SQA**
VII[152]	Br	alkyne	$Pd(PPh_3)_4$	DIPA	THF	60 °C/9 d	-
VIII[120, 140]	I	alkyne	$Pd(C_6H_5CN)_2Cl_2$/ P^tBu_3	DIPA	dioxane	75 °C/24 h	**PySQA-3**, **Py_2SQA**
IX[120, 140]	I	alkyne	$Pd(C_6H_5CN)_2Cl_2$/ P^tBu_3	TEA	dioxane	60 °C/3 d	**PySQA-3**, **Py_2SQA**
X[173]	I	alkyne	$Pd(MeCN)_2Cl_2$/ XPhos	DIPA	dioxane	60 °C/12 d	**PySQA-3**
XI[154]	I	alkyne	$Pd(PPh_3)_4$	TEA	toluene	rt/24 h	**PySQA-3**, **Py_2SQA**

Conditons IX and XI were tested on a higher scale, but in both cases the reaction stopped at the mono coupled product. Therefore the reaction mixture was worked up and subjected to the same conditions again, which led to formation of the final product **Py_2SQA** in both cases (see Scheme 14).

It was found that the first coupling step proceeds better with the $Pd(C_6H_5CN)_2Cl_2$ catalyst, as these conditions are less prone to dehalogenation and for the second step the $Pd(PPh_3)_4$-catalyst gives the best results, as it is the more reactive catalytic system.

Using these two conditions, the desired product could be synthesised but the purification failed. Neither column chromatography nor GPC helped as always partly decomposition made purification impossible.

Absorption Spectroscopy

The symmetrical triads **Py_2B** and **Py_2SQB** were investigated in cyclohexane, toluene, CH_2Cl_2 and $CHCl_3$ and compared with their parent compounds. Their photophysical properties are summarised in Table 5.

The absorption spectrum of **Py-7** in CH_2Cl_2 shows the typical vibrationally resolved absorption bands of the $S_2 \leftarrow S_0$ excitation of the pyrene core with the maximum at around 29400 cm^{-1} (340 nm) (see Figure 37b). For **Py-9** the absorption spectrum is not as well resolved, as there are additional bands at higher energies (see Figure 37b). This was also observed by *Marder et al*., who investigated the 2-phenylethylene-pyrene and assigned the additonal bands to the rotation of the benzene ring.[60] The extinction coefficients are in a similar range with 33200 $M^{-1}cm^{-1}$ for **Py-7** and 45800 $M^{-1}cm^{-1}$ for **Py-9**.

The absorption spectrum of **Py_2B** covers a broad wavenumber range with one maximum at lower energies and one at the blue edge of the spectrum (see Figure 37a). In each solvent an intense maximum at around 17200 cm^{-1} (581 nm) and an additional, weak and broader band between 22000–28000 cm^{-1} (357–455 nm) define the spectra. The low energy absorption originates from the $S_1 \leftarrow S_0$ transition of bodipy, while the small, broader band is covering transitions from the S_0 state to the S_2 and S_3 state.[174] While there is no solvent dependence detectable (see Figure 37a) the bodipy band is red shifted and broadened in comparison to **BODIPY-3** (fwhm: **Py_2B**: 1790 cm^{-1}; **BODIPY-3**: 1080 cm^{-1}) and accordingly the extinction coefficient drops from 83200 $M^{-1}cm^{-1}$ for **BODIPY-3** to an extinction coefficient of 69600 $M^{-1}cm^{-1}$ for **Py_2B** (see Figure 37b). The most profound difference of the parent compound to the triad can be seen in the pyrene absorption area (28000–32000 cm^{-1} (313–357 nm)).

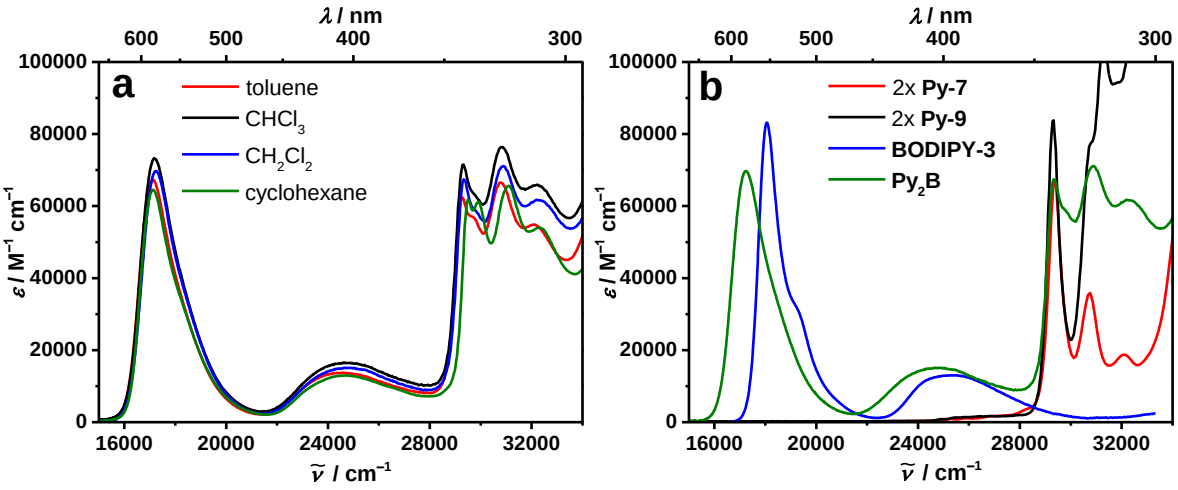

Figure 37 Absorption spectra of **Py_2B** in different solvents (**a**) and comparison with the parent compounds **BODIPY-3**, **Py-7** and **Py-9** (**b**) in CH_2Cl_2 at rt.

A comparison of **Py_2B** with the pyrene molecules **Py-7** and **Py-9** shows that the pyrene absorption bands in **Py_2B** are more similar to the later but are less well resolved (see Figure 37b). The intense absorption escpecially above 29000 cm^{-1} points towards additional bands, steming from ground state interactions between the constituents. The assumption of electronic communication between the subunits is confirmed by the broadened, red shifted bodipy absorption band. For comparison of **Py_2SQB** with its parent squaraine the monomeric **SQB** chromophore was used. Spectroscopic data were partly adapted from the Ph.D thesis of Dr. Sebastian Völker.[175]

Table 5 Absorption maxima ($\tilde{\upsilon}_{abs}$), extinction coefficients (ε), absorption transition moments (μ^2_{abs}), fluorescence maxima ($\tilde{\upsilon}_{fl}$), fluorescence transition moments (μ^2_{fl}) and fluorescence quantum yields (ϕ_{fl}) of the symmetric triads and the according reference compounds in various solvents at rt.

	solvent	$\tilde{\upsilon}_{abs}$ /cm^{-1} (nm) [fwhm]	ε /M^{-1} cm^{-1}	μ^2_{abs} /D^2	$\tilde{\upsilon}_{fl}$ /cm^{-1} (nm) [fwhm]	μ^2_{fl} /D^2	ϕ_{fl}* ($\tilde{\upsilon}_{ex}$/cm^{-1})
Py-7	$CHCl_3$	29300 (341)	38500	1.14[a]/14.2[b]			
	CH_2Cl_2	29400 (340)	33200	0.98[a]/12.6[b]	25200 (397)	0.22	0.10 (29400)
	toluene	29300 (341)	41500	0.76[a]/15.6[b]	25200 (397)	1.26	0.27 (29200)
	cyclohexane	29500 (339)	43400	0.97[a]/14.2[b]	24800 (403)		
Py-9	$CHCl_3$	29300 (341)	44200	1.23[a]/13.5[b]	24800 (403)		
	CH_2Cl_2	29300 (341)	45800	0.91[a]/12.9[b]	24800 (403)	0.26	0.13 (29300)
	toluene	29300 (341)	44200	1.28[a]/12.9[b]	24800 (403)	0.55	0.33 (29200)
	cyclohexane	29500 (339)	52700	0.65[a]/12.5[b]	24400 (410)		
BODIPY-3	$CHCl_3$	18000 (555) [1020]	85400	46.1	17500 (571) [970]		
	CH_2Cl_2	18100 (552) [1080]	83200	48.4	17600 (568) [1030]	48.5	0.84 (20000)
	toluene	18000 (555) [950]	86900	44.9	17500 (571) [932]	47.9	0.92 (18900)
SQB	CH_2Cl_2	14600 (685) [770]	207300	112	14300 (704) [800]	93.5	0.48 (15900)
	toluene	14300 (700) [660]	202000	92.7	14000 (714) [840]	92.2	0.75 (15400)
Py_2B	$CHCl_3$	17200 (582) [1810] 30800 (324)	73300 76700	59.5	16200 (617) [1350]		
	CH_2Cl_2	17200 (581) 30900 (324) [1790]	69600 70900	58.7	16300 (613) [1370]	79.3	0.82 (29200) 0.72 (18900)
	toluene	17100 (584) [1770] 30800 (325)	67400 66500	53.2	16200 (617) [1170]	78.5	0.92 (29200) 0.84 (24500)
	cyclohexane	17100 (594) [1760] 31100 (322)	64500 65700	50.2	16400 (610) [960]		0.92 (31100) 0.86 (18200)
Py_2SQB	$CHCl_3$	13700 (730) [690]	188000	92.7	13500 (741) [700]		
	CH_2Cl_2	13800 (725) [706]	179600	95.6	13500 (741) [710]	156.2	0.65 (29200) 0.67 (14700)
	toluene	13500 (741) [640]	195000	86.2	13300 (752) [670]	146.5	0.91 (29200) 0.88 (15000)
	cyclohexane	13400 (746) [544]	201000	86.2	13300 (752) [610]		0.85 (31100) 0.85 (15000)

*For the symmetric triads two quantum yields, depending on excitation at the high or low energy absorption band were obtained. The corresponding excitation wavenumbers are given in parenthesis. [a] Transition dipole moment of the $S_1 \leftarrow S_0$ transition. [b] Transition dipole moment of the $S_2 \leftarrow S_0$ transition.

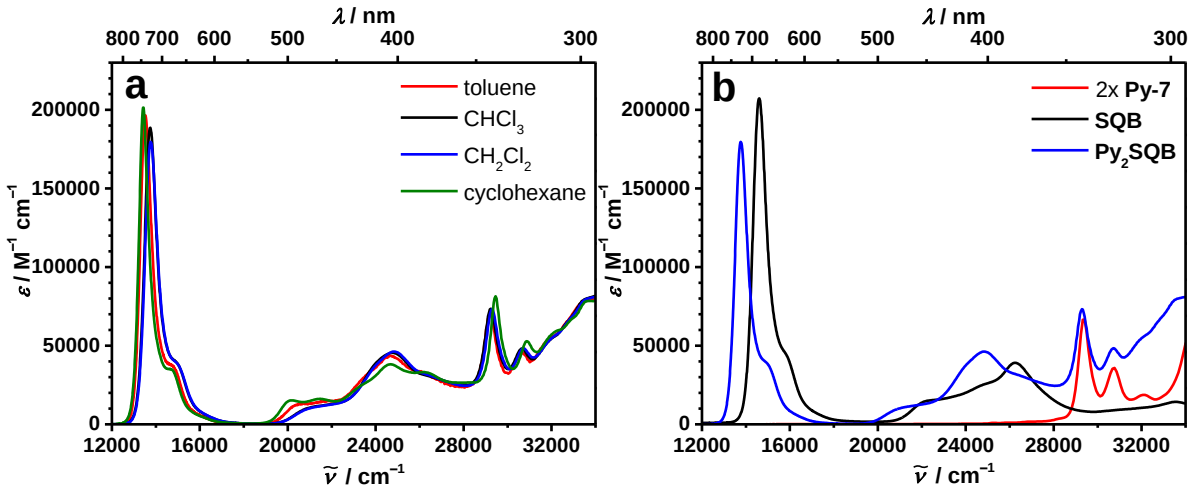

Figure 38 Absorption spectrum of **Py₂SQB** in different solvents at rt (**a**) and in comparison to the monomers **SQB** and **Py-7** in CH_2Cl_2 at rt (**b**).

The absorption spectrum of **Py₂SQB** (see Figure 38b) is dominated by a narrow intense band at 13800 cm^{-1} (725 nm) in CH_2Cl_2 which is shifted about 800 cm^{-1} to the red in comparison to the main absorption of **SQB** at 14600 cm^{-1} (685 nm). The smaller, more broadened band in the triad shows similar behaviour with a shift of about 2500 cm^{-1} to lower wavenumbers. Recently it could be shown by TD-DFT calculations and fluorescence excitation anisotropy that this band originates from two electronic transitions in **SQB** to higher excited states.[116] At higher wavenumbers an absorption band reminicent of the pyrene chromophore is observable, consisting of several vibrationally resolved transitions. These bands are left unchanged compared to **Py-7** and considering that the *cis*-squaraine shows only a small absorption coefficient in that wavenumber range, are about twice as intense as the monomeric parent compound. Further at the blue edge of the spectra a high energy band is partially overlapping with the pyrene absorption, but its origin is unknown. This is not the case for **Py₂B** as here the band intensities in this wavenumber area are interchanged refering to **Py-7** and hence differ in intensity. This implies that interaction between the constituents in **Py₂B** is stronger leading to new states, which are not observed in **Py₂SQB**. No profound solvent dependence is observeable, only the low energy band shows a slight shift to higher wavenumbers in less polar solvents (see Figure 38a). In contrast to **Py₂B** the full width at half maximum (fwhm) of the lowest energetic absorption band of **Py₂SQB** in CH_2Cl_2 is with 706 cm^{-1} smaller than the one of **SQB** with 770 cm^{-1}.

The transition-dipole moments of the triads are summarised in Table 5 and can be calculated from spectral properties using equation (41):[176]

$$\mu_{\mathrm{abs}}^2 = \frac{3hc\varepsilon_0 \ln 10}{2000\pi^2 N_{\mathrm{AV}}} \frac{9n}{(n^2+2)^2} \int \frac{\varepsilon}{\tilde{\nu}} d\tilde{\nu} \quad (41)$$

The resulting transition-dipole moments of the main absorption bands of **Py₂B** (μ^2 = 58.7 D^2) and **Py₂SQB** (μ^2 = 95.6 D^2) in CH_2Cl_2 show oscillaor strengths of a similar magnitude as the parent compounds and therefore the electronic character seems to be preserved in the triads.

Nevertheless, the spectral shifts and the variation of the fwhm of both triads suggest a moderate interaction in the ground state. To get a better insight into the strength of these interactions exciton coupling theory can be applied. The large energy difference between the interacting chromophores leads to small spectral shifts and more localised states.[97] Hence, no conclusion about the level of interaction can be drawn just from the shifts. Therefore, the exciton coupling energy J is calculated by using:

$$\delta E = 2\sqrt{\Delta E^2 + 2J^2} \quad (42)$$

With $\Delta E = (E_{\mathrm{Py}} - E_{\mathrm{SQB/B}})/2$ and E_{B}, E_{SQB} and E_{Py} being the energies of the main absorption of the undisturbed monomer states of **BODIPY-3** or **SQB** and the $S_2 \leftarrow S_0$ transition of **Py-7** and δE being the difference between the maxima of the two main absoprtion bands in the triads. This leads to an overall excitonic coupling $|J|$ = 1790 cm^{-1} for **Py₂SQB** (with δE: 15550 cm^{-1}, ΔE: 7350 cm^{-1}). The same calculation yields $|J|$ = 1520 cm^{-1} for **Py₂B** (with δE: 12030 cm^{-1}, ΔE: 5620 cm^{-1}). Taking into account that this is only a crude estimation, it can be said that the coupling strengths of both triads are of similar magnitude and can be assigned to the strong coupling regime with J exceeding 1000 cm^{-1}. Still the lowest exciton state is localised almost completely on the squaraine or bodipy chromophore, so that most spectral characteristics are preserved. Nevertheless, the strong coupling resulting from applying this theory is surprising, especially considering the energy difference between the constituents. To evaluate if the spectral shifts actually origin from an excitonic coupling based on dipole-dipole interactions the latter can be calculated using equation (43):

$$V = \frac{1}{4\pi\varepsilon_0 hc} \frac{|\mu_{\mathrm{A}}||\mu_{\mathrm{B}}|}{r^3} (cos\theta_{\mathrm{AB}} - 3cos\theta_{\mathrm{A}} cos\theta_{\mathrm{B}}) \quad (43)$$

With h being Planck's constant, ε_0 the permittivity, and c the speed of light. The interacting dipoles μ_{A} and μ_{B} were calculated using the absorption spectra of the monomers in CH_2Cl_2 according to equation (41) and the distance *r* between the constituents in the triads is taken from DFT computations[1] (r = 10.98 × 10^{-10} m (**Py₂B**), r = 15.1 × 10^{-10} m (**Py₂SQB**). θ_{A} and θ_{B} define the angle between the transition-dipole moment and the connecting vector from the center of molecule A to the center of molecule B and θ_{AB} is the angle between the two transition-dipole moments. θ_{AB} (compare Figure 4 in Chapter 2) is assumed to be 0° for both

triads, which would be true for a coupling of the S_2 state of pyrene and the S_1 or S_3 state of bodipy or squaraine. While this assumption might be true for **Py₂B**, in **Py₂SQB** the bent geometry leads to angles that derivate from zero (see Figure 39). Due to the angles used for the calculation the transition moment of **Py-7** of the S_2 state (3.55 D) and the S_1 state of **BODIPY-3** (6.96 D) were used for the calculation. This yields an interaction of −187.89 cm^{-1}, a value distinctly lower than the 1520 cm^{-1} evaluated by applying exciton theory. In case of **Py₂SQB** an interaction of −110.04 cm^{-1} is yielded when the transition moment of μ = 10.6 D of the S_1 state of **SQB** is implemented. These results show that the spectral characteristics are not resulting from a dipole-dipole interaction as this proves to be too small. Hence the red shift of the absorption bands cannot be explained by utilising exciton theory but should be caused by the conjugated connection, which is known to enable electronic communication.[96] It has to be mentioned that the calculated coupling is an upper estimation of the actually present situation in the molecules.

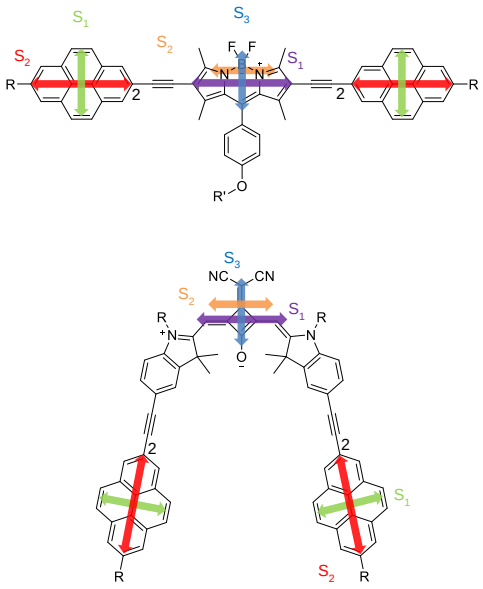

Figure 39 **Py₂SQB** and **Py₂B** with direction of transition moments depicted by bold arrows. Additionally the C_2-position of pyrene is marked.

***DFT Calculations of the Molecular Orbitals*[1]**

As the absorption spectra of both triads showed signs of ground state interaction, the molecular orbitals of **Py_2SQB** and **Py_2B** were calculated by DFT to see whether the electron density is localised on the constituents or delocalised over the whole superchromophore. (see Figure 40). In both cases the HOMO-1 is pyrene centered while for the LUMO electron density is localised on the bodipy or squaraine only, but it is noted that for **Py_2B** the LUMO includes the ethynylene bridge as well, which shows no contribution in the LUMO of **Py_2SQB**.

The difference between the absorption spectra of the two triads can be explained when looking at the HOMO. The HOMO of **Py_2SQB** is mostly localised at the squaraine but shows electron density at the ethynylene bridge as well. The HOMO of **Py_2B** on the other hand has a quite different distribution of electron density. The HOMO is extended over a big part of the molecule showing electron density at pyrene as well as the bodipy chromophore. This states that in **Py_2B** the subunits are less separated and stronger interactions appear in the ground state. In **Py_2SQB** no coupling could be proved and the states show electron density only at the subunits. It can be argued that the smaller energy difference of the constituents of the **Py_2B** triad leads to a stronger mixing of states. On the contrary, no conclusion concerning the exciton coupling can be drawn from the less delocalised electron density in **Py_2SQB**. The limitation of the orbital contributions in **Py_2SQB** on the energetically wider separated chromophores could just be due to a more localised excitonic state. Such a behaviour would be expected for great energy differences between the interacting chromophores.[5, 26]

[1] The DFT calculations were carried out by *Dr. Marco Holzapfel*.

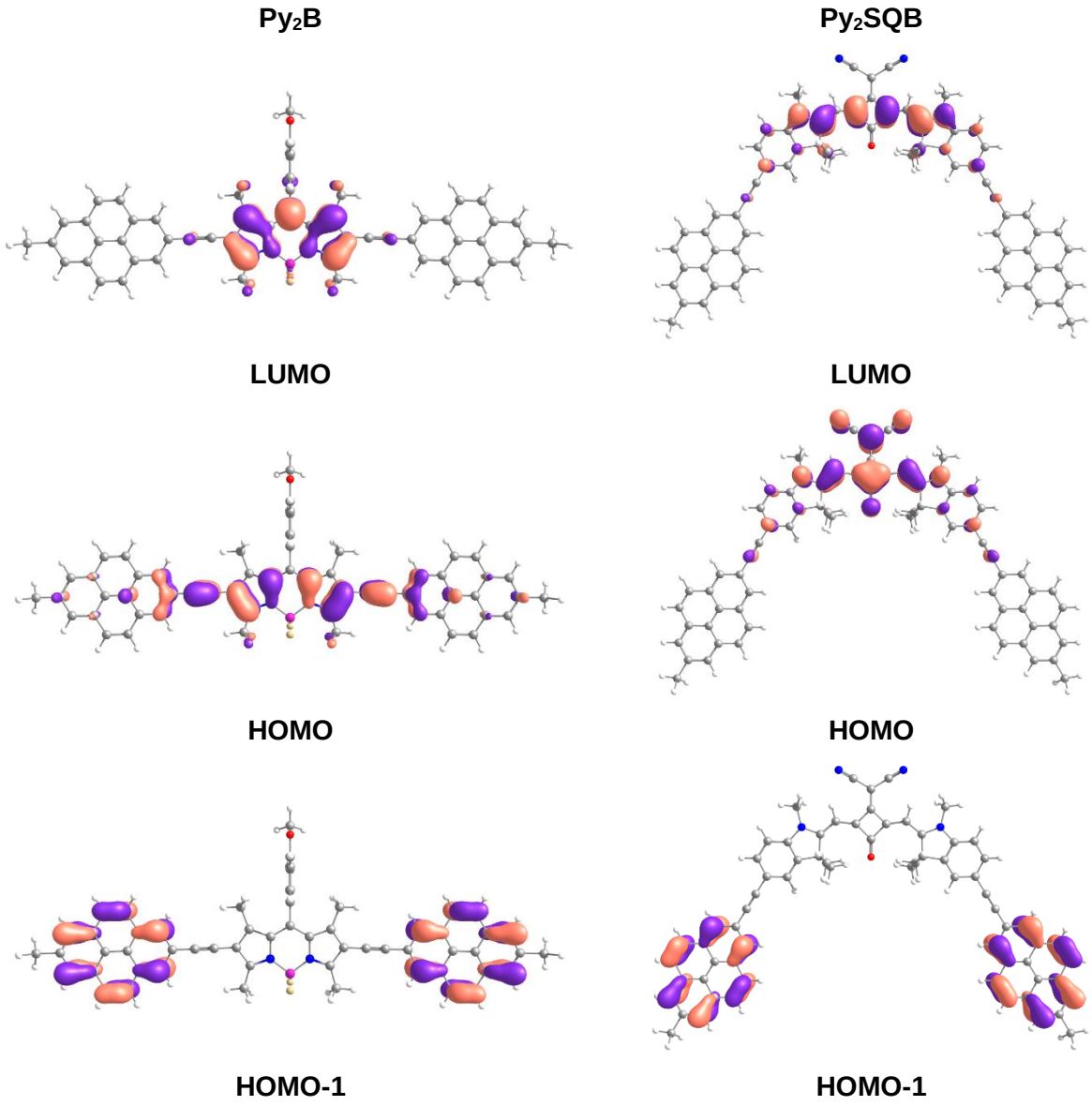

Figure 40 Orbitals of **Py₂SQB** and **Py₂B** from TD-DFT computations at B3LYP/6-31G* level of theory.

Fluorescence Spectroscopy

For a summary of the photophysical properties of the triads and their parent compounds see Table 5.

The fluorescence spectra of all symmetrical dye conjugates were measured at two different excitation wavenumbers to see if energy transfer takes place.

Excitation at the low energy band of **Py_2B** at 18900 cm^{-1} (530 nm) results in strong bodipy-like fluorescence at 16300 cm^{-1} (613 nm), that is solvent independent (see Figure 43a) and shows a *Stokes* shift of 900 cm^{-1} (see Figure 42a). In CH_2Cl_2 the band is red shifted about 1300 cm^{-1} in comparison to the monomer **BODIPY-3** (see Figure 41a). Furthermore the band width of the fluorescence (fwhm: 1370 cm^{-1}) is narrowed in relation to the absorption spectra (fwhm: 1790 cm^{-1}), which is different to what is observed for **BODIPY-3** (see Figure 42a). This behaviour can be explained with a more flexible ground state geometry, causing a flatter hypersurface than the excited state. Geometrical changes are possible due to rotation around the triple bond, which is less pronounced in the excited state where all chromophores are co-planar.[177]

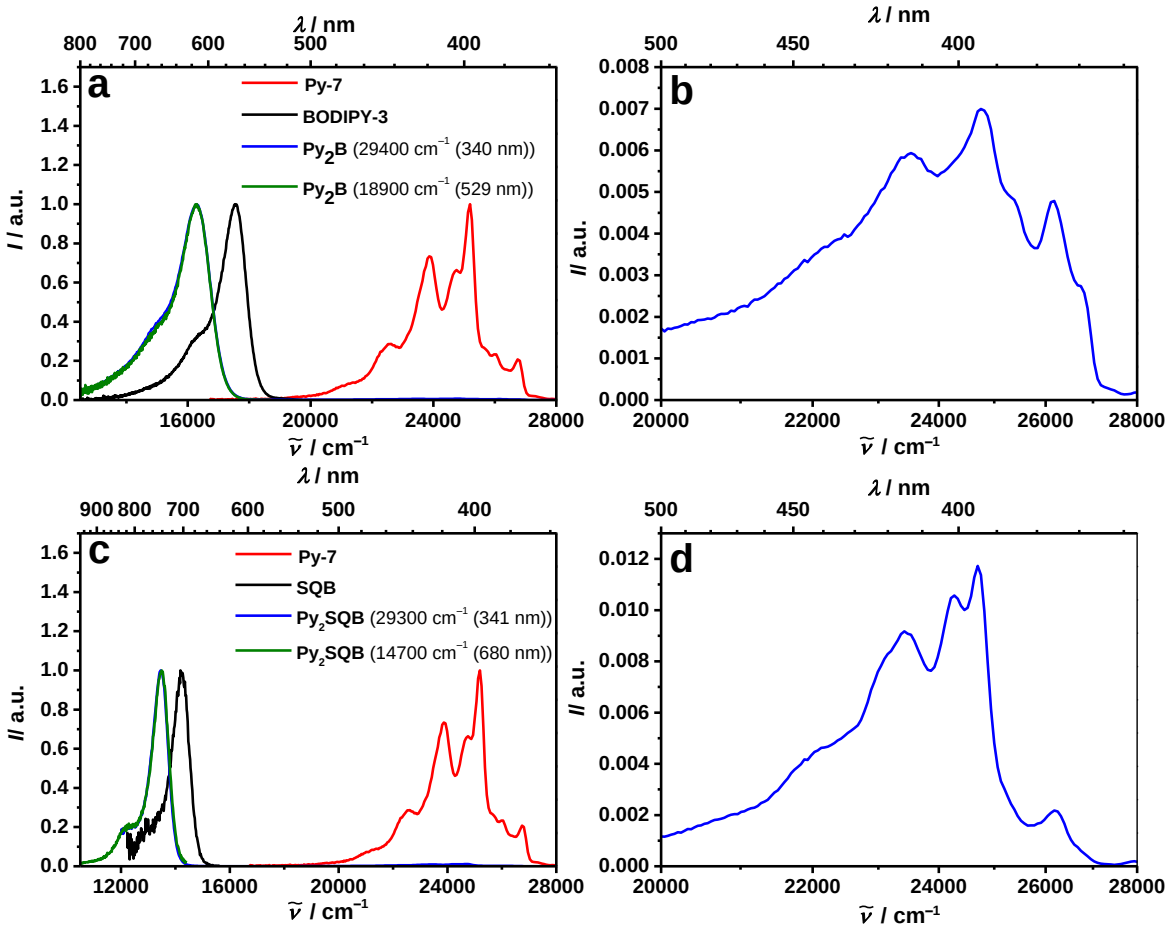

Figure 41 Fluorescence spectra of **Py_2B** (**a**) and **Py_2SQB** (**c**) in comparison to their monomers in CH_2Cl_2 at rt. (**b**) and (**d**) show a magnification of the high energy fluorescence after excitation at 29400 cm^{-1} (340 nm) for **Py_2B** and 29300 cm^{-1} (341 nm) for **Py_2SQB**.

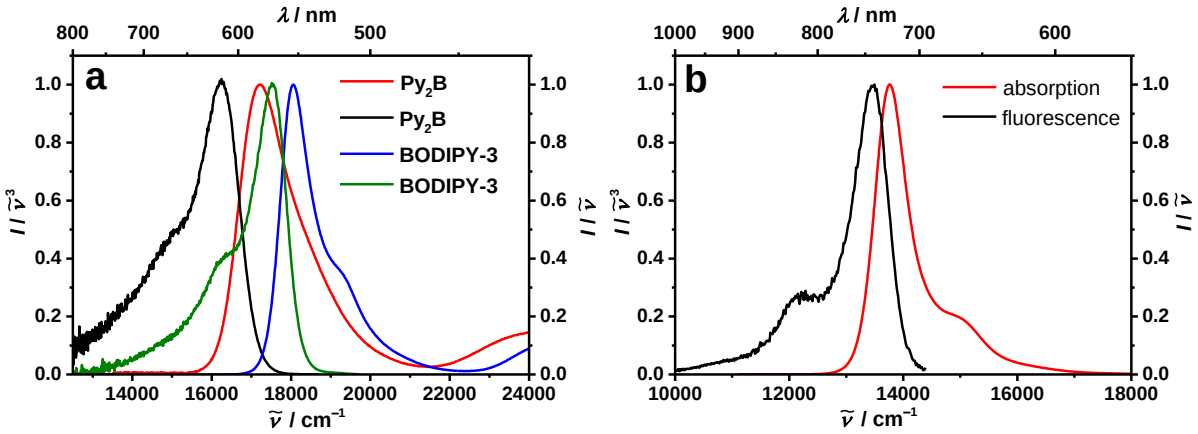

Figure 42 Absorption spectra $(I/\tilde{\nu})$ (red) and reduced fluorescence $(I/\tilde{\nu}^3)$ (black) of **Py_2B** excited at 18900 cm^{-1} (529 nm) in comparison to **BODIPY-3** absorption (blue) and fluorescence (green) excited at 20000 cm^{-1} (500 nm) (**a**) and of **Py_2SQB** (**b**) excited at 14700 cm^{-1} (680 nm) (red) in CH_2Cl_2 at rt.

In the case of **Py_2SQB** similar features can be observed when excited at low wavenumbers. In CH_2Cl_2 the main fluorescence band at 13500 cm^{-1} (741 nm) is subjected to a small red shift of 800 cm^{-1} compared to the parent squaraine (see Figure 41c). The narrow band shows a slight solvent dependence (see Figure 43b), a small *Stokes* shift of 300 cm^{-1} and reaches into the NIR up to 10000 cm^{-1} (see Figure 42b).

Again the squaraine fluorescence shows mirror image behaviour to the absorption and the fwhm are almost the same with 710–720 cm^{-1} (see Figure 42b).

In both triads additional to the main fluorescence band a second, less intense fluorescence becomes apparent when the conjugates are excited at high energies (see Figure 41). A comparison to the fluorescence from the pyrene compounds **Py-7** and **Py-9** supports the assumption that this fluorescence originates from a pyrene-like state. In both cases, the main fluorescence bands originate from the energetic low lying state having mostly bodipy or squaraine character and is identical to the main fluorescence band recorded after excitation at low energies (see Figure 41). Compared to the spectra recorded after excitation at the low energetic absorption band no shift or broadening is observed. As the two fluorescence bands are spaced far apart on the wavenumber scale, two different detectors are necessary to record the whole spectrum of **Py_2SQB**. The main fluorescence band of **Py_2B** and **Py_2SQB** are of similar structure, being narrow with a shoulder on the red edge of the spectrum and independent of excitation wavelength. (see Figure 41a and Figure 41c). The minor band assigned to fluorescence from a state similar to pyrene shows a solvent dependent intensity relative to the main emission band of the triad, which is highest in intensity in toluene for **Py_2B** and in cyclohexane for **Py_2SQB**. (see Figure 43a and Figure 43b).

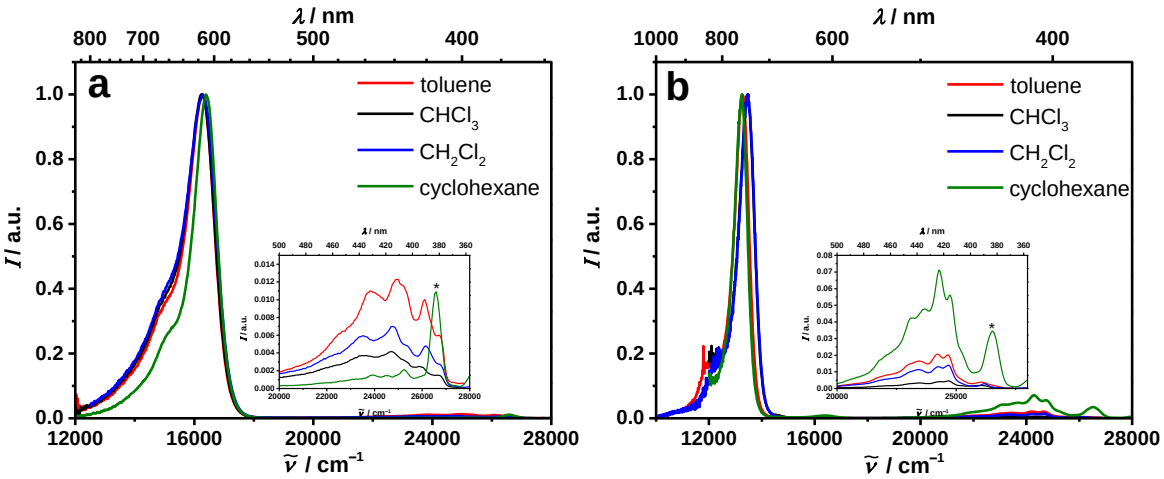

Figure 43 Fluorescence spectra of **Py₂B** (**a**) and **Py₂SQB** (**b**) in different solvents at rt after excitation at around 29000 cm^{-1}. The inset depicts a magnification of the pyrene fluorescence wavenumber region. The signals at 26600 cm^{-1} in cyclohexane (*) are representing raman bands. In order to record the whole spectral range of the emission of **Py₂SQB** two different detectors were used. The resulting spectra were combined into one, which are shown in (**b**).

All these spectral features suggest that after excitation at the absorption wavelength of pyrene most of the energy is transferred to the energetically lowest state but still a competing deactivation by fluorescence occurs. The solvent dependency of the band ratio of high to low energy fluorescence could be a hint that the energy transfer/internal conversion (IC) is least efficient in toluene for **Py₂B** and in cyclohexane for **Py₂SQB**. The energy transfer/IC to the lower state is always by far the favoured process in both triads, but the more intense fluorescence from the high energy state could be due to a diversity of structures depending on the specific solvent. A different structure could lead to a change in oscillator distribution or an increase of the energy gap between the two states. Both processes could lead to a decrease of energy transfer/IC and an enhanced fluorescence of the state higher in energy. The quantum yields were measured for excitation at high or low energy, giving similar results (see Table 5). For **Py₂B** quantum yields of 0.72–0.82 are resulting in CH_2Cl_2. Further on **Py₂B** shows no enhancement of the quantum yield compared to the monomer **BODIPY-3** (0.84) and shows similar behaviour in cyclohexane and toluene. In the case of **Py₂SQB** the quantum yield in CH_2Cl_2 distinctly increases with 0.67 in comparison with the monomeric squaraine (0.48). The quantum yields of **Py₂SQB** in cyclohexane and toluene are somewhat higher but overall show the same trend.

The excitation spectra of **Py₂B** result in two different band structures for pyrene depending on the monitored emission wavelength (see Figure 44a). If the excitation spectrum is measured at low emission wavenumbers a good match with the absorption spectrum up till

29000 cm^{-1} (345 nm) is resulting. Small discrepancies in the blue area of the spectrum should be due to an improper correction of the detector. If the emission at high energies is monitored, the resulting spectra do not fit with the absorption spectrum at all, but a band that resembles more the undisturbed pyrene absorption spectrum is occuring. This can be explained by the additional bands in the absorption spectra stemming from a state that has its origin in the interaction of pyrene and bodipy. The fluorescence in the high energy area can hence be ascribed to a more localised pyrene state where no interaction with the low energy chromophore is occuring. The coupled state does not lead to pyrene-like fluorescence but to fluorescence from a more bodipy-centered state.

For **Py_2SQB** the excitation spectrum of the high energy fluorescence matches with the absorption spectrum (see Figure 44b). Additional peaks, that can only be resolved in the excitation spectra measured at the pyrene fluorescence could be due to additional rotational bands.

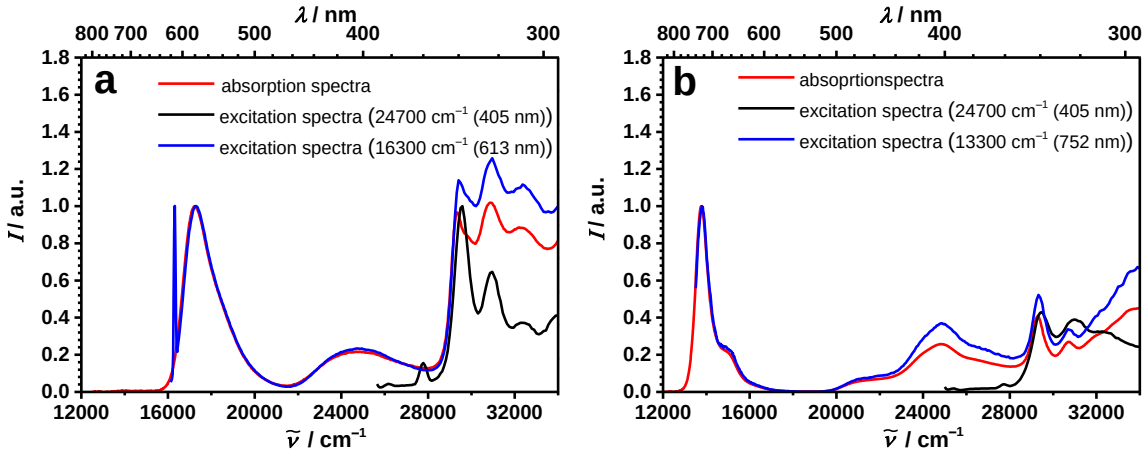

Figure 44 Excitation spectra of **Py_2B** (**a**) and **Py_2SQB** (**b**) at different monitored emission wavenumbers in comparison to their absorption spectra in CH_2Cl_2 at rt. Monitored emission wavenumbers are given in brackets.

Steady-State Fluorescence Anisotropy Measurements

To study the relative orientation of the transition moments of **Py_2B** excitation anisotropy in poly-THF was recorded. The high viscosity of the solvent should inhibit rotation of the molecules during the fluorescence lifetime. The measurement of the fluorescence anisotropy puts the relative orientation of excitation and fluorescence transition-dipole moments into relation according to:

$$r = \frac{2}{5}\left(\frac{3\cos^2\theta - 1}{2}\right) \tag{44}$$

Where θ denotes the angle between the polarisation excitation and the emitted light. Hereby an anisotropy of $r = 0.4$ is resulting from a parallel alignment, and $r = -0.2$ from a perpendicular orientation.[178]

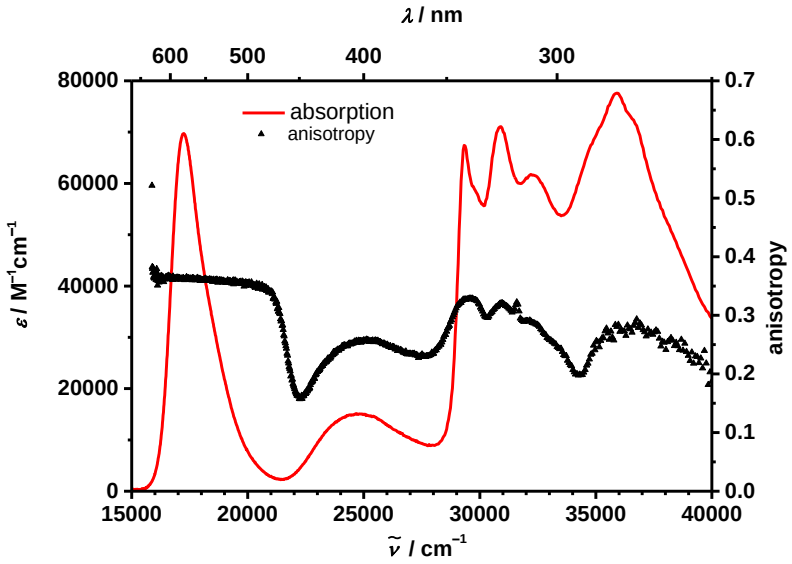

Figure 45 Excitation anisotropy spectrum in poly-THF (black triangles) at an emission wavelength of 15800 cm^{-1} (633 nm) and absorption of **Py_2B** (red) in CH_2Cl_2 at rt.

In the spectra a high anisotropy is visible at 16000–21000 cm^{-1} (476–625 nm) in the whole absorption region of the S_1 state of the bodipy chromophore. The value of $r = 0.36$ is close to the expected 0.4 of parallel alligned transition moments. The deviation can be explained by residual rotation in the solution. The orientation of the transition moment of the first excited state of bodipy is known to be polarised along the long axis of the molecule,[174] so that from this conclusions of the orientations of the other transition moments in the triad can be deduced. The broad band between 21500–27900 cm^{-1} (358 –465 nm) covers several transitions of which at least one has to be oriented perpendicular to the transiton moment of the $S_1 \leftarrow S_0$ transition to explain the low anisotropy values. Between 28000–32000 cm^{-1} (313 –357 nm) an increase up to 0.33 is observable. As the $S_2 \leftarrow S_0$ transition of pyrene is situated in this region and should be polarised parallel to the bodipy $S_1 \leftarrow S_0$ transition this fits

with the observed data. The additional transition originating from an interacting state of pyrene and bodipy (32000–33000 cm^{-1} (313 –303 nm)) has to be oriented in the same plane as the pyrene transition as a perpendicular orientation would cause an anisotropy of r = –0.2 and a distinct decrease of r would be expected.

Time-Dependent Fluorescence Measurements

The fluorescence lifetimes of the triads were measured by TCSPC (see Table 6). When the triad is excited at the main absorption band **Py_2SQB** shows lifetimes of 2.43 ns in CH_2Cl_2, which is longer than the one of the monomer squaraine **SQB** with 1.76 ns. For **Py_2B** a lifetime of 3.03 ns in CH_2Cl_2 is resulting after excitation at low wavenumbers, which is distinctly shorter than the lifetime of the monomer **BODIPY-3** which shows a decay of 4.93 ns in CH_2Cl_2. When the lifetime is measured after excitation at the high energy band, the results are somewhat different. When the fluorescence lifetime is recorded at the low energy band of **Py_2B** or **Py_2SQB** similar lifetimes are obtained for the excitation of the lower lying states (2.48 ns and 3.09 ns, respectively). On the other hand, when the fluorescence lifetime is recorded at 25000 cm^{-1} (400 nm) both triads show biexponential decays, with one long lifetime comparable to the pyrene monomer fluorescence of 34.8 ns and a fast one in the single-digit nanosecond range (see Table 6). **Py_2SQB** decays with 2.62 ns and 33.2 ns, with the longer lifetime contributing about 91 % to the total decay. The same trend is true in **Py_2B** where the longer lifetime (23.0 ns) contributes 87 % to the total decay. Similar results are obtained from lifetime measurements in toluene. If the lifetime of a pyrene state involved in energy transfer is mentioned in literature, it is in the picosecond range but no biexponential decay has ever been mentioned.[66, 96] To study the origin of the different lifetimes of the residual emission, fluorescence decay spectra at various wavenumbers using TCSPC were recorded. For **Py_2SQB** and **Py_2B** the measurement was done in toluene, but the signal to noise ratio of **Py_2B** was too poor to get an appropriate fit. Only for **Py_2SQB,** where the residual fluorescence shows the higher intensity, the emission could be globally fitted leading to three decay associated spectra. When the fit is compared with the steady-state fluorescence spectrum (see Figure 46), it leads to the assumption that the fastest time maybe an artefact as it shows maximum intensity where there is no pyrene fluorescence. The two longer lifetimes do not differ a lot but a close look reveals that the longer time is leaning more towards higher wavenumbers and is less broad. A geometrical rearrangement in the excited state was already discussed for the high energy fluorescence and could also explain the two lifetimes in this case. With this assumption in mind, a possible explanation for the time resolved data would be a different degree of coupling between the subunits for different geometries. A stronger coupled state leads to a faster energy transfer/IC and

accounts for the short lifetime, while fluorescence from a less coupled state shows a lifetime of 22.9 ns, more similar to the pyrene chromophore.

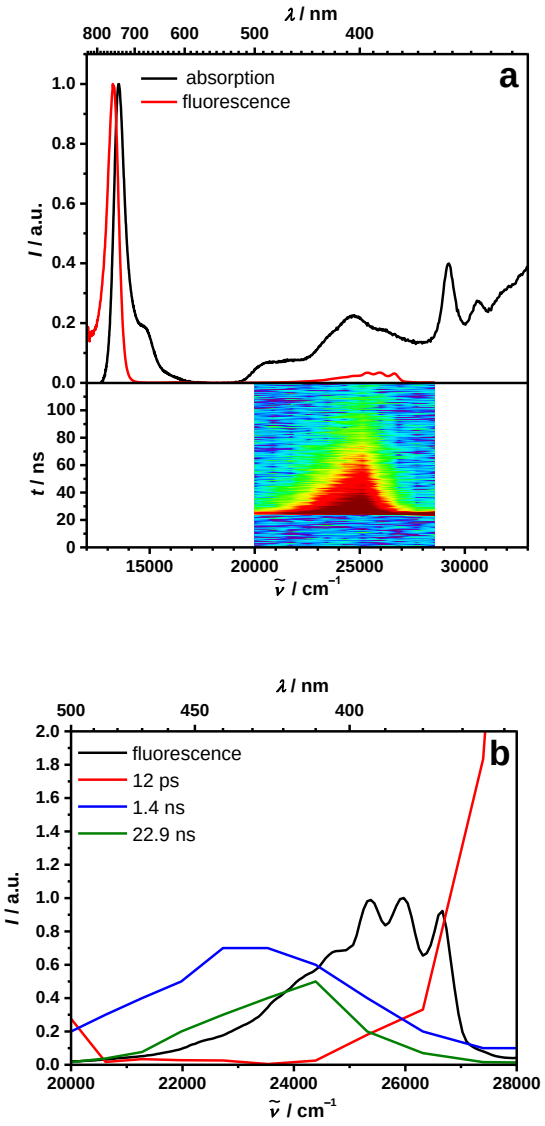

Figure 46 Absorption spectrum and fluorescence spectrum of **Py_2SQB** measured after excitation at 29200 cm^{-1} (342 nm) in toluene at rt. The fluorescence emission maps reflect the intensity and decay dynamics for excitation at 29200 cm^{-1} (342 nm) (**a**). The decay associated spectra (parallel model) resulting from a global fit are depicted together with the fluorescence spectrum (**b**). The maximum of the fit is shifted in relation to the stationary fluorescence spectrum to the low energy side. This is due to the spectral difference between the time-resolved map and the stationary fluorescence spectrum, which could be due to a correction issue.

With the average lifetimes the transition moment of the fluorescence μ_{fls} can be calculated by using the *Strickler-Berg*-equation:[179]

$$k_{\mathrm{fl}} = \frac{16 \cdot 10^6 \pi^3}{3h\varepsilon_0} \frac{n\left(n^2+2\right)^2}{9} \langle \tilde{\nu}_{\mathrm{fl}}^{-3} \rangle_{av}^{-1} \mu_{\mathrm{fl}}^2 \qquad (45)$$

Where $\langle \tilde{\nu}_{\mathrm{fl}}^{-3} \rangle_{av}^{-1} = \int I_{\mathrm{fl}} d\tilde{\nu} / \int I_{\mathrm{fl}} \tilde{\nu}^{-3} d\tilde{\nu}$ is the average cubic fluorescence energy, $k_{\mathrm{fl}} = \phi_{\mathrm{fl}} / \tau_{\mathrm{fl}}$ is the radiative rate constant and n the refractive index of the solvent.

For both triads the fluorescence transition-dipole moment of the lowest energetic bands were calculated, (see Table 5) which gave values greater than the sum of the transition-dipole of the respective monomers. Furthermore, when one compares the fluorescence transition moments to the ones calculated from the absorption spectra, an enhancement can be observed in case of the triads. For the monomers no change of the transition moments is noticed, which is expected as such small molecules should not show great structural reorganisation. The triads however show an increase of the transition-dipole moments of 35 % for **Py₂B** and 63 % for **Py₂SQB** from absorption to fluorescence. One possible interpretation for this is a more planar structure in the excited state, which allows a greater coupling and hence an increase of the transition moments of the fluorescence. This explanation is validated by the smaller fwhm of the fluorescence band of the bodipy-like state compared to the fwhm of the absoprtion band of **Py₂B**, but the same cannot be said for **Py₂SQB**, where the fwhm of absorption and fluorescence bands are of similar values.

Transient Absorption Spectroscopy (TA)[1]

The steady-state photophysical properties of the two triads give first hints of intramolecular interactions between the chromophores. To further study these processes, fs-time resolved TA measurements were performed. Both triads were measured in CH_2Cl_2 at rt and excited at high wavenumber (**Py_2B**: 30800 cm^{-1} (325 nm); **Py_2SQB**: 29850 cm^{-1} (335 nm)). The excitation energy was choosen slightly above the 0-0 transition of the S_2 state of pyrene to be able to observe the dynamics of the pyrene S_2 state at the 0-0 transition without interference of scattered pump light. Due to the additional band in the absorption spectra of **Py_2B** ascribed to a state resulting from interaction of the constituents, the pyrene subunit cannot be excited exclusively. Analogous experiments with reference compounds or excitation at low wavenumber of the triads (**Py_2B**: 17200 cm^{-1} (581 nm); **Py_2SQB**: 22200 cm^{-1} (450 nm))were performed. For the excitation at high energies, two different probe areas were recorded for **Py_2SQB**, one at the low energy side from 25000 cm^{-1} to 12500 cm^{-1} (400–800 nm) and a second at higher energies from 30800 cm^{-1} to 14800 cm^{-1} (325–676 nm). The spectral ranges were combined before the fitting was done. The same procedure was applied for the measurement of the parent compound **SQB**. **Py_2B** was probed between 15000 cm^{-1} (667 nm) and 30000 cm^{-1} (333 nm). The TA absorption spectra along with evolution associated difference spectra (EADS), decay associated difference spectra (DADS) and time scans at certain wavelengths are depicted in Figure 47 for **Py_2SQB** and in Figure 49 for **Py_2B**. The EADS and DADS are resulting from a global analysis of the transient map and give the minimal amount of independent spectral components.

[1]The femtosecond spectroscopy measurements were performed by *Alexander Schmiedel* and the analysis was carried out by *Dr. Marco Holzapfel*.

Table 6 Time-resolved optical data of pyrene triads and their parent compounds in toluene and CH_2Cl_2 at rt.

	τ/ns (TCSPC)[a] Excit. at high wavenumber		τ/ns (TCSPC)[a] Excit. at low wavenumber		τ/ps (TA)[b] [pump wavenumber]	τ/ps (TA)[b] [pump wavenumber]	τ/ps (FLUC)[c]
	CH_2Cl_2	toluene	CH_2Cl_2	toluene	CH_2Cl_2	CH_2Cl_2	toluene
Py-7	34.8	17.1					
Py-9	41.5	51.4					
SQB			1.76	3.45	0.86 14 1800 [30800]		
BODIPY-3			4.93	4.50			
Py_2SQB	2.62 (0.09), 33.2 (0.91) [25000] 2.48 [13330 (750)]	2.80 (0.22), 24.6 (0.78) [25000] 3.04 [13330 (750)]	2.43	3.04	0.64 7.5 2400 [29850]	0.67 10.6 2719 [22200]	7.54 (−0.27) 2546 (1) [29200/13300]
Py_2B	2.32 (0.13), 23.0 (0.87) [25000] 3.05 [16290]	2.98 (0.25), 35.9 (0.75) [25000] 3.09 [16290]	3.03	3.08	0.12 1.6 22 460 3100 [30800]	0.772 13.6 627 2967 26730 [17200]	0.431 (1) 175 (0.08) [29300/23500] 14.3 (−0.26) 1096 (1) [29300/15400]

[a] Fluorescence spectra measured by TCSPC, for pyrene excitation at 31650 cm^{-1} (316 nm), for bodipy at 23920 cm^{-1} (418 nm), for squaraine at 15240 cm^{-1} (656 nm), monitored wavelength for triads **Py_2SQB** and **Py_2B** are given in square brackets [cm^{-1}]. Lifetime measurements of pyrene in some cases lead to two lifetimes. The ratio of these is given in brackets. [b] Globally fitted lifetimes of SADS measured by TA [pump wavenumber in cm^{-1} (nm)] in CH_2Cl_2.[c] Decay lifetimes measured by FLUC in toluene at rt (amplitude)[excitation/probe wavenumber].

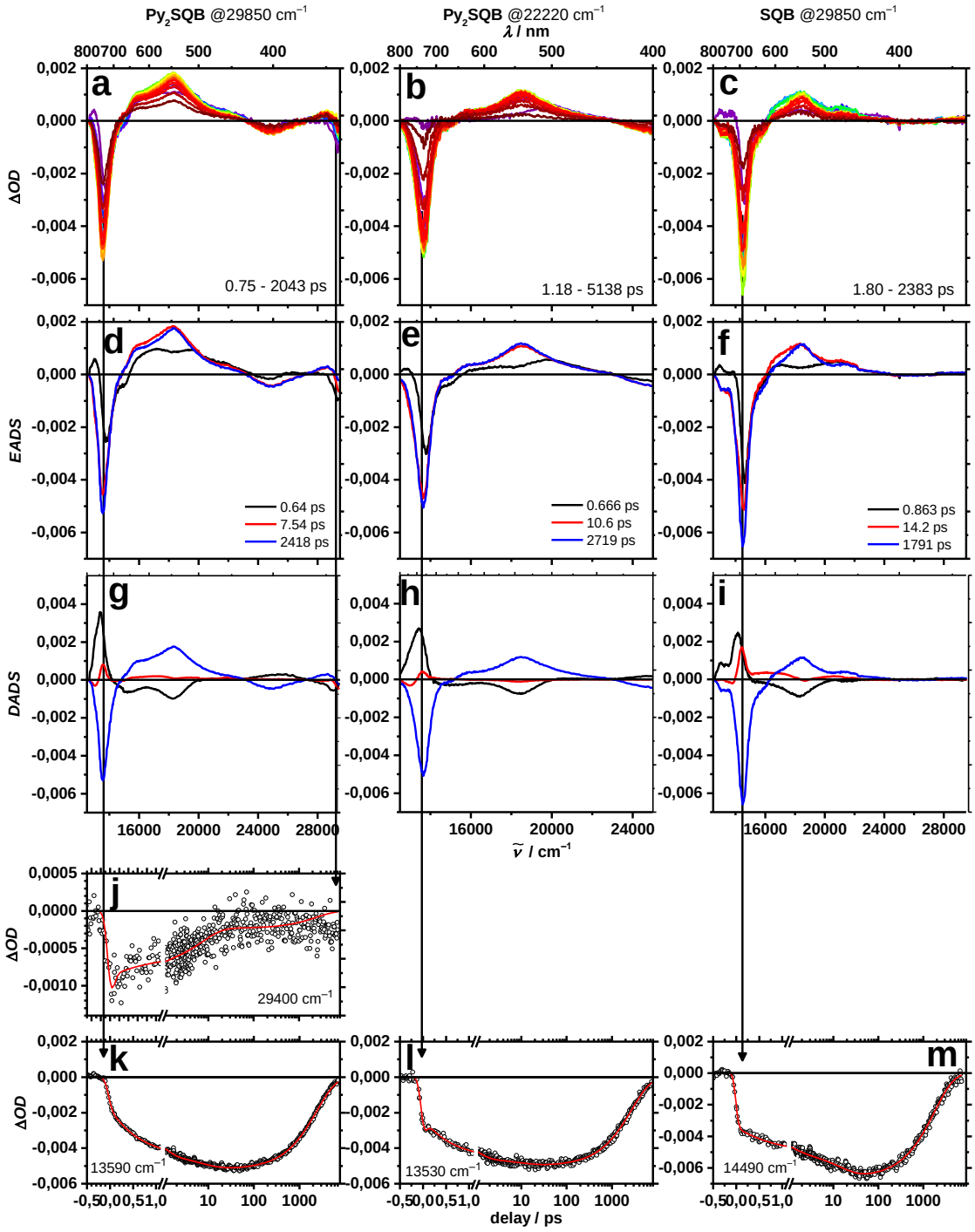

Figure 47 Transient absorption spectra of **Py_2SQB** (**a**) excitation at 29850 cm^{-1} (335 nm) and (**b**) excitation at 22220 cm^{-1} (450 nm) and **SQB** (**c**) excitation at 29850 cm^{-1} (335 nm) in CH_2Cl_2 at rt. Early spectra are given in blue, later spectra in red. Evolution associated (**c**–**f**) and decay associated spectra (**g**–**i**) resulting from the TA spectra and time scans at selected wavenumbers (**j**–**m**). Transient absorption spectra and time scans were corrected for chirp and scattered light.

Py$_2$SQB was excited at 29850 cm^{-1} (335 nm) and within the instrument response (ca. 100 fs) a TA spectra evolves. It consists of two ground state bleaches (GSB), a more prominent at 13500 cm^{-1} (741 nm) and two smaller ones at 29300 cm^{-1} (341 nm) and 24800 cm^{-1} (403 nm). These negative signals are accompanied by excited state absorption (ESA) between 15000 cm^{-1} (667 nm) to 23400 cm^{-1} (427 nm) and 25000 cm^{-1} (400 nm) to 29000 cm^{-1} (345 nm). Global analysis gives three DADS and EADS. The EADS at 0.64 ps shows two GSB signals which can be accounted to the squaraine S_1 and the 0-0 transition of the pyrene S_2 state by comparison with the negative absorption spectra (see Figure 48a). The prescence of both signals in the TA spectra at early times and the vanishing extinction coefficient of the squaraine parent compound at 29850 cm^{-1} (335 nm) proves that the **Py$_2$SQB** molecule as whole was excited and transition density is spread over the chromophores. No stimulated emission (SE) from the S_2 state of pyrene was observed. This can be explained by the ultrafast internal conversion (IC) to the pyrene S_1 state. The latter state has a forbidden transition to the S_0 state and hence no oscillator strength. Therefore it does not show a SE signal. To interpret the occurance of the EADS with a time constant of τ = 7.54 ps it is helpful to look at the DADS. Here a wave-like behaviour at 13500 cm^{-1} (741 nm) of the spectrum at τ = 7.54 ps indicates spectral shifts, which can be assigned to relaxation processes. The last spectral component at 2.4 ns fits well with the lifetime of the TCSPC measurements and describes ground state recovery.

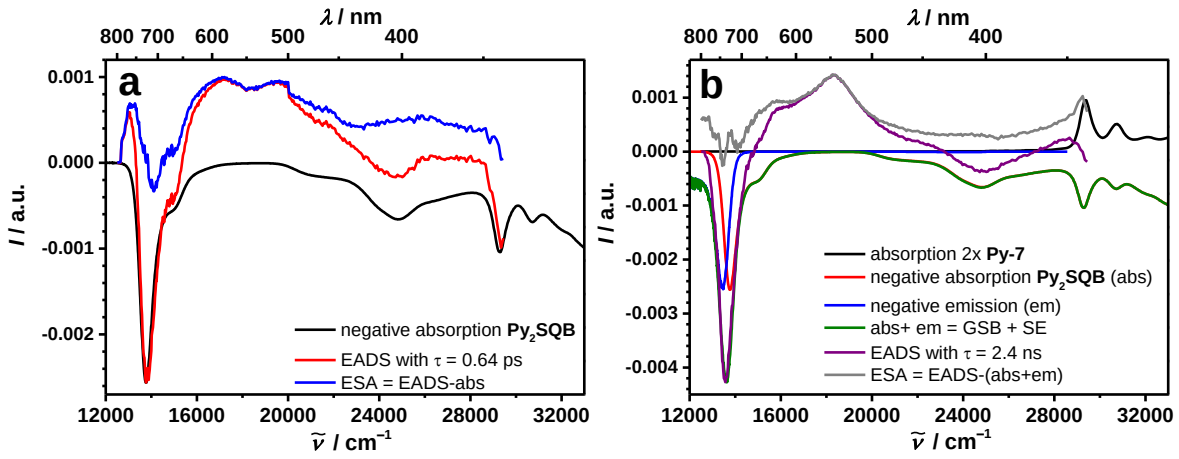

Figure 48 Reconstruction of ESA spectra from EADS at (**a**) 0.64 ps and (**b**) 2.4 ns using steady state absorption and emission spectra.

To discern different possible spectral contributions the GSB and SE were modelled by using the steady state spectra. Therefore the sum of the fluorescence spectrum (divided by $\tilde{\upsilon}^2$)[180] and the steady state absorption spectrum were plotted, which are given in Figure 48b and subtracted this from the EADS at τ = 2.4 ns. By doing so, we can see from the comparison of the EADS and the simulated GSB and SE that these two contributions are in fact causing the

negative signal at 13500 cm^{-1}. Thus, it can be concluded that the S_1 state of the squaraine is now populated as otherwise no SE could be observed. The simulated ESA shows a slightly enhanced positve peak at around 29300 cm^{-1} (341 nm) which matches with the pyrene absorption. This is due to the substraction of the absoprtion spectra and shows that the population of pyrene in the excitd state was overexagerated by this procedure. Hence not both pyrene molecules are excited at longer times and transition density is not spread over all three chromophores. On the contrary at early times (see Figure 48a) there is no positive contribution in the pyrene absorption area. Thus, the simulation of the ESA by using the absorption spectra was correct and both pyrene are excited at short delay times. Hence it can be deduced from this analysis that at early times excitation energy is delocalised, incooperating both pyrene molecules. At larger delay times the system gets more localised and the excitation is only delocalised over one pyrene molecule, which can be explained by symmetry breaking. The origin of this behaviour is not known but can possibly be attributed to solvent interactions.

A second measurement with **Py_2SQB** was performed, where the triad was excited at 22220 cm^{-1} (450 nm) (see Figure 47b, e, h). This leads to excitation of the S_2 state of squaraine, which is situated well below the pyrene localised states. Again a time constant of 0.67 ps was found by the global fitting, which should result from the IC from the squaraine S_2 state to the S_1 state. From these results it can be concluded that the dynamic processes leading to energy transfer from the pyrene localised states to squaraine must happen on a faster time scale and these processes are beyond the time resolution of our set up. To reinforce this conclusion, analogous TA experiments were performed with **SQB**. These measurements leads to similar spectra and dynamics (see Figurec, f, i) of the squaraine after excitation at 29850 cm^{-1} (335 nm). Again three spectral components resulted from the global fit. The EADS with the shortest lifetime (τ = 0.86 ps) shows a dominant GSB at 14500 cm^{-1} (690 nm), but the SE at lower energies is missing. Hence it can be concluded that the excited S_1 state of squaraine is not populated yet and IC is quite slow. The vibrational relaxation is happening on the picosecond timescale which can be observed by wave-like behaviour of the DADS spectrum with a time constant of 14.2 ps. The longest time constant of 1.79 ns can be accounted for ground state recovery, matching nicely with the TCSPC measurements. From these experiments it can be concluded that in **Py_2SQB** the IC is also the reason for the slow population of the lowest energy state.

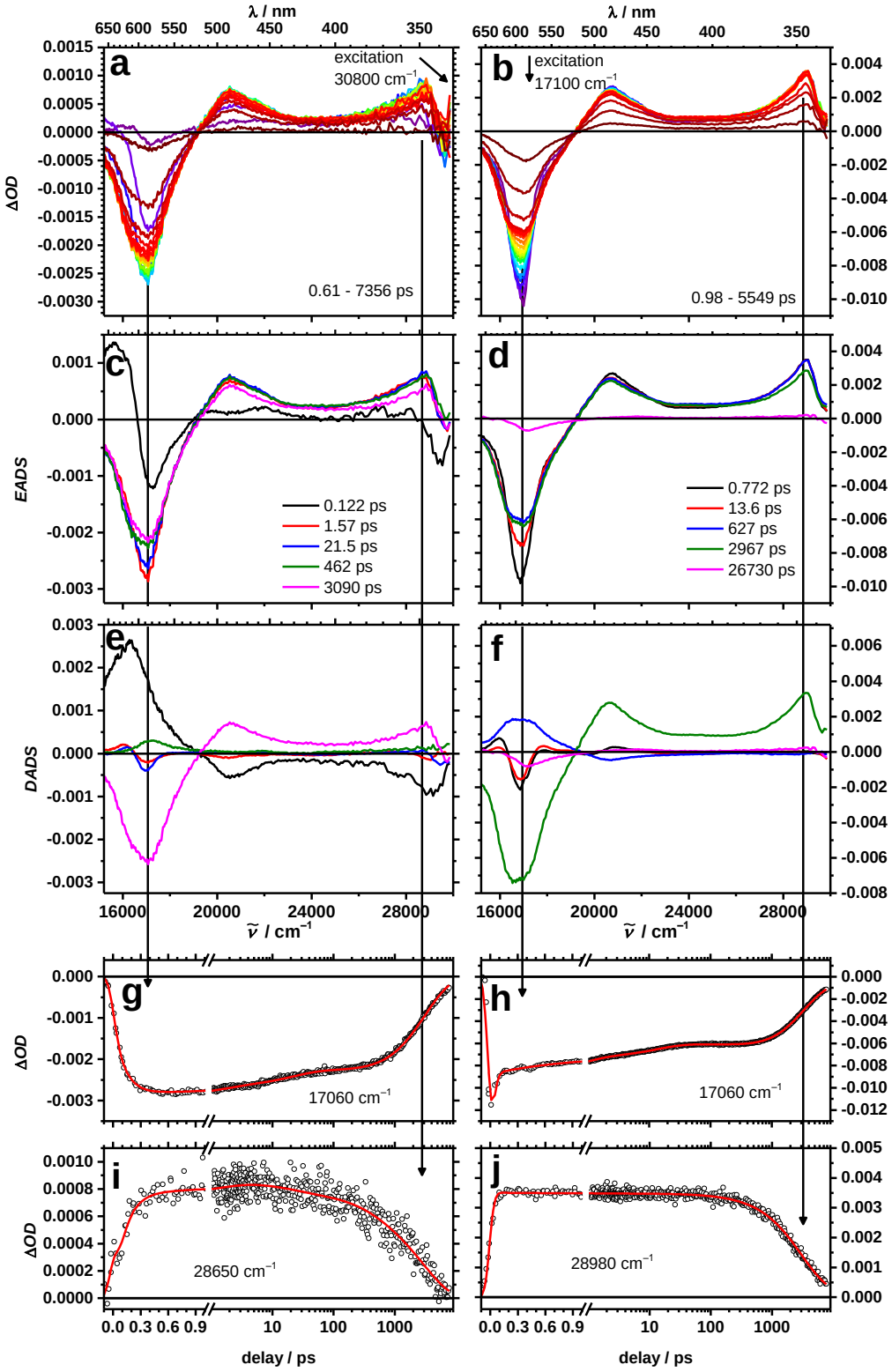

Figure 49 Transient absorption spectra of **Py_2B** in CH_2Cl_2 at rt (**a**) excitation at 30800 cm^{-1} (325 nm) (**b**) excitation at (17200 cm^{-1} (581 nm)). Early spectra are given in blue, later spectra in red. Evolution associated spectra (**c** and **d**) and decay associated spectra (**e** and **f**) resulting from the TA spectra and time scans at selected wavenumbers (**g–j**). Transient absorption spectra and time scans were corrected for chirp and scattered light.

For **Py_2B** excitation at 30800 cm^{-1} (325 nm) leads to a GSB at 17000 cm^{-1} (588 nm) which overlapps with the SE (see Figure 49a). Additional to this negative peak, two postive ESA signals with maxima at 20500 cm^{-1} (488 nm) and 28700 cm^{-1} (348 nm) are part of the spectra, whereof the latter one can be assigned to the absorption of the S_1 state of the bodipy chromophore.[181] From a gloabl fit five DADS and EADS are resulting of which two spectra with time constants of 1.57 ps and 21.5 ps can be assigned to structural reorganisation as they show the typical wave-like signature in the DADS. A further time constant of 462 ps results from the fit that cannot be accounted to any specific process but shows similar spectral features than the spectra with the longest time constant (3.1 ns). The latter one is in excellent agreement with the lifetime measurement from the TCSPC and hence is representing ground state recovery. The first EADS with τ = 0.12 ps shows both the GSB associated with the bodipy absorption and the pyrene 0-0 transition at the S_2 state of the respective wavelength. The instant occurance of the GSB of bodipy and the presence of the GSB of pyrene at all time delays proves that the triad is excited as a whole with transition density delocalised over the molecule. To investigate if the excitation energy is spread over the whole molecule, the emission and absorption spectra are used to simulate the ESA (see Figure 50a and b). The first EADS with τ = 0.12 ps matches well with the stationary absorption spectra. For the last EADS with τ = 3.1 ps the stationary emission has to be included for a good agreement at low energies. Furthermore, at higher energies (29300 cm^{-1} (341 nm)) an ESA signal is found, which matches very well with the pyrene steady-state absorption. From this it can be concluded that the excitation energy is at first delocalised over the complete molecule, incorporating both pyrene chromophores, but over time the excitation gets more localised. Additional TA measurements of **Py_2B** with excitation at the low energetic state (17200 cm^{-1} (581 nm)) lead to similar EADS and time constants, expect for the shortest one which is missing (see Figure 49b and d). Again the GSB at 29300 cm^{-1} (341 nm) is present through the whole detected time range, stating that the bodipy and pyrene chromophores are coupled and cannot be excited separately. Analogous TA measurements with **BODIPY-3** could not successfully be performed as the compound proved to be instable under the experimental conditions. Still from the collected data the time constant of 0.12 ps can be assigned to an IC process or several IC prossess from the S_2 of pyrene state to the lowest exciton state.

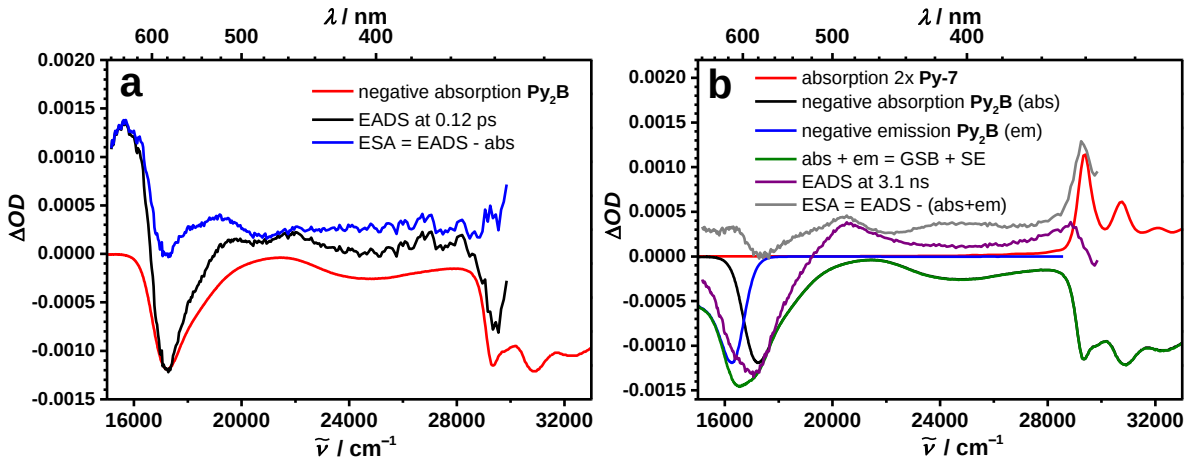

Figure 50 Reconstruction of ESA spectra from EADS at (**a**) 0.12 ps and (**b**) 3.1 ns using steady state absorption and emission spectra.

Fluorescence Upconversion Measurements (FLUC)[1]

Additional to the TA measurements FLUC was used to study the dynamics in the triads further.

Both triads were excited at 29300 cm^{-1} (341 nm) and fluorescence at the low energy state was upconverted. Due to the low quantum yield and therefore bad signal to noise ratio in the case of **Py_2SQB** no signal could be recorded at the pyrene emission wavelength. It was possible to gather a signal for **Py_2B** at the pyrene emission wavelength, but due to the low intensity the decay times resulting from the fit are less accurate and should only be taken as estimations.

Upconversion of the high energy fluorescence at 23500 cm^{-1} (426 nm) in **Py_2B** yields one lifetime on the fs-timescale and was fitted including a constant offset (see Figure 51b). The offset accounts for the long lifetime of the fluorescence band in the wavenumber range around 23500 cm^{-1} (426 nm) that resulted from TSCPC measurements (τ_1 = 2.98 ns, τ_2 = 35.9 ns). If the bodipy fluorescence at 15400 cm^{-1} (649 nm) is up-converted (see Figure 51a) a rise time of 14.3 ps is resulting, which can originate from shifts of the fluorescence due to vibrational relaxation (VR). No short time constant that fits the results from the TA spectra and can hence be ascribed to IC/energy transfer process happening in **Py_2B** is found in the upconversion measurement. A possible explanation could be the tendency of toluene to broaden the instrument response function due to its strong group velocity and hence the time resolution drops. This means that 14 ps is not the real rise time, but no shorter time could be resolved under the measured circumstances.

[1]The femtosecond spectroscopy measurements were performed by *Alexander Schmiedel* and the analysis was carried out by *Dr. Marco Holzapfel*.

The longer time constant of τ = 1096 ps describes the decay of the signal, but is way shorter than the values that resulted from TSCPC measurements (τ = 3.09 ns). It is not obvious if the too short decay times from the FLUC measurements of **Py_2B** result from a systematic error or are due to other reasons.

For **Py_2SQB** a decay time of 2.46 ns results when the emission signal at 13300 cm^{-1} (752 nm) was upconverted (see Figure 52). This fits well with the ground state recovery from the TA measurements. The short time constant of 7.54 ps should again be due to fast relaxation processes. The large IRF (1.36 ps) of this measurements, which is due to the large energy difference between the excitation wavelength and the measured emission wavelength, makes the observation of any fast processes in the molecule impossible.

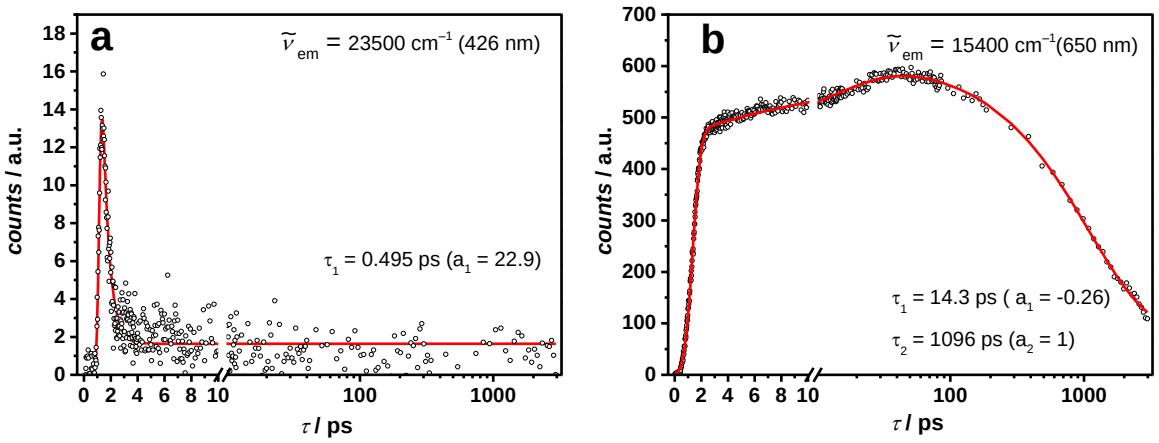

Figure 51 Fluorescence decay from fluorescence upconversion measurements of **Py_2B** in toluene at rt after excitation at 29300 cm^{-1} (341 nm). (**a**) IRF: 313 fs, (**b**) IRF: 328 fs. The amplitudes that resulted from the fit are given in brackets.

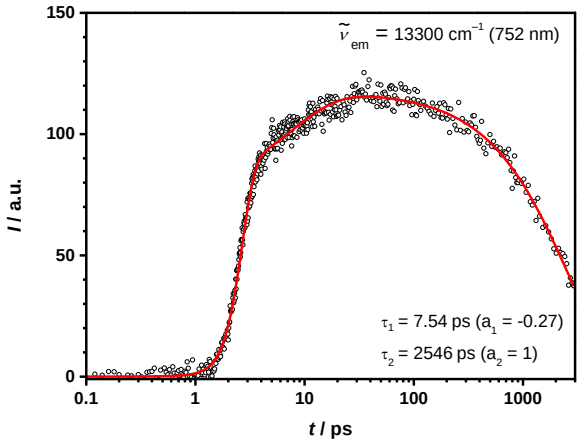

Figure 52 Fluorescence decay from fluorescence upconversion measurement of **Py_2SQB** in toluene at rt after excitation at 29200 cm^{-1} (342 nm) (IRF: 1.36 ps). The amplitudes that resulted from the fit are given in brackets.

Conclusion

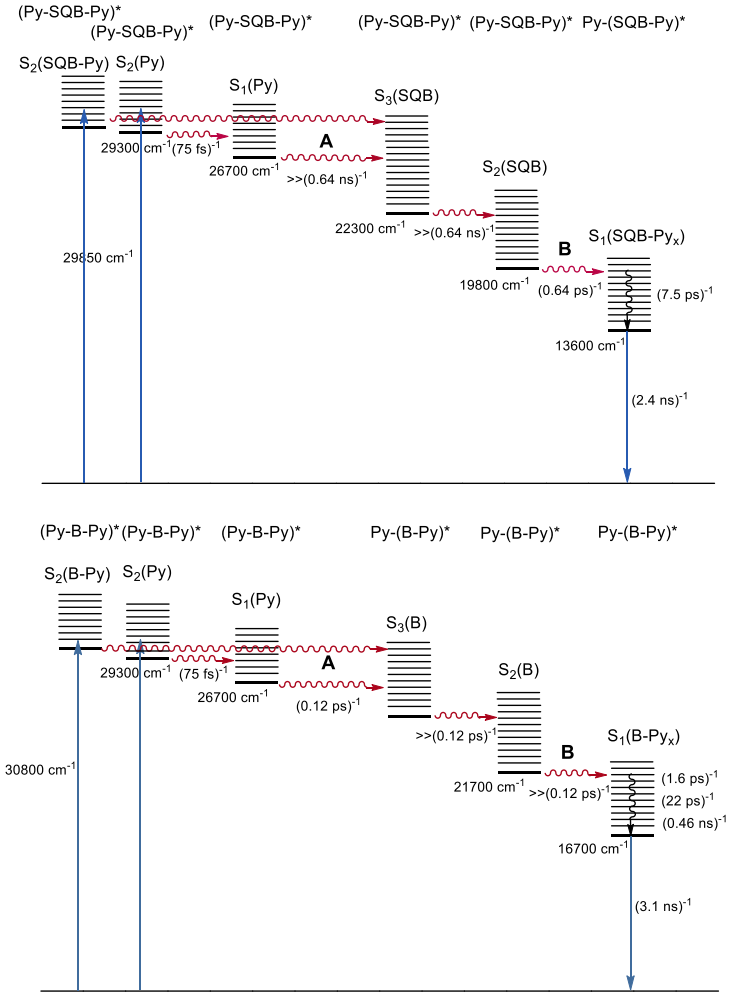

Figure 53 State diagrams for the photophysical processes in **Py₂SQB** (top) and **Py₂B** (bottom). The assignment is made for the local chromophore states, as abbreviated in parentheses. These are labeled according to the spectroscopic character of the state as it was observed in the steady-state measurements. The labels in the top row refer to the degree of localisation of the excitation energy, which was deduced from the TA spectra. (Py-SQB-Py)* or (Py-B-Py)* describes the complete delocalisation of the excitation energy, while Py-(SQB-Py)* or Py-(B-Py)* refers to a more localised excitation. The 0-0 state energies of the diverse states were estimated as follows: for S_2(Py) from the most intense absorption peak. For S_1(Py) from the highest energy peak of the fluorescence spectrum. For S_3(SQB), S_2(SQB) and S_2(Bodipy) from the intersection of a tangent to the lowest energy flank of the corresponding absorption spectrum with the x -axis. For S_1(SQB) and S_1(Bodipy) from the intersection of absorption and emission spectra. The energy of the partially delocalised S_2(S-Py) and S_2(Bodipy-Py) states are estimated from the additional bands present in the steady-state absorption spectra of the triads. The labels of the states are used for further discussion, but should not indicate whether these states are more localised or delocalised.

The state diagrams for the triads **Py₂SQB** and **Py₂B**, which can be deduced from the collected data are summarised in Figure 53. It has to be mentioned that the observed states are labeled and therefore imply specific electronic characters of the excited states. These labels are helpful for the further discussion but one has to keep in mind that it is by no means the purpose to appoint whether these states are more localised on the specific chromophore in the lable or more delocalised over other parts of the triad. In both triads excitation into the pyrene S_2(Py) state is followed by fast relaxation leaving us with population in the S_1(Py) state. From here IC/energy transfer to the S_3(SQB) or S_2(SQB) state of **Py₂SQB** or the S_3(Bodipy) state of **Py₂B** is characterised by different rates. For the photophysical processes in **Py₂B** this step is rate determining with 0.12 ps, while it is considerable faster in **Py₂SQB**. Due to the uncertainty of localised and delocalised states it is not obvious if this step can be described as an energy transfer between pyrene and the low energy chromophore or if it is characterised by an internal conversion within a superchromophore. It might be, that both processes occur parallel to each other. Comparison of the TA spectra of **SQB** with that of **Py₂SQB** reveal the IC from the S_2 state of the squaraine to the S_1 state as rate limiting step in this triad. An explanation for the low rate of this conversion can be found when looking at the state energies. This shows that the greater energy gap in the squaraine (6000 cm^{-1}) than in **BODIPY-3** (5000 cm^{-1}) leads to slower IC, following the energy gap rule.[182]

In the following, possible mechanisms are discussed to elucidate which is the best description of the dynamics in the triads. To start with the concept of energy transfer according to *Förster* is used, which was deduced from *Fermis* Golden Rule in chapter 2.2.2:

$$k_{\mathrm{EnT}}^{\mathrm{dd}} = \frac{9000(\ln 10)\kappa^2 Q_{\mathrm{D}} J_{\mathrm{C}}}{128\pi^5 n^4 N_{\mathrm{AV}} R^6 \tau_{\mathrm{D}}} \qquad (16)$$

Where τ_{D} and Q_{D} are the lifetime and the quantum yield of the donor in abscence of the acceptor, N_{AV} is the Avogadro constant, n the refractive index of the solvent, R the distance between the chromophores, κ describes the relative orientation of the transition-dipole moments of the chromophores and J_{C} is the overlap integral between the normalised fluorescence spectrum of the donor and the absorption spectrum of the acceptor.

The distance R used for the calculation originates from DFT computations (see appendix) (10.98 × 10^{-8} cm (**Py₂B**) and 15.1 × 10^{-8} cm (**Py₂SQB**)). The refraction index of CH_2Cl_2 is n = 1.4242 and for **Py-7** Q_{D} = 0.10 and τ_{D} = 34.8 ns are used. The overlap integral J_{C} was determined from the fluorescence spectrum of **Py-7** and the absorption spectrum in the S_2/S_3 region of the respective squaraine or bodipy dye in the triads to J_{C} = 3.35 × 10^{-14} dm^3 mol^{-1} cm^3 (**Py₂B**) and J_{C} = 9.19 × 10^{-14} dm^3 mol^{-1} cm^3 (**Py₂SQB**). For the calcualtion it is assumed that the transition moments are oriented face to face giving κ^2 = 1. This would be true if energy is transfered from the pyrene S_1 state to the higher excited dye

state whose transition moment is aligned perpendicular to the local C_2 axis (S_3 for **SQB**,[116] S_3 for **BODIPY-3**[174]) of the respective squaraine or bodipy dye and if all chromophores are in plane (see Figure 39). This is surely not the case for **Py₂SQB** because of the bent triad geometry, so that κ and J_C are overestimated. This leads to energy transfer rates that are too high and hence serve as an upper limit. Thereby, the evaluation yields $k_{\mathrm{EnT}}^{\mathrm{dd}}$ = (85 ps)$^{-1}$ for **Py₂B** and (210 ps)$^{-1}$ for **Py₂SQB**. The calculated energy transfer rate of **Py₂B** is more than twice the one of **Py₂SQB** while the ratio of the overlapp integrals show the opposite relation. Hence the faster rate must be due to the shorter distance in **Py₂B**. The closely spaced chromophores put the applicability of the *Förster* mechanism to question, as the description of the electron density in terms of transition-dipole moments gets incorrect at short distances. As these calculated rates are by two magnitudes too slow compared to the measured ones, we can exclude *Försters* energy transfer as the operating mechanism. Energy transfer rates that were calculated by using *Försters* dipole-dipole mechanism often result in too slow values, which is reported in literature for several conjugates incorporating pyrene and bodipy dyes.[66, 95, 106, 110] Mostly, the described experimental transfer rates happen on the low picosecond timescale, but calculation of the rates following *Försters* theory lead to considerably higher values. The authors mainly assign this discrepancy to small intramolecular distances between the chromophores or the presence of additional through-bond transfer. From calculations they estimated that the dominant mechanism for the transfer is following exchange interactions. A theory describing these was formulated by Dexter and relies on orbital overlap so that short distances between the molecules are a requirement:

$$k_{\mathrm{EnT}}^{\mathrm{ex}} = \frac{2\pi}{h} K J_{\mathrm{D}} e^{(-2r/L)} \qquad (25a)$$

A drawback of this model is that equation (25a) is not based on spectroscopically characterizable properties and hence not easy to estimate. The overlap integral J_D in this equation is implemented in normalised form so that the transfer rate does not depend on the exctinction coefficient. The constant K describes the orbital overlap between the chromophores and also depends on the symmetry of the orbitals. Due to the nodal plane of the HOMO and LUMO at the 2,7-position of pyrene K should be small. This would conclude to a rather slow *Dexter* transfer. However, the S_1 state of pyrene is formed by a CI mixing of the HOMO-1 to the LUMO and a HOMO to LUMO+1 transition.[121] Taking all the possible configurations into account, a considerable amount of electron density at the C_2 position (see Figure 39) is resulting. Furthermore, the edge to edge distance r is rather small with about 4 Å, so that K could be of considerable size and the *Dexter* mechanism could be operating as the dominant mechanism. Additionally the coupling between the chromophores could be

enhanced by the alkyne bridging unit, as it is known that this spacer ensures good electronic conduit.[96]

Assuming a more delocalised excited state, the process must be discussed in terms of IC. The rate constant of the IC can be formulated based on the energy difference between the states of the coupled chromophores.[182] Additional structural properties and various coupling terms influence the rate, but these cannot be determined for larger molecules, hence no exact calculation of the IC rate constant for the triads is possible. However, the energy gap shows the greatest influence on the transfer rate between two states. This energy gap can be determined for **Py_2SQB** (ΔE = 4400 cm^{-1}) and for **Py_2B** (ΔE > 5000 cm^{-1}), so that a faster IC for **Py_2B** can be expected but no comparison to the experimental data is possible because the rate cannot be calculated.

Looking at the TA spectra, **Py_2B** shows a GSB at 29300 cm^{-1} that fits well with the pyrene absorption region occurring on the same time sale as the GSB at the bodipy absorption. From this observation, a distinct coupling in the excited state can be assumed, but the character of the state is much like the pyrene S_2 state. The later point mentioned, strongly suggests energy transfer as the operating mechanism, while the strong interaction, visible in the TA points more towards an IC in a superchromophore. Similar considerations are valid for the low excitonic state, where the GSB still marks an electronic coupled state, but the intensity is lower than expected for a complete delocalised system. Similar observations are made for **Py_2SQB**. Taking all this into account the most likely description of the system is an intermediate coupling case, which leads to parallel excitation of the whole triad, but the spectroscopic characteristics are reminiscent of the electronic states of the constituents. This conclusion is supported by simulating the ESA by using the negative absorption spectra. The procedure works well at short times, proving excitation being delocalised over the whole triad. The same method applied to spectra at longer times leads to a positive signal in the pyrene absorption area, which states a localisation of excitation energy towards squaraine or bodipy over time. A possible explanation might be given by the orientation of the transition-dipole moment of the S_2 state of pyrene along the local C_2 axis of the triad (see Figure 39). This could lead to a minimization of the excitonic interaction with the S_3/S_2 states of bodipy or squaraine that are nearest in energy. A recent quantumdynamical study on dimers consisting of two different squaraines showed that transition density is transferred between the two excitonically coupled S_1/S_2 states but in addition also between the two squaraine chromophores.[183] These processes happen on a time scale of 100 fs after excitation. A similar situation could describe the energetic dynamics in the triads. The energy difference between the constituents leads to dynamic energy hopping followed after short time by localisation on the low energy side.

Hence, in the macroscopic ensemble, more bodipy than pyrene is excited and a weaker GSB than expected in the pyrene absorption area is the consequence. Similar calculations to investigate the dynamics in the triads are currently in progress.

5.2.2 Triads Consisting of Bodipy and *cis*-Indolenine Squaraine[1]

In order to synthesis the desired triads **$(SQB)_2B$-4** and **B_2SQB-3** either an asymmetrical bodipy or squaraine is needed. As the synthesis of the asymmetric bodipy and squaraine chromophores need more steps or lead to lower yields than the symmetrical ones, a reaction screening was done beforehand with the latter mentioned on a small scale to find the optimal coupling conditions. One would expect that in the case of the two symmetrical substituted compounds, polymerisation could be a problem, but no noteworthy amount could be detected.

Synthesis

Synthesis of **$(SQB)_2B$-4**

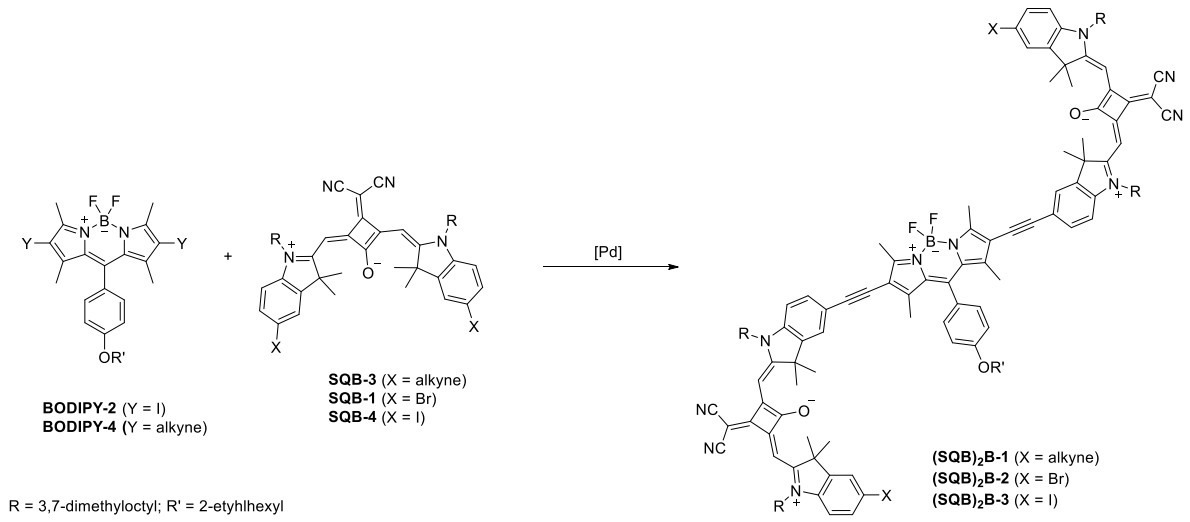

Scheme 15 *Sonogashira* test reactions for the synthesis of (**$(SQB)_2B$**.

[1]Reproduced or adapted in parts with permission from : *Exciton Coupling Enhancement in the Relaxed Excited State*, N. Auerhammer, A. Schmiedel, M. Holzapfel, C. Lambert, *J. Phys. Chem. C.,* **2018**, DOI**:** 10.1021/acs.jpcc.8b03337.

The overall tested conditions with the symmetrical chromophores are summarised in Table 7 (see Scheme 15). The coupling was tried with alkynylated, brominated and iodinated squaraines **SQB-1**, **SQB-3** and **SQB-4** and the appropriate bodipy. The iodinated squaraine **SQB-4** can be synthesised in the same manner as the transoid analogon **SQA-4** (see Scheme 16).

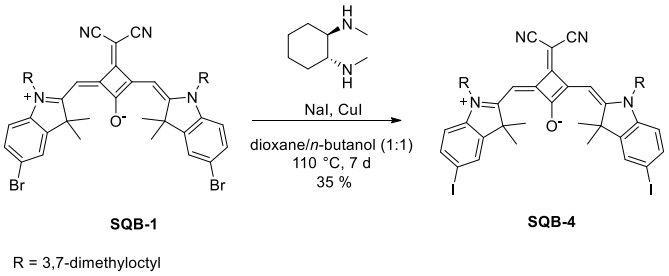

SQB-1

R = 3,7-dimethyloctyl

SQB-4

Scheme 16 Halogen exchange reaction of the symmetrical *cis*-squaraine yielding **SQB-4**.

Sonogashira Test Reactions with Symmetric Chromophores

Table 7 Screening of *Sonogashira* coupling conditions for *cis*-squaraine with bodipy (for X and Y compare Scheme 15).

	X	Y	catalyst/ligand	base	solvent	T/t	result
I[158]	alkyne	I	$Pd(dppf)Cl_2 \cdot CH_2Cl_2$	TEA	THF	50 °C/6 d	g
II[172]	alkyne	I	$Pd(PPh_3)_2Cl_2$	TEA	THF	65 °C/1 d	g
III[120, 140]	alkyne	I	$Pd(C_6H_5CN)_2Cl_2$/ P^tBu_3	DIPA	dioxane	50–65 °C/2 d	g
IV[97]	Br	alkyne	$Pd_2(dba)_3$/P(*o*-tol)	TEA	toluene	90 °C/2 h	a*
V[184]	Br	alkyne	$Pd(OAc)_2$/RuPhos	TEA	THF/H_2O	70 °C/1 h	g*
VI[185]	Br	alkyne	$Pd(C_6H_5CN)_2Cl_2$/ PPh_3	DIPA	dioxane	65 °C/4 d	e
VII[120, 140]	Br	alkyne	$Pd(C_6H_5CN)_2Cl_2$/ P^tBu_3	DIPA	DMF	75 °C/20 h	g
VIII[120, 140]	Br	alkyne	$Pd(C_6H_5CN)_2Cl_2$/ P^tBu_3	DIPA	dioxane	75 °C/6 d	d
IX[173]	Br	alkyne	$Pd(MeCN)_2Cl_2$/ XPhos	DIPA	dioxane	90 °C/7 d	d
X[172]	Br	alkyne	$Pd(PPh_3)_2Cl_2$	TEA	THF	70 °C/5 d	e
XI[120, 166]	Br	alkyne	$Pd(PPh_3)_2Cl_2/P^tBu_3$	DBU	DMF	150 °C, 10 min MW	g*
XII[165]	I	alkyne	salicylic acid, $CuCl_2$	Cs_2CO_3	DMF	130 °C/1 d	a*
XIII[158]	I	alkyne	$Pd(dppf)Cl_2 \cdot CH_2Cl_2$	TEA	THF	50 °C/1 d	a
XIV[172]	I	alkyne	$Pd(PPh_3)_2Cl_2$	TEA	THF	65 °C/1 d	a
XVI[186]	I	alkyne	$Pd(PPh_3)_2Cl_2/PPh_3$	TEA	DMF	100 °C/2 h	a
XVII[97]	I	alkyne	$Pd_2(dba)_3$/P(*o*-tol)	TEA	toluene	90 °C/1 d	a*
XVIII[167]	I	alkyne	$Pd_2(dba)_3/PPh_3$	TEA	toluene	90 °C/1 d	g
XIX[120, 140]	I	alkyne	$Pd(C_6H_5CN)_2Cl_2$/ P^tBu_3	DIPA	dioxane	rt/3 d	a
XX[120, 140]	I	alkyne	$Pd(C_6H_5CN)_2Cl_2$/ P^tBu_3	DIPA	dioxane	40 °C/4 d	a
XXI[120, 140]	I	alkyne	$Pd(C_6H_5CN)_2Cl_2$/ P^tBu_3	DIPA	dioxane	60 °C/1 d	d
XXII[120, 140]	I	alkyne	$Pd(C_6H_5CN)_2Cl_2$/ P^tBu_3	DIPA	dioxane	75 °C/1 d	d

	X	Y	catalyst/ligand	base	solvent	T/t	result
XXIII[120, 140]	I	alkyne	$Pd(C_6H_5CN)_2Cl_2$/ P^tBu_3	DIPA	dioxane	100 °C/3 d	d
XXIV	I	alkyne	$Pd(C_6H_5CN)_2Cl_2$/ P^tBu_3	DIPA	AcN	150 °C/10 min, MW	a
XXV[173]	I	alkyne	$Pd(MeCN)_2Cl_2$/ XPhos	DIPA	dioxane	90 °C/3 h	a
XXVI[152, 154]	I	alkyne	$Pd(PPh_3)_4$	TEA	THF	60° C/1 d	d, f*
XXVII[154]	I	alkyne	$Pd(PPh_3)_4$	TEA	toluene	60° C/1 d	d
XXVIII[154]	I	alkyne	$Pd(PPh_3)_4$	TEA	toluene	rt/2 d	c*
XXIX[154]	I	alkyne	$Pd(PPh_3)_4$	TEA	toluene	rt/2 d	d, e

* without CuI, a: only starting material or decomposed squaraine; b: only mono coupled product; c: mono and bi coupled product; partly debrominated; d: debrominated product; e: product; f higher coupling products; g: not identified.

Using the alkynylated squaraine **SQB-3** and the iodinated (bodipy) **BODIPY-2** three coupling conditions were tested. The first two were using either $Pd(dppf)Cl_2 \cdot CH_2Cl_2$ (see Table 7, condition I)[154] or $Pd(PPh_3)Cl_2$ (see condition II)[172] in THF. These conditions both worked in *Sonogashira* couplings with the bodipy framework before, but didn't yield any product in these reactions.

The last condition that was tested with this substitution pattern was the $Pd(C_6H_5CN)_2Cl_2$ catalyst with P^tBu_3 as ligand,[120, 140] but again no product could be isolated (see Table 7, condition III).

The *trans*-squaraine analogon was already successfully coupled with bodipy in a previous work.[97, 162] In this *Sonogashira* reaction the brominated squaraine **SQA-1** was used, therefore this coupling pattern was adapted to the reaction of the *cis*-squaraine.

In the mentioned synthesis with *trans*-squaraine copper-free conditions[97] were applied in order to minimise the homo coupled bodipy side product and prevent a decrease of the yield. Unfortunately no product could be isolated when the *cis*-squaraine was subjected to these conditions (see Table 7, condition IV).

Another copper-free procedure that was tested using $Pd(OAc)_2$ and the RuPhos-ligand[184] in a THF/water mixture only gave unidentified species, but the starting materials seemed to degenerate very fast under these conditions (see Table 7, condition V).

Next, three variations of the $Pd(C_6H_5CN)_2Cl_2$ catalysed reaction conditions – used succesfully already several times in this work – were tried (see Table 7, conditions VI–VIII). The use of PPh_3 as ligand instead of P^tBu_3 was investigated, as the steric hinderance of the phosphine

ligand can influence the *Sonogashira* reaction quite dramatically.[187] In the reaction with PPh_3 (see Table 7, condition IV) only brominated product was formed, but in the case of using the P^tBu_3 as a ligand in dioxane (see Table 7, condition VIII) the mixture was stirred longer and time is an important factor for dehalogenation.[188] This could be the reason why in this test reaction partly debrominated as well as fully brominated product was found. If the reaction was carried out in DMF no product whatsoever could be found (see Table 7, condition VII).

The next applied conditions were using the $Pd(MeCN)_2Cl_2$ catalyst at 90 °C, using the sterically demanding XPhos ligand (see Table 7, condition IX).[173] In comparison to the results from the test reaction with the $Pd(C_6H_5CN)_2Cl_2$ catalyst, these conditions seemed more promising, as there still was debromination of the product, but the overall conversion seemed to be better.

At last the $Pd(PPh_3)_2Cl_2$ catalyst was tested under two different conditions. One reaction was carried out in a microwave oven[120, 166] but didn't led to any product formation (see Table 7, condition XI), while at 70 °C in THF[172] product could be detected (see Table 7, condition X).

As the conversions of the brominated squaraine **SQB-1** were still quite slow under all tested conditions and therefore debromination as a competing reaction was a big problem, the iodinated squaraine **SQB-4** was tested as well, to see if the higher reactivity leads to faster coupling and hence less dehalogenation.

In order to find the best coupling conditions for the iodinated *cis*-squaraine **SQB-4** a broad spectrum of reaction conditions was tested. Detection of the product was always done by mass spectrometry and in some cases a more detailed screening was done for the promising reactions to optimise the conditions.

As dehalogenation in these *Sonogashira* couplings is occuring due to a combination of palladium-, copper-catalyst and base, a palladium-free reaction was tested. In this protocol a copper(II)/salicylic acid complex acts as the catalyst and caesiumcarbonate is used as base[165] (see Table 7, condition XII). However after reluxing in DMF overnight only starting material could be detected.

Further on the $Pd(dppf)Cl_2 \cdot CH_2Cl_2$ catalyst in THF was tested, which worked well in the pyrene bodipy coupling. However in this case no reaction took place and only starting material was remaining (see Table 7, conditions XIII).

Next, the coupling of **SQB-4** with **BODIPY-4** was tried to be achieved with $Pd_2(dba)_3$ with two different ligands. The P(*o*-tol) ligand led to high yields in the *trans*-squaraine bodipy coupling,[97] while PPh_3 was used in a coupling of a squaraine to a porphyrin[167]. Unfortunately only starting material could be found in both cases (see Table 7, conditions XVI and XVII).

The $Pd(PPh_3)_2Cl_2$ catalyst was tested without ligand[172] and with PPh_3 (see Table 7, conditions XIV and XV) in order to generate the $Pd(PPh_3)_4$ catalyst in situ[186]. Under none of these conditions any product was formed and only starting material was remaining.

As the $Pd(MeCN)_2Cl_2$ catalyst gave the best results with the brominated squaraine **SQB-1** it was expected that it would perform even better with the iodinated squaraine **SQB-4** under these conditions. However no reaction progress could be monitored and only starting material was present in the mixture (see Table 7, condition XXV).

Therefore the $Pd(C_6H_5CN)_2Cl_2$ catalyst that led to conversion for most of the tested couplings was used next. It showed promising results, but also deiodinated products, hence a temperature screening was done (see Table 7, conditions XIX–XXIII). The reaction was carried out at room temperature and at 40 °C, 60 °C, 75 °C, 100 °C. An additional reaction was performed in a microwave oven in acetonitrile (see Table 7, condition XXIV). Only starting material was found by reactions carried out at room temperature, 40 °C or under microwave irradiation. At 60 °C, 75 °C and 100 °C deiodination was observable in all cases but at 100 °C only deiodinated product was found. At 60 °C and 75 °C there were only small amounts of product formed and starting material prevailed extensivly.

Therefore the performance of the more active $Pd(PPh_3)_4$ catalyst was investigated (see Table 7, conditions XXVI–XXIX).

First the $Pd(PPh_3)_4$ catalyst was tested in THF without CuI as cocatalyst[152] (see Table 7, condition XXVI) and in toluene with CuI[154] (see Table 7, condition XXVII) at 60 °C. In both cases the product was formed, but in THF also higher coupling products were identified, however only in dehalogenated form. In toluene on the other hand the triad was formed exclusivly. To study the influence of the CuI on the deiodination and the formation of higher coupling products, the reaction was carried out in toluene without CuI (see Table 7, condition XXVIII). This reaction did not suffer from dehalogenation badly, but a considerable amount of mono coupled product and starting material was still present. None of the higher coupling products formed in THF were present in the reaction mixture. Lastly the reaction was carried out at room temperature in toluene with CuI (see Table 7, condition XXIX) to study the temperature dependence of the dehalogenation in this system. These conditions showed the best ratio of conversion, with slightly more product than starting material and only a medium amount of dehalogenation product, so they were choosen to be applied to the coupling of the symmetrical bodipy **BODIPY-2** with the asymmetric iodinated squaraine **SQB-6**.

*Synthesis of the asymmetric Squaraines **SQB-5** and **SQB-6***

To synthesise the desired triad the asymmetrical squaraine **SQB-6** is needed. Therefore **Ind-2** is reacted with 3,4-diethoxycyclobut-3-ene-1,2-dione to get the semisquaraine **Ind-3**. The semisquaraine is then converted with malonitrile in ethanol to yield **Ind-4**. In the final step the semisquaraine **Ind-4** is deprotected and condensated with 1-(3,7-dimethyloctyl)-2,3,3-trimethyl-3*H*-indole-1-ium iodine (**Ind-5**) to give the desired product **SQB-5** (see Scheme 17).[134]

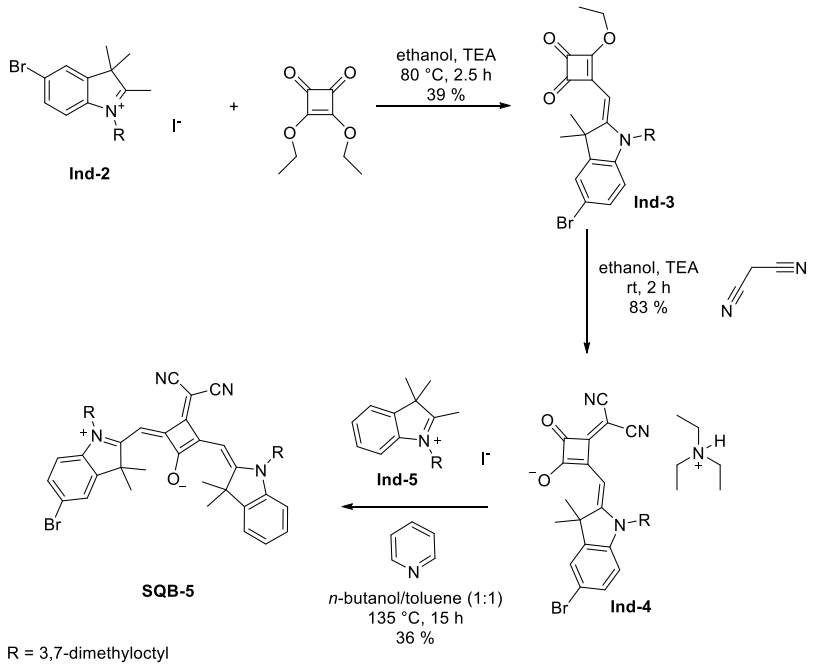

Scheme 17 Synthesis of asymmetrical substituted *cis*-squaraine **SQB-5**.

The brominated mono functionalised squaraine **SQB-5** can be converted to the iodinated analogon **SQB-6** (see Scheme 18).[170, 171]

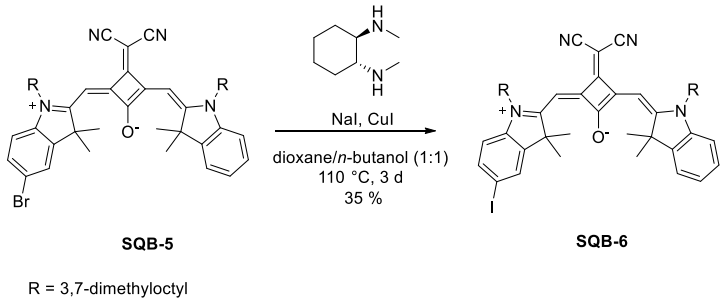

Scheme 18 Synthesis of squaraine **SQB-6**.

Sonogashira Coupling to ***(SQB)$_2$B-4***

Finally the mono iodinated squaraine **SQB-6** could be coupled with the symmetrical alkynylated **BODIPY-4** by using the $Pd(PPh_3)_4$ catalyst at room temperature (see Scheme 19). After purification by GPC in $CHCl_3$ the desired triad was received in 44 % yield.

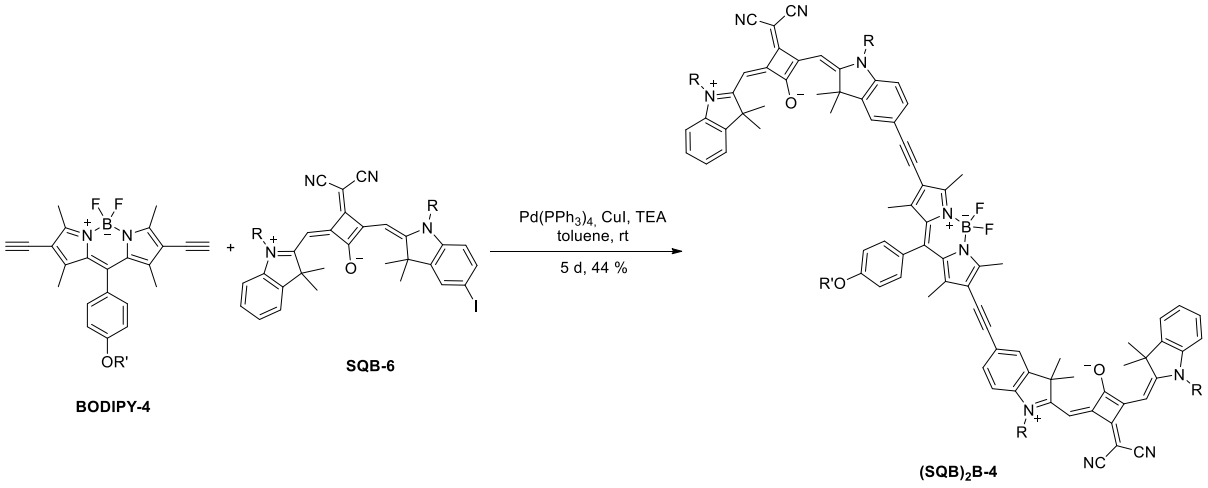

Scheme 19 Synthesis of **(SQB)$_2$B-4.**

Synthesis of **B$_2$(SQB)-3**

In order to find suitable *Sonogashira* conditions for **B$_2$(SQB)-3** additional test reactions were carried out. It was assumed that no change in reactivity should occur compared to the test reactions already discussed for the synthesis of **(SQB)$_2$B-4** as the only difference is the equivalent of the subjected constituents (Scheme 20).

Sonogashira Test Reactions with the Symmetrical Chromophores

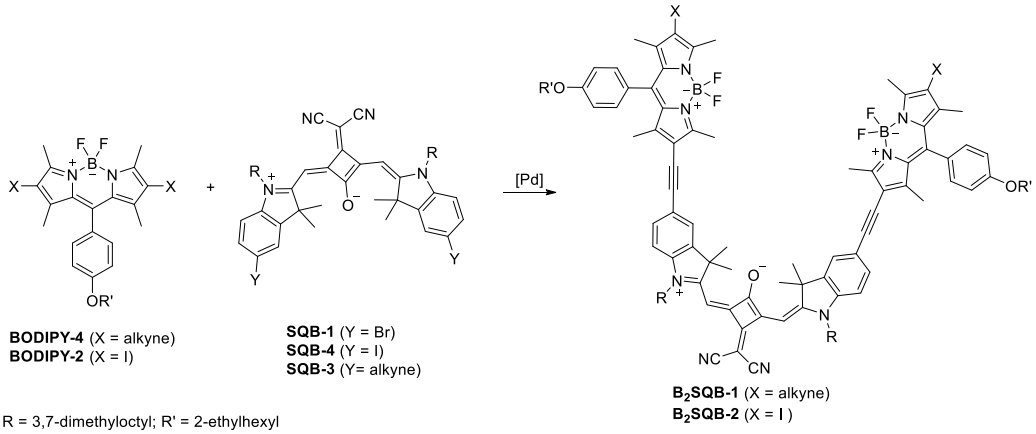

Scheme 20 Tested couplings of symmetrical bodipy and symmetrical squaraine.

Table 8 Tested *Sonogashira* conditions for the coupling of symmetrical bodipy and *cis*-squaraines to yield **B_2SQB-1** and **B_2SQB-2** (for X and Y compare Scheme 20).

	X	Y	catalyst/ligand	base	solvent	T/t	conversion
I[173]	I	alkyne	$Pd(MeCN)_2Cl_2$/ XPhos	DIPA	dioxane	100 °C/2 d	-
II[120, 140]	alkyne	Br	$Pd(C_6H_5CN)_2Cl_2/P^tBu_3$	DIPA	DMF	150 °C/15 min, MW	a
III[120, 140]	alkyne	Br	$Pd(C_6H_5CN)_2Cl_2/P^tBu_3$	DIPA	dioxane	75 °C/4 d	b, c
IV[120, 140]	alkyne	Br	$Pd(C_6H_5CN)_2Cl_2/P^tBu_3$	DIPA	DMF	75 °C/4 d	-
V[173]	alkyne	Br	$Pd(MeCN)_2Cl_2$/ XPhos	DIPA	dioxane	90 °C/2 d	b, c, d
VI[173]	alkyne	Br	$Pd(MeCN)_2Cl_2$/ XPhos	DIPA	dioxane	100 °C/3 h, MW	-
VII[120, 140]	alkyne	I	$Pd(C_6H_5CN)_2Cl_2$/ P^tBu_3	DIPA	dioxane	75 °C/24 h	-
VIII[173]	alkyne	I	$Pd(MeCN)_2Cl_2$/ XPhos	DIPA	dioxane	90 °C/4 d	-
IX[154]	alkyne	I	$Pd(PPh_3)_4$	TEA	toluene	rt/24 h	-

a: only bodipy found, b: homo coupled bodipy, c: mono coupled product, partly debrominated, d: partly debrominated product.

As a screening was done for the **$(SQB)_2$B-4** coupling, it was assumed that the same conditions should work for the **B_2SQB-3** synthesis, just the equivalents needed to be changed.

Overall reactions with DMF as a solvent (see Table 8, condition II and IV) or the alkynylated squaraine **SQB-3** (see Table 8, condition I) as coupling partner did not work at all. The $Pd(C_6H_5CN)_2Cl_2$ catalyst[120, 140] led to some mono coupled product, when the reaction is carried out in dioxane, but no triad was formed (see Table 8, condition III).

The best coupling conditions for the brominated squaraine **SQB-1** were the one with $Pd(MeCN)_2Cl_2$ as catalyst and XPhos[173] as ligand if conventional heating and no microwave irradiation is used (see Table 8, conditions V and VI). However this protocol leads to a very widespread mixture of mono coupled product, triad, debrominated mono coupled product and starting material.

Suprisingly both of these reaction conditions tried with the iodinated squaraine **SQB-4** lead to no product whatsoever (see Table 8, conditions VII and VIII). Lastly the very reactiv $Pd(PPh_3)_4$ catalyst was tried,[154] but also no compound could be identified after the reaction (see Table 8, condition IX). As the only difference between the synthesis of **$(SQB)_2$B-4** and **B_2SQB-3** is the higher amount of **BODIPY-4**, this was assumed to be the issue. In no case, if **SQB-6** was used, starting material or any side products could be identified, so degradation seemed to occur.

Synthesis of the asymmetrical Bodipy

To synthesise the **B_2SQB-3** triad, an asymmetrical bodipy as coupling partner is needed. The synthesis follows the procedure already described in literature.[97]

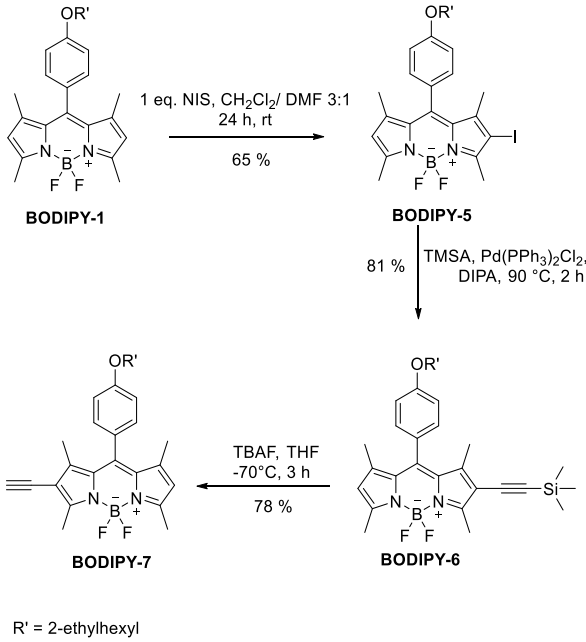

Scheme 21 Synthesis of asymmetrical bodipy.

The bodipy core **BODIPY-1** was iodinated with *N*-iodosuccinimide and subsequently was treated with TMSA using $Pd(PPh_3)_2Cl_2$ as catalyst in pure DIPA in a *Sonogashira* reaction. The deprotection of the trimethylsilyl group is carried out at low temperature in THF and yields

78 % of the product **BODIPY-7** (see Scheme 21). The low temperature is necessary, as the in situ formed acetylide anion is nucleophilic enough to lead to substitution at the boron center by exchanging the fluorine atom.[154]

*Synthesis of **B_2SQB-3***

Due to the assumption that an excess of alkynylated bodipy leads to degradation of the starting material, the **B_2SQB-3** synthesis with the asymmetric bodipy was tried by adding the alkyne gradually. In order to do that, the conditions that worked best for **SQB-6** in the couplings to **$(SQB)_2$B-4** were choosen. The reaction progress was followed *via* mass spectrometry. Only after the bodipy was consumed and the mono coupled product was formed, additional bodipy was added. With this slow addition of the alkyne using $Pd(PPh_3)_4$ as catalyst the desired triad could finally be synthesised in 27 % yield (see Scheme 22).

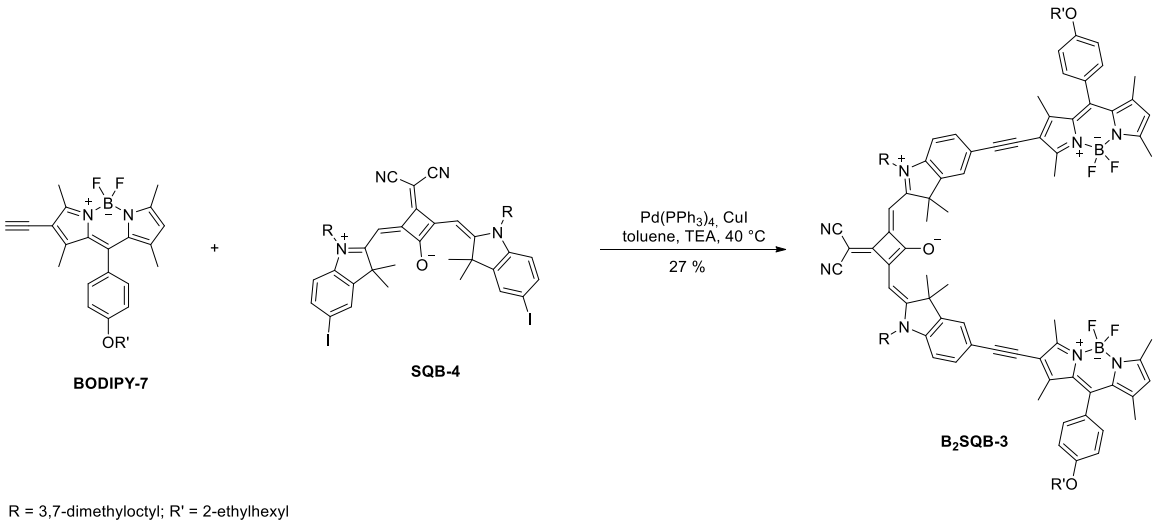

Scheme 22 Successful coupling conditions of asymmetrical bodipy **BODIPY-7** with iodinated squaraine **SQB-6**.

Absorption Spectroscopy

The symmetrical triads **B_2SQB-3** and **$(SQB)_2$B-4** were investigated in cyclohexane, toluene and CH_2Cl_2 and compared with their parent compounds. Their photophysical properties are summarised in Table 9.

The triad **B_2SQB-3** shows a small solvent dependency concerning the extinction coefficient which always shows values around 190000 $M^{-1}cm^{-1}$ at its maximum at around 13500 cm^{-1} but gets sligthly pronounced in less polar solvents. (see Figure 54a). This absorption of **B_2SQB-3** is nearly independent of the solvent polarity only the main absorption gets slighly red shifted from 13580 cm^{-1} in CH_2Cl_2 to 13270 cm^{-1} in cyclohexane. A comparison of the dye conjugate to its parent compounds shows several notable features (see Figure 54b). The absorption spectrum below wavenumbers of 22000 cm^{-1} (455 nm) is broad and structurless. The high energy band with its maximum at 18800 cm^{-1} (532 nm) in toluene is not doubled in intensity compared to the bodipy monomer but broadened. Nevertheless the integrals of the main absorption bands of **BODIPY-6** and the bodipy-like band of **B_2SQB-3** show the expected 2:1 ratio. The low energy band at 13400 cm^{-1} (746 nm) in toluene is shifted to higher wavenumbers compared to the undisturbed squaraine compound of 930 cm^{-1} but no broadening of the band is occuring.

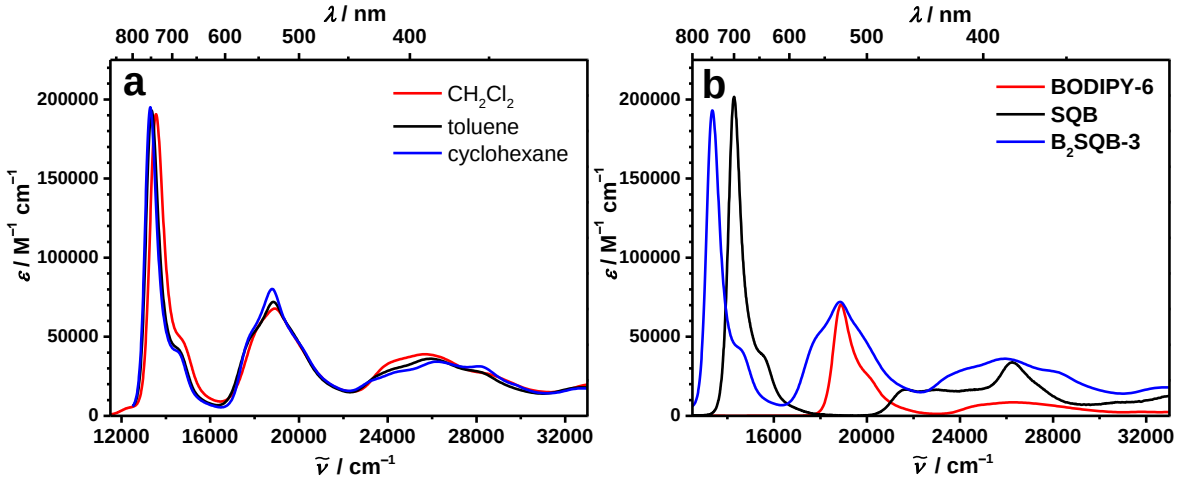

Figure 54 Absorption spectra of **B_2SQB-3** in different solvents at rt (**a**) and **B_2SQB-3** in comparison to the monomers **BODIPY-6** and **SQB** in toluene at rt (**b**).

$(SQB)_2$B-4 shows a small solvent dependency of the major absorption band from 13800 cm^{-1} (725 nm) in CH_2Cl_2 to 13600 cm^{-1} (735 nm) in toluene (see Figure 55a). Compared to the monomer **SQB** the main absorption band in the dye conjugate is shifted to the red about 680 cm^{-1} (see Figure 55b). The extinction coefficient of **$(SQB)_2$B-4** is doubled in intensity as expected. The rest of the spectrum is broad and featureless, therefore it is difficult to distinguish any maximum belonging to a bodipy-like state. This might be due to the

broadening of this band that was already described for **B₂SQB-3** and the *trans*-squaraine analogon of **(SQB)₂B-4**.[97] The broadening resulted in a decrease of the extinction coefficient.

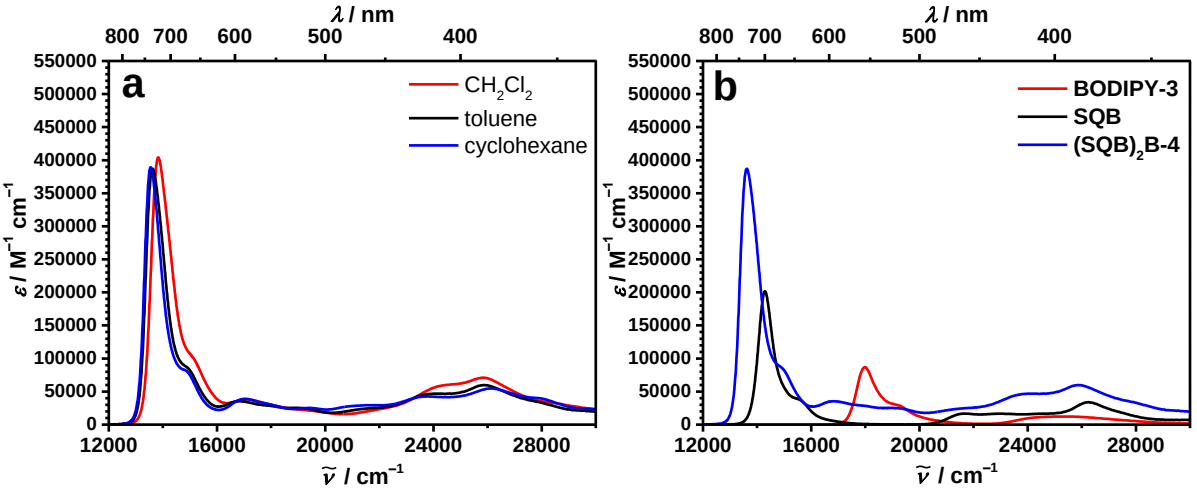

Figure 55 Absorption spectra of **(SQB)₂B-4** in different solvents at rt (**a**) and in comparison to the monomers **BODIPY-3** and **SQB** in toluene at rt (**b**).

The absorption transition-dipole moment of the energetically lowest band of **(SQB)₂B-4** is about twice the size of the main absorption band of **SQB** (210 D^2 vs 92.7 D^2) in toluene. This additive behaviour of the transition-dipole moment in addition to the broadened absorption band compared with the undisturbed monomer makes the assumption of two excitonic states being covered by this band reasonable. The interaction of n chromophores leads to n excitonic states, hence in this case three states are expected (see Figure 56). As two of the chromophores are identical, the middle excitonic state resembles mostly the undisturbed monomer, leading to energies closer to the lower excitonic state in **(SQB)₂B-4** and close to the upper excitonic state in **B₂SQB-3**. The lower and upper excitonic state are separated by δE:

$$\delta E = 2\sqrt{\Delta E^2 + 2J^2} \qquad (42)$$

With $\Delta E = (E_B - E_{SQB})/2$ and E_B and E_{SQB} being the energies of the non-interacting states of **BODIPY-3** or **BODIPY-6** and **SQB** and J is the exciton coupling energy. δE of **B₂SQB-3** can be calculated from the energy difference of the highest excitonic state and the lowest excitonic state (5500 cm^{-1}) and ΔE from the maxima of the undisturbed monomers (2300 cm^{-1}) using equation (42). This leads to an overal excitonic coupling $|J|$ = 1070 cm^{-1} for **B₂SQB-3**. This value fits nicely with the triad containing the *trans*-indolenine squaraine ($|J|$ = 1100 cm^{-1}).[97] The smaller red shift of **B₂SQB-3** in relation to **SQB** in comparison of the one of **B₂SQA** to **SQA** described in literature is due to the larger ΔE which leads to a small

decrease of the lower energetic excitonic state. (see Figure 56). For **(SQB)$_2$B-4** this coupling cannot be evaluated due to the lack of the maximum of the upper excitonic state. The prescence of different conformers possible due to relative orientations of the bodipy to the squaraine leads to different transition-dipole moments only for **(SQB)$_2$B-4**, while for **B$_2$SQB-3** rotation has no influence on the resulting transition due to the parallel alignment of the transition moment of bodipy in regard to the triple bond. A comparison of the transition-dipole moments of **SQB** (92.7 D^2), **B$_2$SQB-3** (101 D^2) and **(SQB)$_2$B-4** (210 D^2) proves the additive behaviour of the transition-dipole moments and the absence of intensity borrowing at the extent of the upper excitonic state. For **B$_2$SQB-3** integration from 16500 cm^{-1} to 22200 cm^{-1} leads to a transition moment of 83.2 D^2. This absorption area includes the middle and the high energy excitonic state and is about twice the size of the bodipy monomer. The enhancement of the oscillator strength of the lowest excitonic state was observed for **B$_2$SQA**, so it states the question why this is not observed for the *cis*-squaraine containing triads. A possible explanation would be the smaller angle between the bodipy and squaraine in **B$_2$SQB-3** compared to **B$_2$SQA**. The more linear geometry of **B$_2$SQA** leads to a larger transition moment of the lowest excitonic state.

Table 9 Absorption maxima ($\tilde{\upsilon}_{abs}$), extinction coefficients (ε), absorption transition moments (μ^2_{abs}), fluorescence maxima ($\tilde{\upsilon}_{fl}$), fluorescence transition moments (μ^2_{fls}) and fluorescence quantum yields (ϕ_{fl}) of the triads and the according reference compounds in various solvents at rt.

	solvent	$\tilde{\upsilon}_{abs}$ /cm^{-1} (nm) [fwhm]	ε /M^{-1} cm^{-1}	μ^2_{abs} /D^2	$\tilde{\upsilon}_{fl}$ /cm^{-1} (nm) [fwhm]	μ^2_{fls} /D^2	ϕ_{fl}* ($\tilde{\upsilon}_{ex}$/ cm^{-1})
SQB	CH_2Cl_2	14600 (685) [770]	207000	112	14200 (704) [800]	93.5	0.48 (15900)
	toluene	14300 (699) [680]	202000	92.7	14000 (714) [840]	92.2	0.75 (15400)
BODIPY-3	$CHCl_3$	18000 (556) [1020]	85400	46.1	17500 (571) [970]		
	toluene	18000 (556) [950]	86900	44.9	17500 (571) [932]	47.9	0.92 (18900)
BODIPY-6	$CHCl_3$	18900 (529) [1205]	70200	40.6	18200 (549) [1148]		
	toluene	18900 (529) [1085]	70600	36.5	18300 (546) [1117]	33.1	0.78 (20000)
B_2SQB-3	CH_2Cl_2	13600 (735) [778]	190000	96.1	13200 (756) [715]		
	toluene	13400 (746) [680]	193000	101	13000 (769) [640]	135	0.62 (18900) 0.67 (14700)
	cyclohexane	13300 (752) [659]	195000	104	13000 (769) [629]	141	0.54 (18900) 0.65 (14700)
(SQB)$_2$B-4	CH_2Cl_2	13800 (725) [918]	403800	237	13600 (735) [698]		
	toluene	13600 (735) [822]	387000	210	13400 (746) [620]	149	0.71 (17900) 0.77 (14700)
	cyclohexane	13500 (741) [746]	388000	207	13400 (746) [532]	147	0.82 (17900) 0.81 (14700)

*For the triads two quantum yields, depending on excitation at the high or low energy absorption band were obtained. The corresponding excitation wavenumbers are given in parenthesis.

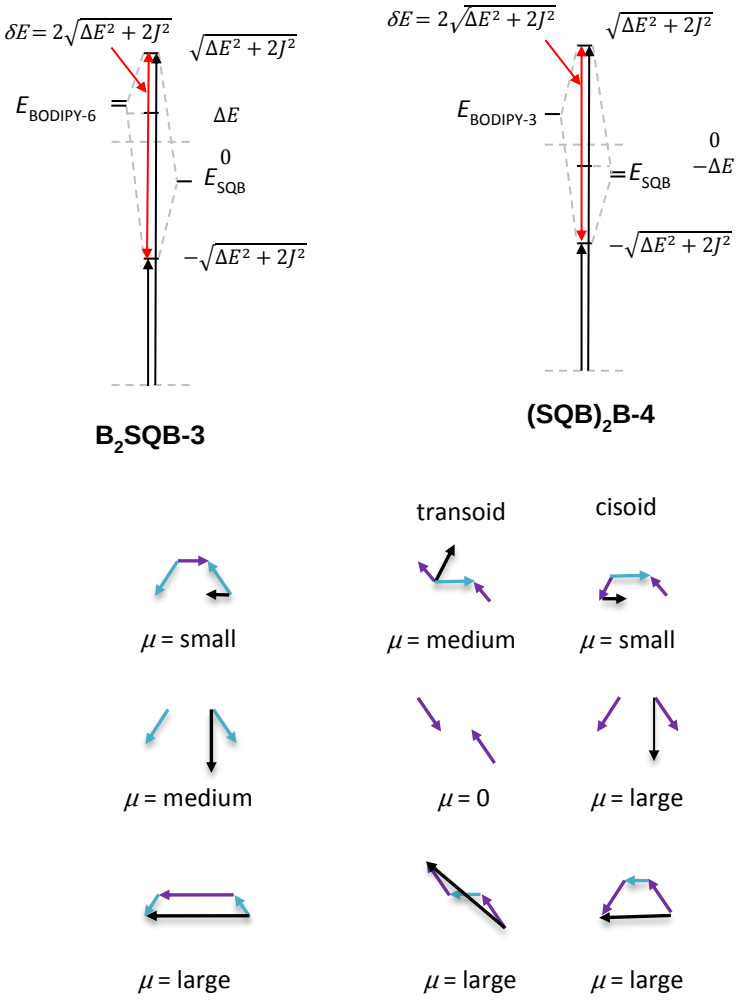

Figure 56 Energy diagram of exciton states of the two triads. The diagram neglects a possible total stabilisation of all exciton states relative to those of the parent chromophores. The transition moment vector diagrams refer to the sequence of the exciton state. The localized transition moments are given in purple for **SQB** and in blue for **BODIPY-3** and **BODIPY-6** with the orientation of the arrow indicating the phase relationship. The estimated resulting transition moment for each exciton state is given in black. The orientation and length of transition moments are estimates using the equations for the coefficients of eigenvectors as given in the SI of Ref. [97]

***DFT Calculations of the Molecular Orbitals*[1]**

In the **B_2SQB-3** triad the HOMO-1 is mostly located on the bodipy chromophore but parts of the squaraine are included as well (see Figure 57). The HOMO is concentrated on the center squaraine with a small expansion onto the ethynylene bridges, but shows no bodipy contribution. The LUMO gathers mostly all electron density at the squaraine but a very small part is located at the bodipy as well. Therefore a small electronic coupling is definitly present in the molecule, whereas one cannot talk of a complete mixture of states.

The molecular orbitals of **$(SQB)_2$B-4** are in principle similar to the ones of **B_2SQB-3** put in a different order (see Figure 57). The HOMO-1 is located at the outer squaraines only, while the HOMO includes the squaraines and the ethynylene bridge. Most spread out electron density is found for the LUMO where bodipy and squaraine are equally contributing. This hints towards a distinctly stronger mixing of states in **$(SQB)_2$B-4** than for **B_2SQB-3**, although no complete decoupled system is found for the later one.

[1]The DFT calculations were carried out by *Dr. Marco Holzapfel*.

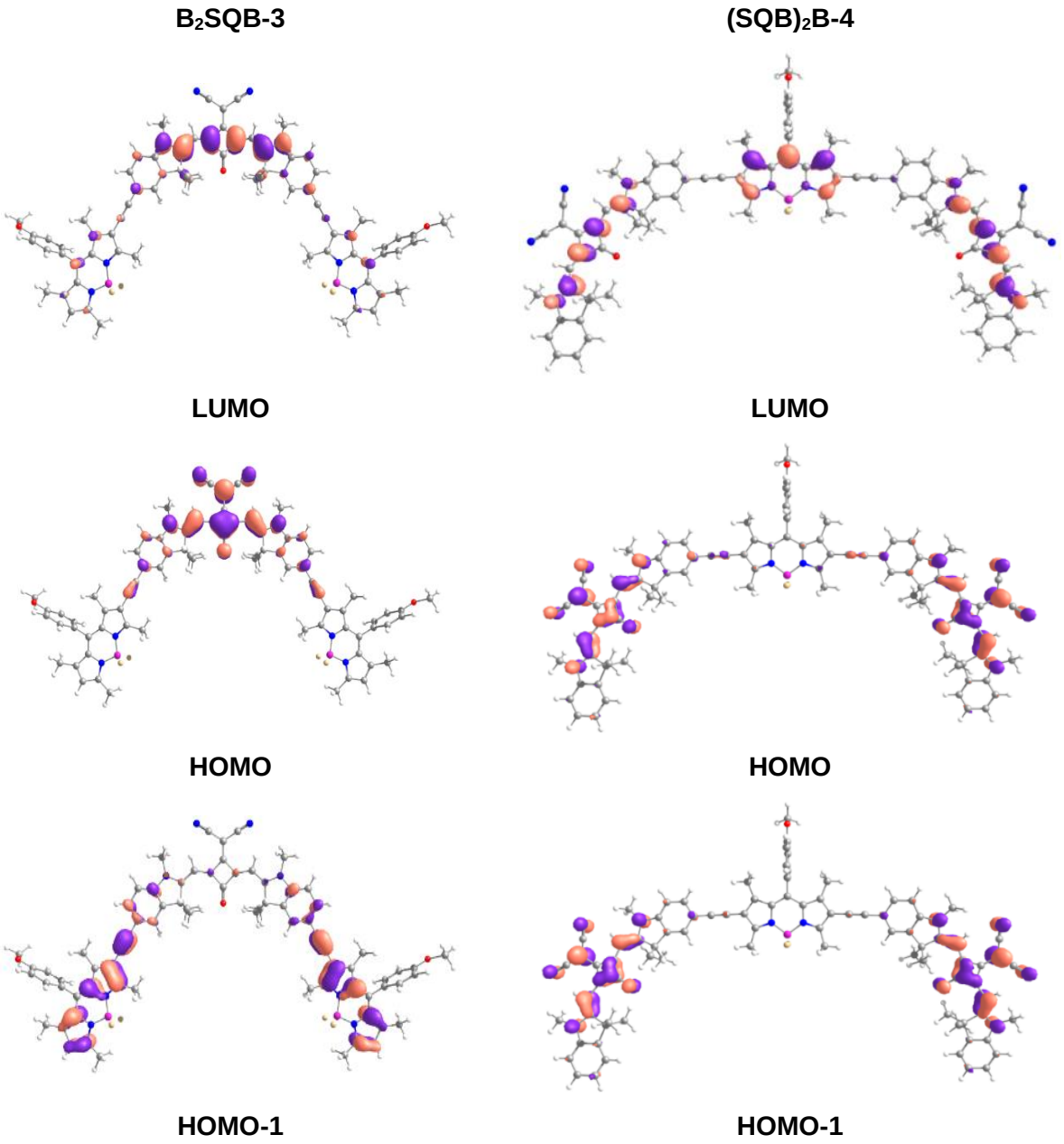

Figure 57 Orbitals of **(SQB)$_2$B-4** and **B$_2$SQB-3** from TD-DFT calculations at B3LYP/6-31G* level of theory.

Fluorescence Spectroscopy

For both triads fluorescence spectra were recorded at two different excitation wavelengths. For **B_2SQB-3** excitation both at low energies (14700 cm^{-1} (680 nm)) corresponding to an excitation of the bodipy and high energies (18900 cm^{-1} (529 nm)), corresponding to an excitation of the squaraine leads to the same fluorescence spectrum with a maximum at 13000 cm^{-1} (769 nm) (see Figure 58). This narrow band shows all the typical properties of the squaraine monomer fluorescence, that is a slight solvent dependency, shifting from 13200 cm^{-1} (758 nm) in CH_2Cl_2 to 13000 cm^{-1} (763 nm) in cyclohexane (see Figure 58b) and a small *Stokes* shift compared to the squaraine associated absorption of the triad of 260 cm^{-1} in toluene (see Figure 58b). A comparison of **B_2SQB-3** to its parent compounds reveals a red shift of the emissive state of about 920 cm^{-1} (see Figure 58a). Fluorescence from a higher state at around 17000 cm^{-1} (588 nm) is only observed in cyclohexane but not in toluene or CH_2Cl_2 (see Figure 59a). This fluorescence band is similar, both in energy and shape to the fluorescence of **BODIPY-3**.

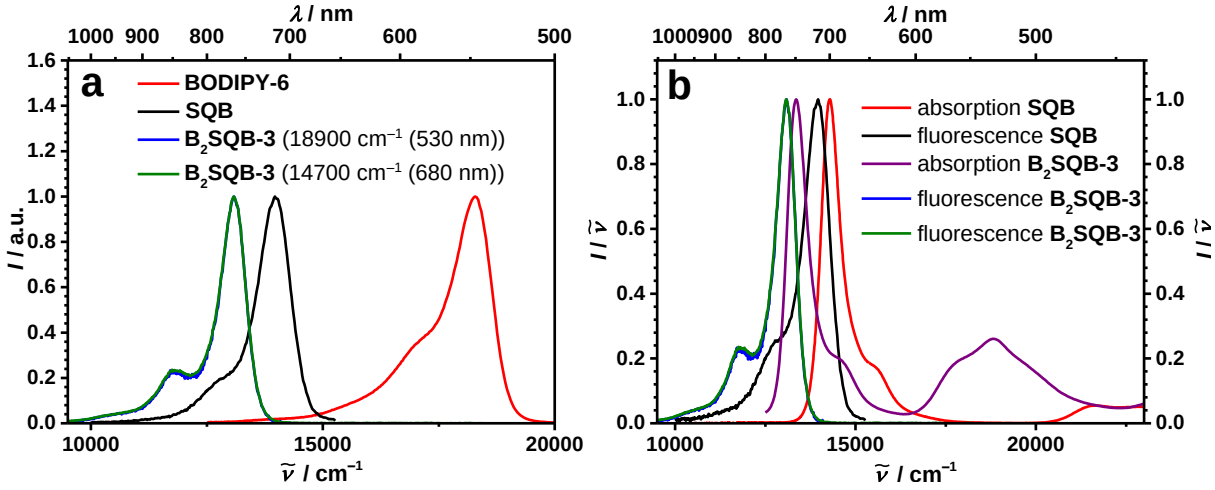

Figure 58 Comparison of **B_2SQB-3** with the corresponding monomers **SQB** and **BODIPY-6** in toluene at rt (**a**) and absorption and reduced fluorescence spectra of **B_2SQB-3** (**a**) in comparison with **SQB** in toluene at rt. The excitation wavelengths of the triad are as follows: **B_2SQB-3** 18900 cm^{-1} (530 nm) (blue curve), 14700 cm^{-1} (680 nm) (green curve).

The quantum yield of **B_2SQB-3** is higher in toluene (0.62) in case of excitation at the high energy band than in cyclohexane (0.54), but even in cyclohexane the contribution to the overall quantum yield of 0.54 is below 1 % for the fluorescence from the upper state. Quantum yields gathered after excitation at the low energy band, lead to values of similar magnitude and deviations can most likely be assigned to intrinsic errors of the measurement connected with the use of different detectors due to the wide measurement range.

The distinct geometry that the triads adapt depends on the solvent and leads to more fluorescence from the high energy state in cyclohexane for **B_2SQB-3**. **$(SQB)_2$B-4** also shows a strong fluorescence at 13400 cm^{-1} (746 nm) in toluene after excitation at both the upper (16800 cm^{-1} (595 nm) and lower (14700 cm^{-1} (680 m) excitonic state (see Figure 60). This fluorescence band shows a slight solvent-dependency (see Figure 61a), a small *Stokes* shift of 200 cm^{-1} in toluene (see Figure 60b) and has a broad shoulder reaching into the NIR up to 1100 cm^{-1} (909 nm) (see Figure 61b). The symmetrical triad **$(SQB)_2$B-4** shows a narrower fluorescence band in comparison with the undisturbed **SQB** and additionally **$(SQB)_2$B-4** is in relation to **SQB** shifted to the NIR region of about 580 cm^{-1} (see Figure 60a). A comparison of the full width at half maximum (fwhm) of both triads with the monomer shows that the fluorescence of the dye conjugates both are characterised by a narrowing from 840 cm^{-1} for **SQB** to 640 cm^{-1} for **B_2SQB-3** and 620 cm^{-1} for **$(SQB)_2$B-4**. This trend could be explained by exchange narrowing (see Chapter 2.3.3). In contrast to this the width of the absorption bands are 680 cm^{-1} for **SQB** as well as **B_2SQB-3**. **$(SQB)_2$B-4** shows a more broadened low energy absorption but this can be explained by two excitonic states being responsible for this band. Taking both observations into account, one can assume that exciton coupling is more pronounced in the relaxed excited state than in the Franck-Condon State.

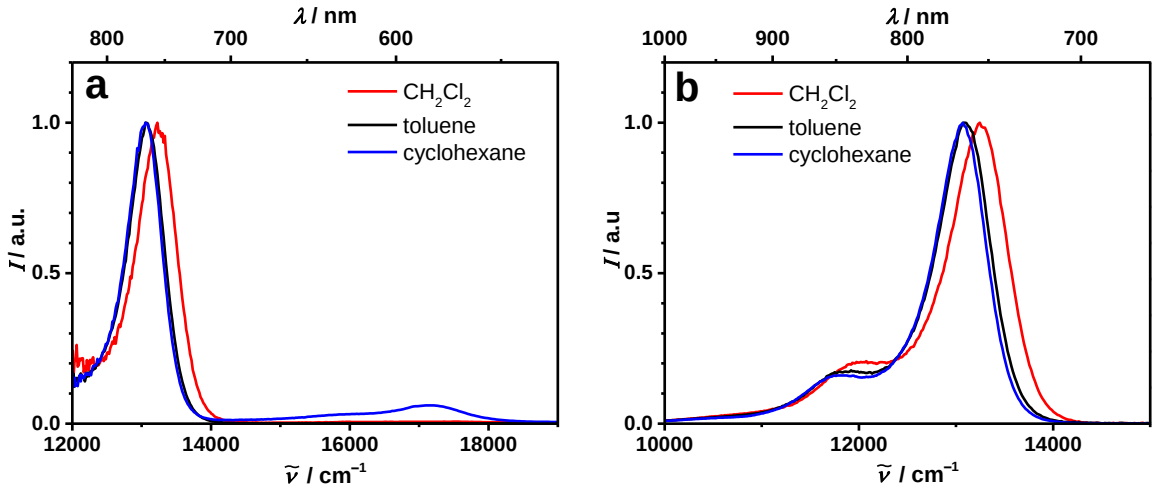

Figure 59 Fluorescence spectra of **B_2SQB-3** in different solvents at rt excited at long wavenumbers (18900 cm^{-1} (530 nm) recorded with the PMT detector (**a**) or with the NIR detector (**b**).

The fluorescence band of the upper excitonic state in **$(SQB)_2$B-4** (see Figure 61a) at around 16500 cm^{-1} (606 nm) is difficult to resolve, especially next to the intense squaraine band which has a quantum yield of 0.77 in toluene. The most prominent high energy fluorescence can be recorded in CH_2Cl_2 and just as observed for **B_2SQB-3** shows the same spectral features as **BODIPY-3**. Since in **B_2SQB-3** no fluorescence of the upper excitonic state can be observed, cyclohexane was choosen for the further investigation since here, both

triads show dual-emission. For **(SQB)$_2$B-4** the quantum yield in cyclohexane is independent of the excitation wavelength and leads in both cases to quantum yields of about 80 %. Again the contribution of fluorescence from the upper excitonic state is below the 1 % mark. A small enhancement of the quantum yield of **(SQB)$_2$B-4** relative to **SQB** is observed, while for **B$_2$SQB-3** the quantum yield is smaller. The comparison of the reduced fluorescence and absorption spectra of the squaraine band leads to the same conclusion for both **B$_2$SQB-3** and **(SQB)$_2$B-4**. For both triads small enhancement of the vibronic shoulder can be observed in the fluorescence spectra, otherwise the spectra are behaving as mirror images (see Figure 58b and Figure 60b).

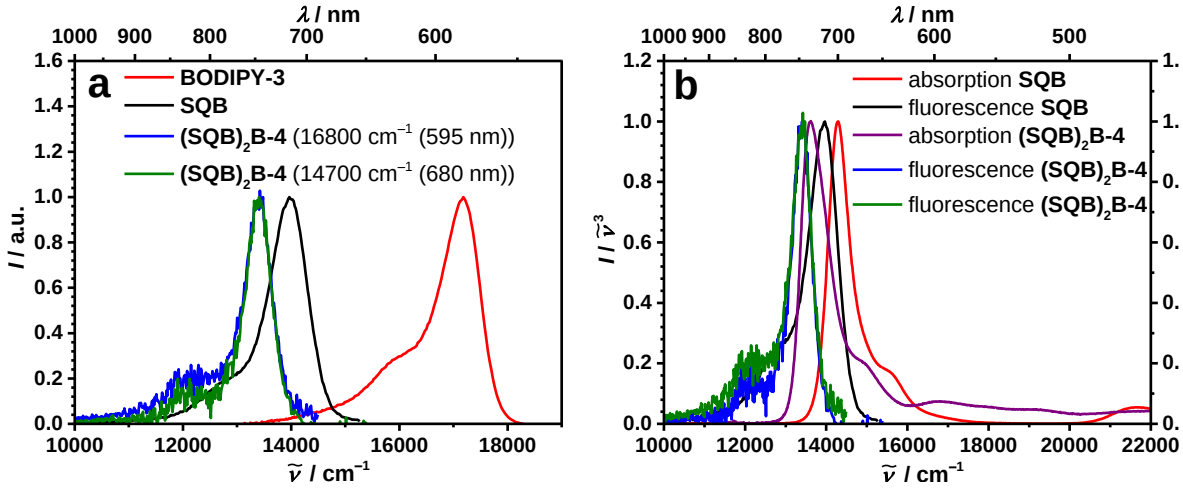

Figure 60 Fluorescence spectrum of **(SQB)$_2$B-4** at different excitation wavelengths in comparison with its parent compounds in toluene at rt (**a**) and absorption spectra $(I/\tilde{\nu})$ (red) and reduced fluorescence spectra $(I/\tilde{\upsilon}^3)$ of **(SQB)$_2$B-4** (**b**) in comparison with **SQB** in toluene at rt. The excitation wavelengths of the triad are as follows: 16800 cm^{-1} (595 nm) (blue curve), 14700 cm^{-1} (680 nm) (green curve).

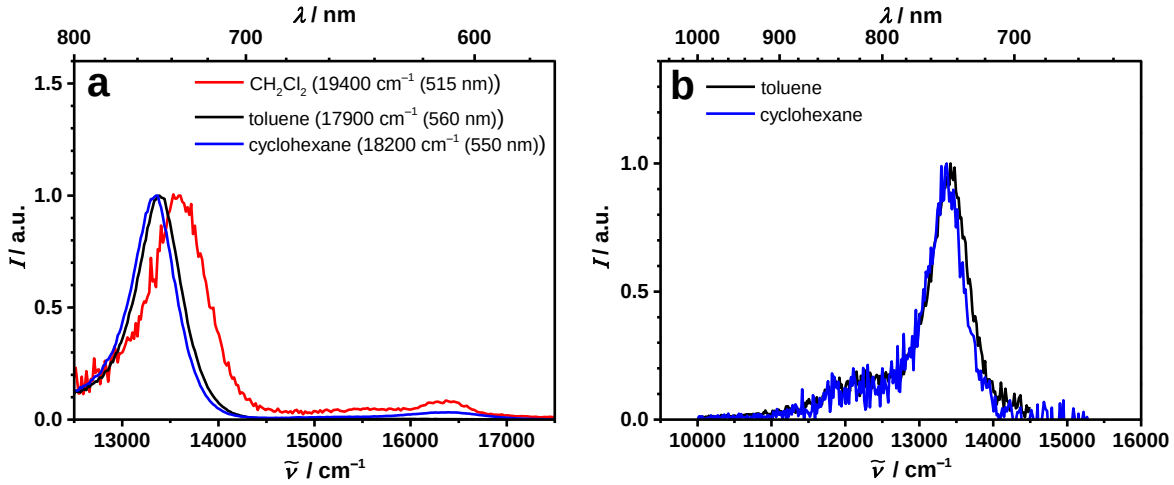

Figure 61 Fluorescence spectra of **(SQB)$_2$B-4** in different solvents at long wavenumbers (excitation wavelength) (**a**) and short wavenumbers (excitation at 14700 cm^{-1} (680 nm)) (**b**).

Excitation spectra are discussed for cyclohexane, as here both triads show a noticable high energy emission band. Monitoring of **B$_2$SQB-3** at 17200 cm^{-1} (581 nm) leads to a spectrum that does not match with the absorption spectrum at higher wavenumbers, but the bodipy is resembled well (see Figure 62a). When the fluorescence of the squaraine is monitored at 12240 cm^{-1} (817 m) the form of excitation spectrum fits very well with the absorption spectrum, but the bodipy contribution is overexaggerated. The excitation monitored at the squaraine band matches reasonable well with the absorption spectrum of **(SQB)$_2$B-4**, only in the high energy region some minor derivations are apparent. This discrepancy for both triads between absorption and excitation spectra at higher energies can be assigned to an insufficient correction of the detector, as this problem occured always when emission wavenumbers below 19500 cm^{-1} (513 nm) where monitored (see Figure 62b). The matching spectra suggests that fluorescence in the squaraine region originates from the lowest excitonic state and energy transfer/internal conversion is quantiative.

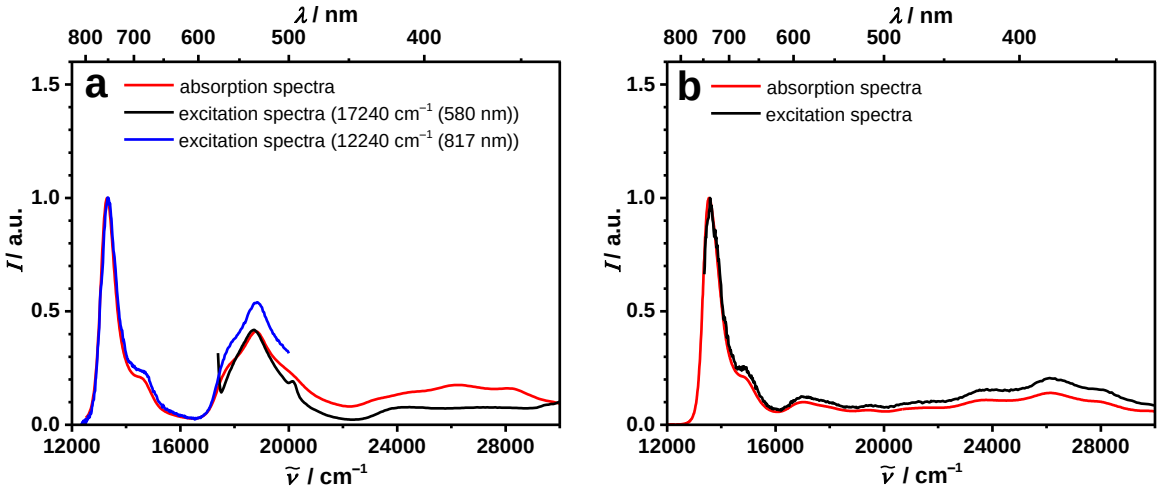

Figure 62 Excitation spectrum of **B_2SQB-3** measured at different fluorescence wavenumbers (black and blue) in comparison with the absorption spectrum (red) in cyclohexane at rt (monitored emission wavenumbers are given in brackets) (**a**) and excitation spectrum of **(SQB)$_2$B-4** (black) measured at 13300 cm^{-1} (752 nm) in comparison with the absorption spectrum (red) (**b**) in cyclohexane at rt.

Time-Dependent Fluorescence Measurements

The fluorescence lifetimes of both triads were measured by TCSPC (see Table 10). For **(SQB)$_2$B-4** and **B$_2$SQB-3** at both excitation energies the low energy fluorescence in toluene has somewhat shorter lifetimes than the typical 4.5 ns of the undisturbed squaraine. For **B$_2$SQB-3** in toluene 2.4 ns after excitation at the high energy absorption band and 2.6 ns after excitation into the lower excitonic state are recorded. Lifetime measurements of **(SQB)$_2$B-4** lead to 2.3 ns if the upper excitonic state is excited and 2.5 ns if excitation is ensued into the low energy band. The lifetime of the main emission band in CH_2Cl_2 is distinctly shortened to 0.05 ns after excitation at the low energy absorption band and same decrease occurs in **B$_2$SQB-3**, leading to a lifetime of 1.1 ns after excitation at low wavenumbers. As the high energy fluorescence band is not present in both triads in toluene or CH_2Cl_2, additional lifetime measurements were performed in cyclohexane, where a distinct fluorescence around 16400 cm^{-1} (610 nm) in **(SQB)$_2$B-4** and around 17200 cm^{-1} (581 nm) in **B$_2$SQB-3** can be seen. Overall **B$_2$SQB-3** and **(SQB)$_2$B-4** show similar lifetimes in cyclohexane. Excitation of the low energy absorption band leads to a lifetime of 2.7 ns in both dye conjugates. For **B$_2$SQB-3** the same decay time results from excitation into the upper excitonic state if fluorescence is measured at low wavenumbers, but for **(SQB)$_2$B-4** the lifetime is reduced slightly to 2.1 ns. Measurement of the high energetic fluorescence leads to biexponential decays. The longer lifetimes are with 3.1 ns in **B$_2$SQB-3** and 2.7 ns in **(SQB)$_2$B-4** quite similar while the fast decay times differ with 397 ps for **B$_2$SQB-3** and 1.2 ns for **(SQB)$_2$B-4**. In both conjugates the longer lifetime has the bigger amplitude.

With the average lifetimes the transition moment of the fluorescence μ_{fls} can be calculated by using the *Strickler-Berg*-equation.[179]

For **B$_2$SQB-3** and **(SQB)$_2$B-4** the transition-dipole moments of the lowest energetic bands were calculated (see Table 9). In the absence of structural reorganisation, the transition-dipole moments of absorption and fluorescence should be equal. This is true for the monomers **SQB**, **BODIPY-3** and **BODIPY-6**. For **B$_2$SQB-3** the transition-dipole moment of the fluorescence is about 30 % higher than the one of the absorption. **(SQB)$_2$B-4** shows opposite behaviour with a decrease of the fluorescence transition-dipole moment of about 20 %. This observation is more explainable if these results are compared with the dye conjugates having a *trans*-indoleine squaraine as the low energy absorbing chromophore. Here the lowest exciton band is broadened because different conformers are responsible for the fluorescence. Assuming a similar situation for **(SQB)$_2$B-4** the fluorescence transition-dipole moment belongs to only one exciton state that is fluorescent, while the absorption band consists of the two lower excitonic states. Hence, the calculated absorption transition moment is overestimated. As it is not possible to calculate the low excitonic state solely from

the absorption spectrum, integration down to 20000 cm^{-1} including the whole excitonic manifold was performed and yields a squared transition moment of 254 D^2. This matches nicely with the sum of the transition moments of the monomers of 234 D^2. Hence, the *Thomas-Reiche-Kuhn* sum rule is fulfilled.[26] This still does not explain the enhancement of the fluorescence transition-dipole moment of **B_2SQB-3**. A sufficient explanation can be given by the already mentioned enhanced coupling in the relaxed excited state. The stronger interaction between the chromophores can be enabled by structural reorganisation on the excited state surface.

Transient Absorption Spectroscopy (TA)[1]

In order to gain insight into the photoinduced dynamics transient absorption spectra of **B_2SQB-3** and **$(SQB)_2$B-4** were measured after excitation at the upper excitonic state and the lowest excitonic state. Due to the similar behaviour of the dye conjugates in toluene and cyclohexane (see Table 10), only the later one was chosen for the fs-time resolved measurements. In these experiments, the samples were pumped by a ca. 140 fs pump pulse at the appropriate wavenumber and were probed by a white light continuum (ca. 140 fs) in the range of 12500–25000 cm^{-1} (400–800 nm).

For **B_2SQB-3** the transient spectra for both excitation wavenumbers are depicted in Figure 63 along with decay associated difference spectra (DADS) resulting from a global analysis of the transient map and time traces at selected wavenumbers. The GSB at 13200 cm^{-1} (758 nm) dominates the spectra and is accompanied by several ESA on the high energy side in the region of 15000–20000 cm^{-1} (486–669 nm). Excitation into the upper exciton state at 18800 cm^{-1} (532 nm) leads to four components after deconvolution. The DADS describing the shortest lived state is characterised by a time constant of 0.12 ps and hence shorter than the width of the excitation pulse. For this reason a relatively big error has to be assumed for this decay time. This DADS is defined by a rise of the TA signal and should be due to population transfer from the high excitonic state to the lower excitonic state.

[1]The femtosecond spectroscopy measurements were performed by *Alexander Schmiedel* and the analysis was carried out by *Dr. Marco Holzapfel*.

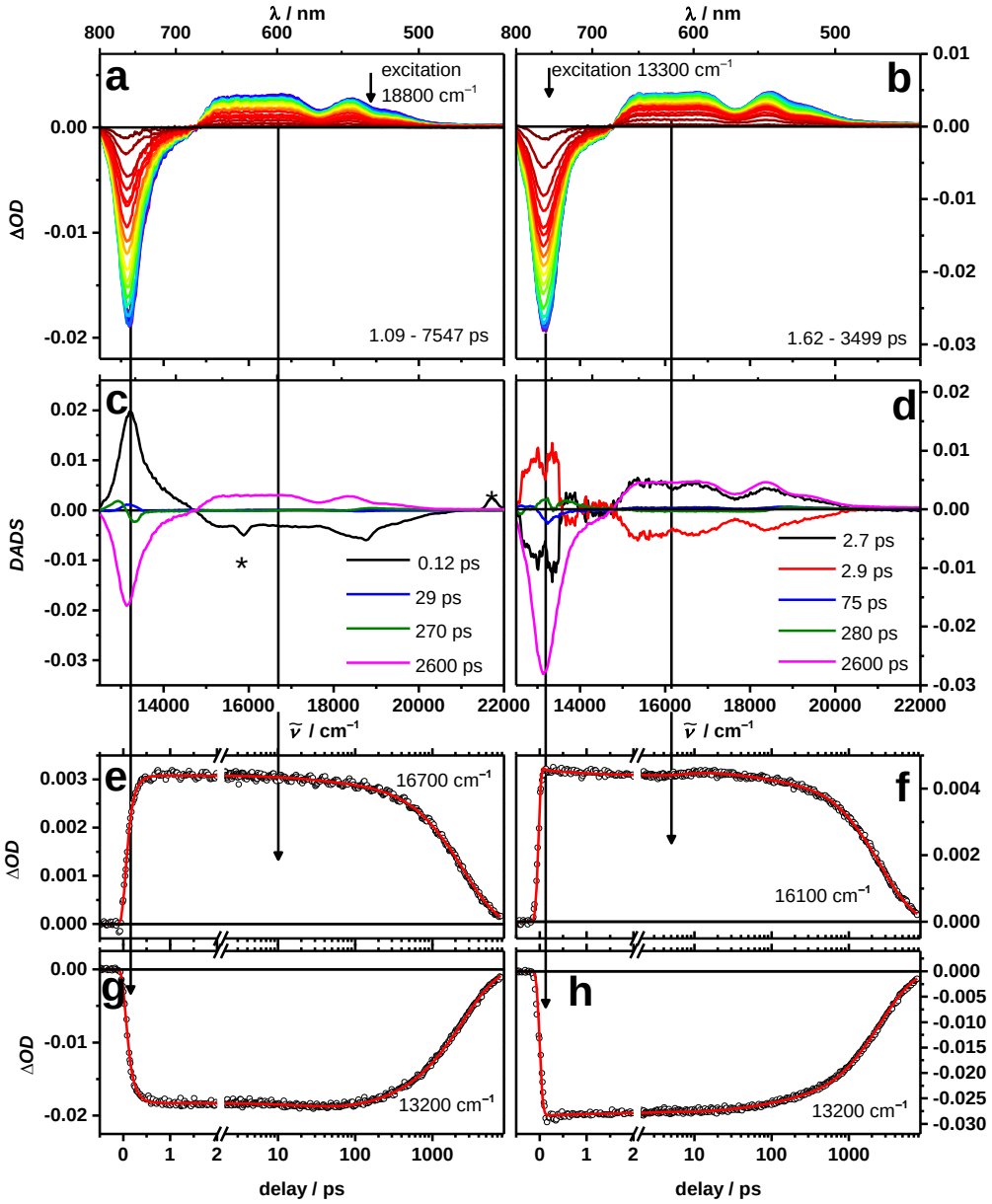

Figure 63 Chirp corrected transient absorption spectra of **B_2SQB-3** in cyclohexane at rt after excitation at 18800 cm^{-1} (533 nm) (**a**) and 13300 cm^{-1} (753 nm) (**b**). Early spectra are given in blue, later spectra in red. Decay associated spectra resulting from the TA spectra (**c** and **d**) and time scans at selected wavenumbers (**e-h**). The features marked with * are caused by Raman scattered light.

Two time components in the ps-time range (29 and 270 ps) are describing shift dynamics at around 13000 cm^{-1} (769 nm). This conclusion can be drawn as the two DADS spectra show the typical wave-like behaviour in the mentioned wavenumber region. These shifts can be of different origins: One explanation would be hot ground state population, which would influence an overlaying absorption signal and lead to a shift of the GSB/SE signal to lower energies.[189] It is also possible that the dynamic shifts of the SE are due to vibrational relaxation in the excited state.[190, 191] Solvent reorganization contributions (dynamic *Stokes*

shift) can be discarded as explanation for these shifts because of the low polarity of the cyclohexane solvent. However, the viscoelastic response of the solvent due to the change of solute volume upon excitation may play a role here instead of the dielectric response.[192, 193] The intense DADS with a time component of 2.6 ns shows almost mirror image behaviour to the DADS associated with the shortest lifetime. This is caused by a depletion of ground state population during the excitation and the high extinction coefficient of the squaraine absorption at this wavenumber. There is also significant ESA around 15000–20000 cm^{-1} (667–500 nm). The time constant of this DADS fits nicely with the one from the TCSPC measurement in cyclohexane (2.7 ns, see Table 10) and can therefore be assigned to ground state recovery.

Excitation of **B_2SQB-3** at the maximum absorption of the lowest excitonic band at 13300 cm^{-1} (752 nm) gives a very similar transient spectrum, which rises with the instrument response. As the additional rise time observed after excitation 18800 cm^{-1} (532 nm) is absent (see e.g. time traces in Figure 63g and h around t = 0) the interpretation above might still be true despite the time constant being shorter than the pump pulse. The global analysis shows five contributions, one DADS with a 2.6 ns lifetime and again two DADS with wave-like shapes and 75 ps and 280 ps lifetimes. Due to the good agreement with the other experiment these again can be assigned to ground state recovery and general shifts of SE and ESA. It has to be noted that the DADS with wave-like shape represent shifts whose dynamics cannot necessarily be represented by exponential functions. Therefore, the lifetimes of these shift components are difficult to compare directly. Two DADS components with lifetimes between 2–3 ps are necessary for a good fit of the transient map around 15000–20000 cm^{-1} (667–500 nm). These two components show almost mirror image behaviour and were necessary to describe a decrease followed by a slight rise on the lower ps-time domain. This can nicely be seen in the time trace in Figure 63f and 63h.

For **$(SQB)_2$B-4** excitation at the upper exciton level leads to similar results as for **B_2SQB-3** (see Figure 64). The shortest lived DADS (τ = 0.05 ps) represents the population transfer from the upper to the lower exciton state. The fast decay of this state, being close to the time resolution of our set-up, entails the noticeable contributions from the coherent artefact, which can be seen in the associated DADS around 14000 cm^{-1} (714 nm) and 20000 cm^{-1} (500 nm). Similar to the previous investigation of **B_2SQB-3** a DADS with a wave-like signature around 13500 cm^{-1} (741 nm) and a lifetime of 480 ps can be found and maybe a result of shifting dynamics. Again, the most prominent DADS shows the longest lifetime (τ = 2.54 ns) and agrees very well with that of the fluorescence lifetime (2.7 ns). The second pump-probe experiment was again performed for excitation at the lowest excitonic level of **$(SQB)_2$B-4** (13500 cm^{-1} (741 nm)). The results fit nicely with the observations already discussed for

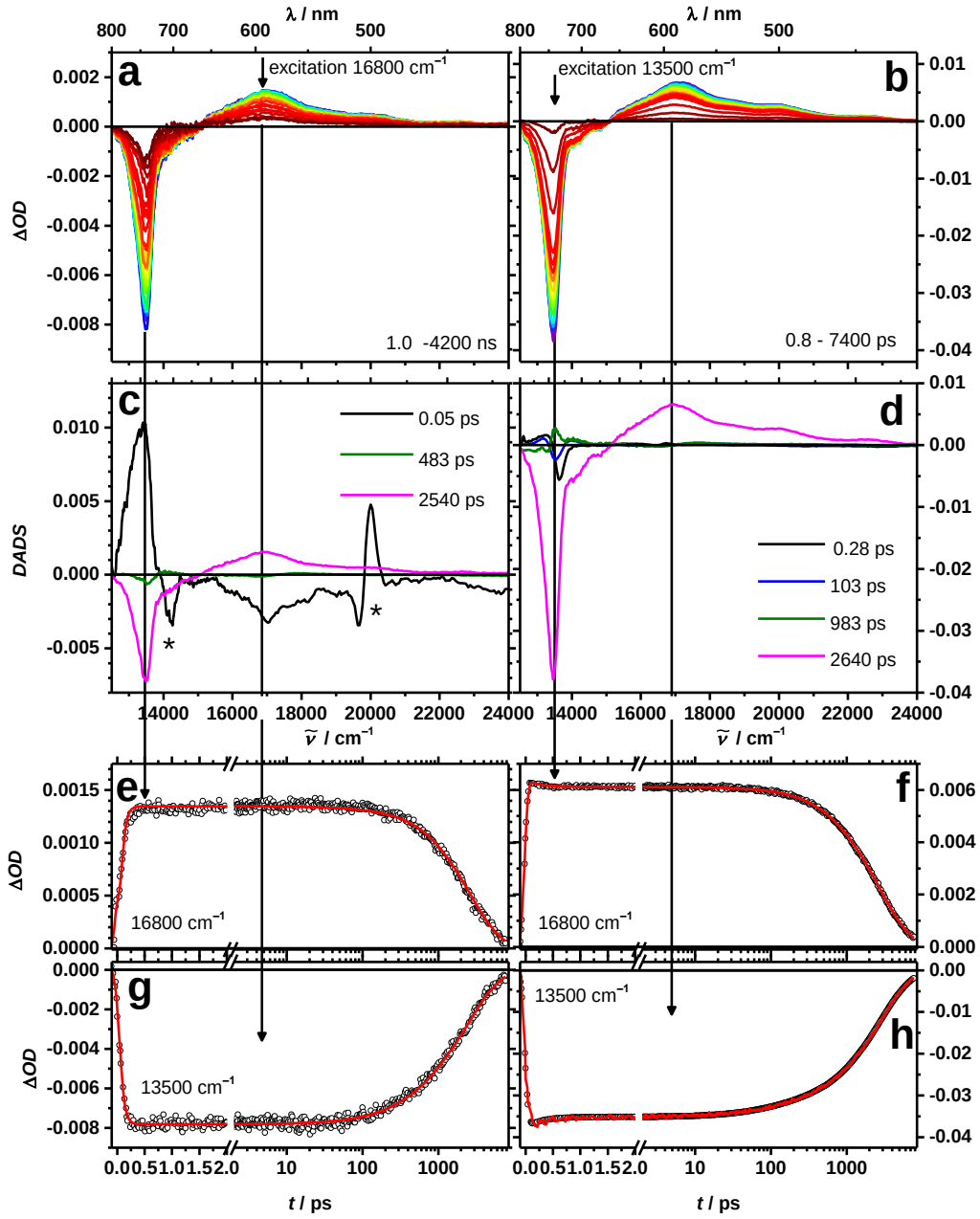

Figure 64 Chirp corrected transient absorption spectra of (**SQB)$_2$B-4** in cyclohexane at rt after excitation at 16800 cm^{-1} (594 nm) (**a**) and 13500 cm^{-1} (741 nm) (**b**). Early spectra are given in blue, later spectra in red. Decay associated spectra resulting from the TA spectra (**c** and **d**) and time scans at selected wavenumbers (**e-h**). The features marked with * are caused by Raman scattering.

B$_2$SQB-3. Three DADS with time constants of 0.28 ps, 100 ps and 980 ps are associated with dynamic shifts around 13500 cm^{-1} (741 nm) and the most intense DADS is with τ = 2.64 ns again the longest lived component.

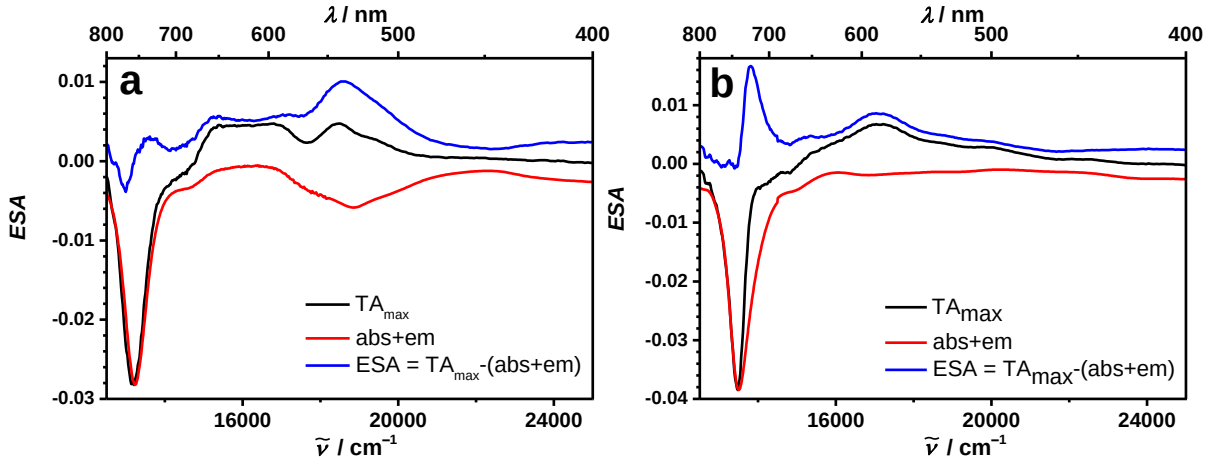

Figure 65 Difference spectra of TA spectrum at maximum negative intensity and the sum of steady state absorption and emission spectra for **B_2SQB-3** (**a**) and **(SQB)$_2$B-4** (**b**).

The comparison of the shape of the DADS of t = 2.54 ns of **(SQB)$_2$B-4** resulting from the excitation in the upper excitonic state with the DADS of the same experiment for **B_2SQB-3** (τ = 2.6 ns) reveals a distinct difference. The GSB signal at 13500 cm^{-1} (741 nm) of **(SQB)$_2$B-4** shows an unusually steep flank at the high energy side. To discern different possible spectral contributions we modelled the sum of GSB and SE by using the steady state spectra. Therefore we plotted the sum of the fluorescence spectrum (divided by $\tilde{\upsilon}^2$)[180] and the steady state absorption spectrum which are given in Figure 65b and subtracted them from the transient absorption spectrum with maximum amplitude at 13500 cm^{-1} (741 nm). By doing so, we ended up with a difference spectra that represents the ESA contribution, which shows a prominent positive absorption at 13800 cm^{-1} (725 nm). This ESA is situated at slightly higher energy than the GSB, which is typical of an excitation into a two-exciton state. Applying the same procedure to the spectra of **B_2SQB-3** reveals an ESA at 18600 cm^{-1} (538 nm) which also is related to a two-exciton state (see Figure 65). This signal appears at a higher energy than that of **(SQB)$_2$B-4**, because this two-exciton state has greater contribution of the bodipy chromophores while the two exciton state of **(SQB)$_2$B-4** has more squaraine character.

Table 10 Time-resolved optical data of squaraine and bodipy containing triads and their parent compounds in toluene and cyclohexane at rt.

	solvent	τ/ns (TCSPC)[a]	τ/ns (TCSPC)[a]	τ/ps (TA)[b] [pump wavenumber]	τ/ps (TA)[b] [pump wavenumber]	τ/ps (FLUC)[c]
BODIPY-6	toluene	4.7[1]				
BODIPY-3	CH_2Cl_2	4.93[1]				
	toluene	4.5[1]				
SQB	CH_2Cl_2		1.76			
	toluene		4.5			
B_2SQB-3	CH_2Cl_2		1.1			
	toluene	2.4 [13100][2]	2.6			
	cyclohexane	0.397 (0.09)/ 3.1 (0.91) [16100][2] 2.7 [13000][2]	2.7	0.119 29.3 268 2570 [18800]	2.7 2.9 7.5 280 2600 [13300]	0.20 (−0.65) 14 (−0.17) 910 (−0.11) 2200 (1.00) [18800/12700]
$(SQB)_2$B-4	CH_2Cl_2		0.05			
	toluene	2.3 [13300 (750)][2]	2.5			
	cyclohexane	1.2 (0.31)/ 2.7 (0.69) [15600][2] 2.1 [13300][2]	2.7	0.05 483 2540 [16800]	0.28 103 983 2640 [13500]	0.12 (−0.17) 79 (−0.10) 2650 (1.00) [18200/12800]

[a] Fluorescence spectra measured by TCSPC, for bodipy at 23920 cm^{-1} (418 nm)[1] or 19420 cm^{-1} (515 nm)[2], for squaraine at 15240 cm^{-1} (656 nm), monitored wavelength for **B_2SQB-3** and **$(SQB)_2$B-4** given in square brackets. Lifetime measurements of bodipy lead in some cases to two lifetimes, the ratio of these is given in brackets. [b] Globally fitted lifetimes of SADS measured by TA [pump wavenumber]. [c] Decay lifetimes measured by FLUC in cyclohexane at rt (amplitude)[excitation/probe wavenumber].

Fluorescence Upconversion Measurements[1]

Both triads show very similar dynamics in the fluorescence upconversion measurements (FLUC) when excited in the upper excitonic state and probed at the lower one (see Figure **66**). Three to four components were necessary for a good fit, of which the short ones in the 0.1–1000 ps range have a negative amplitude, marking a rise time of the fluorescence signal. As these times are on the picosecond time scale, they can be assigned to vibrational relaxation of the molecules.[97, 194] This leads to a shift of the fluorescence signal towards lower energies, which is visible as a rise time in the spectra due to the probe wavelength being at the red falling flank of the emission. An alternative explanation for the components with $t < 1$ ps could be population transfer from the upper to the lower excitonic state. To distinguish between these two processes time resolved fluorescence spectra would be necessary, but the measurement of them is impossible due to the small stokes shift. Taking the limited range of the delay stage into account the ns-time components fit well with the lifetime from the TCSPC measurements and hence are due to ground state recovery.

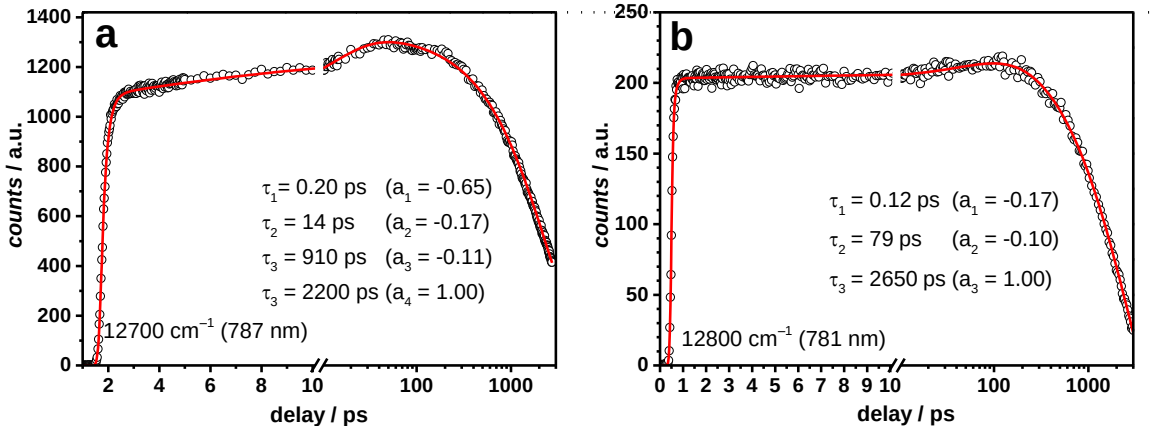

Figure 66 Fluorescence decay from fluorescence upconversion measurements of **B_2SQB-3** excited at 18800 cm^{-1} (532 nm) (IRF: 190 fs) (**a**) and **$(SQB)_2$B-4** excited at 18200 cm^{-1} (549 nm) (IRF: 150 fs) (**b**) in cyclohexane at rt.

[1]The femtosecond spectroscopy measurements were performed by *Alexander Schmiedel* and the analysis was carried out by *Dr. Marco Holzapfel*.

Conclusion

The absorption spectra of both triads are dominated by a squaraine-like band in the NIR region that is slightly red-shifted compared to the monomer due to exciton coupling with the bodipy chromophore. The transition-dipole moments show additive behaviour increasing from **SQB** (92.7 D^2) to **B_2SQB-3** (101 D^2) and yield the highest value for **$(SQB)_2$B-4** (210 D^2). The emission bands from the lowest excitonic state of both triads show exchange narrowing with a fwhm from 840 cm^{-1} for **SQB** to 640 cm^{-1} for **B_2SQB-3** and 620 cm^{-1} for **$(SQB)_2$B-4**. Taking this observation and the increase of the fluorescence transition moments into account a possible explanation can be given by geometric changes that influence the spectroscopic characteristica of the triads. These can be described by a steep potential energy surface in the excited state, whereas in the ground state is defined by a more shallow curve. Small fluctuations in the ground state have a great influence on the coupling and reduce the interaction between the chromophores so that the absorption band width is comparable to the undisturbed monomer and the absorption transition-dipole moment behaves additive. The steep potential of the excited state leads to a narrow fluorescence and hence a reduced full width at half maximum in regard to the undisturbed monomer. As a second consequence from the form of the excited state potential energy surface, fluctuations in geometry are small and by this the coupling in the relaxed excited state is greatly enhanced in comparison to the absorption into the Franck-Condon state. This explains the enhancement of the fluorescence transition-dipole moment. In the TA spectra a decrease and increase at around 16000 cm^{-1} was visible which can then be assigned to relaxation phenomena. In conclusion, it could be proven that the exciton coupling is influenced strongly by the difference between the Franck-Condon and the relaxed excited state.

5.3 Asymmetrical Triads[1]

In contrast to the symmetrical conjugates a broader absorption range is covered by the implementation of a third chromophore with different spectral properties. Furthermore, the energy transfer process in the asymmetrical triads (see Scheme 23) may consist of more steps than the energy transfer process in the symmetrical ones. Starting from pyrene, the energy can be directly transfered to the energetically lowest chromophore, that is squaraine. Alternatively the bodipy chromophore can be used as an energetically bridge between pyrene and squaraine. Whether a one step energy transfer or a two step process is favoured depends on the spacial alignment of the chromophores. To make the two step energy transfer possible, the single chromophores need to show high emission quantum yields and the energy transfer processes must be fast, minimizing side reactions.[9, 72] Additional to the two triads **PyB(SQB)** and **PyB(SQA)**, which posses an energy gradient from pyrene down to squaraine, as a third conjugate **Py(SQB)B** was synthesised. In this triad pyrene and bodipy are separated by the squaraine, which is lowest in energy of the three. Therefore through-space energy transfer between pyrene and bodipy should be possible due to the spatial arrangement.

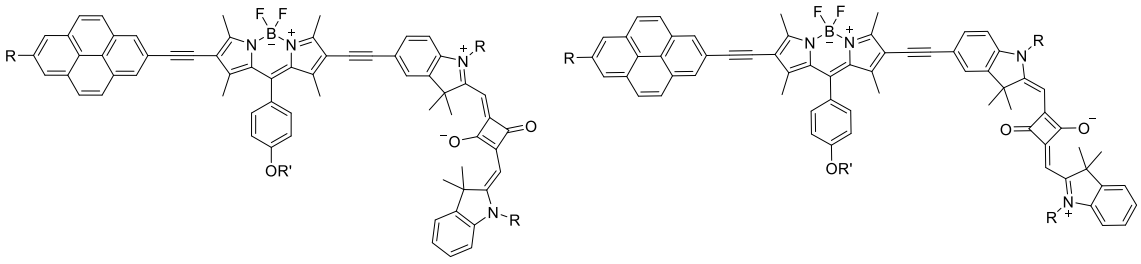

PyB(SQB)

PyB(SQA)

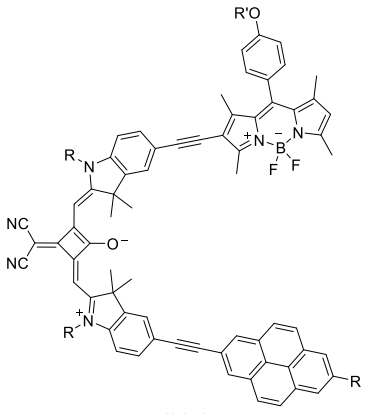

Py(SQB)B

R = 3,7-dimethyloctyl; R' = 2-ethylhexyl

Scheme 23 Asymmetrical triads **PyB(SQB)**, **PyB(SQA)** and **Py(SQB)B**.

[1]Some results presented in this chapter were worked out in a Bachelor thesis under the supervision of N. Auerhammer: N. Jordan, Bachelor Thesis, Julius-Maximilians-Universität (Würzburg), 2017.

The synthetic concept is first to couple two of the chromophores which then can be subjected to a second coupling with the third monomer. Therefore the stability of the heterodimer is of crucial importance and the dehalogenation of the squaraines under *Sonogashira* conditions has to be considered (see Chapter 5.2.2). Hence, for **PyB(SQB)** and **PyB(SQA)** the heterodimer consisting of pyrene and bodipy is synthesised first, which is subsequently coupled with the appropriate squaraine. The reaction conditions that proved most successful for the symmetrical triads are tested first.

To synthesis **Py(SQB)B** a terminal squaraine has to be dealt with in either possible case. As the **B(SQB)** heterodimer formation was already observed in mass spectra in the course of the synthesis of the symmetric triad **B_2SQB-3** this was used as a starting point, as it proved to be stable enough for a second *Sonogashira* reaction.

5.3.1 Synthesis

Synthesis of PyB(SQB) and PyB(SQA)

The first step of this synthetic pathway is the coupling of pyrene and bodipy to get the appropriate heterodimer. As the alkynylated squaraines gave mixed results in the *Sonogashira* couplings, the free alkyne group should be attached to the pyrene-bodipy conjugate and subsequently be coupled to the iodinated squaraine.

Synthesis of Pyrene-Bodipy Heterodiads

The coupling of bodipy to pyrene starts from the iodinated bodipy since the alkynylated bodipy is prone to homo coupling in contrast to pyrene, which showed rarely such reactivity. To get only mono coupled product, a high excess of **BODIPY-2** was used and pyrene **Py-8** was dropped in slowly using a dilution principle apparatus.[138] This procedure still leads to the symmetrical triad **Py_2B**, but also 38 % of pure mono coupled product could be isolated under the conditions shown in Scheme 24.

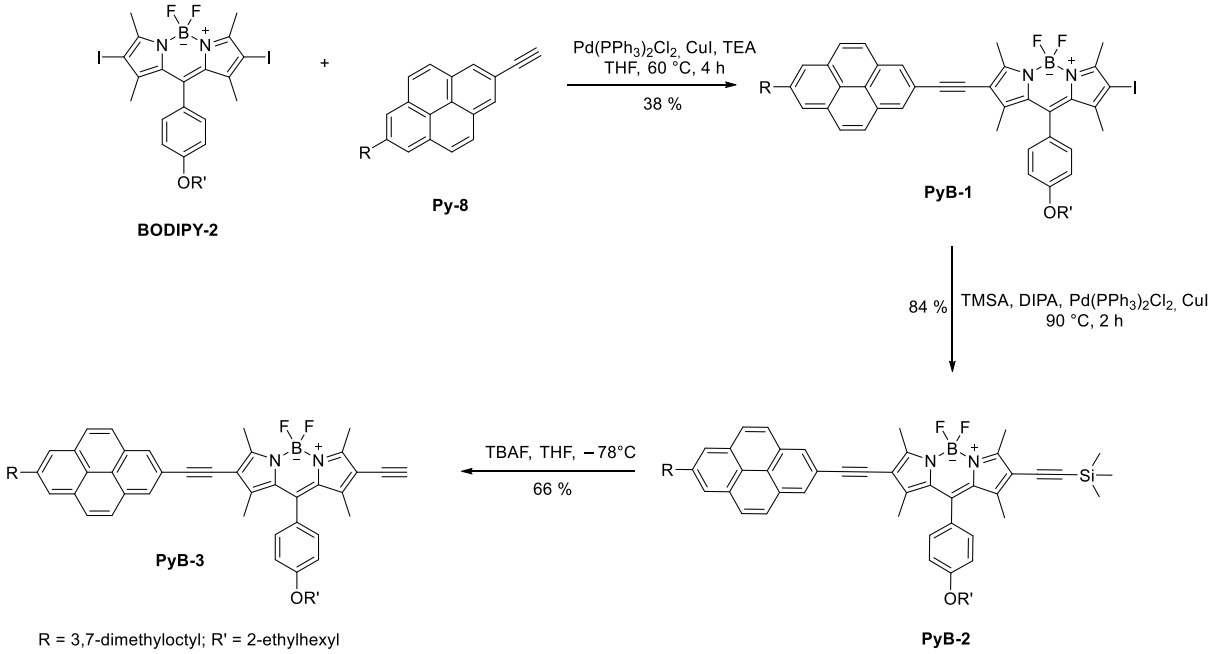

Scheme 24 Coupling of pyrene **Py-8** with **BODIPY-2** and subsequent alkynylation and deprotection.

A *Sonogashira* coupling with TMSA and subsequent deprotection using the same conditions as for **BODIPY-4** and **BODIPY-7** were applied to **PyB-1** to yield the final product **PyB-3** (see Scheme 24).

Synthesis of Asymmetrical Squaraines

The synthesis of **SQB-6** is discussed in Chapter 5.2.2.

To get access to the brominated transoid squaraine **SQA-5** 1-(3,7-dimethyloctyl)-2,3,3-trimethyl-3*H*-indole-1-ium iodine (**Ind-5**) is condensated with 3,4-diethoxycyclobut-3-ene-1,2-dione by refluxing in ethanol for 2.5 h (see Scheme 25). The protecting group is cleaved under basic conditions and afterwards the semisquaraine **Ind-6** is converted to the squaraine **SQA-5** in a one pot deprotonation and condensation reaction with 5-bromo-1-(3,7-dimethyloctyl)-2,3,3-trimethyl-3*H*-indole-1-ium iodine (**Ind-2**).[169]

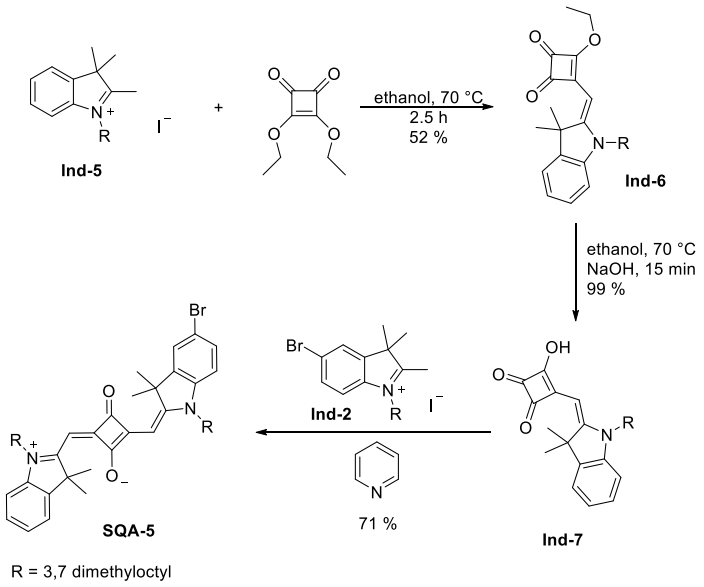

Scheme 25 Synthesis of asymmetrical substituted **SQA-5**.

The halogen exchange reaction follows the same procedure as for the symmetrical squaraines, resulting in 92 % yield of **SQA-6** (see Scheme 26).[170, 171] The noticable difference in the yields of the iodinated squaraines is not due to the reaction itself, but to the instability of the asymmetrical *cis*-squaraine **SQB-6** on silica, which led to a high loss during purification.

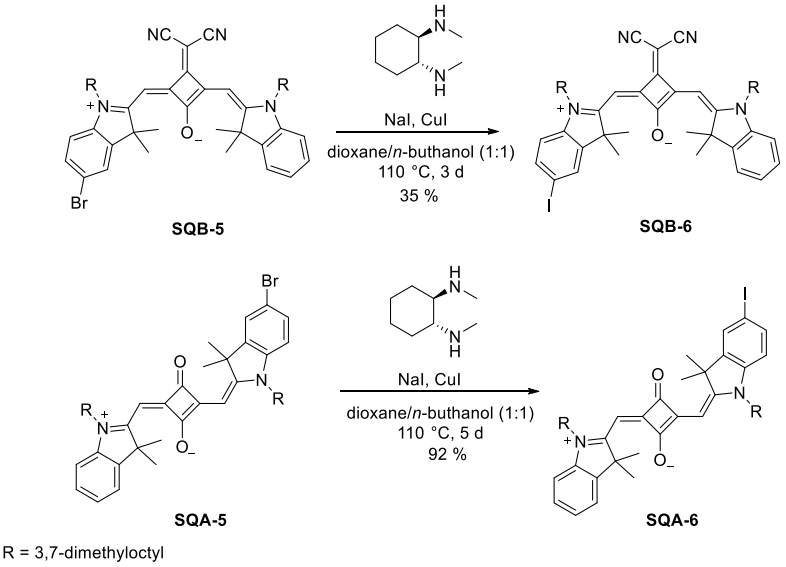

Scheme 26 Halogen exchange reaction of asymmetrical squaraines.

<u>*Sonogashira* Test Reactions for the Synthesis of **PyB(SQB)** Starting from **PyB-3**</u>

For the coupling of the mono iodinated squaraine **SQB-6** to **PyB-3** (see Scheme 27) a small reaction screening was done of which the results are summarised in Table 11. The most promising results in this work so far were obtained by using the highly reactive $Pd(PPh_3)_4$ catalyst in toluene[154] (see Table 11, condition I) and the less active $Pd(C_6H_5CN)_2Cl_2$ with P^tBu_3 as ligand[120, 140] (Table 11, condition II). These conditions worked well for most of the couplings yielding the symmetrical compounds, therefore they were tested for the synthesis of the asymmetrical conjugates first. Unfortunately both conditions failed, leading to no reaction progress whatsoever.

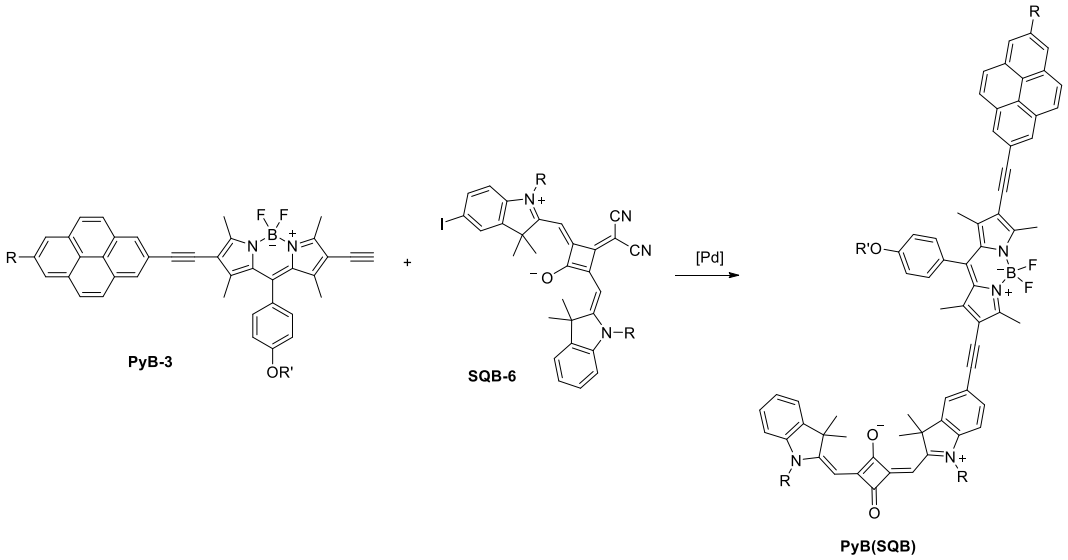

Scheme 27 Attempted coupling of **PyB-3** with cisoid squaraine **SQB-6**.

As the tryouts of the symmetrical chromophores showed that addition of CuI sometimes leads to faster deiodination of the squaraine (see Chapter 5.2.2), the condition using the reactive $Pd(PPh_3)_4$ catalyst was tried with and without CuI (see Table 11, condition III and IV). Additionally a more polar solvent which could improve the stabilisation of the intermediates was used for performing the reactions, as this was shown to give good results for copper-free *Sonogashira* reactions.[163] The reaction without CuI didn't yield any product, but the **PyB-3** was not present in the reaction mixture anymore, while the squaraine **SQB-6** was remaining. When CuI was used as a co-catalyst, both squaraine **SQB-6** and **PyB-3** were consumed after one day, but no coupling product could be identified.

Table 11 Conditions tested to synthesise **PyB(SQB)**.

	catalyst./ligand	co-catalyst	base	solvent	T/ t	conversion
I[154]	$Pd(PPh_3)_4$	CuI	TEA	toluene	rt→40°C/ 4 d	-
II[120, 140]	$Pd(C_6H_5CN)_2Cl_2$/ P^tBu_3	CuI	DIPA	dioxane	60 °C/1 d	-
III	$Pd(PPh_3)_4$	-	TEA	THF	40 °C/1 d	-
IV[152]	$Pd(PPh_3)_4$	CuI	TEA	THF	40 °C/1 d	-

Synthesis of PyB(SQB) from (SQB)B

As coupling of **PyB-3** to **SQB-6** was not successful, a different approach was tried to get access to the **PyB(SQB)** triad. The synthesis was tested starting from **(SQB)B** instead of **PyB-3** (see Scheme 28). The conditions that worked for the **$(SQB)_2$B-4** synthesis should be a good starting point to try to synthesise the mono coupled product. As the iodinated squaraine **SQB-6** is not stable enough to carry out reactions under higher temperatures and no suitable solvent with a low boiling point could be found, the dilution principle apparatus was not an option as it needs to work under reflux.[138]

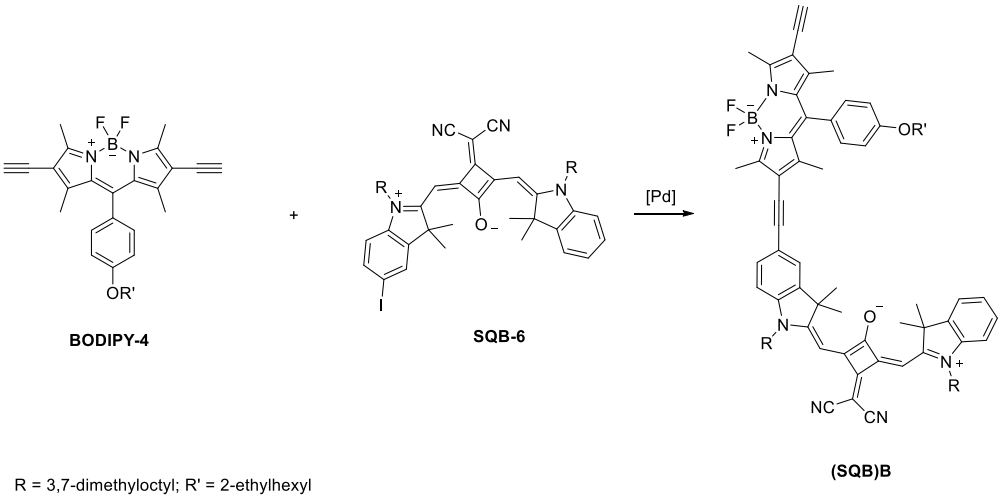

Scheme 28 Coupling of symmetric **BODIPY-4** with mono substituted *cis*-squaraine **SQB-6**.

When the reactive $Pd(PPh_3)_4$ catalyst in toluene[154] was used only the symmetrical triad was found even when higher amounts of **BODIPY-4** were used (see Table 12, condition I). So the two less reactive catalytic systems of $Pd(C_6H_5CN)_2Cl_2$ with P^tBu_3 as ligand[120, 140] (see Table 12, conition II) and $Pd(MeCN)_2Cl_2$ with XPhos as ligand[173] (see Table 12 conition III) were tried. While under conditon II high amounts of starting material were still left and only mono coupled product was found on a small scale, condition III led to no product whatsoever. Unfortunatley it was not possible to synthesise **(SQB)B** on a larger scale, as only the symmetric triad **$(SQB)_2$B-4** was formed then.

Table 12 Tested conditions to yield **(SQB)B**.

	catalyst/ligand	base	solvent	T/t	product
I[154]	$Pd(PPh_3)_4$	TEA	toluene	rt/2 d	**$(SQB)_2B$-4**
II[120, 140]	$Pd(C_6H_5CN)_2Cl_2$/ P^tBu_3	DIPA	dioxane	60 °C/1 d	**(SQB)B**
III[173]	$Pd(MeCN)_2Cl_2$/ XPhos	DIPA	dioxane	60 °C/1 d	-

Attempt to Synthesise **PyB(SQB)** in a One Pot Reaction

A last attempt to synthesise **PyB(SQB)** was made by trying to synthesise the triad directly by adding all the monomeric chormophores in at once, without the synthesis of a mono coupled product beforehand (see Scheme 29). The problem in such a one pot synthesis is, that not only the asymmetric triads can be formed, but the symmetric conjugates **Py_2B** and **$(SQB)_2B$-4** are likley side products. Regarding the results of the attempted heterodimer synthesis of **(SQB)B** the $Pd(C_6H_5CN)_2Cl_2$ catalyst seemed to be a good choice for this test reaction. Surprisingly the coupling not only worked quite well, forming the desired **PyB(SQB)**, but there were also only very small amounts of the expected side products. Nevertheless it was not possible to get rid of these impurities, although GPC in $CHCl_3$, column chromatograhy and precipitation from different solvents were tried.

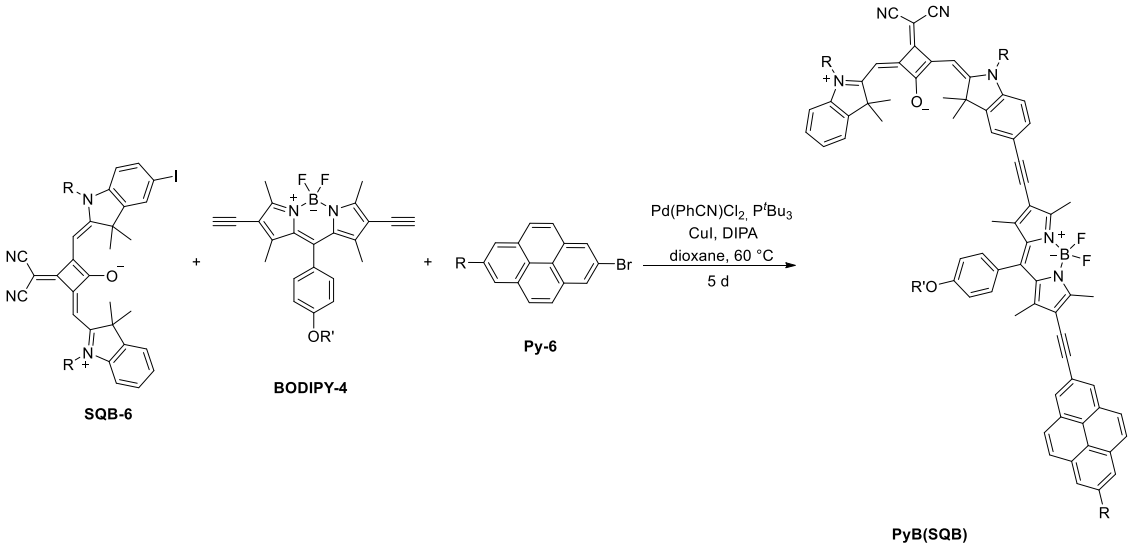

Scheme 29 Attempted synthesis of the **PyB(SQB)** triad starting directly from the monomers.

Synthesis of PyB(SQA)

Surprisingly the coupling of the **PyB-3** to the *trans*-squaraine **SQA-6** worked well with $Pd(PPh_3)_4$ in toluene, yielding 33 % of the desired triad containing some small amounts of impurities (see Scheme 30). Unfortunately during the purification the product seemed to decompose on silica and slower on GPC in $CHCl_3$. Precepitation and recrystallisation in different solvents and solvent mixtures were tried to get rid of the last impurities but failed.

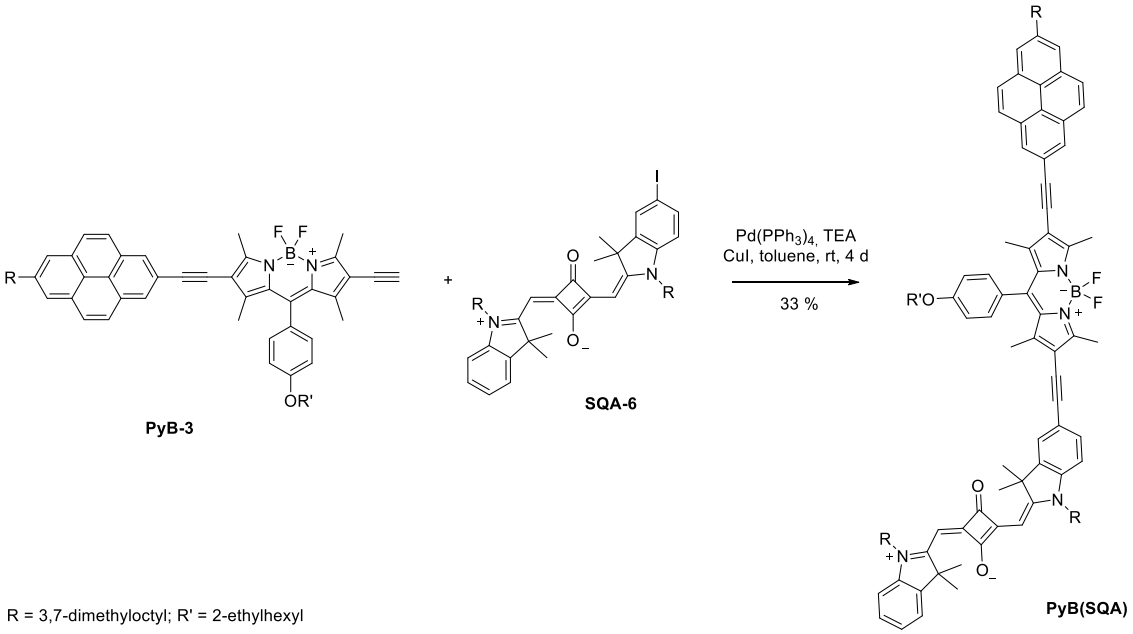

Scheme 30 Synthesis of **PyB(SQA)** from **PyB-3**.

Synthesis of Py(SQB)B

For the **Py(SQB)B** synthesis two pathways using two different heterodimers as coupling partners in the *Sonogashira* reaction are possible. First, the synthesis using **B(SQB)** as an intermediate product was tried.

Synthesis of **B(SQB)**

To synthesise **B_2SQB-3** it was necessary to add the alkynylated bodipy stepwise, but the reaction control *via* mass spectrometry showed that it is possible to stop the reaction at the mono coupled product. This assumption proved to be true and the reaction also works quite efficient at larger scales without yielding high amounts of the symmetric triad as side product (see Scheme 31). The product was roughly purified using GPC in $CHCl_3$ but small impurities were still present. Nevertheless this was enough to subject the mono coupled product to a test reaction for the coupling to yield the asymmetric triad.

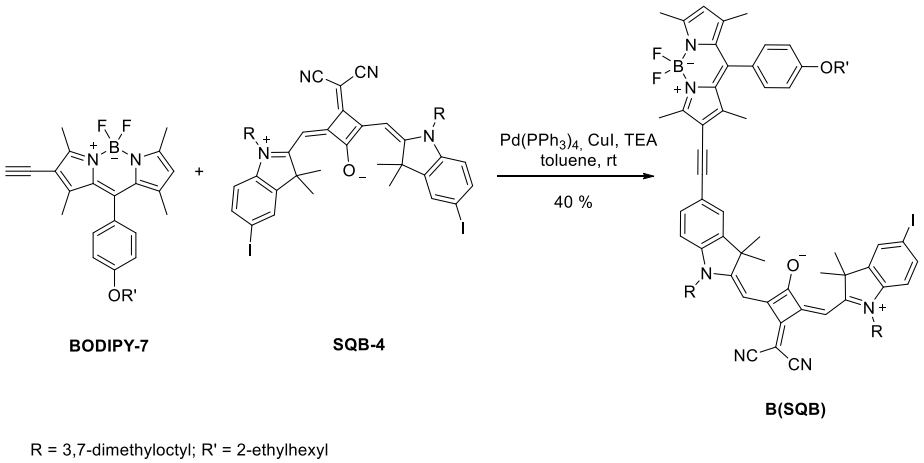

Scheme 31 Synthesis of **B(SQB)**.

Synthesis of **Py(SQB)B** Starting from **B(SQB)**

For the final synthesis of the asymmetrical triad using the **B(SQB)** heterodimer two catalytic systems were tested (see Scheme 32).

Table 13 Tested conditions for the synthesis of **Py(SQB)B**.

	catalyst/ligand	base	solvent	T/t	product
I[154]	$Pd(PPh_3)_4$	TEA	toluene	rt/7 h	**Py(SQB)B**
II[154]	$Pd(PPh_3)_4$	TEA	toluene	40 °C/1 d	**Py(SQB)B**
III[120, 140]	$Pd(C_6H_5CN)_2Cl_2/P^tBu_3$	DIPA	dioxane	60 °C/1 d	**Py-1, BODIPY-1**

With the $Pd(C_6H_5CN)_2Cl_2$[120, 140] catalyst no reaction took place and only decomposed starting material remained in the mixture (see Table 13, condition III). Using the $Pd(PPh_3)_4$ catalyst,[154] the asymmetrical triad **Py(SQB)B** was formed at rt and at 40 °C (see Table 13, condition I and II), but another main product under these conditions was a mono coupled product consisting of pyrene and squaraine (see Figure 67). This could be a hint, that the formed dye conjugate is instable under these conditions and breaks into smaller parts. Nevertheless these conditions led to the best result.

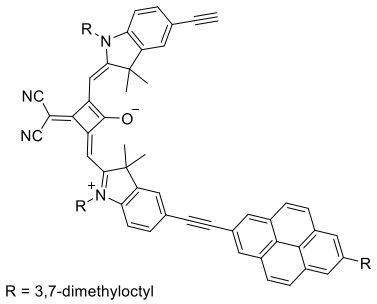

Figure 67 Side product under the coupling conditions I+II from Table 13.

The purification of the product is aggravated as it is not stable on silica for a longer period of time. Thus instead of coulumn chromatography the crude product is directly subjected to purification *via* GPC in $CHCl_3$ to separate the desired triad from the decomposed parts. Unfortunately it was not possible to get rid of all the impurities despite the vast amount of solvents that were tried for percepitation and recrystallisation. The product proved to be too unstable to be purified completely. Therefore the second pathway including the synthesis of the **PySQB** heterodimer was pursued (see Scheme 32).

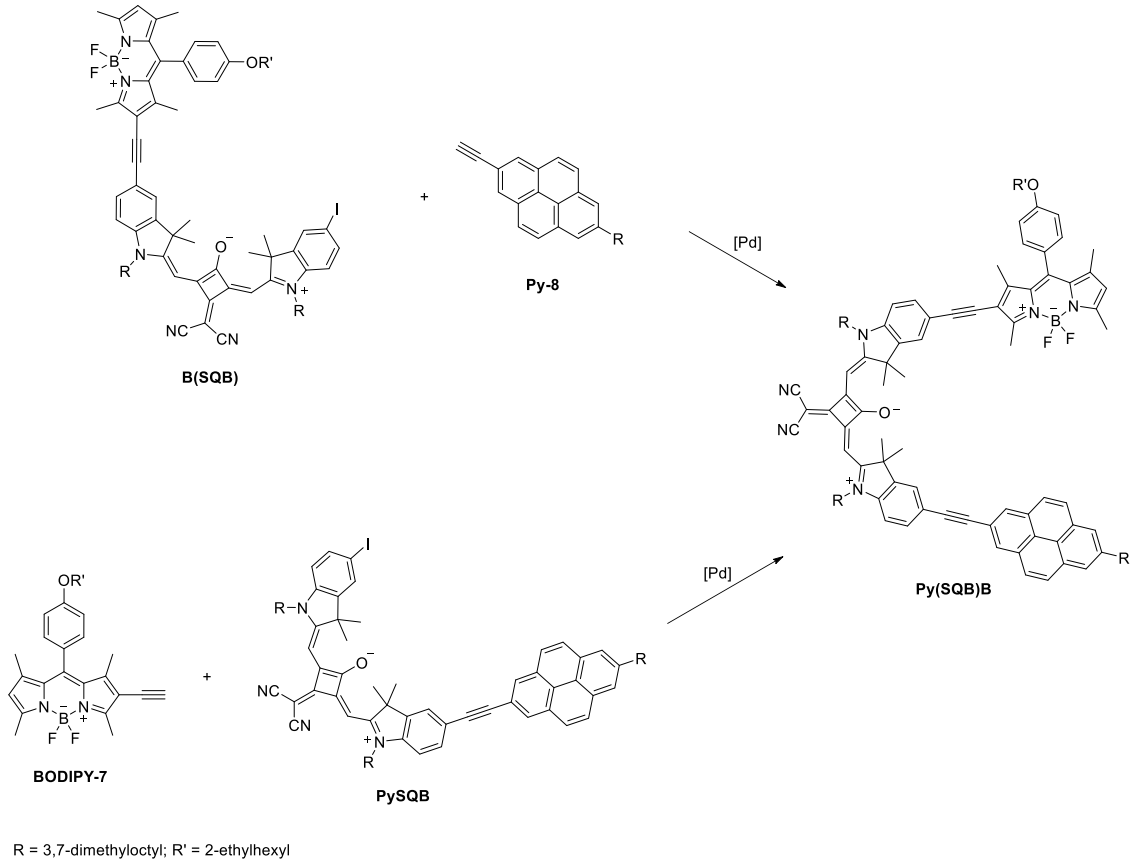

Scheme 32 Synthetic pathways to get to the asymmetrical triad **Py(SQB)B**.

Synthesis of **PySQB**

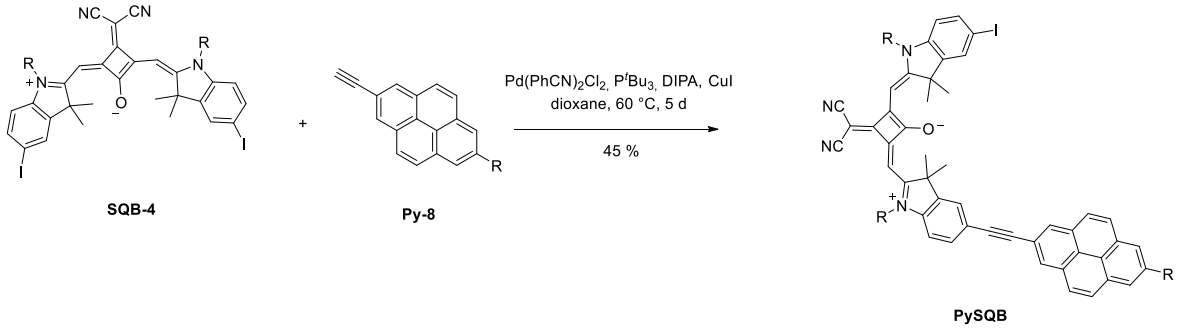

R = 3,7-dimethyloctyl

Scheme 33 Synthesis of the heterodimer **PySQB**.

Several conditions were tested in order to synthesise **PySQB** and a summary of these can be found in Table 14.

To synthesise **PySQB** the $Pd(PPh_3)_4$ catalyst[154] proved to be too reactive and led only to the symmetrical product **Py_2SQB** (see Table 14, condition I). As the $Pd(C_6H_5CN)_2Cl_2$ catalyst[120, 140] was succesfully applied in the synthesis of **Py_2SQB** and is less reactive than $Pd(PPh_3)_4$ it was tested next. In order to reduce the symmetrical substitution, a dilution principle apparatus [138] was used (see Table 14, condition II). As the iodinated squaraine **SQB-6** is not stable under higher temperatures and no appropriate solvent with a low boiling point was found, the reaction was tried under reduced pressure. Unfortunatly only traces of product could be detected. Therefore the same catalytic system was tried without the dilution principle apparatus and instead only a high excess of squaraine was used (see Table 14, conition III). This worked quite well leading almost exclusivly to the asymmetrical heterodimer (see Scheme 33). After a crude work-up this product was used for a test reaction for connecting to the bodipy chromophore.

Table 14 Synthesis of the **PySQB** heterodimer.

	catalyst./ligand	base	solvent	T/t	product
I[154]	$Pd(PPh_3)_4$	TEA	toluene	rt/1 d	**Py_2SQB**
II[120, 140]	$Pd(C_6H_5CN)_2Cl_2$/ P^tBu_3	DIPA	dioxane	60 °C/6 h	**PySQB** (traces)[a]
III	$Pd(C_6H_5CN)_2Cl_2$/ P^tBu_3	DIPA	dioxane	60 °C/6 d	**PySQB**

[a] reaction was carried out under reduced pressure.

Attempted *Sonogashira* Couplings Starting from **Py(SQB)**

Unfortunately in all cases where **Py(SQB)** served as the coupling partner, there was no desired product found but on the contrary symmetrical **Py_2SQB** was detected (see Table 15, conditions I–IV). The starting material was tested again in case that this was just an impurity coming from the previous reaction, which could not be confirmed. Also only very small amounts of remaining bodipy were found. Afterall it could not be concluded what happened under these reaction conditions.

Table 15 Attempted synthesis of **Py(SQB)B** starting from the **PySQB** heterodimer.

	catalyst/ligand	base	solvent	T/t	product
I[154]	$Pd(PPh_3)_4$	TEA	toluene	rt/1 d	**Py_2SQB**
II[154]	$Pd(PPh_3)_4$	TEA	toluene	40 °C/1 d	**Py_2SQB**
III[120, 140]	$Pd(C_6H_5CN)_2Cl_2$/ P^tBu_3	DIPA	dioxane	60 °C/1 d	**Py_2SQB**
IV[173]	$Pd(MeCN)_2Cl_2$/ XPhos	DIPA	dioxane	60 °C/1 d	**Py_2SQB**

5.3.2 Conclusion

Even if all three desired asymmetrical triads could be synthesised by *Sonogashira* couplings, the purification failed in all cases due to instability of the products. Nevertheless the synthetic insights from this study could be applied in the next chapter to yield the pentades.

5.4 Pentades

As the asymmetrical triads were decomposed during the purification process (see Chapter 5.3.1), a solution which would allow to still study the energy transfer in such a chromophoric array was searched for.

As the symmetric dye conjugates were easily purified and showed no signs of decomposition, an additional substitution of the triads, leading again to a symmetrical compound might improve the stability of the chromophoric array. Therefore the synthesis of the two pentades **$(PyB)_2$SQA** and **$(PyB)_2$SQB** was envisaged. The synthesis follows the same approach as for the asymmetrical conjugates, just with one symmetric squaraine subjected to the coupling process with the prior synthesised **PyB-3**. Additionally, a third triad with a different chromophoric order was tried to synthesise. To obtain **$(PySQB)_2$B** two coupling reactions to the final pentamer are possible, either using the **$(SQB)_2$B-3** or **PySQB**. Both have the disadvantage of terminal iodinated squaraines incommon and therefore dehalogenation could be a problem in these couplings. The conditions for obtaining **$(SQB)_2$B-3** were already optimised in the test reactions for the synthesis of the symmetrical triad **$(SQB)_2$B-4** and showed different degrees of dehalogenation, being very sensitive to time, temperature and solvent polartity. On the other hand in the synthesis of **PySQB** the symmetrical product **Py_2SQB** is formed as a side product in the coupling procedure, but here the separation of the two compounds should be possible, while the dehalogenated and the halogenated triads are an inseparable mixture.

5.4.1 Synthesis of $(PyB)_2$SQB and $(PyB)_2$SQA[1]

The coupling of **PyB-3** with the mono iodinated cisoid squaraine **SQB-6** did not lead to the desired asymmetric triad, while the reaction of the transoid squaraine **SQA-6** with **PyB-3** proved to be successful without formation of noticable sideproducts. Therefore one might expect the coupling of **PyB-3** with the symmetrical squaraine **SQB-4** not being promisingly, but it turned out that the symmetrical and asymmetrical squaraine act quite differently in these *Sonogashira* reactions (see Chapters 5.2.2 and 5.3.1). Using the $Pd(PPh_3)_4$ catalyst[154] to couple the symmetric *cis*-squaraine **SQB-4** with the **PyB-3** heterodimer led to the desired pentad, with only small amounts of asymmetrical **PyB(SQB)** (see Scheme 34). Nevertheless the purification failed again due to decomposition of the product.

[1]Some results presented in this chapter were worked out in a Bachelor thesis under the supervision of N. Auerhammer: N. Jordan, Bachelor Thesis, Julius-Maximilians-Universität (Würzburg), 2017.

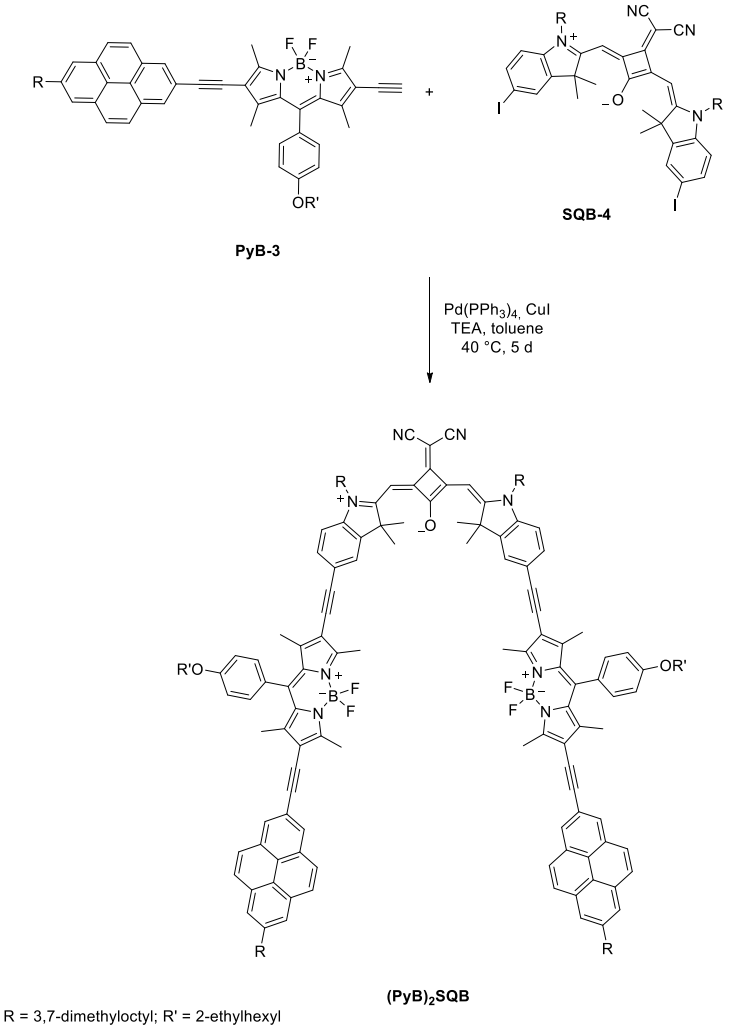

Scheme 34 Synthesis of **$(PyB)_2$SQB**.

The synthesis of **$(PyB)_2$SQA** was again straightforward, just like the corresponding triad (see Scheme 35). The coupling of **PyB-3** with **SQA-4** using the $Pd(PPh_3)_4$ catalyst was tried at rt and 40 °C, whereof the later one was the more promising, as at room temperature a lot of mono coupled product was still present in the reaction mixture. When the reaction was carried out on a larger scale, the almost pure product already precipitated from aceton after column filtration, but all further attempts to remove the last impurities failed. Again the instability of the product not only on silica but apparently also in a lot of solvents led to complete degeneration of the product to indole and **PyB-3**.

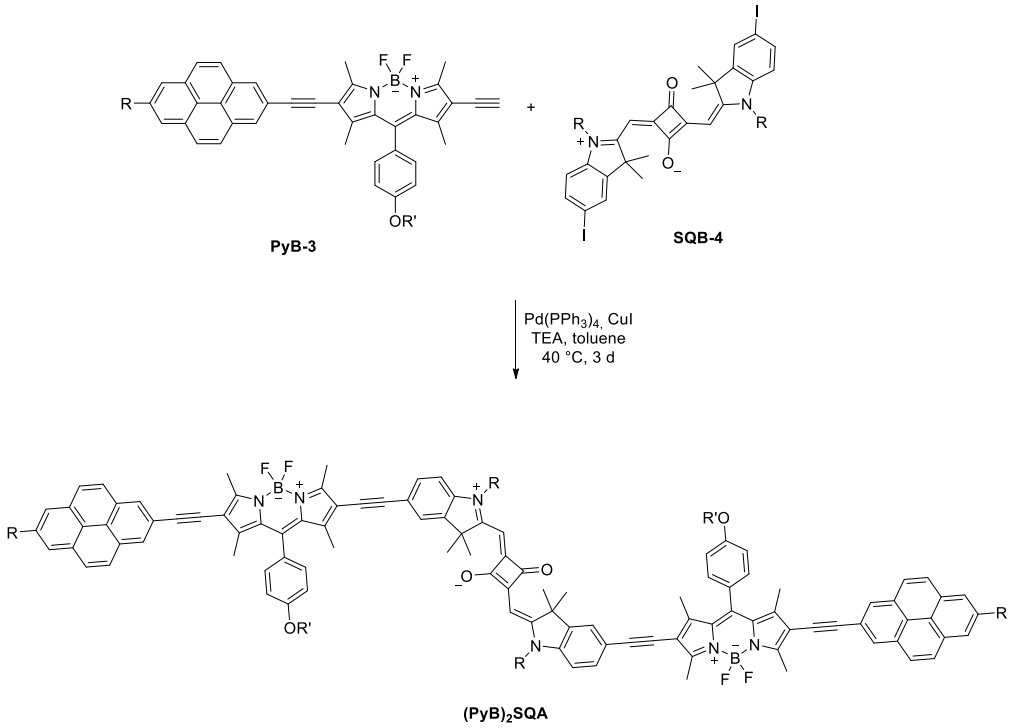

Scheme 35 Synthesis of **(PyB)$_2$SQA**.

5.4.2 Synthesis of $(PySQB)_2B$

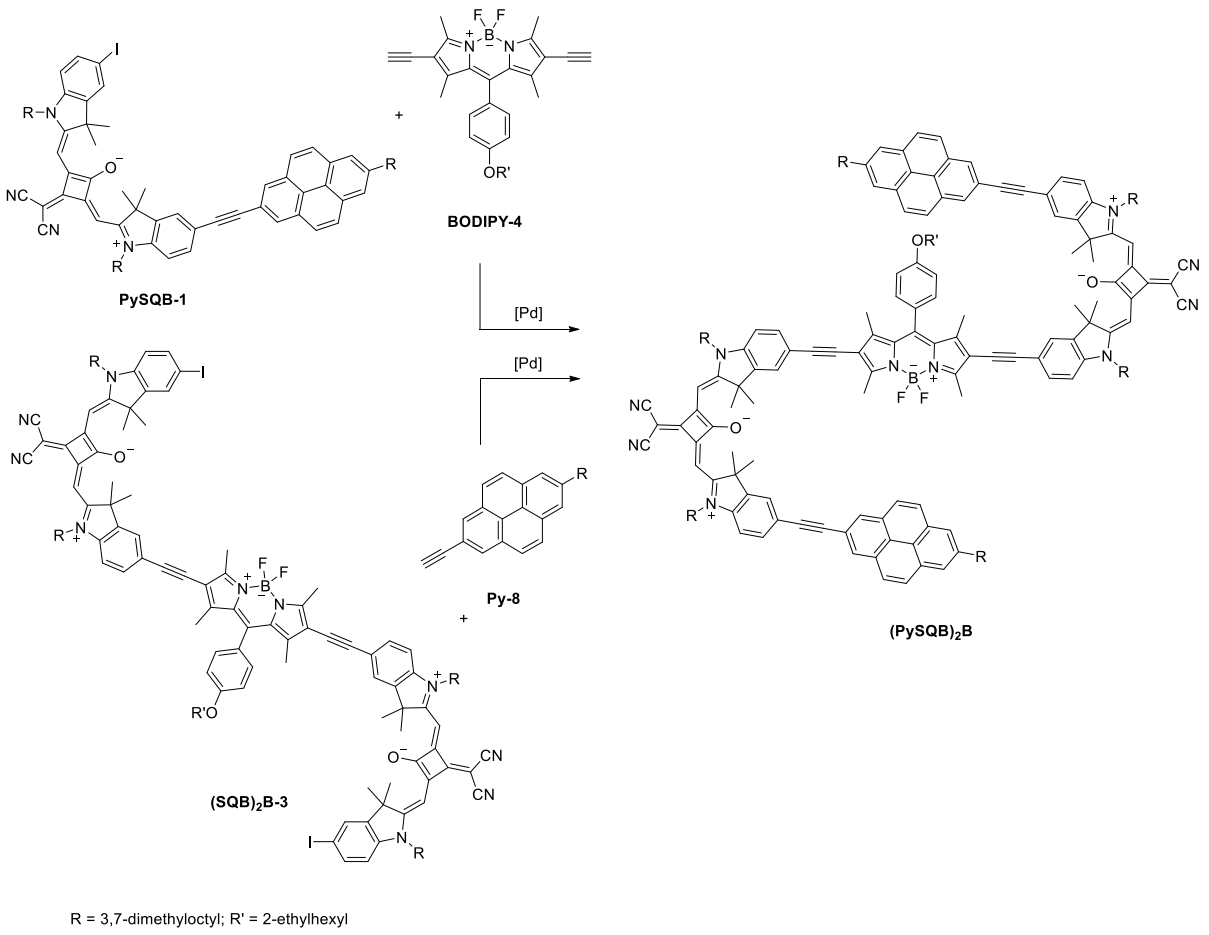

Scheme 36 The two different routes tried for the synthesis of **$(PySQB)_2B$**.

Attempted Sonogashira Couplings Starting from PySQB

The first attempt to synthesise (**$(PySQB)_2B$** was to use the **PySQB-1** heterodimer with the alkynylated bodipy **BODIPY-4** (see Schema 35) but the same problem as already discussed for **Py(SQB)B** was occuring (see Chapter 5.3.1). No product was formed under any of the tested conditions (see Table 16, condtion I and II) and only **Py_2SQB** could be detected.

Attempted Sonogashira Couplings Starting from $(SQB)_2B$-3

Based on the test reactions carried out for the symmetric conjugate **$(SQB)_2B$-4** suitable conditions for the synthesis of **$(SQB)_2B$-3** were figured out that lead to moderate yields and keept deiodination at a low level. In order to minimise this side reaction in the coupling of **$(SQB)_2B$-3** to **Py-8** the same reaction conditions, using the highly reactive $Pd(PPh_3)_4$ catalyst

in toluene,[154] were also applied for this coupling and were successful. At room temperature only mono coupled product was present (see Table 16, conditions III), thus a second testrun at 40 °C was tried to figure out if the higher temperature would only lead to faster deiodination instead of a faster conversion. It turned out that **$(SQB)_2$B-4** was formed and no mono coupled product was remaining in the mixture at 40 °C so that afterall the conversion at higher temperature was better (see Table 16, condition IV). Therefore **$(PySQB)_2$B** was synthesised by coupling of **$(SQB)_2$B-3** with **Py-8** using the $Pd(PPh_3)_4$ catalyst at 40 °C. The purification proved to be quite problematic, since the pentad is just as the asymmetric triads unstable on silica, and GPC in $CHCl_3$ alone was not sufficient to yield pure product. Several attempts to precipitate or recrystallise the product were made, but the purity either didn't improve or the product was degenerating, so that only indole and **PyB-3** could be regained.

Table 16 Reaction conditions tested to synthesise **$(PySQB)_2$B**.

	halogen	alkyne	catalyst/ligand	base	solvent	T/ t	product
I[154]	**PySQB**	**BODIPY-4**	$Pd(PPh_3)_4$	TEA	toluene	rt/1 d	**Py_2SQB**
II[120, 140]	**PySQB**	**BODIPY-4**	$Pd(C_6H_5CN)_2Cl_2/P^tBu_3$	DIPA	toluene	60 °C/1 d	**Py_2SQB**
III[154]	**$(SQB)_2$B-3**	**Py-8**	$Pd(PPh_3)_4$	TEA	toluene	rt/2 d	**$(SQB)_2$B-4**
IV[154]	**$(SQB)_2$B-3**	**Py-8**	$Pd(PPh_3)_4$	TEA	toluene	40 °C/1 d	**$(SQB)_2$B-4**, **$(PySQB)_2$B**

5.5 Bridged Squaraines[1]

The interaction of coupled squaraines has been extensively studied and mostly the excitonic coupling model could sucessfully be applied.[112, 116, 122, 134, 149, 195, 196] Previously a trimer, dimer and monomer were compared, where excitonic coupling theory could be used to explain the observed spectral features. Due to rotational freedom around the connecting biaryl axis different conformers were adapted, leading to complex spectra.[134] To exclude rotational conformers another dimer with a *trans*-indolenine-squaraine moiety, this time connected *via* a fixed non-conjugated bridge was synthesised to disrupt electronic communication. A single sharp fluorescence signal and a high extinction coefficient should be the consequence.

5.5.1 Synthesis

Retrosynthetic Analysis

For the synthesis of the rigidly-bridged squaraine **SQA$_2$Anth** the semisquaraine **Ind-7** and the diindole **Ind-8** are needed as precoursers (see Scheme 37). The synthesis of the later is already discussed in Chapter 5.3.1 and will therefore be skipped here.

To get to the diindole **Ind-8** two different synthetic pathways were evolved. Starting from the unsubstituted anthracene has the disadvantage that selective substitution in the desired *trans*-positions could be difficult and an inseparable mixture of regioisomers could be formed. Once the substitution product is succesfully isolated standard protocols should lead to the desired diindole **Ind-8**. To exclude the problem of different regio-isomers a pathway starting from 2,6-diaminoanthraquinone was envisaged, where after reduction of the keto groups, the methylation is the crucial step.

[1]Some results presented in this chapter were worked out in a Bachelor thesis under the supervision of N. Auerhammer: S. Ricker, Bachelor Thesis, Julius-Maximilians-Universität (Würzburg), 2017.

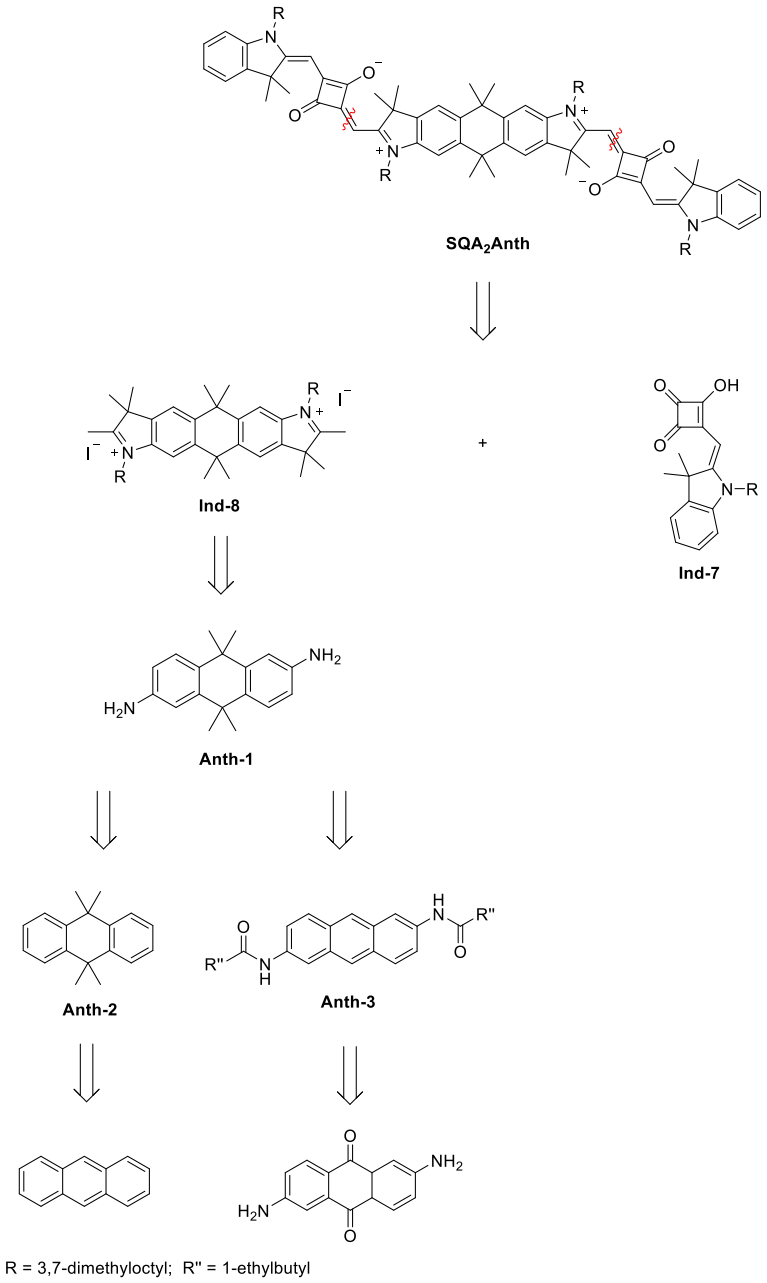

Scheme 37 Retrosynthetic analysis of the bridged squaraine **SQA$_2$Anth**.

Attempt of the Synthesis of the Diindole Ind-8 from 2,6-Diaminoanthraquinone

The first two steps follow the literature prodcedure of *Revell et al.*[197] and start with the protection of the amino function by using an acyl group (see Scheme 38).

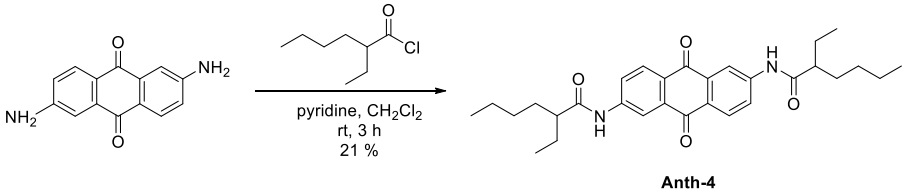

Scheme 38 Protection of the amino group in 2,6-diaminoanthraquinone through acylation.

This protection is not only favourable for the later planed methylation, but also only then the reduction with sodium borhydride is possible (see Scheme 39).[197]

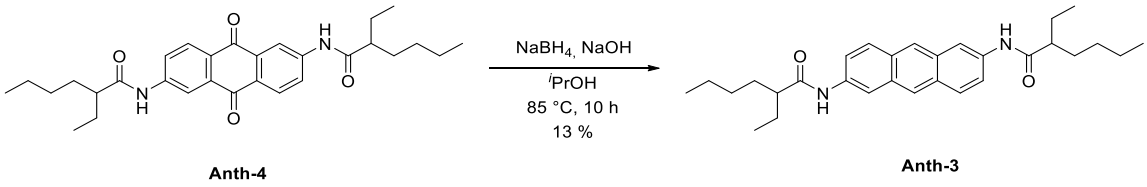

Scheme 39 Reduction of **Anth-4** with sodium borohydride to **Anth-3**.

The low yields in the first two steps are explainable by the poor solubility of the compounds **Anth-3** and **Anth-4** in all common organic solvents. Recrystallisation was only possible in dimethylsulfoxid.

To insert the methyl groups at the center ring, a protocol that describes the synthesis of 9,9,10,10-tetramethyl-9,10-dihydroanthracence was applied.[198] The methylation of substituted anthracene (**Anth-3**) did not yield any product, but the high solubility of the crude mixture indicates that not only starting material was regained (see Scheme 40). Neither mass nor NMR spectrometry could clarify what exactly happened during the reaction. As all compounds in this synthetic route showed very poor solubility, no futher effort was put into the methylation of **Anth-3**, but the second pathway to yield the indole was tried.

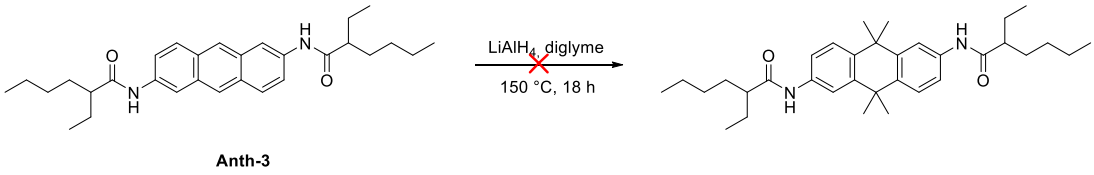

Scheme 40 Attempted methylation of **Anth-3**.

Synthesis of the Diindole Ind-8 Starting from Anthracene

The first step, the methylation of the anthracene core, is literature known[198] and the product could be isolated in moderate yields (see Scheme 41).

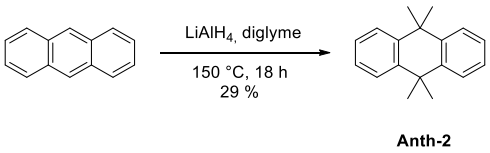

Scheme 41 Methylation of anthracene to **Anth-2**.

The nitration of the methylated anthracene (**Anth-2**) was thought of being the most problematic step in this protocol due to the formation of regioisomers. The *cis*-isomer to the desired product is indeed formed, but the separation of the two was easily accomplished by simple recrystallisation from toluene/diethylether (see Scheme 42).[199]

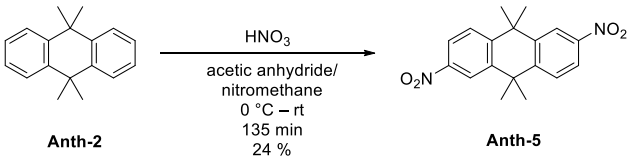

Scheme 42 Nitration of **Anth-2** to **Anth-5**.

D'Arasmo et al.[200] describe a synthesis were they were able to convert the nitro group to the hydrazine through simple substitution. This method was tried first as it would entail one step less compared to the standard reduction to the amin and subsequently diazotisation to the hydrazine. Unfortunately in this case the substitution failed and only starting material was recovered (see Scheme 43).

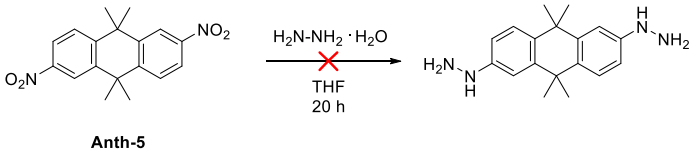

Anth-5

Scheme 43 Attempted conversion of **Anth-5** through substitution of the nitro-group.

The reduction of the nitro to the amino group was therefore the next step. First tin(II)chlorid was used as reducing agent.[201] The reaction seemed to proceed without any problems (see Scheme 44), but complete separation of the tin(II)chlorid from the desired product was not possible due to very similar solubility.

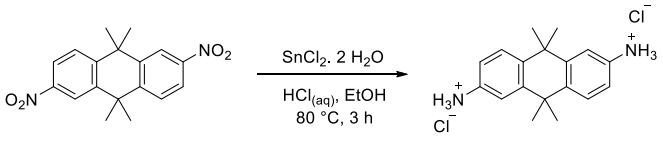

Anth-5 Anth-6

Scheme 44 Reduction of the nitro group of **Anth-5** to the corresponding amine **Anth-6** with tin(II)chloride.

Therefore a different protocol was used, with iron as reducing agent instead (see Scheme 45).[202] Here **Anth-1** could successfully be isolated in 43 % yield.

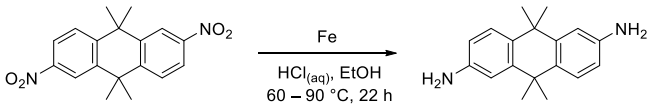

Anth-5 Anth-1

Scheme 45 Reduction of the nitro group to the corresponding amine **Anth-1** with iron.

For the synthesis of the indole **Ind-7** a procedure which was already successfully applied to diamines was used.[203] The amin **Anth-1** is treated with 3-bromo-3-methyl-butanone, which is attacked by the nucleophilic amin group (see Scheme 46). This first step seemed to lead to the desired product, so the reaction mixture was subjected to further conversion without purification.

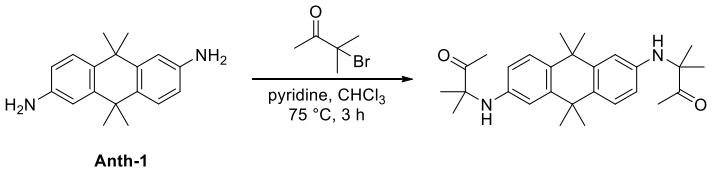

Anth-1

Scheme 46 Conversion of **Anth-1** with 3-bromo-3-methyl-butanone.

Unfortunately the cyclisation did not yield any product and the NMR spectra showed that only starting material was present in the crude reaction mixture (see Scheme 47).

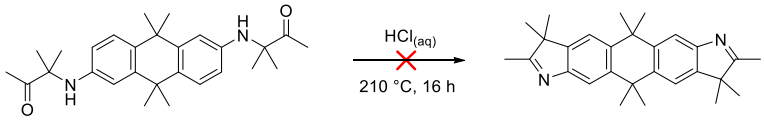

Ind-9

Scheme 47 Attempted cyclisation to get to the diindole **Ind-9**.

A very common way of synthesising an indole is *via* the diazonium salt using the *Fischer* indole synthesis. The reaction is often performed in a one pot synthesis where after diazotisation, the product is directly subdued to cyclisation with the ketone.[204] This route was tried in a first attempt to synthesise **Ind-9** but no product could be isolated (see Scheme 48).

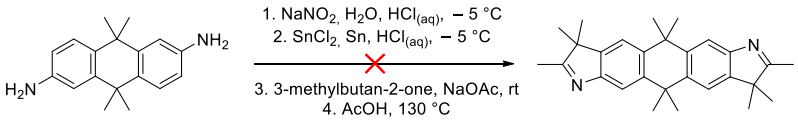

Anth-1 **Ind-9**

Scheme 48 One pot procedure to synthesise the diindole **Ind-9** from the diamine **Anth-1**.

To see whether the formation of the diazonium salt or the conversion to the indole was the problem, the reaction was split into two parts and after the first step the diazonium salt **Anth-6** was isolated and characterised (see Scheme 49). So it could be concluded that the second step was the problem. The conditions used in the one pot synthesis were tried again and proved to form no product.

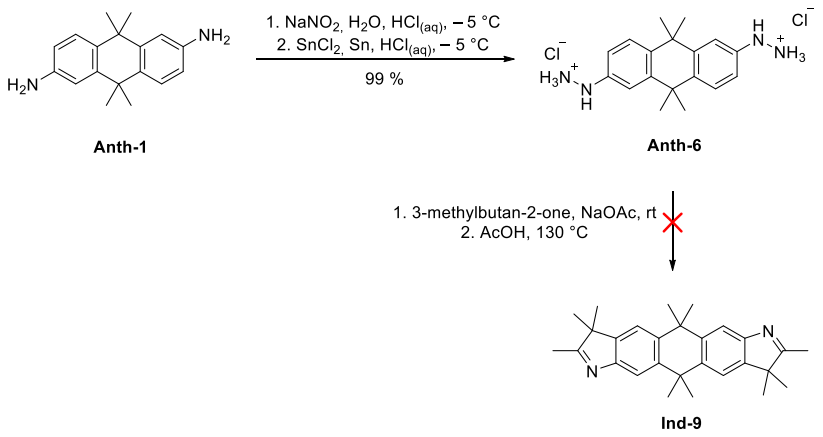

Scheme 49 Stepwise conversion of **Anth-1** to the diazonium salt and subsequently cyclisation.

An in depth literature research revealed several similar protocols, only using lower temperatures and no base.[205-207] The application of likewise conditions yielded the desired product, but also the *cis*-regioisomer in an almost 1:1 ratio (see Scheme 50). Before trying to separate this mixture, a further test reaction was carried out to try to get the desired *trans*-indole **Ind-9** as the major product.

Scheme 50 Mild conditions tested to yield the diindole Ind-**9**.

When the reaction was performed in the microwave oven at 160 °C[208] still some undesired side product was formed, but prevailing the diindole **Ind-9** (see Scheme 51). The separation of the regioisomer from the product was unproblematic due to different solubility. Simple extraction already led to sufficiently pure product.

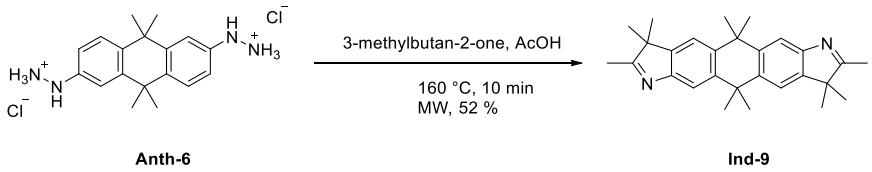

Anth-6 **Ind-9**

Scheme 51 Conversion of **Anth-6** to the diindole **Ind-9** under microwave irradiation.

The diindole Ind-9 could be alkylated with 1-iodo-3,7-dimethyloctane using the same conditions as for the other indoles in this work[134] and resulted in good yields of 65 % (see Scheme 52).

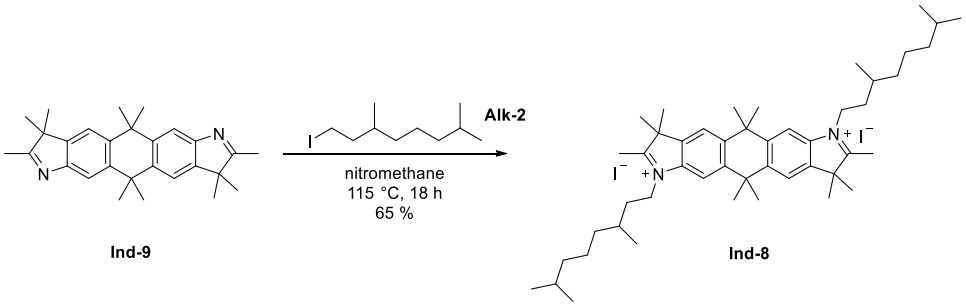

Ind-9 **Ind-8**

Scheme 52 Alkylation of the diiondole Ind-**9** to **Ind-8**.

Synthesis of the Bridged Trans-Squaraine

The final reaction to synthesise the bridged *trans*-squaraine **SQA$_2$Anth** was performed following standard procedures for indolenine squaraines[169] and led to 40 % yield after GPC purification (see Scheme 53).

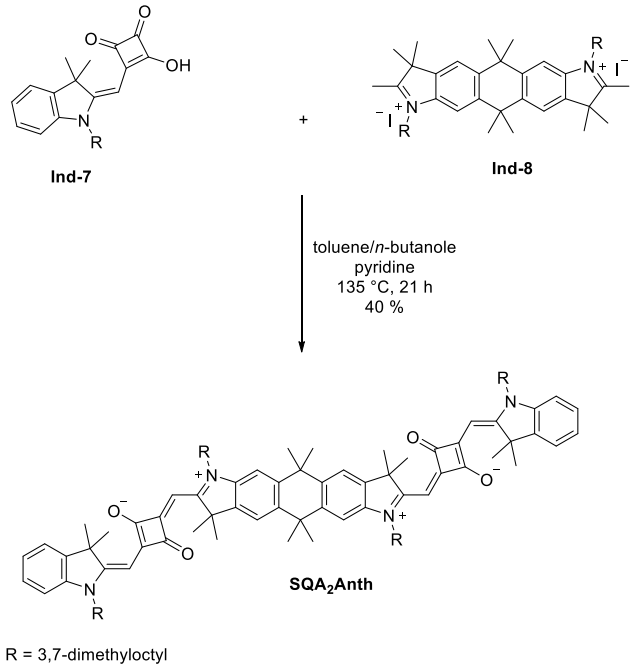

Scheme 53 Synthesis of **SQA$_2$Anth**.

5.5.2 Absorption Spectroscopy

As the goal of this study is the investigation of the influence of the ridgid bridge onto the spectroscopic properties of the coupled *trans*-squaraine, two additional molecules will be discussed regarding their photophysics (see Figure 68). Both molecules used for comparison were measured in toluene and an in depth discussion of their photophysics was already described elsewhere.[134] The summarised spectral properties can be found in Table 18.

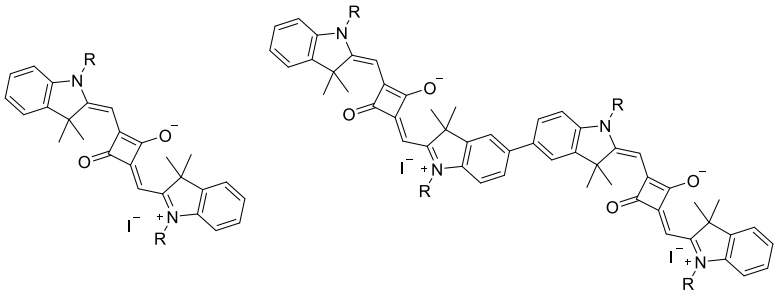

Figure 68 Monomer **SQA** and flexible dimer **SQA-SQA** used for comparison in the following section.

The squaraine monomer **SQA** shows the typical squaraine absorption spectrum with one narrow major band, a steep rise on the red edge and a shoulder on the high energy side (see Figure 69). This maximum can be assigned to the HOMO-LUMO transition and shows a high extinction coefficient of 367100 M^{-1} cm^{-1}. The dimer **SQA-SQA** shows a profound red shift of about 1050 cm^{-1} compared to the monomer and two side peaks on the blue side of the spectrum.

To explain these spectral properties exciton theory can be applied. For a head-to-tail dimer of C_2 symmetry two excitonic transitions are predicted. In the flexible **SQA-SQA** dimer two ideal conformations are possible: a bent and a linear structure. While in the linear case only the lower exciton transition is allowed, for the bent dimer the transition-dipole moment of both transitions are unequal to zero and hence allowed. The side peaks in the absorption spectrum are due to these different conformations that can be adapted by the molecule through rotation around the biaryl axis. The rotation around the central axis leads to one strong allowed excitonic transition with a vibrational shoulder and a weaker allowed high energy transiton.[134] The absorption spectrum of **SQA_2Anth** was recorded in $CHCl_3$ and toluene and shows no strong solvatochromism, with the main absorption band being shifted about 80 cm^{-1} to higher energies when moving from toluene to $CHCl_3$ (see Figure 69). The shape of the spectrum resembles the typical squaraine absorption band shape with the

strong main absorption at 15000 cm^{-1} (667 nm) and the vibrational shoulder at higher wavenumbers.

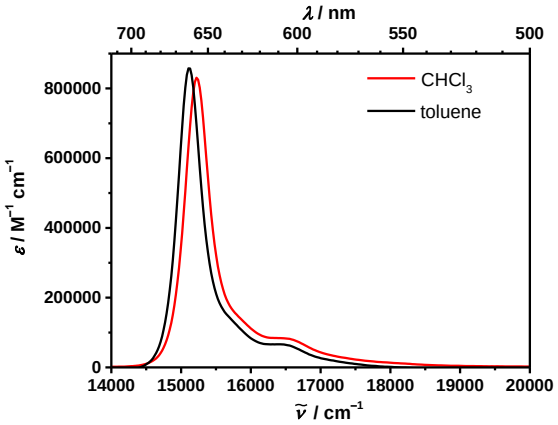

Figure 69 Absorption spectra of **SQA_2Anth** in different solvents at rt.

A comparison of the ridgid dimer **SQA_2Anth** to the monomer shows that the extinction coefficient with 858000 M^{-1} cm^{-1} in toluene is more than twice the number of the monomeric extinction (see Figure 70). The flexible bridged **SQA-SQA** on the other hand has a distinctly lower extinction coefficient of 467800 M^{-1} cm^{-1}. The side peaks arising from the rotational conformers of the flexible dimer are missing in the spectrum of the stiff dimer **SQA_2Anth**, as rotation is prevented through the ridgid bridge, so that only one excitonic transition is allowed. The red shift of **SQA_2Anth** compared to the monomer **SQA** is with 410 cm^{-1} smaller than the one of **SQA-SQA**. Assuming an excitonic coupled dimer, the red shift is due to the *Davidov*-splitting and can be seen as a measure of the coupling strength.[18] In the case where both exciton states are allowed, as it is true for **SQA-SQA** the coupling constant *J* can be calculated from the difference between the two bands.[134] Despite the lacking of the second exciton band in the spectrum of **SQA_2Anth** a comparison of the red shift of the two different dimers give a rough estimation of the coupling. As a consequence the coupling in **SQA_2Anth** has to be much weaker than in the more bathochromically shifted dimer **SQA-SQA**. A more decisive evidence for the presence of excitonic coupling is the exchange narrowing.[20] A comparison of the full width at half maximum (fwhm) of the absorption spectra depicts a reduction of the band width from 550 cm^{-1} of the monomer **SQA** to 400 cm^{-1} of **SQA_2Anth**.

The squared transition moments of **SQA_2Anth** and **SQA-SQA** (see Table 18) are the same in the experimental uncertainty and show nearly additive behaviour compared to the monomer. Therefore they follow the *Thomas-Reiche-Kuhn* sum rule[26] and hence no other electronic transitions should contribute to the excitonic manifold.

For a better comparison of the coupling strength of the molecules **SQA-SQA** and **SQA$_2$Anth**, it is helpful to calculate the maximum coupling of the squaraines in **SQA$_2$Anth** with equation (43):

$$V = \frac{1}{4\pi\varepsilon_0 hc}\frac{|\mu_A||\mu_B|}{r^3}(cos\theta_{AB} - 3cos\theta_A cos\theta_B) \qquad (43)$$

With h being Planck's constant, ε_0 the permittivity and c the speed of light. μ_A and μ_B denote the transition dipole-moments of the coupled molecules which are the same in the case of a homodimer. In the linear orientation of the chromophores the angle between the transition moments of the chromophores (θ_{AB}) gets zero. The distance *r* between the transition dipole-moments of the molecules is 18.734 10^{-10} m and was caculated by DFT computations.[1] The angle between the the transition dipole-moments and the connecting vector is estimated to 0°. Using the value of the transition moment of **SQA** in toluene (μ_{abs} = 11.27 D) an upper limit for the coupling of the chromophores in the **SQA$_2$Anth** molecule can be evaluated as 195 cm^{-1}. This value is about a quarter ot the coupling strength, that was calculated by using exciton theory for **SQA-SQA** (J = 800 cm^{-1}). This result is in good agreement with the spectral shifts, which also suggest a stronger coupling in **SQA-SQA** than in **SQA$_2$Anth**.

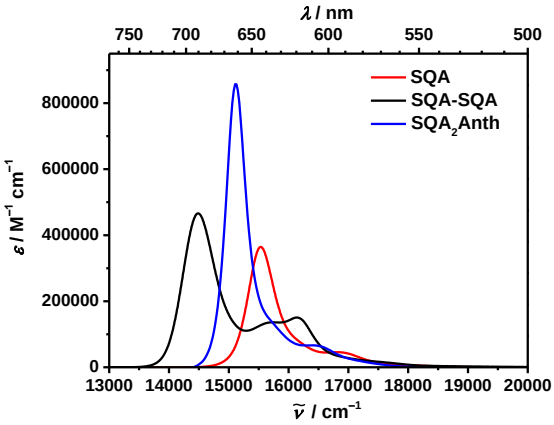

Figure 70 Absorption spectrum of **SQA$_2$Anth** in comparison to the monomer **SQA** and the dimer **SQA-SQA** in toluene at rt.

[1]The DFT calculations were carried out by *Dr. Marco Holzapfel*.

5.5.3 Fluorescence Spectroscopy

The fluorescence spectrum of **SQA$_2$Anth** in toluene is dominated by one narrow band at 15000 cm^{-1} (667 nm) from which a small vibrational shoulder emerges at its red side of the spectrum (see Figure 71a). The *Stokes* shift is with 120 cm^{-1} very low (see Figure 71b), as it is common for squaraines[209] and furthermore the fluorescence is only emitted from the lowest excitonic state, hence following Kasha's rule.[210] **SQA$_2$Anth** only shows a minor solvent dependency with a shift of about 80 cm^{-1} when changing the solvent from toluene to $CHCl_3$.

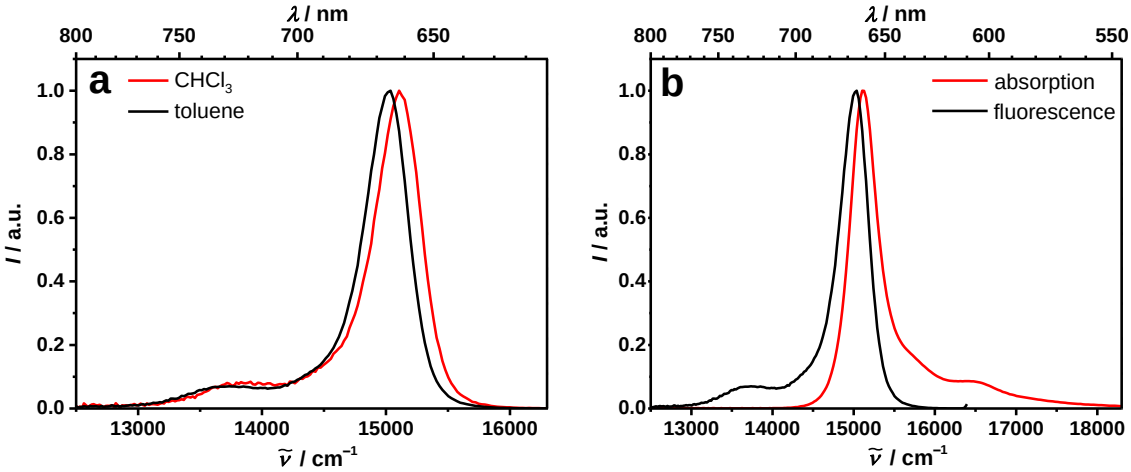

Figure 71 Fluorescence spectra of **SQA$_2$Anth** in different solvents (**a**) and absorption (red) and fluorescence spectra (black) in toluene at rt (**b**).

A comparison with the monomer **SQA** and the flexible dimer **SQA-SQA** shows the same red shift as discussed for the absorption spectra before (see Figure 72). Furthermore the exchange narrowing is for **SQA$_2$Anth** again easy to recognise in the spectrum.

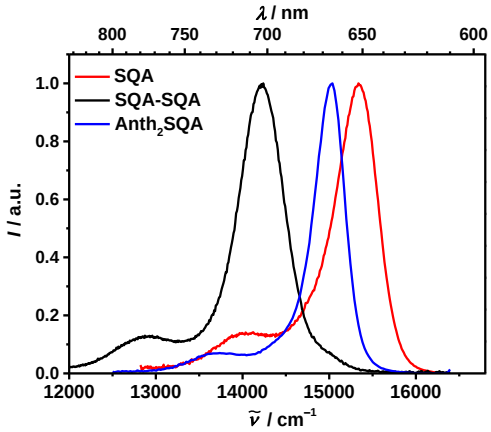

Figure 72 Fluorescence of **SQA$_2$Anth** and **SQA-SQA** in comparison with their parent compound **SQA** in toluene at rt.

For an excited excitonic state delocalised over two monomers a ratio of $\sqrt{2}$ of the fwhm's of the monomer and the dimer is expected (see Table 17).[20] This is pretty close to the values gathered from **SQA$_2$Anth** for the absorption (1.38) as well as the fluorescence (1.36). For **SQA-SQA** on the other hand the calculation gives smaller values for both spectra (absorption: 0.86; fluorescence 0.90), which is due to the rotational freedom and hence hindered delocalisation of the excitonic state in some conformers. The quantum yield of **SQA$_2$Anth** is slightly higher than the monomer and similar to the value of the **SQA-SQA** dimer in toluene. The fluorescence enhancement of both can be explained by a superradiant effect.[20]

Table 17 Full width at half maximum (fwhm) of fluorescence and absorption bands

	$fwhm_{abs}/cm^{-1}$	$fwhm_{fl}/cm^{-1}$
SQA	550	570
SQA-SQA	640	630
SQA$_2$Anth	400	420

Lifetime measurements of **SQA$_2$Anth** in toluene at excitation wavenumbers of 15300 cm^{-1} (654 nm) lead to multiexponential decays. Different fitting routines and functions, such as a *Kohlrausch* equation and a distribution analysis were applied to yield the average lifetime. But still every fit for **SQA$_2$Anth** resulted in two lifetimes, which is also reported for **SQA**.[134]

Therefore the average lifetime was calculated by using:

$$\bar{\tau} = \frac{a_1\tau_1^2+a_2\tau_2^2}{a_1\tau_1+a_2\tau_2} \quad (46)$$

With a_x being the amplitude and τ_x the lifetime.[41]

With the average lifetimes the transition moment of the fluorescence μ_{fls} can be calculated using the *Strickler-Berg*-equation (eq. (45)).

Table 18 Absorption maxima ($\tilde{\upsilon}_{abs}$), extinction coefficients (ε), absorption transition moments (μ^2_{abs}), fluorescence maxima ($\tilde{\upsilon}_{fl}$), fluorescence transition moments (μ^2_{fls}) and fluorescence quantum yields (ϕ_{fl}) of the bridged squaraines and their parent chromophore **SQA** in various solvents at rt.

	solvent	$\tilde{\upsilon}_{abs}$ /cm^{-1} (nm)	ε/M^{-1} cm^{-1}	μ^2_{abs}/D^2	$\tilde{\upsilon}_{fl}$ /cm^{-1} (nm)	μ^2_{fls}/D^2	ϕ_{fl}
SQA	$CHCl_3$	15700 (637)	347000	129	15500 (645)	121	0.53
	toluene	15500 (645)	365000	127	15300 (654)	114	0.62
SQA-SQA	$CHCl_3$	14600 (685)	454000	274	14300 (699)	172	0.42
	toluene	14500 (690)	466000	248	14200 (704)	172	0.82
SQA$_2$Anth	$CHCl_3$	15200 (658)	831000	243	15100 (662)		
	toluene	15100 (662)	858000	231	15000 (667)	177	0.71

The squared transition moment of **SQA-SQA** is less than additive and of similar value as for **SQA$_2$Anth** (see Table 18). The squared transition moments can be explained by a microscopic superradiant effect i.e. collective emission from delocalised states of chromophore aggregates.[20, 116] For an excitonically coupled dimer one would expect to get half of the radiant lifetime of the monomer. **SQA$_2$Anth** actually shows with 1.87 ns a smaller radiant lifetime than the monomer with 2.65 ns, but is not as small as the expected value (see Table 19). For **SQA-SQA** the radiant lifetime is of similar value than the monomer. Given that the oscillator strength in **SQA-SQA** is spread between several allowed exciton states due to different conformers, a similar lifetime for the flexibel dimer compared to **SQA** is reasonable. However **SQA$_2$Anth** shows only one excitonic transition which should collect all the oscillator strength and hence lead to the shortest radiative lifetime of the three chromophores. The long radiant lifetime could arise from small deviations of **SQA$_2$Anth** from a perfectly delocalised system.

5.5.4 Transient Absorption Measurements[1]

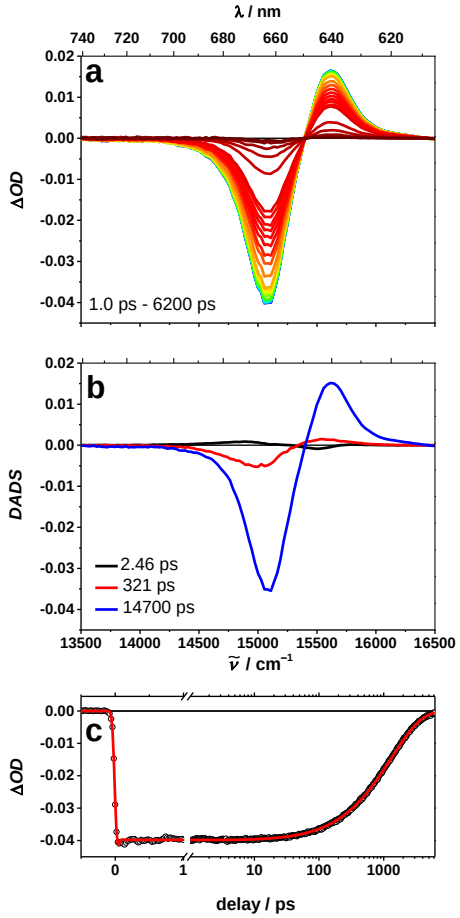

Figure 73 Transient absorption spectra of **SQA$_2$Anth** in toluene at rt after excitation at 15150 cm^{-1} (660 nm) (magic angle measurement, for transient absorption spectra of perpendicular and parallel oriented probe and pump pulse see appendix) (**a**) and decay associated difference spectra of transient absorption measurement under magic angle resulting from a combined global fit (**b**) (for decay associated difference spectra of parallel and perpendicular orientation of probe and pump see appendix); time scans of transient absorption spectra of **SQA$_2$Anth** after excitation at 15150 cm^{-1} (660 nm) at different wavenumbers (**c**). Transient absorption spectra and time scans were corrected for chirp and scattered light. Early spectra are given in blue, later spectra in red.

SQA$_2$Anth was investigated by fs-transient absorption spectroscopy in toluene to get a detailed understanding of the excited state properties. First the spectral features of **SQA$_2$Anth** will be described, afterwards a discussion of the observed time development in comparison with **SQA-SQA** will follow. **SQA$_2$Anth** was excited at its maximum at 15150 cm^{-1} (660 nm) and probed with white light between 20800–12500 cm^{-1} (481–800 nm). The gained transient maps were analysed by a global fit resulting in decay associated spectra (DADS).

[1]The femtosecond spectroscopy measurements were performed and analysed by *Dr. Henning Marciniak.*

The transient map measured under magic angle orientation of probe and pump pulse, DADS and selected time scans are given in Figure 73. The spectral features of **SQA$_2$Anth** will be compared with the TA of **SQA-SQA** after excitation at the lower energetic band (14500 cm^{-1} (690 nm)).

Table 19 Time-resolved optical data of bridged squaraine dimers and their parent chromophore in toluene and $CHCl_3$ at rt.

	solvent	τ/ns (TCSPC)[a]	$\bar{\tau}$/ns[b]	T_{rad} ($\bar{\tau}/\phi_{fl}$)/ns	τ/ps (TA)[e]
SQA	$CHCl_3$	0.26 (0.40) 1.47 (0.60)	1.33	2.51	
	toluene	0.07 (0.03) 0.20 (0.10) 1.72 (0.87))	1.64[c] (0.97)	2.65	
SQA-SQA	$CHCl_3$	0.05 (-0.34) 0.11 (0.13) 0.96 (0.53)	0.94[c] (0.99)	2.2	
	toluene	0.15 (-0.31) 0.25 (0.30) 1.82 (0.39)	1.67[d]	2.69	0.28 17 660 1900
SQA$_2$Anth	$CHCl_3$	0.54 (0.04) 1.28 (0.96)	1.27		
	toluene	0.37 (0.02) 1.34 (0.98)	1.33	1.87	1.73[f] (2.26)[g] 410[f] (300)[g] 1500[f] (1460)[g]

[a] Multiexponential fit of fluorescence decay measured by TSCPC, excitation at 15250 cm^{-1} (656 nm). Amplitudes are given in brackets. [b] Average lifetime calculated with eq. (46). [c] Lifetime acquired by stretched exponential analysis. Stretching exponent in brackets. [d] Lifetimes acquired by distribution analysis. [e] Globally fitted lifetimes of DADS measured by TA at a pump wavenumber of 15100 cm^{-1} (662 nm).[f] Lifetimes resulting from combined fit. [g] Lifetimes resulting from fitting with eq. (48a) and eq. (48b).

The excitation of **SQA$_2$Anth** at 15100 cm^{-1} (662 nm) gives rise to a dominant negative signal at 15100 cm^{-1} (662 nm), which is composed of a GSB and a SE, shifted to lower energies. Overall three ESA are observable in the spectra. The most intense ESA is formed at 15600 cm^{-1} (641 nm) associated with the absorption into the two exciton state. This normally forbidden transition is visible in the TA due to subsequent absorption of two photons, using the one-exciton state as intermediate state.[20] The other two ESA, of which one is broad (17500–22000 cm^{-1} (571–455 nm)) and one narrower (16600–17400 cm^{-1} (602–575 nm)) are much less intense and show similar time development. All bands decay on the same

three decay times of which the fastest one with 2.46 ps can be attributed to relaxation of the excited state as it shows the typical wave-like behaviour in the DADS expected for a spectral shift. The time constant of 321 ps is in the time range where rotational diffusion of squaraines can be observed.[149] The change of signs of the associated amplitude in the TA measurements under parallel and perpendicular alignment of the pump and probe pulse is often interpreted as a hint towards rotational diffiusion. However, as this time constant is also necessary for fitting the data from the magic angle measurement accurately this would exclude rotational diffusion as explanation of this spectral component. Therefore no definite interpretation can be given at this stage, but further investigations are necessary to clarify the origin of this time constant. The time constant of 1.47 ns is in reasonable agreement with the 1.34 ns of the TCSPC measurement and therefore corresponds to the ground state recovery.

The transient spectra of **SQA-SQA** shows very similar features[134] to the one described above when excited at the lowest exciton band except for an additional shift of GSB, SE and ESA due to stronger coupling that was already observed in the steady-state measurements. The chromophores show similar lifetimes, but one additional time is needed for fitting the transient map of **SQA-SQA**, due to more rotational freedom.

5.5.5 Time-Dependent Anisotropy Measurements.[1]

To confirm the assignment of the rotational diffusion time constant in the TA measurement anisotropy decay curves were recorded. The anisotropy shows high values close to 0.4 at all selected wavelengths and decays after 933 ps, 922 ps and 827 ps to zero (see Figure 74). This depolarisation should be due to the rotational diffusion of the molecules as other depolarising processes such as energy transfer can be excluded.

[1]The femtosecond spectroscopy measurements were performed and analysed by *Dr. Henning Marciniak.*

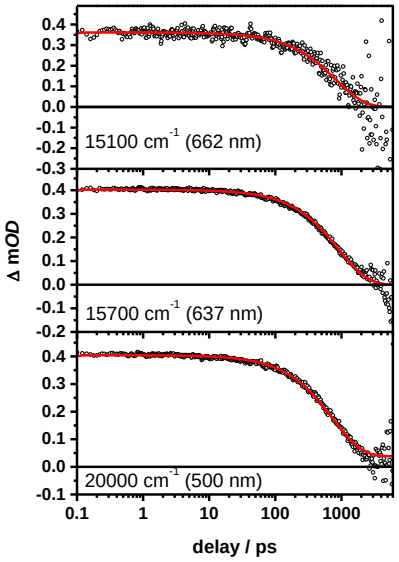

Figure 74 Time-dependent anisotropy decay at selected wavenumbers in toluene at rt.

Nevertheless the time constant gathered from the combined fit of the TA absorption (see appendix) with 410 ps and the decay of the anisotropy are quite different. A separate fite of the magic angle measurement results in three time constants as well with 320 ps being closest to the one from the combined fit. The rotational diffusion should be excluded in magic angle measurements and this makes the assumption obvious that the pump and probe alignment was imperfect. To test this assumption some basic correlations of the intensities measured at different orientations and the anisotropy are need to be considered.[211] The time-dependent intensities and the anisotropy $r(t)$ can be writen as:

$$I_{\mathrm{MA}}(t) = \frac{I_{\parallel}(t)+2I_{\perp}(t)}{3} \tag{47a}$$

$$I_{\parallel}(t) = 3I_{\mathrm{MA}}(t) - 2I_{\perp}(t) \tag{47b}$$

$$I_{\perp}(t) = \frac{3I_{\mathrm{MA}}(t)+I_{\parallel}(t)}{2} \tag{47c}$$

$$r(\mathrm{t}) = \frac{\mathrm{I}_{\parallel}(\mathrm{t})-\mathrm{I}_{\perp}(\mathrm{t})}{\mathrm{I}_{\parallel}(\mathrm{t})+2\mathrm{I}_{\perp}(\mathrm{t})} = \frac{\mathrm{I}_{\parallel}(\mathrm{t})+\mathrm{I}_{\perp}(\mathrm{t})}{\mathrm{I}(\mathrm{t})} \tag{47d}$$

Where $I_{\parallel}(t)$ is the time-dependent intensity at parallel orientation of the pump and probe pulse and $I_{\perp}(t)$ the time-dependent intensity at perpendicular orientation of the pump and probe pulse. $I_{\mathrm{MA}}(t)$ is the intensity at a magic angel orientation between the two pulses. If the time traces and the anisotropy are fitted with equation (47d) all data can be reproduced if the intensity $I_{\mathrm{MA}}(t)$ is scaled by a factor of 0.89. This means that the orientation of pump and probe was aligned correctly and only the intensity ratio was improper. Therefore a closer look at the relation of the rotational diffiusion time gathered from the anisotropy measurements

and the time constants of the DADS is necessary. For parallel and perpendicular orientation of probe and pump pulse the following relations are valid:

$$I_{\parallel}(t) = \frac{I_{\mathrm{MA}}(t)}{3}(1 + 2r(t)) \tag{48a}$$

$$I_{\perp}(t) = \frac{I_{\mathrm{MA}}(t)}{3}(1 - \mathrm{r}(t)) \tag{48b}$$

For the **SQA$_2$Anth** dimer the intensity decay and the time-dependent anisotropy are proportional to:

$$I_{\mathrm{MA}}(t) \sim a_1\, \mathrm{e}^{-t/\tau_1} + a_2 \mathrm{e}^{-t/\tau_2} \tag{49a}$$

$$I_{\parallel}(t) \sim b_1\, \mathrm{e}^{-t/\tau_1} + b_2 \mathrm{e}^{-t/\tau_2} + b_3 \mathrm{e}^{-t/\tau_3} \tag{49b}$$

$$I_{\perp}(t) \sim c_1\, \mathrm{e}^{-t/\tau_1} + c_2 \mathrm{e}^{-t/\tau_2} + c_3 \mathrm{e}^{-t/\tau_3} \tag{49c}$$

$$r(t) \sim \mathrm{e}^{-t/\theta} \tag{49d}$$

Where a_i, b_i and c_i are preexponential factors and τ_i is the time constant resulting from the global fit of the TA spectra and θ is the rotational diffusion time given by the anisotropy decay.

τ_1 can be neglected because $\tau_1 <<< \tau_2, \tau_3$ and the use of equation (48a), $I_{\parallel}(t)$ and $r(t)$ leads to:

$$I_{\parallel}(t) \sim \frac{1}{3}\, b_2 \mathrm{e}^{-t/\tau_2} + \frac{2}{3} b_2 e^{-t/\tau_2} \cdot \mathrm{e}^{-t/\theta}$$

$$\sim \frac{1}{3}\, b_2 \mathrm{e}^{-t/\tau_2} + \frac{2}{3} b_2 \mathrm{e}^{-t\left(\frac{\theta+\tau_2}{\tau_2 \cdot \theta}\right)} \tag{50}$$

If the rotational diffiussion from the anisotropy of 933 ps and the decay time τ_2 = 1500 ps from the transient anisotropy are used to calculate the third time constant 575 ps are yielded, which is larger than the measured decay time of 410 ps from the TA. If on the other hand the time constant of 410 ps is implemented in equation (50) and the rotational diffiusion time is calculated, a time constant of 564 ps is resulting which is distinctly smaller than 933 ps. This leads to the conculsion that the 321 ps from the fit of the TA of the magic angle measurements is occuring due to a biexponential decay of the molecule. In the combined fit of the transient spectra of the different angluar orientations of probe and pump pulse, no distinguistion between the time constants of 933 ps and 321 ps is possible, leading to the intermediate value of 410 ps. If equation (48a) and (48b) are used for fitting all three measurements, a good agreement (see Figure 75) with the beforehand discussed fit

resulting for the MA measurement alone is yielded and the assignment of the time constants is varified.

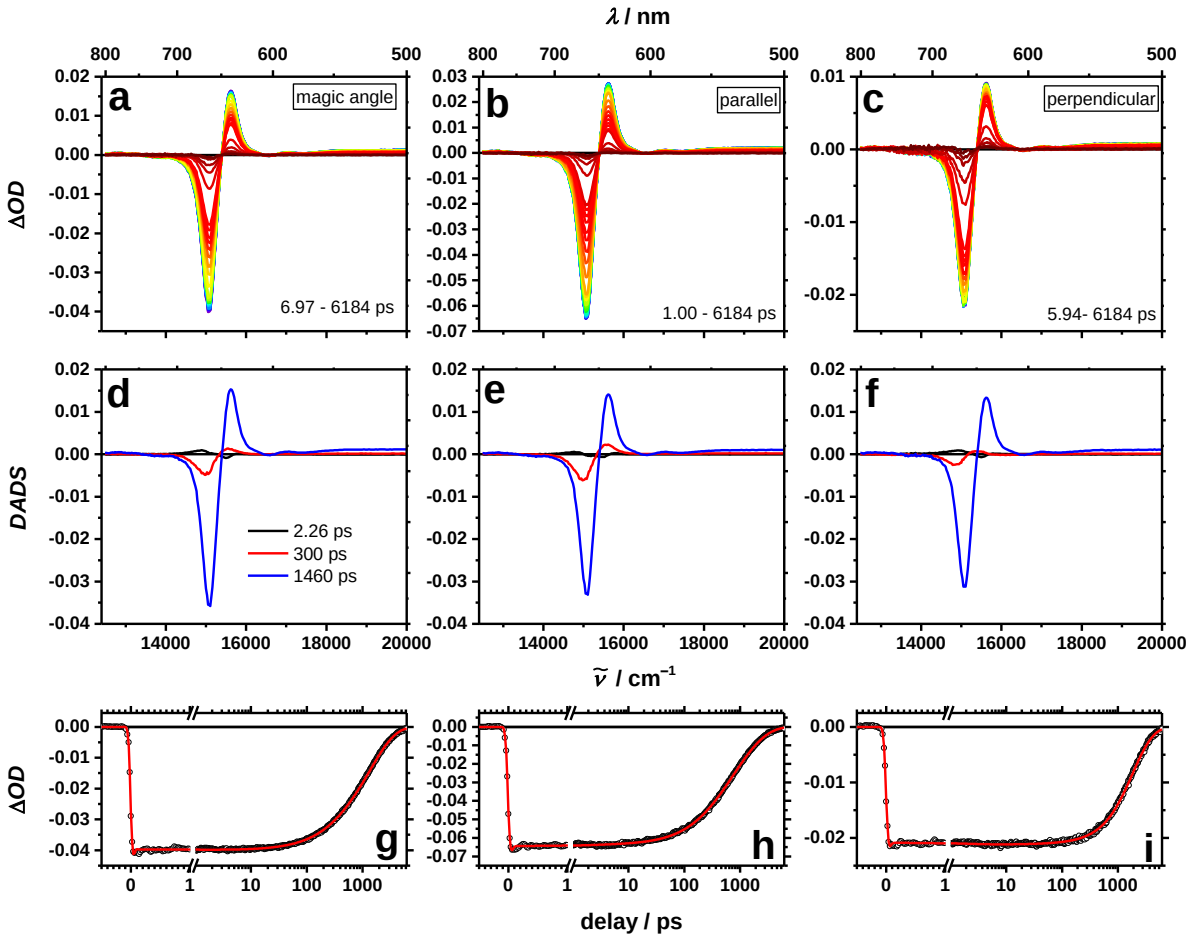

Figure 75 Transient absorption spectra of **SQA$_2$Anth** in toluene at rt after excitation at 15150 cm^{-1} (660 nm) (**a**-**c**) and decay associated spectra resulting from the TA spectra at different orientations of probe and pump pulse by using equations (47a) and (47b). (**d**-**f**) Time scans of transient absorption spectra of **SQA$_2$Anth** after excitation at 15150 cm^{-1} (660 nm) at different orientations of pump and probe pulse (**g**-**i**). Transient absorption spectra and time scans were corrected for chirp and scattered light. Early spectra are given in blue, later spectra in red.

5.5.6 Conclusion

The influence of a rigidly non-conjugated bridge on the excitonic coupling of a *trans*-squaraine was studied. It could be proven that the stiffening of the molecule and hence lack of rotational freedom lead to a perfectly delocalised excitonic state with a high extinction coefficient. Because of the rigid bridge no rotational conformers can be adapted and therefore the excitonic state is delocalised over the whole molecule, resulting in the exchange narrowing of the fluorescence band and absorption bands. Nevertheless the red shift of the absorption spectrum is drasticly reduced due to weaker excitonic coupling strength in comparison to the more flexible **SQA-SQA**. The lower coupling in **SQA$_2$Anth** is most likely due to the non-conjugating spacer between the two squaraine units, minimising electronic interaction. The TA measurements revealed a biexponential decay, with a short time constant of 321 ps that lies in the same magnitude as rotational diffiusion of the molecules.

6 Summary

In this work the energy transfer and excitonic coupling in different chromophore arrangements were investigated. A difference in the coupling strength was introduced by varring the connecting unit and the spacial orientation relative to each other.

The synthesis of the 2,7-substituted pyrene compounds could be optimised and good yields of **HAB 1** and **HAB 2** and small amounts of **HAB 2** could be achieved by cobalt-catalysed trimerisation or *Diels Alder* reaction in the end. Absorption and fluorescence spectra reveal strong intramolecular interactions between the pyrene molecules in the **HAB 1**. Excitation spectra recorded at the high and low energy fluorescence suggest the contribution of two components to the spectra. One being similar to the ground state aggregate and a second species similar to undisturbed pyrene. All these feature can be accounted to two different fluorescent states which are due to electronical decoupling in the excited state. Due to the strong intramolecular coupling already in the ground state of the molecule, no energy transfer could be studied, as the six pyrene units cannot be seen as separate spectroscopic entities between which energy could be transferred.

In the second part of this thesis dye conjugates of different size and alignment were synthesised to study the interaction of the transition-dipole moments. Therefore a systematic investigation of *Sonogashira* conditions was performed in order to obtain good yields of the desired compounds and keep dehalogenation at a minimum level. Nevertheless only the symmetrical triads could be purified as the asymmeric triads and pentades proved to decompose during purification.

The pyrene containing triads **Py_2B** and **Py_2SQB** show small interactions already in the ground state represented by red shifts of the spectra and a broadening of the bands. Nevertheless, these interactions are in the weak coupling regime and energy transfer between the constituents is possible. On the contrary in the TA spectra it is obvious that always the whole triad, at least to some extend is excited. To question if the excitation of the high energy state is deactivated by energy transfer or rather IC in a superchromophore could not be distinguished in the course of this work. At present additional time-dependent calculations of the dynamics are in progress to get a deeper understanding of the photophysical processes taking place in the triads.

The dye conjugates **B_2SQB-3** and **$(SQB)_2B$-4** can be assigned to the strong interaction range and hence are describable by exciton theory. The transition-dipole moments proved to be more than additive and increase for both compounds from absorption to fluorescence. This can be explained by an enhancement of the coupling in the relaxed excited state

compared to the absorption into the Franck-Condon state due to a more steep potential energy surface in the excited state and hence smaller fluctuations.

In the last part of this thesis the influence of disrupting electronical communication by implementing a rigid non-conjugated bridge in a bichromophoric *trans*-squaraine system was tested. While the flexible linked squaraines show complex spectra due to different conformers the **SQA$_2$Anth** compound is rigified and no rotation is possible. This change in flexibility is represented in the steady-state spectra where just one main absorption and fluorescence band is present due to a single allowed excitonic state. The system proves to own an excited state that is completely delocalised over the whole molecule.

7 Experimental

7.1 Materials and Methods

Microwave oven

- µCHEMIST microPREP Microwave Digestion System ATC-FO 300 from MLS (Leutkirch, Germany)

For the temperature control of the microwave reactions a fibre optical thermometer sensor (ATC-FO, 0–270 °C) was used. The reaction temperature is regulated by the sensor by change of the output power (0–1200 W) of the microwave oven. The reaction mixture was placed in a pressure quartz vessel (max. 12 bar) with an adapter for the fibre optical thermometer.

Recycling Gel Permeation Chromatography (GPC)

- JASCO Gel Permeation Chromatography System
  - interface box (LC-NetII ADC)
  - intelligent HPLC pump (PU-2080 plus)
  - inline degasser (DG-2080-53)
  - solvent selection valve unit (LV-2080-03)
  - multi wavelength UV/Vis detector 195–700 nm (UV-2077)
  - software Chrompass (v. 6.1)

Gel permeation chromatography (GPC) was done using two preparative GPC columns (styrene-divinylbenzene-copolymer, 50 and 500 Å, 600 × 20.8 mm) from PSS and a four channel UV/Vis-detector (195–700 nm). The flow rate was 4 ml min^{-1} and the solvent used was HPLC grade $CHCl_3$.

NMR Spectrometry

- Avance III HD 400 FT-Spectrometer (^{1}H: 400.03 MHz, ^{13}C: 100.59 MHz) with a Bruker Ascend magnet
- Avance III HD 600 FT-Spectrometer (^{1}H: 600.43 MHz; ^{13}C: 150.98 MHz) with a Bruker Ascend magnet

The 400 MHz spectrometer runs at 300 K, whereas the 600 MHz spectrometer has different temperatures for each solvent (e.g. 303.6 K for $CDCl_3$ or 293.5 K for CD_2Cl_2). All spectra were recorded in deuterated solvents as indicated (e.g. $CDCl_3$, CD_2Cl_2, methanol-d_4, dimethylsulfoxid-d_6) which were used as received. The solvent signal (^{1}H: $CHCl_3$: δ 7.26 ppm, CH_2Cl_2: δ 5.32 ppm, dimethylsulfoxid: δ 2.50 ppm, methanol: δ 3.31; ^{13}C: $CHCl_3$: δ 77.16 ppm, CH_2Cl_2: δ 53.84 ppm, dimethylsulfoxid: δ 39.52 ppm, methanol: δ 49.00 ppm)[212] was used as internal reference. The chemical shift is given in ppm (δ-scale) against TMS. Coupling constants *J* are quoted in Hertz [Hz]. The multiplicity is named as follows: - (no assignment possible), s (singulet), d (dublet), t (triplet), m (multiplet). NMR-data are listed as follows: chemical shift (multiplicity, coupling constant, number of protons, assignment). For ^{13}C-spectra the following abbreviations are used: C_q (quarternary C-atom), CH (tertiary C-atom), CH_2 (secondary C-atom), CH_3 (primary C-atom). For the assignment of the ^{13}C-signals DEPT-135, HSQC- und HMBC-spectra were used.

Mass Spectrometry

- Bruker Daltonik microTOF focus (high resolution ESI)
- Bruker Daltonik autoflex II (MALDI-TOF)
- Finnigan MAT90 (EI)

Mass spectra were recorded with a Bruker Daltonics autoflex II (MALDI) in positive mode (POS) using a DCTB (*trans*-2-[3-(4-*tert*-butylphenyl)-2-methyl-2-propenylidene]malononitrile) matrix or with a Bruker Daltonic microTOF focus (ESI) or with a Finnigan MAT90 (EI). All mass spectrometry peaks are reported as m/z. For calculation of the respective mass values of the isotopic distribution, the software module “Bruker Daltonics IsotopePattern” from the software Compass 1.1 from Bruker Daltonics GmbH, Bremen was used. EI mass peaks are reported in the following order: m/z (relative intensity, fragmentation).

Absorption Spectroscopy

- JASCO V670 UV/Vis/NIR-Spectrophotometer (software SpectraManager v. 2.08.04)
- Cary Model 5000 UV/Vis/NIR-Spectrometer (software Agilent Cary WinUV Analysis and Bio v.4.2)

All experiments were carried out in 1 cm quartz cuvettes in Uvasol® solvents from Merck at rt. The solvents were used as received. The pure solvent was used as a reference. The compound was measured at various concentrations from 10^{-5}–10^{-7} M to exclude aggregation formation. Silylated quartz cuvettes and silylated volumetric flasks were used to prohibit interaction with the glass surface.[134, 213]

Steady-State Emission Spectroscopy

- Edinburgh Instruments FLS980 fluorescence lifetime spectrometer (software F980 version 1.2.2)
  - 450 W Xenon lamp/PMT (R928P)
  - 450 W Xenon lamp/PMT (HR5509)

All experiments were carried out in 1 cm quartz cuvettes in Uvasol® solvents from Merck. In case of **Py₂(SQB)** a silylated quartz cuvette was used to prohibit interaction with the glass surface.[134, 213] The dissolved samples were purged with argon for 15 min before the measurement. In order to exclude self-absorption, the emission spectra were measured with strongly diluted samples (< 0.05 OD at the excitation wavelength).

The quantum yields were determined using optical dense samples in an integrating sphere and equation (51)

$$\phi_{\mathrm{obs}} = \frac{\int F_{\mathrm{sample}}}{\int E_{\mathrm{solvent}} - \int E_{\mathrm{sample}}} \tag{51}$$

Where ϕ_{obs} is the observed quantum yield, F_{sample} is the luminescence emission spectrum of the sample, E_{sample} is the spectrum of the light used to excite the sample and E_{solvent} is the spectrum of the light used for excitation with only the solvent in the cuvette. The self-absorption of the molecule was taken in account by using equation (52):

$$1 - a = \frac{\int_0^\infty F_{\mathrm{fl}}(\lambda)\,d\lambda}{\int_0^\infty F_{\mathrm{emission}}(\lambda)\,d\lambda} \tag{52}$$

Where the fluorescence spectra of the dilute sample F_{fl} is compared with that of an optical dense sample F_{emission}. Here *a* denotes the self-absorption probability of an emitted photon. Finally equation (53) can be used to determine the quantum efficiency ϕ_{fl} of the sample.[214]

$$\phi_{\mathrm{fl}} = \frac{\phi_{\mathrm{obs}}}{1-\mathrm{a}+\mathrm{a}\times\phi_{\mathrm{obs}}} \tag{53}$$

Excitation spectra were recorded with the same set-up that was used for the emission spectroscopy.

For polarized steady-state emission spectra two measurements were performed. One were the incoming beam was polarised parallel to the emission polariser and one with perpendicular orientation of the polarisers. The sample was diluted in poly-THF (Sigma Aldrich, M = 650 g/mol) and to ensure an even distribution in the cuvette, the sample was heated in a water bath for 2 h. Before starting the measurement, the viscose solution was allowed to cool down to rt.

Time-Dependent Fluorescence-Decay

- Edinburgh Instruments FLS980 fluorescence lifetime spectrometer (software F980 version 1.2.2)
  - 15250 cm^{-1} (656 nm) pulsed Laser Diode/PMT (H10720)
  - 19420 cm^{-1} (515 nm) pulsed Laser Diode/PMT (H10720)
  - 23920 cm^{-1} (418 nm) pulsed Laser Diode/PMT (H10720)
  - 31600 cm^{-1} (316 nm) laser pulsed LED/PMT (H10720)

The samples were prepared similar to the steady state emission experiments and measured under magic angle conditions. The instrument response was determined by using a scatterer solution consisting of colloidal silica in deionised water. Lifetimes were determined by fitting the experimental decay curves with an exponential decay function by deconvolution of the experimental decay with the instrument response function using the FAST software (version 3.4.2).

Femtosecond Spectroscopy[1]

- Newport-Spectra-Physics Solstice one box amplified ultrafast Ti:Sapphire laser system with a fundamental wavenumber of 12500 cm^{-1} (800 nm), a pulse length of 100 fs and a repetition rate of 1 kHz
- Newport-Spectra-Physics TOPAS-C optical parametric amplifier as the source for the pump pulses with a pulse length of 140 fs
- Ultrafast Systems Helios transient absorption spectrometer with a CMOS sensor (1.5 nm intrinsic resolution, 12500–28570 cm^{-1} (350–800 nm) sensitivity range).

Femtosecond Tranisent Absorption Spectroscopy

For measurements of **SQA_2Anth**

All experiments were performed in a flow cell from Starna with an optical path length of 0.2 mm and a micro annular gearpump (HNP Mikrosysteme) at rt. The sample was dissolved in toluene and the optical density was adjusted to ca. 0.27 at the corresponding excitation wavenumber.

Before and after every measurement a steady-state absorption spectra was recorded to exclude degradation in course of the time-resolved experiment.

The output beam from the Solstice amplifier was used as a pulse source for the whole setup. The pump pulse was generated by a noncollinear optical parametric amplifier (NOPA)[215] to achieve output wavelengths near the fundamental wavelength of the laser source (800 nm). The resulting pulse was compressed with a fused silica prism compressor to approximatly 20 fs. A white light continuum between 11800 cm^{-1} (850 nm) and 22000 cm^{-1} (450 nm) was gained by focussing a part of the ouput beam of the Solstice amplifier into a 3 mm saphire plate. The resulting beam, which was polarised horizontally was used as the probe pulse. By using a wire grid polariser (Moxtek) the polarisation axis of the pump pulse was set to magic angle relative to the probe pulse. For anisotropy analysis, two further measurements, where probe and pump pulse polarisation were aligned parallel and perpendicular respectivly, were recorded. The pump pulse (10 nJ, Ø ca. 0.3 mm) and the probe pulse (Ø ca. 0.1 mm) met at an angle of approximatly 6° vertically in the cuvette. The probe pulse was measured by means of an CMOS sensor (Ultrafast Systems, Helios) in the range of 11900 cm^{-1} (840 nm) to 25000 cm^{-1} (400 nm) with an intrinsic resolution von 1.5 nm. To compensate fluctuations

[1]The femtosecond spectroscopy measurements were performed by *Alexander Schmiedel* and *Dr. Henning Marciniak* and the analysis was carried out by *Dr. Marco Holzapfel or Dr. Henning Marciniak*.

of the intensity of the white light continuum, a reference beam was split off and detected with an identical spectrograph. Every second probe pulse was blocked by a mechanical chopper (500 Hz) to measure the ratio of I und I_0. The photoinduced optical change in density can than be calculated by the following equation:

$$\Delta OD = -\log\left(\frac{I(\lambda,\tau)}{I_0(\lambda)}\right) \quad (54)$$

The computer-controlled stage (retro reflector in double pass setup) did set the time difference between pump and probe pulse in 20 fs intervalls from –1 fs to 1 ps and 1 ps to >6 ns in logaritmic steps.

To be able to get an accurate fit from the measured data, stray light and white light despersion (chirp) correction were applied beforehand. To obtain the decay associated spectra (DAS) from the corrected data a global exponential fit was applied.

For measurements of **Py_2B**, **Py_2SQB**, **SQB**, **B_2SQB-3**, **$(SQB)_2B$-4**:

All experiments were performed in quartz cuvettes from Spectrocell (Oreland, PA) with an optical path length of 2 mm equipped with a micro-stirrer to allow stirring during the measurement at rt. All samples were dissolved in the solvent indicated, filtered and degassed for 30 min. The optical density was adjusted to ca. 0.2 at the corresponding excitation wavenumber.

Before and after every measurement a steady-state absorption spectra was recorded to exclude degradation in course of the time-resolved experiment.

The output beam from the Solstice amplifier was split into two parts. One part was focussed onto a vertically oscillating CaF_2 crystal to gain a white light continum between 11800 cm^{-1} (850 nm) and 30300 cm^{-1} (330 nm). The resulting beam, which was polarised horizontally was used as the probe pulse. The second pulse was used to pump an optical parametric amplifier (TOPAS-C) from Light Conversion. The generated pulse acted as pump pulse in the experiment and had a puls length of 140 fs at the appropriate excitation wavenumber. By using a wire grid (Moxtek) the polarisation axis of the pump pulse was set to magic angle relative to the probe pulse. The pump pulse (50 nJ, Ø ca. 0.4 mm) and the probe pulse (Ø ca. 0.1 mm) met at an angle of 6° vertically in the cuvette. The probe pulse was measured by means of an CMOS sensor (Ultrafast Systems, Helios) in the appropriate range with an intrinsic resolution von 1.5 nm. To compensate fluctuations of the intensity of the white light continuum, a reference beam was split off and detected with an identical spectrograph. Every second probe pulse was blocked by a mechanical chopper (500 Hz) to measure the ratio of I und I_0. The photoinduced optical change in dencity can than be calculated by equation (54).

The computer-controlled stage (retro reflector in double pass setup) did set the time difference between pump and probe pulse in 20 fs intervalls from 0 fs to 4 ps and 4 ps to 8 ns in logaritmic steps with a maximum length of 200 ps.

To be able to get an accurate fit with GLOTARAN[216, 217] from the measured data, stray light correction was applied beforehand while white light despersion (chirp) correction is implemented in the the fitting routine. To obtain the evolution associated difference spectra (EADS) or the species associated difference spectra (SADS) from the corrected data a sequential or target model was applied.

Femtosecond Fluorescence-Upconversion Spectroscopy

A commercially available fluorescence upconversion setup (Halcyone from Ultrafast Systems) was used for the measurements. The laser system was the same as for the femtosecond transient absorption spectroscopy. All lenses in the setup had a focal length of 100 mm and a thickness of 1.85 mm. The output beam from the Solstice amplifier was split into two pulses of which one part was used to pump an optical parametric amplifier (TOPAS-C) from Light Conversion to generate the pump pulse. The other part of the output beam was used as the gate pulse (12500 cm^{-1}, 800 nm) which was delayed over a maximum of 3 ns in 20 fs steps from 0 fs to 4 ps and in logarithmic steps from 4 ps to 3 ns with a maximum step size of 80 ps with a computer-controlled linear stage. The pump pulse was focused on the cuvette and the resulting fluorescence and the gate beam were focused on a 0.5 mm BBO type I (**B_2SQB-3**, **Py_2B** (emission at 16000 cm^{-1} (625 nm)) or type II (**(SQB)$_2$B-4**, **Py_2B** (emission at 23500 cm^{-1}(425 nm)), **Py_2SQB**) crystal for frequency upconversion. The upconverted light was focused on the entrance slit of a double monochromator and measured by a PMT detector.

7.2 Synthesis

The reactions were performed in standard glassware and chemicals that were obtained from commercial suppliers were used without further purification if not stated elsewise. For reactions under nitrogen atmosphere, the nitrogen was dried with Sicapent® from Merck, oxygen was removed with a cupric oxide catalyst R3-11 from BASF and standard Schlenk techniques were used.[218] Solvent for oxygen and/or moisture sensitive reactions were freshly distilled under nitrogen from the appropriate dehydrating agent (sodium/benzophenone "ketyl blue" for THF, diphenylether, diglyme and dioxane, sodium for toluene, CaH_2 for CH_2Cl_2 and *n*-butanol, molecular sieve 3 Å for TEA, DIPA and DMF) and sparged with dry nitrogen before use. Flash chromatography[219] was performed on silica gel (Macherey-Nagel "Silica 60 M", 40–63 µm) wet-packed in glass columns.

7.2.1 Reagents

The precursors 2-butoxy-3-(dicyanomethylene)-4-oxocyclobut-1-enolate,[164] 1-iodo-3,7-dimethyloctane[220] (**Alk-2**), 5-bromo-2,3,3-trimethyl-3*H*-indolenine (**Ind-1**), [221] **Ind-2**,[134] **Ind-3**,[134] **Ind-4**,[134] 1-(3,7-dimethyloctyl)-2,3,3-trimethyl-3*H*-indole-1-ium iodine (**Ind-5**),[134] **Ind-6**,[134] **Ind-7**,[134] **SQA-1**,[134] **SQA-5**,[134] **SQB-1**,[122] **SQB-5**,[134] **BODIPY-1**,[154] **BODIPY-2**,[154] **BODIPY-3**,[154] **BODIPY-4**,[154] **BODIPY-5**,[97] **BODIPY-6**[97] and **BODIPY-7**[97] were synthesised according to the procedures given in literature.

7.2.2 General Procedures

General Procedure for the *Sonogashira* Coupling I (GPI); According to Literature[120, 140]

Under a nitrogen atmosphere $Pd(C_6H_5CN)_2Cl_2$ (0.06/0.12/0.13 eq), CuI (0.04/0.08 eq.) and the halogenated compound (1 eq.) were dissolved in degassed dioxane/DMF. The solution was freed from oxygen by bubbling a stream of nitrogen through the mixture. DIPA (1.8–20 eq.), P^tBu_3 (0.13/0.24/0.26 eq) and the alkyne (1–10 eq) were added. After stirring for 1–5 d at 60–85 °C under exclusion of light, the solution was cooled to room temperature. The solvent was removed under reduced pressure and the residue was purified by flash column chromatography. For further purification the residue was precipitated from diethylether/acetonitrile, CH_2Cl_2/hexane or CH_2Cl_2/acetonitrile or recrystallised from acetonitrile.

General Procedure for the *Sonogashira* Coupling II (GPII); According to Literature[152, 154]

The halogenated compound (1 eq.), $Pd(PPh_3)_4$ (5.0/7.5 mol%) and CuI (5.0/7.5 mol%) were dissolved in a degassed mixture of toluene and TEA. The solution was degassed for 5 min and the alkyne (1–2.3 eq.) was added. The solution was stirred at rt–40 °C under exclusion of light. After 1d–16 d the solvent was removed under reduced pressure. The crude mixture was purified by flash column chromatography or GPC. For further purification the product was precipitated from CH_2Cl_2/acetonitrile or CH_2Cl_2/methanol or precipitated from acetone.

General Procedure for the Halogen Exchange (GPIII); According to Literature[170, 171]

Under a nitrogen atmosphere the brominated compound (1 eq.), CuI (0.2–0.8 eq.), NaI (100–200 eq.) and *trans*-*N,N*-dimethylcyclohexane-1,2-diamine (0.4–1 eq.) were placed in a Schlenk flask. A degased mixture of dioxane and *n*-butanol (1:1) was added and the flask was heated under exclusion of light for 3–10 d to 110 °C. The reaction mixture was allowed to cool to room temperature and washed with 30 % ammonia and water. The combined aqueous phases were extracted with CH_2Cl_2. After drying over $MgSO_4$ the solvent was removed under reduced pressure. The crude product was purified by flash column chromatography. For further purification the residue was precipitaded from CH_2Cl_2/hexane or CH_2Cl_2/acetonitrile or CH_2Cl_2/methanol.

7.2.3 Precursors and Reference Compounds

2-(3,7-Dimethyloctyl)-4,4,5,5-tetramethyl-1,3,2-dioxaborolane (**Alk-1**)[1]

CA [–]

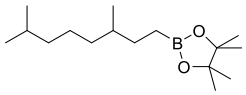

Synthesis according to literature[136]

CuI (96.0 mg, 507 µmol), lithium-*tert*-butoxide (812 mg, 10.1 mmol) and bis(pinacolato)diboron (1.96 mg, 7.71 mmol) were placed in a Schlenk flask. After the flask was evacuated and flushed with nitrogen three times, the mixture was dissolved in dry THF (6 ml) and 1-iodo-3,7-dimethyloctane (1.36 g, 5.07 mmol) was added slowly *via* syringe. The reaction mixture was stirred for 18 h at room temperature. The suspension was diluted with EA and filtrated through silica. The solvent was removed under reduced pressure and the residue was purified by flash column chromatography (eluent: CH_2Cl_2).

Yield: 1.17 g 4.36 mmol 86 % of a colourless liquid

$C_{16}H_{33}BO_2$ [268.24]

^{1}H-NMR (400.0 MHz, $CDCl_3$):

δ [ppm] = 1.56 – 1.46 (m, 1 H, C<u>H</u>), 1.45 – 1.36 (m, 1 H, C<u>H</u>), 1.35 – 0.97 (-, 20 H, 4 × C<u>H</u>$_2$, 4 × CC<u>H</u>$_3$), 0.86 – 0.82 (-, 9 H, 3 × CHC<u>H</u>$_3$), 0.79 – 0.66 (m, 2 H, C<u>H</u>$_2$).

[1]For a full characterisation see literature.[136]

4,4,5,5-Tetramethyl-2-(1-pyrenyl)-1,3,2-dioxaborolane (**Py-2**)

CA [349666-24-6]

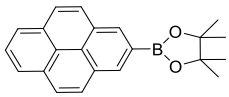

Synthesis according to literature[120]

Under a nitrogen atmosphere **Py-1** (500 mg, 2.47 mmol) that was filtered through silica beforehand, [{Ir(*μ*-OMe)(cod)}$_2$] (17.0 mg, 25.0 µmol) and 4,4‘-di-*tert*-butyl-2,2‘-dipyridyl (13.0 mg, 48.4 µmol) were suspended in a Schlenk flask in degased hexane (20 ml). Then a solution of bis(pinacolato)diboron (596 mg, 2.35 mmol) in degassed hexane (30 ml) was dropped to the suspension during 6 h at 80 °C. The reaction mixture was stirred for 18 h at 80 °C and then filtered through silica with CH_2Cl_2 as eluent. The solvent was removed under reduced pressure and the residue was purified by flash column chromatography (eluent: CH_2Cl_2:PE = 1:1).

Yield: 471 mg 1.44 mmol 58 % of a colourless solid

$C_{22}H_{21}BO_2$ [328.21]

^{1}H-NMR (400.0 MHz, $CDCl_3$):

δ [ppm] = 8.67 (s, 2 H, 2 × C<u>H</u>), 8.17 (d, $^3J_{HH}$ = 7.5 Hz, 2 H, 2 × C<u>H</u>), 8.12 (d, $^3J_{HH}$ = 9.0 Hz, 2 H, 2 × C<u>H</u>), 8.06 (d, $^3J_{HH}$ = 9.0 Hz, 2 H, 2 × C<u>H</u>), 8.01 (t, $^3J_{HH}$ = 7.6 Hz, 1 H, C<u>H</u>), 1.52 (s, 12 H, 3 × CC<u>H$_3$</u>).

2-Bromopyrene (**Py-3**)

CA [1714-27-8]

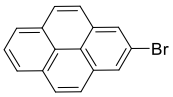

Synthesis according to literature[120]

Py-2 (5.02 g, 15.3 mmol) was dissolved in methanol (166 ml) and $CuBr_2$ (10.3 g, 45.9 mmol) in water (166 ml) was added. The mixture was stirred for 72 h at 95 °C. The solution was extracted with diethylether (3 × 20 ml) and the combined organic phases were washed with brine (3 × 30ml). After drying over Na_2SO_4 the solvent was removed under reduced pressure. The oily residue was purified by flash column chromatography (PE).

Yield: 4.02 g 14.3 mmol 93 % of a colourless solid

$C_{16}H_9Br$ [281.15]

^{1}H-NMR (400.0 MHz, $CDCl_3$):

δ [ppm] = 8.24 (s, 2 H, 2 × C<u>H</u>), 8.17 (d, $^3J_{HH}$ = 7.7 Hz, 2 H, 2 × C<u>H</u>), 8.06 – 7.99 (-, 3 H, 3 × C<u>H</u>), 7.92 (d, $^3J_{HH}$ = 8.8 Hz, 2 H, 2 × C<u>H</u>).

2-(3,7-Dimethyloctyl)pyrene (**Py-4**)[1]

CA [–]

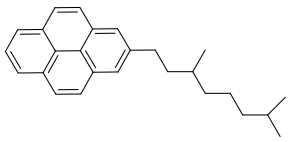

Synthesis according to literature[136]

$Pd_2(dba)_3$ (39.0 mg, 43.0 µmol), 2-dicyclohexylphosphino-2′,6′-di*iso*propoxybiphenyl (42.6 mg, 91.0 µmol) and NaO^tBu (620 mg, 6.46 mmol) were placed in a Schlenk flask under a nitrogen atmosphere. **Alk-1** (523 mg, 1.95 mmol), a solution of **Py-3** (343 mg, 1.22 mmol) in toluene (3.50 ml) and water (0.35 ml) were added *via* syringe. The reaction mixture was stirred for 24 h at 80 °C. Afterwards the solution was filtered through silica and the solvent was removed under reduced pressure. The crude was purified by flash column chromatography (eluent: PE).

Yield: 379 mg 1.11 mmol 91 % of a colourless solid

$C_{26}H_{30}$ [342.52]

^{1}H-NMR (400.0 MHz, $CDCl_3$):

δ [ppm] = 8.24 (d, $^3J_{HH}$ = 7.4 Hz, 2 H, 2 × C<u>H</u>), 8.15 – 8.09 (-, 6 H, 6 × C<u>H</u>), 8.08 – 8.04 (m, 1 H, C<u>H</u>), 3.24 – 3.07 (m, 2 H, C<u>H</u>$_2$), 2.05 – 1.65 (-, 4 H, C<u>H</u>$_2$, 2 × C<u>H</u>),1.60 – 1.30 (-, 6 H, 3 × C<u>H</u>$_2$) 1.18 (d, $^3J_{HH}$ = 6.7 Hz, 3 H, CHC<u>H</u>$_3$), 1.08 – 1.07 (-, 6 H, CH(C<u>H</u>$_3$)$_2$).

[1]For a full characterisation see literature.[136]

2-(7-(3,7-Dimethyloctyl)pyrene-2-yl)-4,4,5,5-tetramethyl-1,3,2-dioxaborolane (**Py-5**)[1]

CA [–]

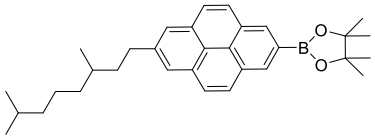

Synthesis according to literature[136]

In a Schlenk flask [{Ir(μ-OMe)(cod)}$_2$] (37.3 mg, 56.0 µmol), 4,4‘-di-*tert*-butyl-2,2‘-dipyridyl (29.8 mg, 111 µmol), bis(pinacolato)diboron (952 mg, 3.75 mmol) and **Py-4** (951 mg, 2.78 mmol) were dissolved in dry dioxane (8 ml) under a nitrogen atmosphere. The reaction mixture was stirred for 21 h at 100 °C. Afterwards the catalyst was removed *via* filtration through silica with CH_2Cl_2 as eluent. The solvent was removed under reduced pressure and the residue was purified by flash column chromatography (eluent: PE:CH_2Cl_2 5:1 ⟶ 4:1 ⟶ 3:1).

Yield: 482 mg 1.03 mmol 37 % of a yellow oil

$C_{32}H_{41}BO_2$ [468.48]

^{1}H-NMR (400.0 MHz, $CDCl_3$):

δ [ppm] = 8.61 (s, 2 H, 2 × C<u>H</u>), 8.08 (d, $^3J_{HH}$ = 8.6 Hz, 2 H, 2 × C<u>H</u>), 8.01 – 7.99 (-, 4 H, 4 × C<u>H</u>), 3.13 – 3.00 (m, 2 H, C<u>H$_2$</u>), 1.91 – 1.50 (-, 4 H, 2 × C<u>H</u>, C<u>H$_2$</u>), 1.47 (s, 12 H, 4 × CC<u>H$_3$</u>), 1.43 – 1.14 (-, 6 H, 3 × C<u>H$_2$</u>), 1.02 (d, $^3J_{HH}$ = 6.6 Hz, 3 H, CHC<u>H$_3$</u>), 0.88 (d, $^3J_{HH}$ = 6.6 Hz, 6 H, CH(C<u>H$_3$</u>)$_2$).

[1]For a full characterisation see literature.[136]

2-Bromo-7(3,7-dimethyloctyl)pyrene (**Py-6**)[1]

CA [–]

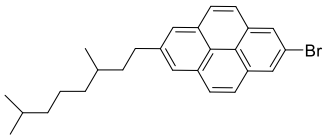

Synthesis according to literature[136]

To a solution of **Py-5** (307 mg, 656 µmol) in methanol (10 ml) and THF (3.5 ml), $CuBr_2$ (586 mg, 2.62 mmol) in water (10 ml) was added. The reaction mixture was heated to 110 °C and stirred for 5 d. Water (10 ml) was added to the mixture and the solution was extracted with diethylether (30 ml). The combined organic layers were washed with brine (2 × 40 ml) and dried over Na_2SO_4. The solvent was removed under reduced pressure and the residue was purified by flash column chromatography (eluent: PE).

Yield: 209 mg 496 µmol 76 % of a colourless solid

$C_{26}H_{29}Br$ [421.41]

^{1}H-NMR (400.0 MHz, $CDCl_3$):

δ [ppm] = 8.25 (s, 2 H, 2 × C<u>H</u>), 8.05 – 8.02 (-, 4 H, 4 × C<u>H</u>), 7.94 (d, $^3J_{HH}$ = 9.0 Hz, 2 H, 2 × C<u>H</u>), 3.13 – 3.00 (m, 2 H, C<u>H$_2$</u>), 1.91 – 1.62 (m, 2 H, C<u>H$_2$</u>), 1.59 – 1.49 (-, 2 H, 2 × C<u>H</u>), 1.45 – 1.13 (-, 6 H, 3 × C<u>H$_2$</u>), 1.02 (d, $^3J_{HH}$ = 6.6 Hz, 3 H, CHC<u>H$_3$</u>), 0.87 (d, $^3J_{HH}$ = 6.6 Hz, 6 H, CH(C<u>H$_3$</u>)<u>$_2$</u>).

[1]For a full characterisation see literature.[136]

2-(Trimethylsilyl-ethynyl)-7-(3,7-dimethyloctyl)pyrene (**Py-7**)

CA [–]

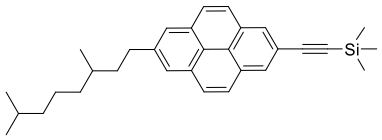

Synthesis according to literature[64, 140]

$Pd(C_6H_5CN)_2Cl_2$ (846 µg, 2.21 µmol), CuI (140 µg, 0.740 µmol) and **Py-6** (31.0 mg, 74.0 µmol) were dissolved in dioxane (1 ml) under a nitrogen atmosphere. DIPA (0.630 µl, 4.41 µmol), P^tBu_3 (1 M in toluene, 4.41 µl, 4.41 µmol) and trimethylsilylacetylene (0.0150 µl, 103 µmol) were added *via* syringe. After stirring for 24 h at 80 °C, the solution was cooled to room temperature and the solvent was removed under reduced pressure. The residue was dissolved in CH_2Cl_2 and washed with water (30 ml). The aqueous phase was extracted with CH_2Cl_2 (2 × 30 ml) and the combined organic layers were dried over Na_2SO_4. The solvent was removed under reduced pressure and the residue was purified by flash column chromatography (eluent: PE).

Yield: 29.9 mg 68.2 µmol 93 % of a yellow solid

$C_{31}H_{38}Si$ [438.72]

MALDI-TOF MS (POS, DCTB : $CHCl_3$ = 1:3):

calc. for $C_{31}H_{38}Si$ [$M^{\bullet+}$]: m/z = 438.274 found: m/z = 438.244

^{1}H-NMR (400.0 MHz, $CDCl_3$):

δ [ppm] = 8.24 (s, 2 H, 2 × C<u>H</u>), 8.03 – 8.00 (-, 4 H, 4 × C<u>H</u>), 7.97 (d, $^3J_{HH}$ = 8.8 Hz, 2 H, 2 × C<u>H</u>), 3.13 – 2.96 (m, 2 H, C<u>H$_2$</u>), 1.90 – 1.61 (m, 2 H, C<u>H$_2$</u>), 1.59 – 1.13 (-, 8 H, 2 × C<u>H</u>, 3 × C<u>H$_2$</u>), 1.01 (d, $^3J_{HH}$ = 6.5 Hz, 3 H, CHC<u>H$_3$</u>), 0.87 (d, $^3J_{HH}$ = 6.6 Hz, 6 H, CH(C<u>H$_3$</u>)$_2$), 0.38 (s, 9 H, Si(C<u>H$_3$</u>)$_3$).

^{13}C-NMR (100.6 MHz, $CDCl_3$):

δ [ppm] = 141.9 (C_q), 131.5 (C_q), 130.8 (C_q), 128.1 (CH), 128.0 (CH), 127.0 (CH), 125.6 (CH), 124.5 (C_q), 123.0 (C_q), 120.1 (C_q), 106.0 (C_q), 94.5 (C_q), 39.8 (CH_2), 39.5 (CH_2), 37.3 (CH_2), 34.2 (CH_2), 32.8 (CH), 28.1 (CH), 24.9 (CH_2), 22.9 (CH_3), 22.8 (CH_3), 19.9 (CH_3), 0.22 (CH_3).

2-Ethynyl-7-(3,7-dimethyloctyl)pyrene (**Py-8**)

CA [–]

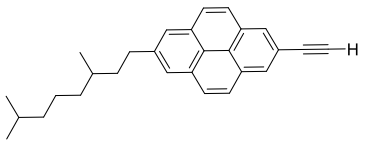

Synthesis according to literature[64]

Under a nitrogen atmosphere **Py-7** (50.0 mg, 114 µmol) was solved in dry THF and a solution of TBAF (1 M in THF, 0.260 ml, 0.260 mmol) was added. After a reaction time of 2 h at rt the solvent was removed under reduced pressure. The residue was dissolved in CH_2Cl_2 and washed with water (3 × 10 ml). The organic layer was dried over Na_2SO_4 and the solvent was removed under reduced pressure.

Yield: 39.2 mg 107 µmol 94 % of a brown oil

$C_{28}H_{30}$ [366.54]

MALDI-TOF MS (POS, DCTB : $CHCl_3$ = 1:3):

calc. for $C_{28}H_{30}$ [$M^{\bullet+}$]: m/z = 366.235 found: m/z = 366.235

^{1}H-NMR (400.0 MHz, $CDCl_3$):

δ [ppm] = 8.26 (s, 2 H, 2 × C<u>H</u>), 8.04 – 8.00 (-, 4 H, 4 × C<u>H</u>), 8.01 (d, $^3J_{HH}$ = 9.0 Hz, 2 H, 2 × C<u>H</u>), 3.23 (s, 1 H, ≡C<u>H</u>), 3.13 – 2.97 (m, 2 H, C<u>H$_2$</u>) 1.91 – 1.61 (m, 2 H, C<u>H$_2$</u>), 1.60 – 1.49 (-, 2 H, 2 × C<u>H</u>), 1.45 – 1.13 (-, 6 H, 3 × C<u>H$_2$</u>), 1.02 (d, $^3J_{HH}$ = 6.6 Hz, 3 H, CHC<u>H$_3$</u>), 0.87 (d, $^3J_{HH}$ = 6.6 Hz, 6 H, CH(C<u>H$_3$</u>)$_2$).

^{13}C-NMR (100.6 MHz, $CDCl_3$):

δ [ppm] = 142.0 (C_q), 131.5 (C_q), 130.9 (C_q), 128.2 (CH), 128.1 (CH), 126.9 (CH), 125.7 (CH), 124.7 (C_q), 122.9 (C_q), 119.0 (C_q), 84.5 (C_q), 77.4 (CH), 39.8 (CH_2), 39.5 (CH_2), 37.4 (CH_2), 34.2 (CH_2), 32.8 (CH), 28.1 (CH), 24.9 (CH_2), 22.9 (CH_3), 22.8 (CH_3), 19.9 (CH_3).

2-Phenylacetylene-7-(3,7-dimethyloctyl)pyrene (**Py-9**)

CA [–]

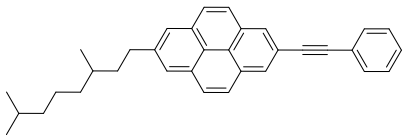

Synthesis according to literature[64, 140]

$Pd(C_6H_5CN)_2Cl_2$ (20.5 mg, 53.0 µmol), CuI (1.70 mg, 8.90 µmol) and **Py-6** (375 mg, 890 µmol) were dissolved in dioxane (10 ml) under a nitrogen atmosphere. DIPA (30.2 µl, 214 µmol), P^tBu_3 (1 M in toluene, 214 µl, 214 µmol) and phenylacetylene (195 µl, 1.78 mmol) were added *via* syringe. After stirring for 72 h at 50 °C, the solution was cooled to room temperature and the solvent was removed under reduced pressure. The residue was dissolved in CH_2Cl_2 and washed with water (30 ml). The aqueous phase was extracted with CH_2Cl_2 (2 × 30 ml) and the combined organic phases were dried over Na_2SO_4. The solvent was removed under reduced pressure and the residue was purified by flash column chromatography (eluent: PE:CH_2Cl_2 5:1) and precipitated from CH_2Cl_2/methanol.

Yield: 330 mg 746 µmol 84 % of a light yellow solid

$C_{34}H_{34}$ [442.64]

MALDI-TOF MS (POS, DCTB : $CHCl_3$ = 1:3):

calc. for $C_{34}H_{34}$ [$M^{\bullet+}$]: m/z = 442.266 found: m/z = 442.257

^{1}H-NMR (400.0 MHz, $CDCl_3$):

δ [ppm] = 8.31 (s, 2 H, 2 × C<u>H</u>), 8.05 – 8.00 (-, 6 H, 6 × C<u>H</u>), 7.66 – 7.63 (m, 2 H, 2 × C<u>H</u>), 7.41 – 7.38 (-, 3 H, 3 × C<u>H</u>), 3.10 – 3.01 (m, 2 H, C<u>H$_2$</u>), 1.91 – 1.62 (m, 2 H, C<u>H$_2$</u>), 1.59 – 1.11 (-, 8 H, 2 × C<u>H</u>, 3 × C<u>H$_2$</u>), 1.02 (d, $^3J_{HH}$ = 6.6 Hz, 3 H, CHC<u>H$_3$</u>), 0.87 (d, $^3J_{HH}$ = 6.6 Hz, 6 H, CH(C<u>H$_3$</u>)$_2$).

^{13}C-NMR (100.6 MHz, $CDCl_3$):

δ [ppm] = 141.7 (C_q), 131.7 (CH), 131.4 (C_q), 130.9 (C_q), 128.4 (CH), 128.3 (CH), 127.9 (CH), 127.7 (CH), 126.9 (CH), 125.5 (CH), 124.3 (C_q), 123.4 (C_q), 122.9 (C_q), 120.2 (C_q), 90.2 (C_q), 89.6 (C_q), 39.6 (CH_2), 39.4 (CH_2), 37.2 (CH_2), 34.1 (CH_2), 32.7 (CH), 28.0 (CH), 24.7 (CH_2), 22.7 (CH_3), 22.6 (CH_3), 19.7 (CH_3).

1,2-Bis(7-(3,7-dimethyloctyl)pyren-2-yl)ethyne (**Py-10**)

CA [–]

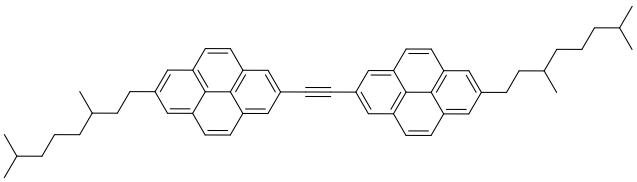

Synthesis according to literature [120, 140]

$Pd(C_6H_5CN)_2Cl_2$ (4.26 mg, 11.0 µmol), CuI (1.41 mg, 7.40 µmol), **Py-6** (156 mg, 370 µmol) and **Py-8** (149 mg, 407 µmol) were placed in a pressure quartz vessel, which was evacuated and flushed with nitrogen afterwards. DIPA (575 µl, 4.07 mmol) and P^tBu_3 (1 M in toluene, 11.0 µl, 11.0 µmol) were added *via* syringe. The mixture was dissolved in freshly degassed DMF und stirred for 20 min in the microwave oven at 150 °C. The solvent was removed under reduced pressure and the residue was dissolved in CH_2Cl_2. The solution was washed with water (30 ml) and the aqueous layer was extracted with CH_2Cl_2 (2 × 30 ml). The combined organic layers were dried over $MgSO_4$, the solvent was removed under reduced pressure and the residue was purified by flash column chromatography (eluent: PE → PE:CH_2Cl_2 5:1).

Yield: 164 mg 232 µmol 63 % of a brown solid

$C_{54}H_{58}$ [707.04]

MALDI-TOF MS (POS, DCTB : $CHCl_3$ = 1:3):

calc. for $C_{54}H_{58}$ [$M^{\bullet+}$]: m/z = 706.453 found: m/z = 706.437

^{1}H-NMR (400.0 MHz, $CDCl_3$):

δ [ppm] = 8.42 (s, 4 H, 4 × CH), 8.06 – 8.03 (-, 12 H, 12 × CH), 3.15 – 2.99 (m, 4 H, 2 × CH_2), 1.93 – 1.63 (m, 4 H, 2 × CH_2), 1.61 – 1.14 (-, 16 H, 4 × CH, 6 × CH_2), 1.03 (d, $^3J_{HH}$ = 6.4 Hz, 6 H, 2 × $CHCH_3$), 0.88 (d, $^3J_{HH}$ = 6.8 Hz, 12 H, 2 × $CH(CH_3)_2$).

^{13}C-NMR (100.6 MHz, $CDCl_3$):

δ [ppm] = 141.9 (C_q), 131.5 (C_q), 131.1 (C_q), 128.1 (CH), 127.9 (CH), 127.1 (CH), 125.7 (CH), 124.4 (C_q), 123.0 (C_q), 120.4 (C_q), 90.6 (C_q), 39.8 (CH_2), 39.5 (CH_2), 37.4 (CH_2), 34.3 (CH_2), 32.8 (CH), 28.1 (CH), 24.9 (CH_2), 22.87 (CH_3), 22.78 (CH_3), 19.9 (CH_3).

Squaraine **SQA-2**

CA [–]

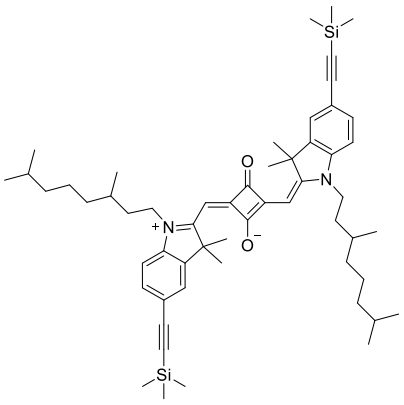

Synthesis according to GPI

SQA-1 (500 mg, 599 µmol), CuI (9.13 mg, 48.0 µmol), $Pd(C_6H_5CN)_2Cl_2$ (27.6 mg, 72.0 µmol), tri-*tert*-butylphosphane (1 M in toluene, 156 µl, 156 µmol), trimethylsilylacetylene (846 µl, 5.99 mmol), DIPA (303 µl, 2.16 mmol), dioxane (35 ml); stirred for 3 d at 75 °C, 3 × flash column chromatography (1. eluent: CH_2Cl_2:methanol 1:0.5 %⟶ 1:1%, 2. eluent: PE:EA 9:1 ⟶ 8:1 ⟶ 7:1 ⟶ 6:1 ⟶ 5:1 ⟶ 4:1 ⟶ 3:1 ⟶ 2:1 ⟶ 1:1 ⟶ EA, 3. eluent: CH_2Cl_2 ⟶ CH_2Cl_2:methanol 1:0.01⟶ 1:0.02 ⟶ 1:0.03 ⟶ 1:0.04 ⟶ 1:0.05 ⟶ 1:0.06 ⟶ 1:0.12 ⟶ 1:0.14 ⟶ 1:0.16 ⟶ 1:0.18 ⟶ 1:0.2 ⟶ 1:0.22 ⟶ 1:0.24 ⟶ 1:0.3 ⟶ 1:0.5 ⟶ 1:0.75); precipitation from CH_2Cl_2/hexane.

Yield: 27.7 mg 31.9 µmol 5 % of a shiny blue solid

$C_{56}H_{80}N_2O_2Si_2$ [869.42]

MALDI-TOF MS (POS, DCTB : $CHCl_3$ = 1:3):

calc. for $C_{56}H_{80}N_2O_2Si_2$ [$M^{\bullet+}$]: m/z = 868.575 found: m/z = 868.582

^{1}H-NMR (600.4 MHz, $CDCl_3$):

δ [ppm] = 7.44 – 7.41 (-, 4 H, 4 × C<u>H</u>), 6.92 (d, 2 H, $^3J_{HH}$ = 8.16 Hz, 2 × C<u>H</u>), 5.94 (s, 2 H, 2 × =C<u>H</u>), 4.09 – 3.90 (m, 4 H, 2 × NC<u>H$_2$</u>), 1.81 – 1.50 (-, 20 H, 2 × C(C<u>H$_3$</u>)<u>$_2$</u>, 2 × C<u>H$_2$</u>, 4 × C<u>H</u>), 1.41 – 1.13 (-, 12 H, 6 × C<u>H$_2$</u>), 1.05 (d, $^3J_{HH}$ = 6.3 Hz, 6 H, 2 × CHC<u>H$_3$</u>), 0.87 (d, $^3J_{HH}$ = 6.7 Hz, 12 H, 2 × CH(C<u>H$_3$</u>)<u>$_2$</u>), 0.25 – 0.26 (m, 18 H, 2 × Si(C<u>H$_3$</u>)<u>$_3$</u>).

^{13}C-NMR (151.0 MHz, $CDCl_3$):

δ [ppm] = 181.9 (C_q) 181.4 (C_q), 169.8 (C_q), 143.0 (C_q), 142.7 (C_q), 132.3 (CH), 126.2 (CH), 118.4 (C_q), 109.6 (CH), 105.4 (C_q), 94.4 (C_q), 87.7 (CH), 49.4 (C_q), 42.6 (CH_2), 39.5 (CH_2), 37.4 (CH_2), 34.1 (CH_2), 31.5 (CH), 28.4 (CH), 27.094 (CH_3), 27.085 (CH_3), 25.1 (CH_2), 22.8 (CH_3), 22.7 (CH_3), 19.7 (CH_3), 0.0 (CH_3).

Squaraine **SQA-3**

CA [–]

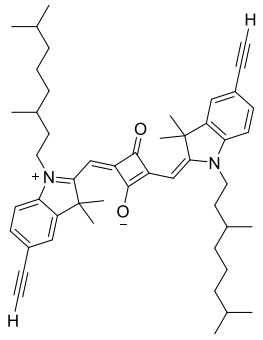

Synthesis according to literature[222]

SQA-2 (114 mg, 131 µmol) was dissolved in CH_2Cl_2 (10 ml) and TBAF × $3H_2O$ (174 mg, 551 µmol) was added. After a reaction time of 2 h at room temperature the solvent was removed under reduced pressure. The residue was dissolved in CH_2Cl_2 and washed with water (20 ml). The aqueous layer was extracted with CH_2Cl_2 (2 × 20 ml) and the combined organic layers were dried over Na_2SO_4 and the solvent was removed under reduced pressure. The residue was precipitated from CH_2Cl_2/hexane.

Yield: 39.7 mg 54.8 µmol 42 % of a blue solid with a red gleam

$C_{50}H_{64}N_2O_2$ [725.06]

MALDI-TOF MS (POS, DCTB : $CHCl_3$ = 1:3):

calc. for $C_{50}H_{64}N_2O_2$ [$M^{\bullet+}$]: m/z = 724.496 found: m/z = 724.487

^{1}H-NMR (400.0 MHz, $CDCl_3$):

δ [ppm] = 7.46 – 7.44 (-, 4 H, 4 × C<u>H</u>), 6.89 (d, $^{3}J_{HH}$ = 8.6 Hz, 2 H, 2 × C<u>H</u>), 5.98 (s, 2 H, 2 × =C<u>H</u>), 4.06 – 3.89 (m, 4 H, 2 × NC<u>H</u>$_2$), 3.11 (s, 2 H, 2 × ≡C<u>H</u>) 1.77 (s, 12 H, 2 × C(C<u>H</u>$_3$)$_2$), 1.96 – 1.10 (-, 20 H, 4 × C<u>H</u>, 8 × C<u>H</u>$_2$), 1.03 (d, $^{3}J_{HH}$ = 6.2 Hz, 6 H, 2 × CHC<u>H</u>$_3$), 0.86 (d, $^{3}J_{HH}$ = 6.6 Hz, 12 H, 2 × CH(C<u>H</u>$_3$)$_2$).

^{13}C-NMR (151.0 MHz, $CDCl_3$):

δ [ppm] = 182.3 (C_q), 180.7 (C_q), 169.9 (C_q), 142.7 (C_q), 142.5 (C_q), 132.4 (CH), 126.2 (CH), 117.2 (C_q), 109.2 (CH), 87.5 (CH), 83.7 (C_q), 49.2 (C_q), 42.4 (CH_2), 39.5 (CH_2), 37.2 (CH_2), 33.9 (CH_2), 31.3 (CH), 28.1 (CH), 27.13 (CH_3), 27.12 (CH_3), 24.8 (CH_2), 22.8 (CH_3), 22.7 (CH_3), 19.7 (CH_3).

One CH signal is missing and is presumably covered by the solvent signal.

This compound was not completely purified.

Squaraine **SQA-4**

CA [–]

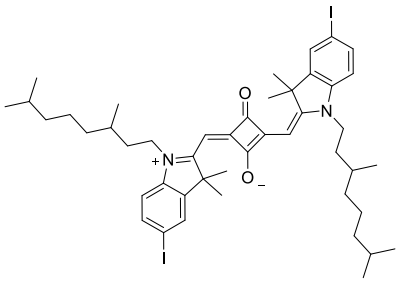

Synthesis according to GPIII

SQA-1 (500 mg, 599 µmol), CuI (22.8 mg, 120 µmol), NaI (18.0 g, 120 mmol), *trans-N,N'*-dimethylcyclohexane-1,2-diamine (34.1 mg, 240 µmol), *n*-butanol (20 ml), dioxane (20 ml); stirred for 8 d, 3 x flash column chromatography (eluent: CH_2Cl_2), precipitation from CH_2Cl_2/hexane.

Yield: 496 mg 534 µmol 89 % of a blue solid with a red gleam

$C_{46}H_{62}I_2O_2N_2$ [928.81]

MALDI-TOF MS (POS, DCTB : $CHCl_3$ = 1:3):

calc. for $C_{46}H_{62}I_2O_2N_2$ [$M^{\bullet+}$]: m/z = 928.290 found: m/z = 928.29

^{1}H-NMR (400.0 MHz, $CDCl_3$):

δ [ppm] = 7.64 – 7.62 (-, 4 H, 4 × C<u>H</u>), 6.78 (d, $^{3}J_{HH}$ = 8.2 Hz, 2 H, 2 × C<u>H</u>), 5.90 (s, 2 H, 2 × =C<u>H</u>), 4.00 (m, 4 H, 2 × NC<u>H</u>$_2$), 1.73 (s, 12 H, 2 × C(C<u>H</u>$_3$)$_2$), 1.63 – 1.13 (-, 20 H, 4 × C<u>H</u>, 8 × C<u>H</u>$_2$) 1.04 (d, $^{3}J_{HH}$ = 6.2 Hz, 6 H, 2 × CHC<u>H</u>$_3$), 0.86 (d, $^{3}J_{HH}$ = 6.6 Hz, 12 H, 2 × CH(C<u>H</u>$_3$)$_2$).

^{13}C-NMR (100.6 MHz, $CDCl_3$):

δ [ppm] = 181.9 (C_q), 181.3 (C_q), 169.2 (C_q), 145.0 (C_q), 142.7 (C_q), 137.0 (CH), 131.7 (CH), 111.7 (CH), 87.3 (CH), 86.7 (C_q), 49.5 (C_q), 42.5 (CH_2), 39.5 (CH_2), 37.4 (CH_2), 34.0 (CH_2), 31.4 (CH), 28.4 (CH), 27.1 (CH_3), 25.1 (CH_2), 22.8 (CH_3), 22.7 (CH_3), 19.7 (CH_3).

Squaraine **SQA-6**

CA [–]

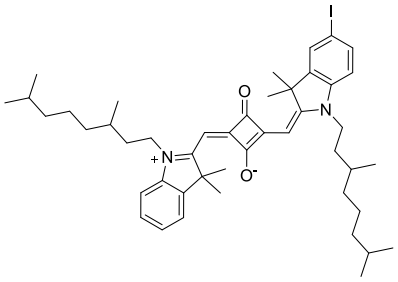

Synthesis according to GPIII

SQA-5 (790 mg, 1.05 mmol), CuI (159 mg, 836 µmol), NaI (31.3 g, 209 mmol), *trans-N,N'*-dimethylcyclohexane-1,2-diamine (149 mg, 1.05 mmol), *n*-butanol (20 ml), dioxane (20 ml); stirred for 5 d, flash column chromatography (eluent: CH_2Cl_2).

Yield: 778 mg 969 µmol 92 % of a blue solid with a red gleam

$C_{46}H_{63}IN_2O_2$ [802.91]

MALDI-TOF MS (POS, DCTB : $CHCl_3$ = 1:3):

calc. for $C_{46}H_{63}IN_2O_2$ [$M^{\bullet+}$]: m/z = 802.393 found: m/z = 802.263

^{1}H-NMR (600.4 MHz, CD_2Cl_2):

δ [ppm] = 7.63 – 7.60 (-, 2 H, 2 × C<u>H</u>), 7.39 – 7.31 (-, 2 H, 2 × C<u>H</u>), 7.18 (ddd, $^{3}J_{HH}$ = 11.2 Hz, $^{3}J_{HH}$ = 11.2 Hz, $^{4}J_{HH}$ = 1.1 Hz, 1 H, C<u>H</u>), 7.04 (d, $^{3}J_{HH}$ = 11.8 Hz, 1 H, C<u>H</u>), 6.8 (d, $^{3}J_{HH}$ = 12.3 Hz, 1 H, C<u>H</u>), 5.94 (s, 1 H, =C<u>H</u>), 5.90 (s, 1 H, =C<u>H</u>), 4.08 – 3.83 (-, 4 H, 2 × NC<u>H_2</u>), 1.83 – 1.13 (-, 20 H, 8 × C<u>H_2</u>, 4 × C<u>H</u>), 1.75 (s, 6 H, C(C<u>H_3</u>)<u>$_2$</u>), 1.73 (s, 6 H, C(C<u>H_3</u>)<u>$_2$</u>), 1.07 – 1.03 (-, 6 H, 2 × CHC<u>H_3</u>), 0.87 – 0.86 (-, 12 H, 2 × CH(C<u>H_3</u>)<u>$_2$</u>).

^{13}C-NMR (100.6 MHz, CD_2Cl_2):

δ [ppm] = 182.2 (C_q), 181.9 (C_q) 180.5 (C_q), 179.5 (C_q), 171.0 (C_q), 169.9 (C_q), 168.0 (C_q), 144.9 (C_q), 142.7 (C_q), 142.6 (C_q), 136.8 (CH), 131.6 (CH), 128.1 (CH), 124.3 (CH), 122.6 (CH), 111.3 (CH), 110.0 (CH), 87.1 (CH), 86.9 (CH), 86.0 (C_q), 49.8 (C_q), 49.2 (C_q), 42.5 (CH_2), 42.3 (CH_2), 42.2 (CH_2), 39.5 (CH_2), 37.4 (2 × CH_2), 34.1 (CH_2), 33.8 (CH_2), 31.49 (CH), 31.43 (CH), 28.3 (2 × CH), 27.2 (CH_3), 27.1 (CH_3), 26.9 (2 × CH_3), 25.0 (2 × CH_2), 22.8 (2 × CH_3), 22.7 (2 × CH_3), 19.7 (2 × CH_3).

Squaraine **SQB-2**

CA [–]

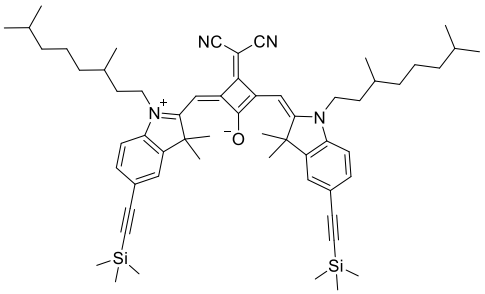

Synthesis according to GPI

SQB-1 (400 mg, 452 µmol), CuI (6.90 mg, 36.2 µmol), $Pd(C_6H_5CN)_2Cl_2$ (20.9 mg, 54.5 µmol), P^{t}Bu$_3$ (118 µl, 1 M in toluene, 118 µmol), trimethylsilylacetylene (640 µl, 4.53 mmol), DIPA (229 µl, 1.63 mmol), dioxane (15 ml); stirred for 4 d at 75 °C, flash column chromatography (eluent: PE:CH_2Cl_2 1:1 ⟶ PE:CH_2Cl_2 2:3); recrystallisation from acetonitrile.

Yield: 144.1 mg 0.157 µmol 35 % of a green solid

$C_{59}H_{80}N_4OSi_2$ [917.47] MALDI-TOF MS (POS, DCTB : $CHCl_3$ = 1:3):

calc. for $C_{59}H_{80}N_4OSi_2$ [$M^{\bullet+}$]: m/z = 916.587 found: m/z = 916.566

^{1}H-NMR (400.0 MHz, CD_2Cl_2):

δ [ppm] = 7.47 – 6.94 (-, 6 H, 6 × C<u>H</u>), 6.53 – 6.43 (m, 2 H, 2 × =C<u>H</u>), 4.08 – 3.95 (m, 4 H, 2 × NC<u>H$_2$</u>), 1.74 (s, 12 H, 2 × C(C<u>H$_3$</u>)$_2$), 1.65 – 1.47 (-, 8 H, 4 × C<u>H</u>, 2 × C<u>H$_2$</u>), 1.41 – 1.12 (-, 12 H, 6 × C<u>H$_2$</u>), 1.01 (d, $^3J_{HH}$ = 6.0 Hz, 6 H, 2 × CHC<u>H$_3$</u>), 0.86 (d, $^3J_{HH}$ = 6.4 Hz, 12 H, 2 × CH(C<u>H$_3$</u>)$_2$), 0.28 – 0.24 (m, 18 H, 2 × Si(<u>CH$_3$</u>)$_3$).

^{13}C-NMR (100.6 MHz, CD_2Cl_2):

δ [ppm] = 173.3 (C_q), 172.0 (C_q), 168.1 (C_q), 167.2 (C_q), 143.0 (C_q), 142.4 (C_q), 132.5 (CH), 126.1 (CH), 119.4 (C_q), 118.9 (C_q), 110.4 (CH), 105.1 (C_q), 95.1 (C_q), 90.1 (CH), 49.6 (C_q), 43.5 (CH_2), 41.0 (C_q), 39.5 (CH_2), 37.5 (CH_2), 34.4 (CH_2), 31.3 (CH), 28.4 (CH), 26.69 (CH_3), 26.65 (CH_3), 25.0 (CH_2), 22.8 (CH_3), 22.7 (CH_3), 19.8 (CH_3), 0.0 (CH_3).

Squaraine **SQB-3**

CA [–]

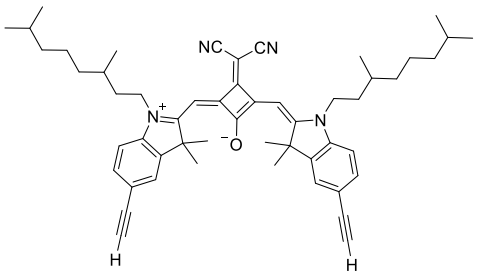

Synthesis according to literature[222]

SQB-2 (144 mg, 157 µmol) was dissolved in CH_2Cl_2 (10 ml) and TBAF × 3 H_2O (173 mg, 549 µmol) was added. After a reaction time of 2 h at room temperature the solvent was removed under reduced pressure. The residue was dissolved in CH_2Cl_2 and washed with water (20 ml). The aqueous layer was extracted with CH_2Cl_2 (2 × 20 ml) and the combined organic layers were dried over Na_2SO_4 and the solvent was removed under reduced pressure. The residue was recrystallised from acetonitrile and purified by flash column chromatography (eluent: PE:EA 9:1).

Yield: 105 mg 136 µmol 87 % of a green solid

$C_{53}H_{64}N_4O$ [773.10]

MALDI-TOF MS (POS, DCTB : $CHCl_3$ = 1:3):

calc. for $C_{53}H_{64}N_4O$ [$M^{\bullet+}$]: m/z = 772.507 found: m/z = 772.506

^{1}H-NMR (400.0 MHz, $CDCl_3$):

δ [ppm] = 7.49 – 7.45 (-, 4 H, 4 × C<u>H</u>), 6.96 (d, $^3J_{HH}$ = 8.4 Hz, 2 H, 2 × C<u>H</u>), 6.52 (s, 2 H, 2 × =C<u>H</u>), 4.09 – 3.95 (m, 4 H, 2 × NC<u>H_2</u>), 3.15 (s, 2 H, 2 × ≡C<u>H</u>) 1.76 (s, 12 H, 2 × C(C<u>H_3</u>)<u>$_2$</u>), 1.63 – 1.47 (-, 8 H, 4 × C<u>H</u>, 2 × C<u>H_2</u>), 1.38 – 1.11 (-, 12 H, 6 × C<u>H_2</u>), 1.01 (d, $^3J_{HH}$ = 6.0 Hz, 6 H, 2 × CHC<u>H_3</u>), 0.85 (d, $^3J_{HH}$ = 6.4 Hz, 12 H, 2 × CH(C<u>H_3</u>)<u>$_2$</u>).

^{13}C-NMR (100.6 MHz, $CDCl_3$):

δ [ppm] = 173.0 (C_q), 171.8 (C_q), 168.0 (C_q), 167.3 (C_q), 142.7 (C_q), 142.3 (C_q), 132.6 (CH), 126.2 (CH), 118.8 (C_q), 118.2 (C_q), 110.0 (CH), 90.0 (CH), 83.5 (C_q), 78.0 (CH), 49.4 (C_q), 43.2 (CH_2), 41.5 (C_q), 39.3 (CH_2), 37.2 (CH_2), 34.2 (CH_2), 31.0 (CH), 28.1 (CH), 26.71 (CH_3), 26.68 (CH_3), 24.7 (CH_2), 22.8 (CH_3), 22.7 (CH_3), 19.8 (CH_3).

Squaraine **SQB-4**

CA [–]

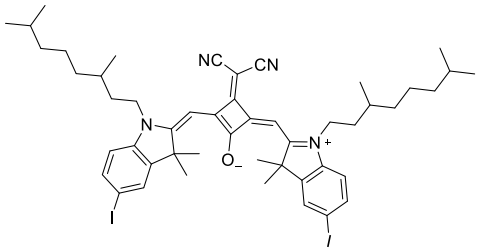

Synthesis according to GPIII

SQB-1 (811 mg, 918 µmol), CuI (35.0 mg, 184 µmol), NaI (27.5 g, 184 mmol), (1R,2R)-*trans*-*N,N'*-dimethylcyclohexane-1,2-diamine (52.2 mg, 367 µmol), *n*-butanol (20 ml), dioxane (20 ml); stirred for 7 d, 3 × flash column chromatography (eluent: CH_2Cl_2), precipitation from CH_2Cl_2/acetonitrile.

Yield: 726 mg 743 µmol 81 % of a green solid with purple gleam

$C_{49}H_{62}I_2N_4O$ [976.85]

MALDI-TOF MS (POS, DCTB : $CHCl_3$ = 1:3):

calc. for $C_{49}H_{62}I_2N_4O$ [$M^{\bullet+}$]: m/z = 976.301 found: m/z = 976.312

^{1}H-NMR (400.0 MHz, $CDCl_3$):

δ [ppm] = 7.64 – 7.60 (-, 4 H, 4 × C<u>H</u>), 6.79 (d, $^3J_{HH}$ = 8.3 Hz, 2 H, 2 × C<u>H</u>), 6.47 (s, 2 H, 2 × =C<u>H</u>), 4.05 – 3.91 (m, 4 H, 2 × NC<u>H</u>$_2$), 1.73 (s, 12 H, 4 × C(C<u>H</u>$_3$)$_2$), 1.65 – 1.09 (-, 20 H, 8 × C<u>H</u>$_2$, 4 x C<u>H</u>), 0.99 (d, $^3J_{HH}$ = 6.4 Hz, 6 H, 2 × CHC<u>H</u>$_3$), 0.83 (d, $^3J_{HH}$ = 6.7 Hz, 12 H, 2 × CH(C<u>H</u>$_3$)$_2$).

^{13}C-NMR (100.6 MHz, $CDCl_3$):

δ [ppm] = 173.0 (C_q), 171.0 (C_q), 168.0 (C_q), 167.1 (C_q), 144.8 (C_q), 141.8 (C_q), 137.1 (CH), 131.5 (CH), 118.7 (C_q), 111.9 (CH), 89.6 (CH), 88.0 (C_q), 49.5 (C_q), 43.1 (CH_2), 41.4 (C_q), 39.3 (CH_2), 37.2 (CH_2), 34.1 (CH_2), 31.0 (CH), 28.1 (CH), 26.70 (CH_3), 26.67 (CH_3), 24.7 (CH_2), 22.8 (CH_3), 22.7 (CH_3), 19.8 (CH_3).

Squaraine **SQB-6**

CA [–]

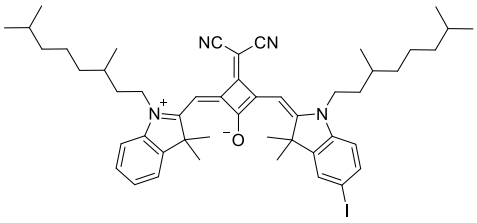

Synthesis according to GPIII

SQB-6 (1.08 g, 1.11 mmol), CuI (102 mg, 537 µmol), NaI (30.2 g, 201 mmol), (1R,2R)-*trans*-*N,N'*-dimethylcyclohexane-1,2-diamine (153 mg, 1.08 mmol), *n*-butanol (20 ml), dioxane (20 ml); stirred for 3 d, flash column chromatography (eluent: CH_2Cl_2), precipitation from CH_2Cl_2/methanol.

Yield: 400 mg 470 µmol 42 % of a green solid with purple gleam

$C_{49}H_{63}IN_4O$ [850.96]

MALDI-TOF MS (POS, DCTB : $CHCl_3$ = 1:3):

calc. for $C_{49}H_{63}IN_4O$ [$M^{\bullet+}$]: m/z = 850.404 found: m/z = 850.494

^{1}H-NMR (400.0 MHz, CD_2Cl_2):

δ [ppm] = 7.67 – 7.64 (-, 2 H, 2 × C<u>H</u>), 7.43 – 7.36 (-, 2 H, 2 × C<u>H</u>), 7.25 (m, 1 H, C<u>H</u>) 7.12 (d, $^3J_{HH}$ = 7.9 Hz, 1 H, C<u>H</u>), 6.82 (d, $^3J_{HH}$ = 9.0 Hz, 1 H, C<u>H</u>) 6.53 (s, 1 H, =C<u>H</u>), 6.43 (s, 1 H, =C<u>H</u>), 4.15 – 3.90 (-, 4 H, 2 × NC<u>H</u>$_2$), 1.84 – 1.13 (-, 20 H, 4 × C<u>H</u>, 8 × C<u>H</u>$_2$), 1.76 (s, 6 H, C(C<u>H</u>$_3$)$_2$), 1.73 (s, 6 H, C(C<u>H</u>$_3$)$_2$), 1.04 – 1.01 (-, 6 H, 2 × CHC<u>H</u>$_3$), 0.87 – 0.86 (-, 12 H, 2 × CH(C<u>H</u>$_3$)$_2$).

^{13}C-NMR (100.6 MHz, CD_2Cl_2):

δ [ppm] = 173.3 (C_q), 173.13 (C_q), 170.2 (C_q) 167.93 (C_q), 167.90 (C_q), 165.9 (C_q), 145.0 (C_q), 143.0 (C_q), 142.3 (C_q), 142.2 (C_q), 137.1 (CH), 131.6 (CH), 128.4 (CH), 125.3 (CH), 122.6 (CH), 119.0 (C_q), 118.9 (C_q), 112.0 (CH), 110.8 (CH), 89. 8 (CH), 89.2 (CH), 87.3 (C_q), 50.1 (C_q), 49.4 (C_q), 43.5 (CH_2), 43.1 (CH_2), 40.8 (C_q), 39.5 (2 × CH_2), 37.2 (2 × CH_2), 34.4 (CH_2), 34.1 (CH_2), 31.3 (CH), 31.2 (CH), 28.3 (2 × CH), 26.8 (CH_3), 26.7 (CH_3), 26.5 (CH_3), 26.4 (CH_3), 25.0 (2 × CH_2), 22.8 (2 × CH_3), 22.7 (2 × CH_3), 19.7 (2 × CH_3).

PyB-1

CA [–]

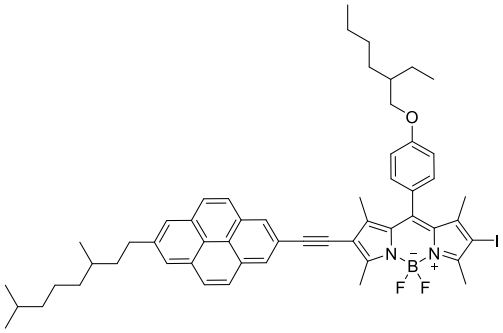

Synthesis according to literature[223]

In a Schlenk flask with dilution principle apparatus[138] and water cooler **BODIPY-2** (1.49 g, 2.11 mmol) was dissolved in a degassed mixture of TEA (6 ml) and THF (60 ml). $Pd(PPh_3)_2Cl_2$ (7.40 mg, 10.5 µmol) and CuI (1.00 mg, 5.27 µmol) were added and the mixture was degassed for 5 min by bubbling a stream of nitrogen through the solution. The mixture was heated to 115 °C and a degassed solution of **Py-8** (96.6 mg, 264 µmol) in THF (80 ml) was dropped to the mixture over the dillution knee during 4 h. The solution was allowed to cool to room temperature and was stirred over night. The solvent was removed under reduced pressure and the crude mixture was purified by flash column chromatography (PE → PE:CH_2Cl_2 9 : 1 → 7:3 → 6:4 → 5:5 → 4:6 → CH_2Cl_2). The residue was precipitated from CH_2Cl_2/hexane and the precipitate was recrystallised from acetonitrile.

Yield: 93.7 mg 99.4 µmol 38 % of a purple-blue solid

$C_{55}H_{62}BF_2IN_2O$ [942.81]

MALDI-TOF MS (POS, DCTB : $CHCl_3$ = 1:3):

calc. for $C_{55}H_{62}BF_2IN_2O$ [$M^{\bullet+}$]: m/z = 942.397 found: m/z = 942.408

^{1}H-NMR (400.0 MHz, $CDCl_3$):

δ [ppm] = 8.20 (s, 2 H, 2 × C<u>H</u>), 8.02 – 7.95 (-, 6 H, 6 × C<u>H</u>), 7.09 (AA', 2 H, 2 × C<u>H</u>), 7.03 (BB', 2 H, 2 × C<u>H</u>), 3.92 (d, $^3J_{HH}$ = 5.9 Hz, 2 H, OC<u>H$_2$</u>), 3.11 – 2.95 (m, 2 H, C<u>H$_2$</u>), 2.83 (s, 3 H, CC<u>H$_3$</u>), 2.69 (s, 3 H, CC<u>H$_3$</u>), 1.89 – 1.76, (m, 2 H, C<u>H$_2$</u>), 1.70 – 1.13 (-, 23 H, 3 × C<u>H</u>, 7 × C<u>H$_2$</u>, 2 × CC<u>H$_3$</u>), 1.02 – 0.93 (-, 9 H, CHC<u>H$_3$</u>, 2 × CH_2C<u>H$_3$</u>), 0.87 (d, $^3J_{HH}$ = 6.6 Hz, 6 H, CH(C<u>H$_3$</u>)<u>$_2$</u>).

^{13}C-NMR (100.6 MHz, $CDCl_3$):

δ [ppm] = 160.5 (C_q), 158.7 (C_q), 156.4 (C_q), 145.0 (C_q), 144.9 (C_q), 142.5 (C_q), 141.9 (C_q), 132.5 (C_q), 131.4 (C_q), 131.3 (C_q), 131.1 (C_q), 129.2 (CH), 128.1 (CH), 127.4 (CH), 126.9 (CH), 126.4 (C_q), 125.7 (CH), 124.3 (C_q), 122.9 (C_q), 120.4 (C_q), 116.5 (C_q), 115.5 (CH), 97.5 (C_q), 85.5 (C_q), 82.0 (C_q), 71.0 (CH_2), 39.8 (CH_2), 39.53 (CH), 39.47 (CH_2), 37.3 (CH_2), 34.3 (CH_2), 32.8 (CH), 30.7 (CH_2), 29.3 (CH_2), 28.1 (CH), 24.9 (CH_2), 24.0 (CH_2), 23.2 (CH_2), 22.9 (CH_3), 22.8 (CH_3), 19.8 (CH_3), 17.3 (CH_3), 16.1 (CH_3), 14.3 (CH_3), 14.0 (2 × CH_3), 11.3 (CH_3).

PyB-2

CA [–]

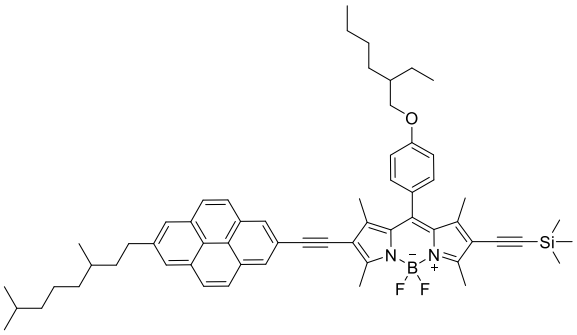

Synthesis according to literature[97]

Under a nitrogen atmosphere **PyB-1** (85.8 mg, 91.0 µmol) was dissolved in degassed DIPA (5 ml) and CuI (86.7 µg, 4.55 µmol) and $Pd(PPh_3)_2Cl_2$ (3.19 mg, 0.455 µmol) were added. The solution was degassed for 5 min by bubbling a stream of nitrogen through the solution. Trimethylsilylacetylene (25.7 µl, 182 µmol) was added and the mixture was heated to 90 °C. After 2 h the solvent was removed under reduced pressure and the residue was purified by flash column chromatography (PE:CH_2Cl_2 70:30).

Yield: 70.0 mg 76.7 µmol 84 % of a purple-blue solid

$C_{60}H_{71}BF_2N_2OSi$ [913.11]

MALDI-TOF MS (POS, DCTB : $CHCl_3$ = 1:3):

calc. for $C_{60}H_{71}BF_2N_2O$ [$M^{\bullet+}$]: m/z = 912.540 found: m/z = 912.616

^{1}H-NMR (400.0 MHz, $CDCl_3$):

δ [ppm] = 8.20 (s, 2 H, 2 × C<u>H</u>), 8.02 – 7.95 (-, 6 H, 6 × C<u>H</u>), 7.11 (AA', 2 H, 2 × C<u>H</u>), 7.03 (BB', 2 H, 2 × C<u>H</u>), 3.92 (d, $^3J_{HH}$ = 5.9 Hz, 2 H, OC<u>H</u>$_2$), 3.12 – 2.95 (m, 2 H, C<u>H</u>$_2$) 2.82 (s, 3 H, CC<u>H</u>$_3$), 2.68 (s, 3 H, CC<u>H</u>$_3$), 1.89 – 1.74 (m, 2 H, C<u>H</u>$_2$), 1.70 – 1.13 (-, 23 H, 3 × C<u>H</u>, 7 × C<u>H</u>$_2$, 2 × CC<u>H</u>$_3$), 1.02 – 0.93 (-, 9 H, CHC<u>H</u>$_3$, 2 × CH_2C<u>H</u>$_3$), 0.87 (d, $^3J_{HH}$ = 6.6 Hz, 6 H, CH(C<u>H</u>$_3$)$_2$), 0.23 (s, 9 H, Si(C<u>H</u>$_3$)$_3$).

^{13}C-NMR (100.6 MHz, $CDCl_3$):

δ [ppm] = 160.4 (C_q), 158.5 (2 × C_q), 145.0 (C_q), 144.3 (C_q), 143.1 (C_q), 141.8 (C_q), 131.9 (C_q), 131.6 (C_q), 131.4 (C_q), 130.9 (C_q), 129.1 (CH), 128.0 (CH), 127.3 (CH), 126.9 (CH), 126.2 (C_q), 125.6 (CH), 124.2 (C_q), 122.9 (C_q), 120.4 (C_q), 116.3 (C_q), 116.2 (C_q), 115.4 (CH), 101.6 (C_q), 97.4 (2 × C_q), 82.0 (C_q), 71.0 (CH_2), 39.7 (CH_2), 39.5 (CH), 39.4 (CH_2), 37.3 (CH_2), 34.2 (CH_2), 32.7 (CH), 30.6 (CH_2), 29.2 (CH_2), 28.1 (CH), 24.8 (CH_2), 23.9 (CH_2), 23.1 (CH_2), 22.8 (CH_3), 22.7 (CH_3), 19.8 (CH_3), 14.2 (CH_3), 13.96 (CH_3), 13.90 (CH_3), 13.7 (2 × CH_3), 11.3 (CH_3), 0.2 (CH_3).

PyB-3

CA [–]

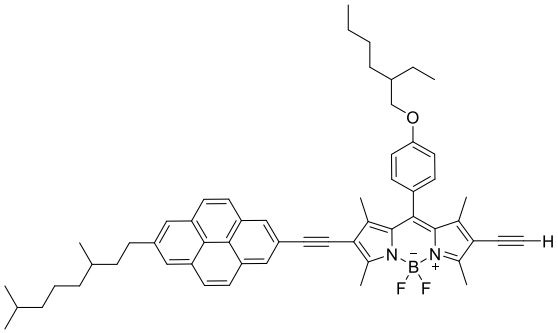

Synthesis according to literature[97]

Under a nitrogen atmosphere **PyB-2** (70.0 mg, 76.7 µmol) was dissolved in dry THF (10 ml) and degassed for 20 min by bubbling a stream of nitrogen through the solution. The mixture was cooled to −70 °C and TBAF (1 M in THF, 770 µmol, 770 µl) was added. The solution was stirred at −70 °C for 2 h and quenched with 5 % acetic acid (15 ml). After warming up to room temperature the solution was washed with water (2 × 50 ml) and the aqueous layer was extracted with CH_2Cl_2 (3 × 100 ml). The combined organic layers were dried over Na_2SO_4. The solvent was removed under reduced pressure and the crude product was purified through flash column chromatography in PE:CH_2Cl_2 (70:30). The residue was precipitated from CH_2Cl_2/acetonitrile.

Yield: 42.8 mg 50.9 µmol 66 % of a purple-blue solid

$C_{57}H_{63}BF_2N_2O$ [840.93]

MALDI-TOF MS (POS, DCTB : $CHCl_3$ = 1:3):

calc. for $C_{57}H_{63}BF_2N_2O$ [$M^{\bullet+}$]: m/z = 840.501 found: m/z = 840.501

^{1}H-NMR (400.0 MHz, $CDCl_3$):

δ [ppm] = 8.20 (s, 2 H, 2 × C<u>H</u>), 8.02 – 7.95 (-, 6 H, 6 × C<u>H</u>), 7.12 (AA', 2 H, 2 × C<u>H</u>), 7.03 (BB', 2 H, 2 × C<u>H</u>), 3.92 (d, $^{3}J_{HH}$ = 5.8 Hz, 2 H, OC<u>H$_2$</u>), 3.3 (s, 1 H, ≡C<u>H</u>) 3.12 – 2.95 (m, 2 H, C<u>H$_2$</u>), 2.83 (s, 3 H, CC<u>H$_3$</u>), 2.68 (s, 3 H, CC<u>H$_3$</u>), 1.89 – 1.74 (m, 2 H, C<u>H$_2$</u>), 1.70 – 1.11 (-, 23 H, 3 × C<u>H</u>, 7 × CH_2, 2 × CC<u>H$_3$</u>), 1.02 – 0.92 (-, 9 H, 3 × CHC<u>H$_3$</u>), 0.87 (d, $^{3}J_{HH}$ = 6.6 Hz, 6 H, C(C<u>H$_3$</u>)$_2$).

^{13}C-NMR (100.6 MHz, $CDCl_3$):

δ [ppm] = 160.4 (C_q), 158.9 (C_q), 158.2 (C_q), 145.2 (C_q), 144.7 (C_q), 143.3 (C_q), 141.8 (C_q), 132.0 (C_q), 131.4 (2 × C_q), 130.9 (C_q), 129.1 (CH), 128.0 (CH), 127.3 (CH), 126.9 (CH), 126.1 (C_q), 125.6 (CH), 124.2 (C_q), 122.9 (C_q), 120.4 (C_q), 116.5 (C_q), 115.4 (CH), 114.8 (C_q), 97.5 (C_q), 84.0 (CH), 81.9 (C_q), 76.2 (C_q), 71.0 (CH_2), 39.7 (CH_2), 39.5 (CH), 39.4 (CH_2), 37.3 (CH_2), 34.2 (CH_2), 32.7 (CH), 30.6 (CH_2), 29.2 (CH_2), 28.1 (CH), 24.8 (CH_2), 24.0 (CH_2), 23.1 (CH_2), 22.8 (CH_3), 22.7 (CH_3), 19.8 (CH_3), 14.2 (CH_3), 14.0 (CH_3), 13.9 (CH_3), 13.6 (2 × CH_3), 11.3 (CH_3).

PySQB

CA [–]

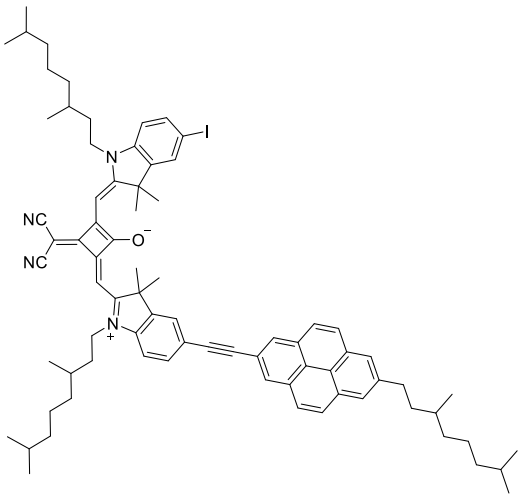

Synthesis according to GPI

SQB-4 (50.0 mg, 51.0 µmol), **Py-8** (19.5 mg, 53.2 µmol), CuI (78.0 µg, 0.410 µmol), $Pd(C_6H_5CN)_2Cl_2$ (2.36 mg, 6.14 µmol), tri-*tert*-butylphosphane (1 M in toluene, 12.0 µl, 12.0 µmol), DIPA (25.0 µl, 178 µmol), dioxane (5 ml); stirred for 5 d at 60 °C, after 24 h and 48 h additional **Py-8** (10 mg, 26.3 µmol) added; flash column chromatography CH_2Cl_2;

Yield: 27.8 mg 23.0 µmol 45 % of a green shiny solid

$C_{77}H_{91}IN_4O$ [1215.48]

MALDI-TOF MS (POS, DCTB : $CHCl_3$ = 1:3):

calc. for $C_{77}H_{91}IN_4O$ [$M^{\bullet+}$]: m/z = 1214.623 found: m/z = 1215.290

^{1}H-NMR (400.0 MHz, $CDCl_2$):

δ [ppm] = 8.33 (s, 2 H, 2 × C<u>H</u>), 8.09 – 8.03 (-, 6 H, 6 × C<u>H</u>), 7.72 – 7.64 (-, 2 H, 2 × C<u>H</u>), 7.38 – 7.34 (-, 2 H, 2 × C<u>H</u>), 7.11 – 7.09 (m, 1 H, 1 × C<u>H</u>), 6.85 – 6.82 (m, 1 H, C<u>H</u>), 6.53 (s, 1 H, =C<u>H</u>), 6.48 (s, 1 H, =C<u>H</u>) 4.13 – 3.91 (-, 4 H, 2 × NC<u>H_2</u>), 3.16 – 2.99 (m, 2 H, C<u>H_2</u>), 1.81 (s, 6 H, C(C<u>H_3</u>)<u>$_2$</u>), 1.75 (s, 6 H, C(C<u>H_3</u>)<u>$_2$</u>), 1.67 – 0.68 (-, 57 H, 6 × C<u>H</u>, 12 × C<u>H_2</u>, 3 × CHC<u>H_3</u>, 3 × CH(C<u>H_3</u>)<u>$_2$</u>).

This compound was not completely purified.

B(SQB)

CA [–]

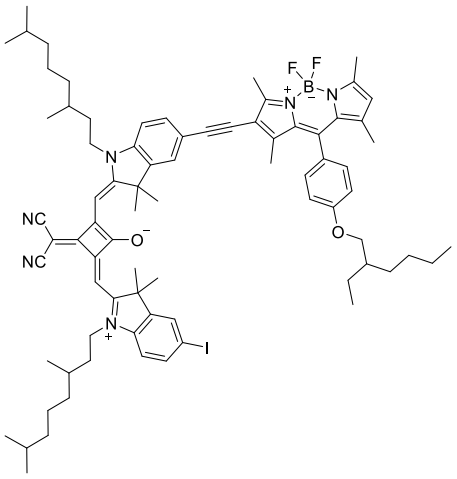

Synthesis according to GPII:

SQB-4 (200 mg, 205 µmol), $Pd(PPh_3)_4$ (9.86 mg, 8.53 µmol), CuI (1.63 mg, 8.56 µmol), **BODIPY-7** (81.0 mg, 170 µmol), toluene (6 ml), TEA (1 ml); stirred at rt for 7 d; purified by GPC in $CHCl_3$; precipitated from CH_2Cl_2/acetonitrile.

Yield: 89.7 mg 67.7 µmol 40 % of a blue solid with a purple gleam

$C_{78}H_{96}BF_2IN_6O_2$ [1325.35]

MALDI-TOF MS (POS, DCTB : $CHCl_3$ = 1:3):

calc. for $C_{78}H_{96}BF_2IN_6O_2$ [$M^{\bullet+}$]: m/z = 1324.671 found: m/z = 1324.708

^{1}H-NMR (400.0 MHz, $CDCl_3$):

δ [ppm] = 7.65 (dd, $^3J_{HH}$ = 8.2 Hz, $^4J_{HH}$ = 1.6 Hz 1 H, CH), 7.61 (d, $^4J_{HH}$ = 1.6 Hz, 1 H, CH), 7.44 (dd, $^3J_{HH}$ = 8.2 Hz, $^4J_{HH}$ = 1.5 Hz, 1 H, CH), 7.39 (d, $^4J_{HH}$ = 1.4 Hz, 1 H, CH), 7.23 (AA', 2 H, 2 × CH), 7.10 (BB', 2 H, 2 × CH), 6.97 (d, $^3J_{HH}$ = 8.3 Hz, 1 H, CH), 6.78 (d, $^3J_{HH}$ = 8.3 Hz, 1 H, CH), 6.52 (s, 1 H, =CH), s (6.47, 1 H, =CH), s (6.04, 1 H, CH), 4.09 – 3.94 (-, 4 H, 2 × NCH_2), 3.91 (d, $^3J_{HH}$ = 5.9 Hz, 2 H, OCH_2), 2.71 (s, 3 H, CCH_3), 2.58 (s, 3 H, CCH_3), 1.81 – 1.14 (-, 29 H, 5 × CH, 12 × CH_2), 1.76 (s, 6 H, $C(CH_3)_2$), 1.74 (s, 6 H, $C(CH_3)_2$), 1.59 (s, 3 H, CCH_3), 1.48 (s, 3 H, CCH_3), 1.03 – 0.91 (-, 12 H, 2 × $CHCH_3$, 2 × CH_2CH_3), 0.86 – 0.85 (-, 12 H, 2 × $C(CH_3)_2$).

This compound was not completely purified.

$(SQB)_2B$-3

CA [–]

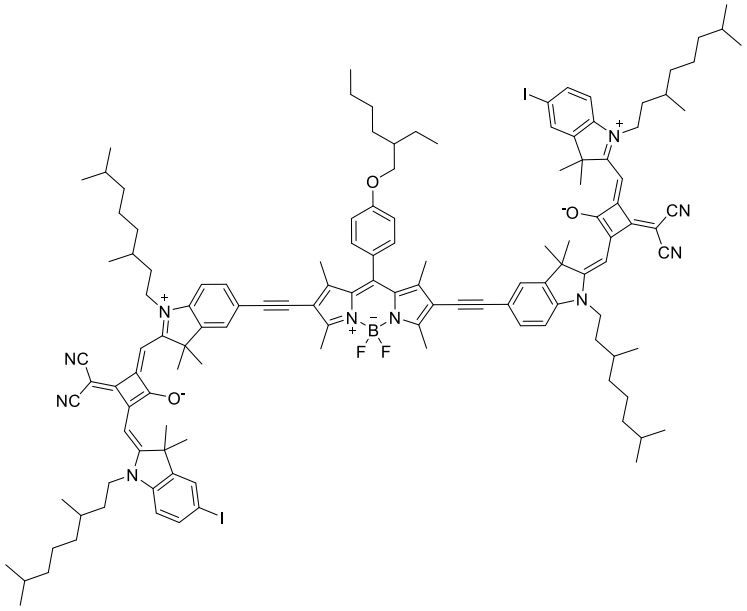

Synthesis according to GPII

SQB-4 (218 mg, 223 µmol), $Pd(PPh_3)_4$ (9.67 mg, 8.37 µmol), CuI (2.98 mg, 15.6 µmol), **BODIPY-4** (55.8 mg, 112 µmol), toluene (6 ml), TEA (1 ml); stirred at rt for 6 d; **BODIPY-4** (5.00 mg, 9.99 µmol) added, stirred at rt for 7 d, stirred for 3 d at 40 °C, purified by GPC in $CHCl_3$.

Yield: 39.0 mg 17.7 µmol 15 % of a blue solid with a purple gleam

$C_{129}H_{157}BF_2I_2N_{10}O_3$ [2198.31]

MALDI-TOF MS (POS, DCTB : $CHCl_3$ = 1:3):

calc. for $C_{129}H_{157}BF_2I_2N_{10}O_3$ [$M^{\bullet+}$]: m/z = 2198.062 found: m/z = 2198.263

^{1}H-NMR (400.0 MHz, CD_2Cl_2):

δ [ppm] = 7.68 – 7.47 (-, 8 H, 8 × C<u>H</u>), 7.22 (AA', 2 H, 2 × C<u>H</u>), 7.09 (BB', 2 H, 2 × C<u>H</u>), 7.03 (d, $^3J_{HH}$ = 8.3 Hz, 2 H, 2 × C<u>H</u>), 6.84 (d, $^3J_{HH}$ = 8.9 Hz, 2 H, 2 × C<u>H</u>), 6.50 (s, 2 H, 2 × =C<u>H</u>), s (6.47, 2 H, 2 × =C<u>H</u>), 4.10 – 3.95 (-, 10 H, 4 × NC<u>H$_2$</u>, OC<u>H$_2$</u>), 2.72 (s, 6 H, 2 × CC<u>H$_3$</u>), 1.81 – 1.14 (-, 49 H, 9 × C<u>H</u>, 20 × C<u>H$_2$</u>), 1.75 (s, 12 H, 2 × C(C<u>H$_3$</u>)<u>$_2$</u>), 1.73 (s, 12 H, 2 × C(C<u>H$_3$</u>)<u>$_2$</u>), 1.64 (s, 6 H, 2 × CC<u>H$_3$</u>), 1.03 – 1.01 (-, 18 H, 4 × CHC<u>H$_3$</u>, 2 × CH_2C<u>H$_3$</u>), 0.86 – 0.85 (-, 24 H, 4 × C(C<u>H$_3$</u>)<u>$_2$</u>).

This compound was not completely purified.

Anth-1

CA [–]

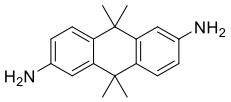

Synthesis according to literature[202]

Anth-5 (2.84 g, 8.70 mmol) was dissolved in ethanol (9 ml) and HCl (2.11 ml, 25.5 mmol) and then iron powder (2.27 g, 40.6 mmol) was added. The mixture was heated in an ultrasonic bath for 6 h to 60 °C and subsequently stirred for 16 h at 90 °C in an oilbath. The iron was removed by column filtration with ethanol as eluent. The solvent was removed under reduced pressure and the residue was dissolved in Na_2CO_3 solution (10 %, 400 ml) and extracted with EA (3 × 100 ml).

Yield: 1.00 g 3.75 mmol 43 % of a yellow solid

$C_{18}H_{22}N_2$ [266.38]

EI-MS: 460.6 (100 %, $[2M–2 \times H, –5 \times CH_3]^+$), 208.2 (42 %, $[M–2 \times NH_2, –2 \times CH_3]^+$).

^{1}H-NMR (400.0 MHz, methanol-d_4):

δ [ppm] = 7.27 (d, $^3J_{HH}$ = 8.5 Hz, 2 H, 2 × CH), 6.91 (d, $^4J_{HH}$ = 2.4 Hz, 2 H, 2 × CH), 6.67 (dd, $^3J_{HH}$ = 8.5 Hz, $^4J_{HH}$ = 2.4 Hz, 2 H, 2 × CH), 1.55 (s, 12 H, 2 × C(CH_3)$_2$).

The signal of the NH_2-group is missing.

^{13}C-NMR (100.6 MHz, methanol-d_4):

δ [ppm] = 145.8 (C_q), 144.2 (C_q), 133.8 (C_q), 128.5 (CH), 116.1 (CH), 114.4 (CH), 37.6 (C_q), 35.3 (CH_3).

Anth-2

CA [24269-10-1]

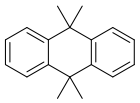

Synthesis according to literature[198]

Anthracene (17.8 g, 100 mmol) and diglyme (270 ml) were placed in a schlenk flask under a nitrogen atmosphere. Slowly $LiAlH_4$ (9.47 g, 250 mmol) was added. The mixture was stirred at 150 °C for 17 h, during which a colour change from grey to green could be observed. After deactivation with diluted HCl (2 l), the suspension was extracted with EA (4 × 250 ml). The combined organic layers were washed with water (500 ml) and dried over Na_2SO_4 and the solvent was removed under reduced pressure.

Yield: 6.87 g 29.1 mmol 29 % of a colourless solid

$C_{18}H_{20}$ [236.35]

^{1}H-NMR (400.0 MHz, CD_2Cl_2):

δ [ppm] = 7.53 – 7.51 (m, 4 H, 4 × CH), 7.25 – 7.23 (m, 4 H, 4 × CH), 1.65 (s, 12 H, 2 × $C(CH_3)_2$).

Anth-3

CA: [–]

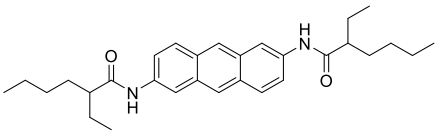

Synthesis according to literature[197]

In a Schlenk flask **Anth-4** (500 mg, 1.02 mmol), an aqueous solution of NaOH (2 M, 1 ml) and *iso*propanol (50 ml) were combined. In 2 h $NaBH_4$ (53.0 mg, 1.33 mmol) was added and the mixture was refluxed for 17 h. After allowing to cool down to 40 °C the suspension was poured into water (40 ml) and stirred for 1 h at room temperature. Filtration of the mixture was followed by extraction with diethylether (50 ml). For final purification the solid was recrystallised from dimethylsulfdoxid.

Yield: 60.0 mg 130 µmol 13 % of a yellow solid

$C_{30}H_{40}N_2O_2$ [460.65]

MALDI-TOF MS (POS, DCTB : $CHCl_3$ = 1:3):

calc. for $C_{30}H_{40}N_2O_2$ [$M^{\bullet+}$]: m/z = 460.308 found: m/z = 460.344

^{1}H-NMR (400.0 MHz, dimethylsulfoxid-d_6):

δ [ppm] = 10.08 (s, 2 H, 2 × NH), 8.50 (d, $^4J_{HH}$ = 1.8 Hz, 2 H, 2 × CH), 8.34 (s, 2 H, 2 × CH), 7.98 (d, $^3J_{HH}$ = 9.1 Hz, 2 H, 2 × CH), 7.56 (dd, $^3J_{HH}$ = 9.1 Hz, $^4J_{HH}$ = 2.0 Hz, 2 H, 2 × CH), 2.32 – 2.40 (m, 2 H, 2 × CH), 1.23 – 1.67 (-, 16 H, 8 × CH_2), 0.84 – 0.91 (-,12 H, 4 × CH_2CH_3).

^{13}C-NMR (100.6 MHz, dimethylsulfoxid-d_6):

δ [ppm] = 174.5 (C_q), 135.6 (C_q), 130.8 (C_q), 129.0 (C_q), 128.4 (CH), 124.8 (CH), 121.2 (CH), 114.2 (CH), 48.4 (CH), 32.0 (CH_2), 29.4 (CH_2), 25.8 (CH_2), 22.3 (CH_2), 14.0 (CH_3), 11.9 (CH_3).

Anth-5

CA [–]

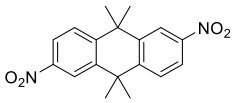

Synthesis according to literature [199]

Anth-2 (6.87 g, 29.1 mmol) was dissolved in acetic acid anhydrid and nitromethane (1:1, 190 ml) and cooled to 0 °C. Nitric acid was dropped to the solution (27 ml) while the temperature was kept under 5 °C. Subsequently stirring was continued for 30 min at 0 °C and 1 h at room temperature. The mixture was poored into ice water (200 ml), filtered and the solid was washed with cold water until the pH of the filtrate was neutral. To separate the *cis*- and the *trans*-isomers the crude mixture was recrystallised from toluene/diethlether (1:1).

Yield: 2.28 g 6.99 mmol 24 % of a colourless solid

$C_{18}H_{18}N_2O_4$ [326.35]

EI-MS: 311.2 (100 %, $[M–CH_3]^+$), 296.1 (47 %, $[M–2 \times CH_3]^+$),266.2 (4 %, $[M–4 \times CH_3]^+$).

^{1}H-NMR (400.0 MHz, $CDCl_3$):

δ [ppm] = 8.41 (d, $^4J_{HH}$ = 2.4 Hz, 2 H, 2 × CH), 8.13 (dd, $^3J_{HH}$ = 8.8 Hz, $^4J_{HH}$ = 2.4 Hz, 2 H, 2 × CH), 7.70 (d, $^3J_{HH}$ = 8.8 Hz, 2 H, 2 × CH), 1.76 (s, 12 H, 2 × C(CH_3)$_2$).

^{13}C-NMR (100.6 MHz, $CDCl_3$):

δ [ppm] = 148.0 (C_q), 147.0 (C_q), 142.6 (C_q), 182.4 (CH), 122.4 (CH), 121.7 (CH), 38.5 (C_q), 35.0 (CH_3).

Anth-6

CA [–]

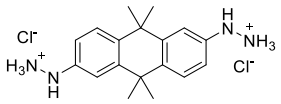

Synthesis according to literature[204]

Anth-1 (740 mg, 2.78 mmol) in water (4 ml) and HCl (konz., 14 ml) was coold to -5 °C. A solution of sodiumnitrite (399 mg, 5.78 mmol) in water (5 ml) was added slowly, while keeping the temperature below 0 °C. Tin (14.0 mg, 118 µmol) and tin(II)-chlorid (2.42 g, 12.8 mmol) were dissolved in boiling HCl (konz., 5 ml). Subsequently, the diazonium salt solution was added to this solution while keeping the temperature at −5 °C. The reaction mixture was stirred at that temperature for 1 h. The solid was collected through filtration and washed with a solution of HCl (konz., 3 ml) in water (3 ml) followed by water (3 ml) and dried under high vacuum.

Yield: 1.02 mg 2.76 mmol 99 % of a yellow solid

$C_{18}H_{26}Cl_2N_4$ [369.33]

EI-MS: 236.3 (100 %, $[M–2 \times NHNH_3Cl]^+$), 221.2 (87 %, $[M–2 \times NHNH_3Cl, –4 \times CH_3]^+$).

^{1}H-NMR (400.0 MHz, methanol-d_4):

δ [ppm] = 7.56 (d, $^3J_{HH}$ = 8.7 Hz, 2 H, 2 × CH), 7.18 (d, $^4J_{HH}$ = 2.6 Hz, 2 H, 2 × CH), 6.93 (dd, $^3J_{HH}$ = 8.7 Hz, $^4J_{HH}$ = 2.6 Hz, 2 H, 2 × CH), 1.64 (s, 12 H, 2 × C(CH_3)$_2$).

The signals of the NH-group and the $(NH_3)^+$-group are missing.

^{13}C-NMR (100.6 MHz, methanol-d_4):

δ [ppm] = 144.5 (C_q), 144.4 (C_q), 137.8 (C_q), 129.3 (CH), 115.3 (CH), 113.9 (CH), 38.3 (C_q), 35.3 (CH_3).

Ind-8

CA [–]

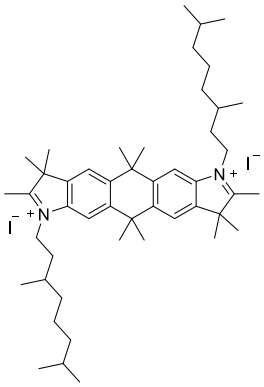

Synthesis according to literature[122]

Ind-9 (507 mg, 1.27 mmol) and 1-iod-3,7-dimethyloctane (**Alk-2**) (629 µl, 3.05 mmol) were heated in nitromethan (12 ml) for 18 h under reflux. The solvent was removed under reduced pressure. Diethylether (10 ml) was added to the residue, what led to the precipitation of a solid. The mixture was storred for 1 h at 4 °C, the solid was collected through filtration and washed with diethylether (15 ml). The crude product was recrystallised from cyclohexane. The product was used without further purification.

Yield: 778 mg 832 µmol 66 % of a dark brown solid

$C_{48}H_{76}I_2N_2$ [934.94]

MALDI-TOF MS (POS, DCTB : $CHCl_3$ = 1:3):

calc. for $C_{48}H_{76}N_2$ [$M^{\bullet+}$]: m/z = 680.600 found: m/z = 679.400

^{1}H-NMR (400.0 MHz, CD_2Cl_2):

δ [ppm] = 7.78 – 7.75 (-, 4 H, 4 × C<u>H</u>), 4.73 – 4.63 (m, 4 H, 2 × NC<u>H$_2$</u>), 3.04 (s, 6 H, 2 × CC<u>H$_3$</u>), 1.95 – 0.87 (-, 62 H, 4 × C<u>H</u>, 8 × C<u>H$_2$</u>, 2 × CHCH$_3$, 2 × CH(C<u>H$_3$</u>)<u>$_2$</u>, 4 × C(C<u>H$_3$</u>)<u>$_2$</u>).

Ind-9

CA [–]

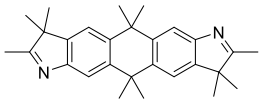

Synthesis according to literature[208]

Anth-6 (900 mg, 2.44 mmol), 3-methylbutanone (1.79 ml, 16.7 mmol) and acetic acid (30 ml) were stirred for 10 min at 160 °C in the microwave oven. After allowing the reation mixture to cool down to rt the solvent was removed under reduced pressure. The residue was parted in water (100 ml) and CH_2Cl_2 (100 ml) and the layers were separated. The aqueous phase was extracted with PE (3 × 50 ml). The combined organic layers were washed with brine (50 ml) and dried over Na_2SO_4. Lastly, the solvent was removed under reduced pressure. The product was used without further purification.

Yield: 507 mg 1.27 mmol 52 % of a wine-red solid

$C_{28}H_{34}N_2$ [398.58]

MALDI-TOF MS (POS, DCTB : $CHCl_3$ = 1:3):

calc. for $C_{28}H_{34}N_2$ [$M^{\bullet+}$]: m/z = 398.271 found: m/z = 397.274

^{1}H-NMR (400.0 MHz, CD_2Cl_2):

δ [ppm] = 7.67 – 7.45 (-, 4 H, 4 × C<u>H</u>), 2.32 (s, 6 H, 2 × CC<u>H</u>$_3$), 1.71 (s, 12 H, 2 × C(C<u>H</u>$_3$)$_2$), 1.35 (s, 12 H, 2 × C(C<u>H</u>$_3$)$_2$).

7.2.4 Hexaarylbenzenes

Hexa-7-(2-(3,7-dimethyloctyl)pyrenyl)benzene (**HAB 1**)

CA [–]

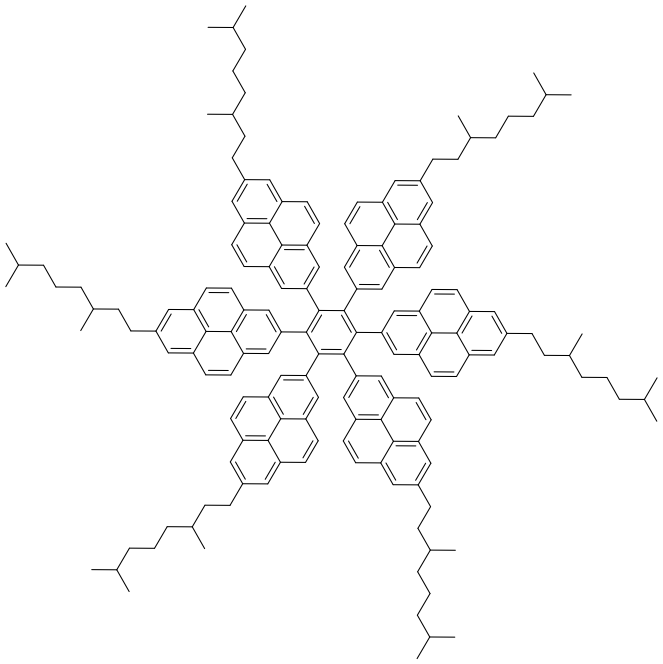

Synthesis according to literature[64]

Under a nitrogen atmosphere **Py-10** (20.0 mg, 28.3 µmol) was dissolved in dry dioxane (5 ml) and the solution was heated to 60 °C. $Co_2(CO)_8$ (1.42 mg, 4.15 µmol) was added and the reaction mixture was refluxed for 20 h. The solvent was removed under reduced pressure and the residue was purified by flash cloumn chromatography (eluent: PE:CH_2Cl_2 5:1 → PE:CH_2Cl_2 1:1). Further purification was accomplished by preparative TLC (eluent: PE:CH_2Cl_2 5:1).

Yield: 5.20 mg 2.45 µmol 26 % of a colourless solid

$C_{162}H_{174}$ [2121.12]

HRMS (ESI): $[M^{\bullet}+H^{+}] = C_{162}H_{175}^{\bullet+}$; calc.: 2120.36440; found: 2120.36494 (Δ = 0.25 ppm)

^{1}H-NMR (400.0 MHz, $CDCl_3$):

δ [ppm] = 8.00 (s, 12 H, 12 × C<u>H</u>), 7.57 (s, 12 H, 12 × C<u>H</u>), 7.50 – 7.44 (-, 24 H, 24 × C<u>H</u>), 2.85 – 2.68 (m, 12 H, 6 × C<u>H</u>$_2$), 1.64 – 1.01 (-, 60 H, 12 C<u>H</u>, 24 × C<u>H</u>$_2$), 0.84 (d, $^{3}J_{HH}$ = 6.4 Hz, 18 H, 6 × CHC<u>H</u>$_3$), 0.78 (d, $^{3}J_{HH}$ = 6.6 Hz, 18 H, 3 × C(C<u>H</u>$_3$)$_2$), 0.77 (d, $^{3}J_{HH}$ = 6.6 Hz, 18 H, 3 × C(C<u>H</u>$_3$)$_2$).

^{13}C-NMR (100.6 MHz, $CDCl_3$):

δ [ppm] = 142.0 (C_q), 140.4 (C_q), 137.9 (C_q), 131.0 (C_q), 129.4 (C_q), 128.2 (CH), 127.1 (CH), 126.6 (CH), 124.4 (CH), 122.7 (C_q), 122.4 (C_q), 39.7 (CH_2), 39.4 (CH_2), 37.2 (CH_2), 33.9 (CH_2), 32.6 (CH), 28.0 (CH), 24.7 (CH_2), 22.8 (CH_3), 22.7 (CH_3), 19.7 (CH_3).

1,2-Di-(7-(2-(3,7-dimethyloctyl)pyrenyl)-3,4,5,6-(tetraphenyl)benzene (**HAB 2**)

CA [–]

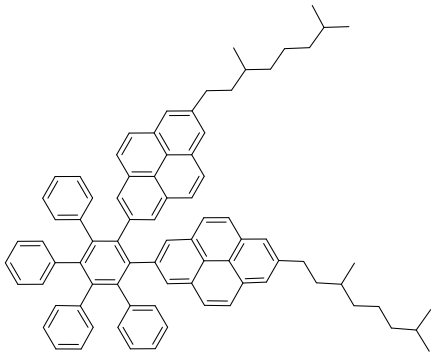

Synthesis according to literature[141]

Under a nitrogen atmosphere **Py-10** (30.0 mg, 42.0 µmol) and 2,3,4,5-tetraphenylcyclopentadienone (163 mg, 424 µmol) were dissolved in freshly degassed diphenylether (6 ml). The reaction mixture was heated in a sand bath at for 42 h 300 °C. Afterwards, the solvent was removed under reduced pressure and the residue was purified by flash column chromatography (eluent: PE:CH_2Cl_2 5:1 ⟶ PE:CH_2Cl_2 4:1 ⟶ CH_2Cl_2). For final purification a second flash column chromatography (PE:CH_2Cl_2 5:3 ⟶ 5:2 ⟶ 5:1) and preparative TLC (eluent: PE:CH_2Cl_2 5:1 ⟶ 5:2 ⟶ 5:3) was necessary.

Yield: 1.30 mg 1.22 µmol 3 % of a light yellow sollid

$C_{82}H_{78}$ [1063.53]

HRMS (ESI): [$M^{\bullet}$+H^{+}] = $C_{82}H_{79}^{\bullet+}$; calc.: 1063.61763; found: 1063.61715 (Δ = 0.45 ppm)

^{1}H-NMR (600.4 MHz, $CDCl_3$):

δ [ppm] = 7.75 – 7.73 (-, 8 H, 8 × C<u>H</u>), 7.64 (d, $^{3}J_{HH}$ = 9.1 Hz, 4 H, 4 × C<u>H</u>), 7.52 (d, $^{3}J_{HH}$ = 9.1 Hz, 4 H, 4 × C<u>H</u>), 6.95 – 6.92 (m, 4 H, 4 × C<u>H</u>), 6.91 – 6.88 (-, 8 H, 8 × C<u>H</u>), 6.87 – 6.83 (m, 2 H, 2 × C<u>H</u>), 6.68 – 6.64 (-, 4 H, 4 × C<u>H</u>), 6.60 – 6.57 (m, 2 H, 2 × C<u>H</u>), 2.95 – 2.80 (m, 4 H, 2 × C<u>H_2</u>), 1.73 – 1.07 (-, 20 H, , 4 × C<u>H</u>, 8 × C<u>H_2</u>), 0.91 (d, $^{3}J_{HH}$ = 6.5 Hz, 6 H, 2 × CHC<u>H_3</u>), 0.81 (d, $^{3}J_{HH}$ = 6.7 Hz, 12 H, 2 × CH(C<u>H_3</u>)<u>$_2$</u>).

^{13}C-NMR (151.0 MHz, $CDCl_3$):

δ [ppm] = 141.2 (C_q), 140.9 (C_q), 140.8 (C_q), 140.73 (C_q), 140.69 (C_q), 140.62 (C_q), 138.0 (C_q), 131.6 (CH), 131.5 (CH), 131.1 (C_q), 129.5 (C_q), 128.4 (CH), 127.4 (CH), 126.8 (CH), 126.7 (CH), 126.5 (CH), 125.4 (CH), 125.3 (CH), 124.6 (CH), 122.8 (C_q), 122.5 (C_q), 39.8 (CH_2), 39.4 (CH_2), 37.3 (CH_2), 34.1 (CH_2), 32.6 (CH), 28.1 (CH), 24.8 (CH_2), 22.82 (CH_3), 22.7 (CH_3), 19.8 (CH_3).

1-(7-(2-(3,7-Dimethyloctyl)pyrenyl)-2,3,4,5,6-(pentaphenyl)benzene (**HAB 3**)

CA [–]

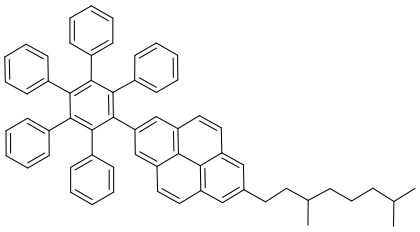

Synthesis according to literature[141]

Under a nitrogen atmosphere **Py-9** (25.0 mg, 56.5 µmol) and 2,3,4,5-tetraphenylcyclopentadienone (326 mg, 847 µmol) were dissolved in freshly degassed diphenylether (5 ml). The reaction mixture was heated in a sand bath for 22 h at 300 °C. Afterwards the solvent was removed under reduced pressure and the residue was purified by flash coloum chromatography (eluent: PE ⟶ PE:CH_2Cl_2 5:1 ⟶ CH_2Cl_2). The resulting crude product was precipitated from CH_2Cl_2/methanol and for final purification preparative TLC (eluent: PE: CH_2Cl_2 10:1 ⟶ 7:1 ⟶ 3:1) was applied.

Yield: 10.1 mg 12.6 µmol 22 % of a light yellow solid

$C_{62}H_{54}$ [799.09]

ESI pos. (high resolution): $[M^{\bullet}+H^{+}]$ = $C_{62}H_{55}^{\bullet+}$; calc.: 799.42983; found: 799.43035 (Δ = 0.65 ppm)

^{1}H-NMR (400.0 MHz, $CDCl_3$):

δ [ppm] = 7.87 (s, 2 H, 2 × C<u>H</u>), 7.80 (d, $^{3}J_{HH}$ = 9.0 Hz, 2 H, 2 × C<u>H</u>), 7.66 – 7.64 (-, 4 H, 4 × C<u>H</u>), 6.91 – 6.82 (-, 19 H, 19 × C<u>H</u>), 6.69 – 6.64 (-, 4 H, 4 × C<u>H</u>), 6.62 – 6.58 (-, 2 H, 2 × C<u>H</u>), 3.06 – 2.90 (m, 2 H, C<u>H$_2$</u>) 1.84 – 1.47 (-, 4 H, 2 × C<u>H</u>, C<u>H$_2$</u>), 1.41 – 1.11 (-, 6 H, 3 × C<u>H$_2$</u>), 0.98 (d, $^{3}J_{HH}$ = 6.48 Hz, 3 H, CHC<u>H$_3$</u>), 0.86 (d, $^{3}J_{HH}$ = 6.6 Hz, 6 H, CH(C<u>H$_3$</u>)$_2$).

^{13}C-NMR (100.6 MHz, $CDCl_3$):

δ [ppm] = 141.0 (C_q), 140.9 (C_q), 140.8 (2 × C_q), 140.64 (C_q), 140.60 (C_q), 140.55 (C_q), 140.5 (C_q), 138.1 (C_q), 131.6 (2 × CH), 131.5 (CH), 131.3 (C_q), 129.6 (C_q), 128.5 (CH), 127.6 (CH), 126.74 (3 × CH), 126.72 (CH), 126.6 (CH), 125.4 (CH), 125.3 (CH), 124.8 (CH), 123.0 (C_q), 122.6 (C_q), 40.0 (CH_2), 39.5 (CH_2), 37.3 (CH_2), 34.2 (CH_2), 32.7 (CH), 28.1 (CH), 24.9 (CH_2), 22.9 (CH_3), 22.8 (CH_3), 19.81 (CH_3).

7.2.5 Symmetrical Triads

Py_2SQB

CA [–]

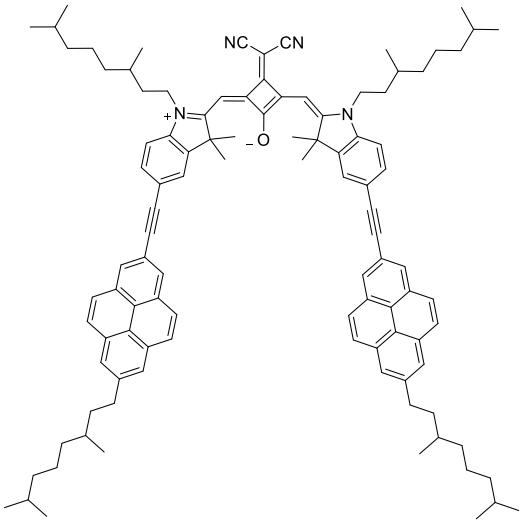

Synthesis according to GPI

SQB-1 (70.6 mg, 91.3 µmol), **Py-8** (61.2 mg, 145 µmol), CuI (1.07 mg, 5.62 µmol), $Pd(C_6H_5CN)_2Cl_2$ (3.23 mg, 8.43 µmol), tri-*tert*-butylphosphane (1 M in toluene, 16.9 µl, 16.9 µmol), DIPA (47.4 µl, 337 µmol), DMF (7 ml); stirred for 3 d at 75 °C, flash column chromatography PE → PE:CH_2Cl_2 1:1 → PE:CH_2Cl_2 2:3 → PE:CH_2Cl_2 1:2 → CH_2Cl_2 → EA; precipitation from CH_2Cl_2/acetonitrile.

Yield: 15.3 mg 10.5 µmol 14 % of a green shiny solid

$C_{105}H_{120}N_4O$ [1454.11]

HRMS (ESI): $[M^{\bullet+}] = C_{105}H_{120}N_4O^{+\bullet}$; calc.: 1452.94567; found: 1452.94739 (Δ = 1.18 ppm)

^{1}H-NMR (400.0 MHz, $CDCl_3$):

δ [ppm] = 8.33 (s, 4 H, 4 × CH), 8.06 – 8.01 (-, 12 H, 12 × CH), 7.64 – 7.61 (-, 4 H, 4 × CH), 7.05 (d, $^3J_{HH}$ = 5.2 Hz, 2 H, 2 × CH), 6.57 (s, 2 H, 2 × =CH), 4.12 – 4.01 (m, 4 H, 2 × NCH_2), 3.13 – 2.98 (m, 4 H, 2 × CH_2), 1.84 (s, 12 H, 2 × $C(CH_3)_2$), 1.67 – 0.68 (-, 76 H, 8 × CH, 16 × CH_2, 4 × $CHCH_3$, 4 × $CH(CH_3)_2$).

^{13}C-NMR (150.6 MHz, CD_2Cl_2):

δ [ppm] = 173.5 (C_q), 172.0 (C_q), 168.3 (C_q), 167.3 (C_q), 143.4 (C_q), 142.7 (C_q), 142.5 (C_q,), 132.5 (CH), 131.9 (C_q), 131.5 (C_q), 128.6 (CH), 127.9 (CH), 127.3 (CH), 126.2 (CH), 126.1 (CH), 124.7 (C_q), 123.2 (C_q), 120.6 (C_q), 119.8 (C_q), 119.1 (C_q), 110.8 (CH), 91.2 (C_q), 90.4 (CH), 90.1 (C_q), 49.9 (C_q), 43.7 (CH_2), 41.2 (C_q), 39.9 (CH_2), 39.7 (CH_2), 39.5 (CH_2), 37.5 (CH_2), 37.4 (CH_2), 34.4 (CH_2), 34.3 (CH_2), 33.2 (CH), 31.5 (CH), 28.4 (CH), 28.3 (CH), 26.79 (CH_3), 26.75 (CH_3), 25.1 (CH_2), 25.0 (CH_2), 22.9 (2 × CH_3), 22.8 (2 × CH_3), 19.84 (CH_3), 19.80 (CH_3).

Py_2SQA

CA [–]

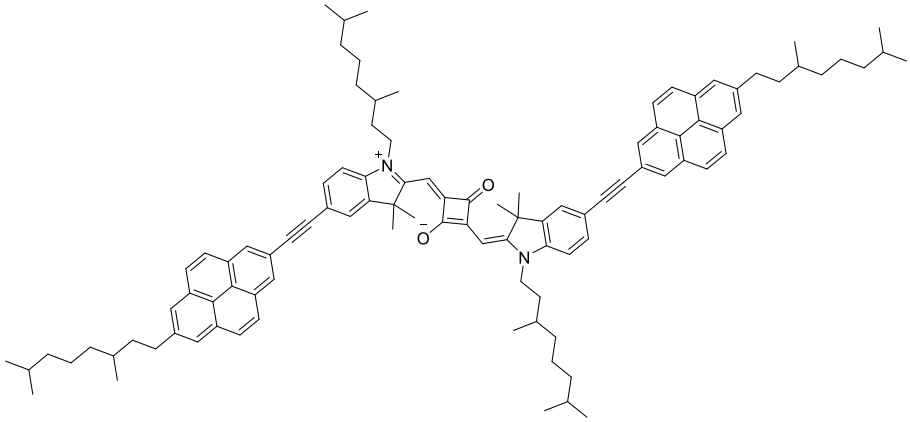

Under a nitrogen atmosphere $Pd(C_6H_5CN)_2Cl_2$ (4.96 mg, 12.9 µmol), CuI (1.64 mg, 8.61 µmol) and **SQA-4** (100 mg, 108 µmol) were dissolved in degassed dioxane (7 ml). The solution was freed from oxygen by bubbling a stream of nitrogen through the mixture. DIPA (50.1 µl, 3.55 mmol), P^{t}Bu$_3$ (1 M in toluene, 28.0 µl, 28.0 µmol) and **Py-8** (47.4 mg, 129 µmol) were added. The solution was stirred for 14 d at 60 °C under exclusion of light and the reaction progression was followed by mass spectrometry. Additional **Py-8** was added after 7 d (23.0 mg, 62.7 µmol), 9 d (23.0 mg, 62.7 µmol) and 11 d (10.0 mg, 27.3 µmol). After no further product formation could be observed the solution was cooled to room temperature. The solvent was removed under reduced pressure and the residue was purified by flash column chromatography in CH_2Cl_2. The crude product **PySQA-3** was subjected to a second *Sonoghasira* coupling without further purification. **PySQA-3** (128 mg, 107 µmol), $Pd(PPh_3)_4$ (6.31 mg, 5,46 µmol) and CuI (1.04 mg, 5.46 µmol) were dissolved in a degassed mixture of toluene (5 ml) and TEA (1 ml). The solution was degassed for 5 min and **Py-8** (84.0 mg, 229 µmol) was added. The solution was stirred at 40 °C under exclusion of light. After 7 d the solvent was removed under reduced pressure. The crude mixture was purified by GPC. For further purification the product was precipitated from diethylether/methanol.

Yield: 16.9 mg 12.0 µmol 16 % of a green shiny solid

$C_{102}H_{120}N_2O_2$ [1406.06]

MALDI-TOF MS (POS, DCTB : $CHCl_3$ = 1:3):

calc. for $C_{102}H_{120}N_2O_2$ [$M^{\bullet+}$]: m/z = 1405.938 found: m/z = 1406.001

^{1}H-NMR (400.0 MHz, $CDCl_3$):

δ [ppm] = 8.32 (s, 4 H, 4 × C<u>H</u>), 8.06 – 8.01 (-, 12 H, 12 × C<u>H</u>), 7.63 – 7.59 (-, 4 H, 4 × C<u>H</u>), 6.99 (d, $^3J_{HH}$ = 7.8 Hz, 2 H, 2 × C<u>H</u>), 6.03 (s, 2 H, 2 × =C<u>H</u>), 4.11 – 3.95 (m, 4 H, 2 × NC<u>H$_2$</u>), 3.14 – 2.98 (m, 4 H, 2 × C<u>H$_2$</u>), 1.86 (s, 12 H, 2 × C(C<u>H$_3$</u>)$_2$), 1.72 – 1.01 (-, 52 H, 8 × C<u>H</u>, 16 x C<u>H$_2$</u>, 4 × CHC<u>H$_3$</u>), 0.90 – 0.86 (-, 24 H, 4 × CH(C<u>H$_3$</u>)$_2$).

This compound was not completely purified.

Py_2B

CA [–]

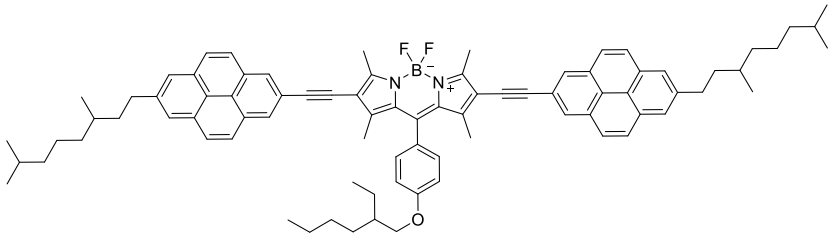

Synthesis according to literature[158]

In a nitrogen atmosphere $Pd(dppf)_2Cl_2 \cdot CH_2Cl_2$(1.59 mg, 1.95 µmol), CuI (0.742 mg, 3.90 µmol) and **BODIPY-2** (22.8 mg, 32.4 µmol) were dissolved in a degased mixture of THF/TEA (5:2). The mixture was again degassed and pyrene **Py-8** (25.0 mg, 68.2 µmol) was added. After stirring for four days at rt the solution was heated to 50 °C and stirred for additional 24 h. The solvent was removed under reduced pressure and the residue was purified by flash column chromatography (eluent: PE ⟶ PE:CH_2Cl_2 7:3 ⟶ PE:CH_2Cl_2 1:1 ⟶ CH_2Cl_2 ⟶ EA). For further purification the resulting product was precipitated from CH_2Cl_2/acetonitrile.

Yield: 19.2 mg 16.3 µmol 50 % of a dark-blue solid.

$C_{83}H_{91}BF_2N_2O$ [1181.43]

HRMS (ESI): $[M^{\bullet+}] = C_{83}H_{91}BF_2N_2O^{\bullet+}$; calc.: 1180.719996; found: 1180.71776 (Δ = 1.89 ppm)

^{1}H-NMR (400.0 MHz, CD_2Cl_2):

δ [ppm] = 8.00 – 7.98 (-, 8 H; 8 × C<u>H</u>), 7.96 – 7.93 (d, $^{3}J_{HH}$ = 9.0 Hz, 4 H, 4 × C<u>H</u>), 7.83 (s, 4 H, 4 × C<u>H</u>), 7.16 (AA', 2 H, 2 × C<u>H</u>), 7.07 (BB', 2 H, 2 × C<u>H</u>), 3.97 (d, $^{3}J_{HH}$ = 5.7 Hz, 2 H, OC<u>H$_2$</u>), 2.76 (s, 6 H, 2 × CC<u>H$_3$</u>), 2.86 (m, 4 H, 2 × C<u>H$_2$</u>), 1.84 – 0.97 (-, 47 H, 5 × C<u>H</u>, 12 × C<u>H$_2$</u>, 2 × CC<u>H$_3$</u>, 2 × CHC<u>H$_3$</u>, 2 × CH$_2$C<u>H$_3$</u>), 0.87 (m, 12 H, 2 × C(C<u>H$_3$</u>)$_2$).

^{13}C-NMR (150.6 MHz, CD_2Cl_2):

δ [ppm] = 161.3 (C_q), 158.1 (C_q), 143.9 (C_q), 142.6 (C_q), 141.6 (C_q), 131.8 (C_q), 131.3 (C_q), 130.8 (C_q), 129.2 (CH), 127.9 (CH), 127.2 (CH), 126.8 (CH), 126.3 (C_q), 125.5 (CH), 124.1 (C_q), 122.9 (C_q), 120.3 (C_q), 116.1 (C_q), 115.3 (CH), 97.4 (C_q), 82.0 (C_q), 71.0 (CH_2), 39.6 (CH_2), 39.5 (CH), 39.4 (CH_2), 37.2 (CH_2), 33.9 (CH_2), 32.7 (CH), 30.7 (CH_2), 29.3 (CH_2), 28.1 (CH), 24.8 (CH_2), 24.0 (CH_2), 23.2 (CH_2), 22.8 (CH_3), 22.7 (CH_3), 19.7 (CH_3), 14.3 (CH_3), 13.9 (CH_3), 13.7 (CH_3), 11.3 (CH_3).

B_2SQB-3

CA [–]

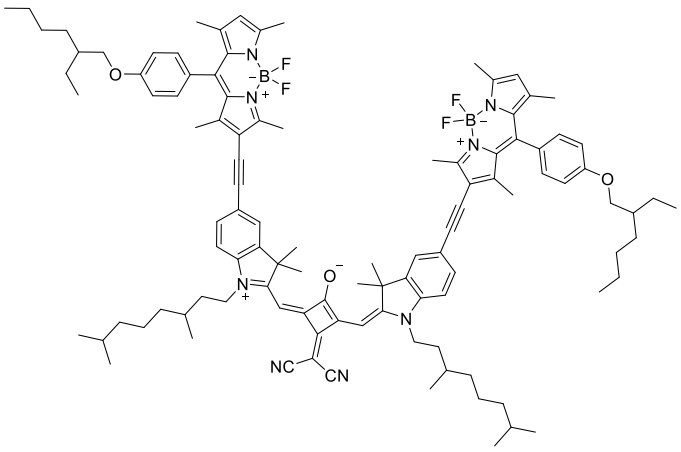

Synthesis according to GPII

SQB-4 (30.0 mg, 30.7 µmol), $Pd(PPh_3)_4$ (1.77 mg, 1.54 µmol), CuI (30.0 µg, 0.158 µmol), **BODIPY-7** (14.6 mg, 30.6 µmol), (6 ml) toluene, TEA (1 ml); stirred for 2 d at 40 °C. **BODIPY-7** (14.7 mg, 30.9 µmol) added; stirred for 6 d at 40 °C; flash column chromatography (eluent: CH_2Cl_2:PE 60:40 → CH_2Cl_2 → EA); precipitated from CH_2Cl_2/acetonitrile.

Yield: 13.9 mg 8.30 µmol 27 % of a purple solid with a green gleam

$C_{107}H_{130}B_2F_4N_8O_3$ [1673.9]

HRMS (ESI): $[M^{+\bullet}] = C_{107}H_{130}B_2F_4N_8O_3^{\bullet+}$; calc.: 1673.04114; found: 1673.03941 (Δ = 1.03 ppm)

^{1}H-NMR (600.4 MHz, $CDCl_3$):

δ [ppm] = 7.43 (-, 2 H, 2 × CH), 7.38 (s, 2 H, 2 × CH), 7.16 (AA', 4 H, 4 × CH), 7.03 (BB', 4 H, 4 × CH), 6.95 (d, $^3J_{HH}$ = 8.2 Hz, 2 H, 2 × CH), 6.50 (s, 2 H, 2 × =CH) 6.04 (s, 2 H, 2 × CH), 4.08 – 3.95 (m, 4 H, 2 × NCH_2), 3.91 (d, $^3J_{HH}$ = 5.9 Hz, 4 H, 2 × OCH_2), 2.71 (s, 6 H, 2 × CCH_3), 2.58 (s, 6 H, 2 × CCH_3), 1.80 – 1.72 (-, 16 H, 2 × CH, 2 × CH_2, 2 × $C(CH_3)_2$), 1.67 – 1.10 (-, 46 H, 4 × CH, 16 × CH_2, 4 × CCH_3), 1.01 (d, $^3J_{HH}$ = 6.5 Hz, 6 H, 2 × $CHCH_3$), 0.98 – 0.91 (-, 12 H, 4 × CH_2CH_3), 0.85 – 0.84 (m, 12 H, 2 × $C(CH_3)_2$).

^{13}C-NMR (151.0 MHz, $CDCl_3$):

δ [ppm] = 173.1 (C_q), 171.4 (C_q) 168.0 (C_q), 166.7 (C_q), 160.3 (C_q), 157.7 (C_q), 156.3 (C_q), 145.0 (C_q), 142.78 (C_q), 142.72 (C_q), 142.5 (C_q), 141.5 (C_q), 133.1 (C_q), 131.7 (CH), 130.8 (C_q), 129.2 (CH), 126.4 (CH), 125.1 (C_q), 122.2 (CH), 119.9 (C_q), 118.8 (C_q), 115.4 (CH), 114.8 (C_q), 110.0 (CH), 95.6 (C_q), 89.9 (CH), 83.2 (C_q), 71.0 (CH_2), 49.4 (C_q), 43.1 (CH_2), 41.2 (C_q), 39.5 (CH), 39.2 (CH_2), 37.2 (CH_2), 34.2 (CH_2), 31.0 (CH), 30.6 (CH_2), 29.2 (CH_2), 28.1 (CH), 26.74 (CH_3), 26.71 (CH_3), 24.7 (CH_2), 24.0 (CH_2), 23.1 (CH_2), 22.8 (CH_3), 22.7 (CH_3), 19.8 (CH_3), 15.0 (CH_3), 14.9 (CH_3), 14.3 (CH_3), 13.7 (CH_3), 13.6 (CH_3), 11.3 (CH_3).

$(SQB)_2$B-4

CA [–]

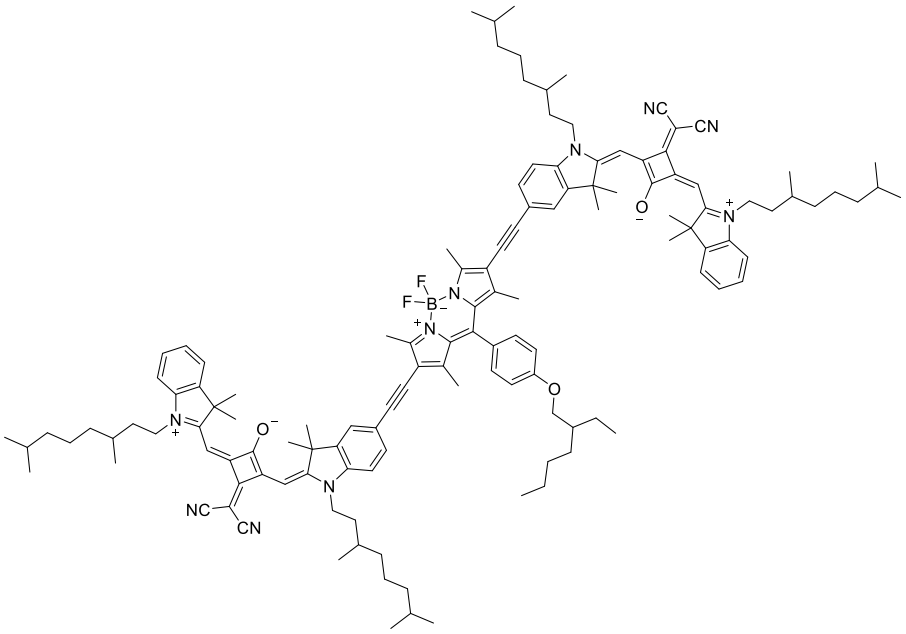

Synthesis according to GPII

SQB-6 (85.0 mg, 100 µmol), $Pd(PPh_3)_4$ (2.89 mg, 2.50 µmol), CuI (476 µg, 2.50 µmol), **BODIPY-4** (25.0 mg, 50.0 µmol), toluene (6 ml), TEA (1 ml); stirred at rt for 5 d; purified by GPC in $CHCl_3$.

Yield: 42.9 mg 22.0 µmol 44 % of a blue solid with a purple gleam

$C_{129}H_{159}BF_2N_{10}O_3$ [1946.52]

HRMS (ESI): $[M^{2+\bullet}] = C_{129}H_{159}BF_2N_{10}O_3^{2+\bullet}$, calc.: 973.134478; found: 973.13536 (Δ = 0.91 ppm)

^{1}H-NMR (600.4 MHz, CD_2Cl_2):

δ [ppm] = 7.47 – 7.44 (-, 4 H, 4 × C<u>H</u>), 7.41 – 7.40 (dd, $^{3}J_{HH}$ = 7.4 Hz, $^{4}J_{HH}$ = 0.6 Hz, 2 H, 2 × C<u>H</u>), 7.38 – 7.36 (ddd, $^{3}J_{HH}$ = 8.2 Hz, $^{3}J_{HH}$ = 7.2 Hz, $^{4}J_{HH}$ = 1.1 Hz, 2 H, 2 × C<u>H</u>), 7.23 (AA', 4 H, 4 × C<u>H</u>), 7.10 (BB', 4 H, 4 × C<u>H</u>), 6.99 (d, $^{3}J_{HH}$ = 8.3 Hz, 2 H, 2 × C<u>H</u>), 6.51 (s, 2 H, 2 × =C<u>H</u>), s (6.44, 2 H, 2 × =C<u>H</u>), 4.12 – 3.97 (-, 8 H, 4 × NC<u>H$_2$</u>), 3.95 (d, $^{3}J_{HH}$ = 5.9 Hz, 2 H, OC<u>H$_2$</u>), 2.71 (s, 6 H, 2 × CC<u>H$_3$</u>), 1.81 – 1.14 (-, 49 H, 9 × C<u>H</u>, 20 × C<u>H$_2$</u>), 1.75 (s, 12 H, 2 × C(C<u>H$_3$</u>)<u>$_2$</u>) 1.74 (s, 12 H, 2 × C(C<u>H$_3$</u>)<u>$_2$</u>), 1.64 (s, 6 H, 2 × CC<u>H$_3$</u>), 1.03 – 1.01 (-, 12 H, 4 × CHC<u>H$_3$</u>), 0.97 (t, $^{3}J_{HH}$ = 7.5 Hz, 3 H, CH_2C<u>H$_3$</u>), 0.93 (t, $^{3}J_{HH}$ = 7.1 Hz, 3 H, CH_2C<u>H$_3$</u>), 0.86 – 0.85 (-, 24 H, 4 × C(C<u>H$_3$</u>)<u>$_2$</u>).

^{13}C-NMR (151.0 MHz, CD_2Cl_2):

δ [ppm] = 173.4 (C_q), 173.0 (C_q), 170.7 (C_q), 167.9 (C_q), 167.7 (C_q), 165.8 (C_q), 160.8 (C_q), 158.4 (C_q), 144.4 (C_q), 143.5 (C_q), 143.0 (C_q), 142.9 (C_q), 142.3 (C_q), 142.1 (C_q), 132.1 (C_q), 131.9 (CH), 129.5 (CH), 128.4 (CH), 126.2 (C_q), 125.3 (CH), 125.2 (CH), 122.6 (CH), 119.2 (C_q), 119.0 (2 × C_q), 116.2 (C_q), 115.7 (CH), 110.8 (CH), 110.1 (CH), 96.8 (C_q), 89.8 (CH), 89.6 (CH), 82.4 (C_q), 71.2 (CH_2), 50.1 (C_q), 49.3 (C_q), 43.5 (CH_2), 43.2 (CH_2), 40.7 (C_q), 39.8 (CH), 39.5 (2 × CH_2), 37.47 (CH_2), 37.46 (CH_2), 34.4 (CH_2), 34.2 (CH_2), 31.3 (CH), 31.2 (CH), 30.8 (CH_2), 29.5 (CH_2), 28.3 (2 × CH), 26.84 (CH_3), 26.80 (CH_3), 26.53 (CH_3), 26.50 (CH_3), 25.02 (CH_2), 25.01 (CH_2) 24.2 (CH_2), 23.4 (CH_2), 22.8 (2 × CH_3), 22.7 (2 × CH_3), 19.78 (CH_3), 19.77 (CH_3), 14.2 (CH_3), 13.9 (CH_3), 13.8 (CH_3), 11.3 (CH_3).

7.2.6 Asymmetrical Triads

PyB(SQB)

CA [–]

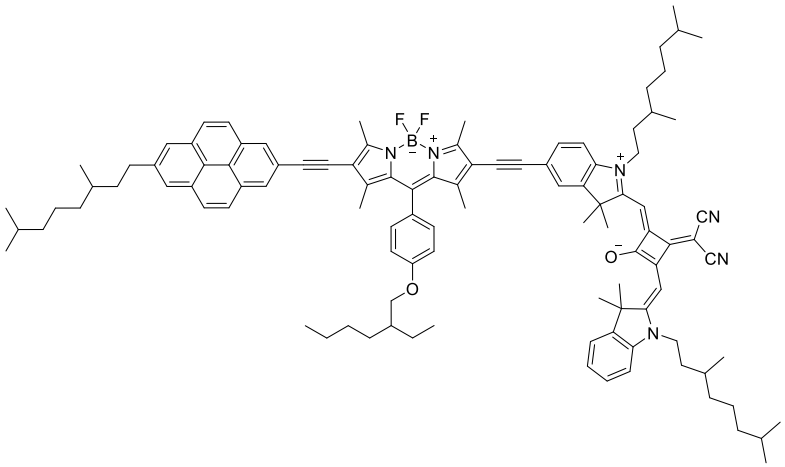

Synthesis according to GPI

SQB-5 (50.0 mg, 62.2 µmol), **BODIPY-4** (49.0 mg, 98.0 µmol), **Py-6** (41.3 mg, 98.0 µmol), CuI (746 µg, 3.92 µmol), $Pd(C_6H_5CN)_2Cl_2$ (4.88 mg, 13.0 µmol), tri-*tert*-butylphosphane (1 M in toluene, 25.0 µl, 25.0 µmol), DIPA (27.6 µl, 196 µmol), dioxane (5 ml); stirred for 1 d at 60 °C, purified by GPC in CH_3Cl; precipitation from diethylether/acetonitrile.

Yield: 13.9 mg 8.89 µmol 14 % of a green shiny solid

$C_{106}H_{125}BF_2N_6O_2$ [1563.98]

MALDI-TOF MS (POS, DCTB : $CHCl_3$ = 1:3):

calc. for $C_{106}H_{125}BF_2N_6O_2$ [$M^{+\bullet}$]: m/z = 1563.996 found: m/z = 1564.002

^{1}H-NMR (400.0 MHz, CD_2Cl_2):

δ [ppm] = 8.26 (s, 2 H, 2 × C<u>H</u>), 8.07 – 8.00 (-, 6 H, 6 × C<u>H</u>), 7.48 – 7.45 (-, 2 H, 2 × C<u>H</u>), 7.42 – 7.35 (-, 2 H, 2 × C<u>H</u>), 7.26 – 7.23 (-, 3 H, 3 × C<u>H</u>), 7.12 – 7.09 (-, 3 H, 3 × C<u>H</u>), 7.00 (d, $^3J_{HH}$ = 8.1 Hz, 1 H, 1 × C<u>H</u>), 6.52 (s, 1 H, =C<u>H</u>), 6.45 (s, 1 H, =C<u>H</u>), 4.15 – 3.96 (-, 6 H, 2 × NC<u>H</u>$_2$, 2 × OC<u>H</u>$_2$), 3.14 – 2.99 (m, 2 H, CH_2), 2.80 (s, 3 H, CC<u>H</u>$_3$), 2.73 (s, 3 H, CC<u>H</u>$_3$), 1.76 – 1.75 (-, 12 H, C(C<u>H</u>$_3$)$_2$), 1.73 (s, 3 H, CC<u>H</u>$_3$), 1.65 (s, 3 H, CC<u>H</u>$_3$), 1.91 – 1.13 (-, 39 H, 7 × C<u>H</u>, 16 × C<u>H</u>$_2$), 1.03 – 0.92 (-, 15 H, 3 × CHC<u>H</u>$_3$, 2 × CH_2C<u>H</u>$_3$), 0.87 – 0.85 (-, 18 H, 3 × CH(C<u>H</u>$_3$)$_2$).

This compound was not completely purified.

Py(SQB)B

CA [–]

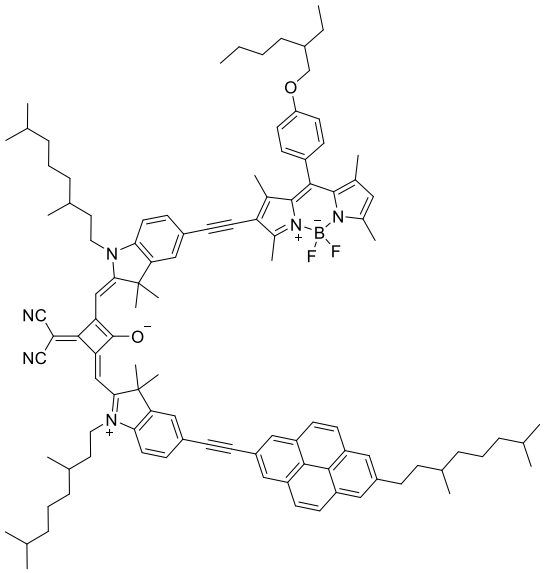

Synthesis according to GPII

B(SQB) (90.0 mg, 68.6 µmol), $Pd(PPh_3)_4$ (3.92 mg, 3.40 µmol), CuI (647 µg, 3.40 µmol), **Py-8** (29.9 mg, 81.6 µmol), toluene (6 ml), TEA (1 ml); stirred at rt for 2 d; purified by GPC in $CHCl_3$, precipitation from CH_2Cl_2/methanol.

Yield: 17.4 mg 11.1 µmol 16 % of a blue solid with a purple gleam

$C_{106}H_{125}BF_2N_6O_2$ [1563.98]

MALDI-TOF MS (POS, DCTB : $CHCl_3$ = 1:3):

calc. for $C_{106}H_{125}BF_2N_6O_2$ [$M^{+\bullet}$]: m/z = 1563.996 found: m/z = 1563.988

^{1}H-NMR (400.0 MHz, CD_2Cl_2):

δ [ppm] = 8.32 (s, 2 H, 2 × CH), 8.09 – 8.03 (-, 6 H, 6 × CH), 7.66 – 7.63 (-, 2 H, 2 × CH), 7.48 – 7.45 (-, 2 H, 2 × CH), 7.19 (AA', 2 H, 2 × CH), 7.09 – 7.00 (-, 4 H, 4 × CH), 6.51 (-, 2 H, 2 × =CH), s (6.08, 1 H, CH), 4.12 – 3.97 (-, 4 H, 2 × NCH_2), 3.93 (d, $^3J_{HH}$ = 5.8 Hz, 2 H, OCH_2), 3.17 – 2.99 (m, 2 H, CH_2), 2.69 (s, 3 H, CCH_3), 2.55 (s, 3 H, CCH_3), 1.92 – 1.13 (-, 39 H, 7 × CH, 16 × CH_2), 1.81 (s, 6 H, $C(CH_3)_2$) 1.77 (s, 6 H, $C(CH_3)_2$), 1.61 (s, 3 H, CCH_3), 1.49 (s, 3 H, CCH_3), 1.06 – 0.86 (-, 33 H, 3 × $CHCH_3$, 2 × CH_2CH_3, 3 × $C(CH_3)_2$).

This compound was not completely purified.

PyB(SQA)

CA [–]

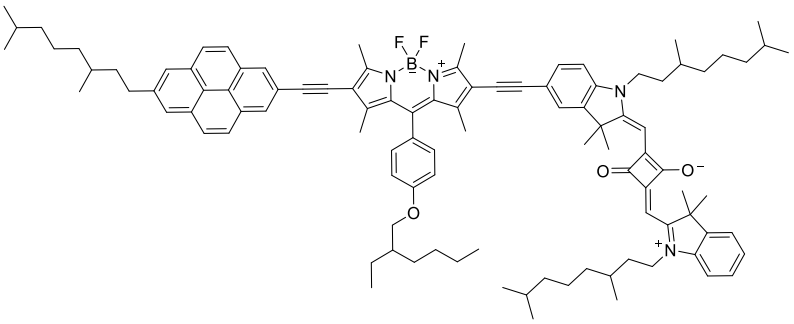

Synthesis according to GPII

SQA-6 (40.1 mg, 49.9 µmol), $Pd(PPh_3)_4$ (2.41 mg, 2.08 µmol), CuI (396 µg, 2.08 µmol), **PyB-3** (35.0 mg, 41.6 µmol), toluene (6 ml), TEA (1 ml); stirred at rt for 4 d; filtration over silica with PE → CH_2Cl_2 → EA, purified by GPC in $CHCl_3$.

Yield: 20.7 mg 13.7 µmol 33 % of a blue solid with a red gleam

$C_{103}H_{125}BF_2N_4O_3$ [1515.93]

MALDI-TOF MS (POS, DCTB : $CHCl_3$ = 1:3):

calc. for $C_{103}H_{125}BF_2N_4O_3$ [$M^{+\bullet}$]: m/z = 1515.985 found: m/z = 1515.892

^{1}H-NMR (400.0 MHz, $CDCl_3$):

δ [ppm] = 8.22 (-, 2 H, 2 × CH), 8.04 – 7.97 (-, 6 H, 6 × CH), 7.42 – 7.30 (-, 4 H, 4 × CH), 7.22 – 7.15 (-, 3 H, 3 × CH), 7.07 (AA', 2 H, 2 × CH), 6.99 (d, $^3J_{HH}$ = 8.2 Hz, 1 H, CH), 6.87 (d, $^3J_{HH}$ = 8.0 Hz, 1 H, CH), 6.00 – 5.95 (-, 2 H, 2 × =CH), 4.07 – 3.94 (-, 6 H, 2 × NCH_2, OCH_2), 3.13 – 2.96 (m, 2 H, CH_2), 2.83 (s, 3 H, CCH_3), 2.76 (s, 3 H, CCH_3), 1.90 – 1.12 (-, 39 H, 7 × CH, 16 x CH_2), 1.79 (-, 12 H, 2 × $C(CH_3)_2$), 1.70 (s, 3 H, CCH_3), 1.63 (s, 3 H, CCH_3), 1.06 – 0.92 (-, 15 H, 3 × $CHCH_3$, 2 × CH_2CH_3), 0.87 – 0.86 (-, 18 H, 3 × $C(CH_3)_2$).

This compound was not completely purified.

7.2.7 Pentades

$(PyB)_2SQB$

CA [–]

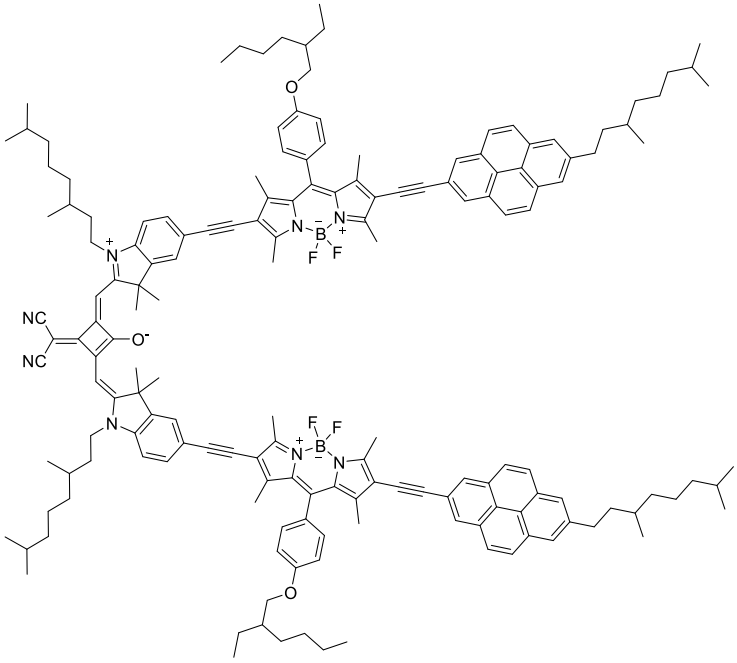

Synthesis according to GPII

SQB-4 (18.0 mg, 18.4 µmol), $Pd(PPh_3)_4$ (1.07 mg, 0.921 µmol), CuI (175 µg, 0.921 µmol), **PyB-3** (31.0 mg, 36.9 µmol), toluene (4 ml), TEA (1 ml); stirred for 5 d at 40 °C; purified by GPC in $CHCl_3$.

Yield: 7.60 mg 3.16 µmol 17 % of a blue solid with a purple gleam

$C_{163}H_{186}B_2F_4N_8O_3$ [2402.89]

MALDI-TOF MS (POS, DCTB : $CHCl_3$ = 1:3):

calc. for $C_{163}H_{186}B_2F_4N_8O_3$ [$M^{+\bullet}$]: m/z = 2402.482 found: m/z = 2402.583

^{1}H-NMR (400.0 MHz, $CDCl_3$):

δ [ppm] = 8.23 (s, 4 H, 4 × CH), 8.04 – 7.97 (-, 12 H, 12 × CH), 7.46 – 7.40 (-, 4 H, 4 × CH), 7.21 (AA', 4 H, 4 × CH), 7.08 (BB', 4 H, 4 × CH), 6.97 (d, $^{3}J_{HH}$ = 8.4 Hz, 2 H, 2 × CH), 6.52 (s, 2 H, 2 × =CH), 4.12 – 3.94 (-, 8 H, 2 × NCH_2, 2x OCH_2), 3.13 – 2.96 (m, 4 H, 2 × CH_2), 2.83 (s, 6 H, 2 × CCH_3), 2.76 (s, 6 H, 2 × CCH_3), 1.90 – 1.12 (-, 58 H, 10 × CH, 24 × CH_2), 1.77 (s, 12 H, 2 × $C(CH_3)_2$) 1.71 (s, 6 H, 2 × CCH_3), 1.64 (s, 6 H, 2 × CCH_3), 1.03 – 0.93 (-, 24 H, 4 × $CHCH_3$, 4 × CH_2CH_3), 0.86 – 0.85 (-, 24 H, 4 × $C(CH_3)_2$).

This compound was not completely purified.

$(PySQB)_2B$

CA [–]

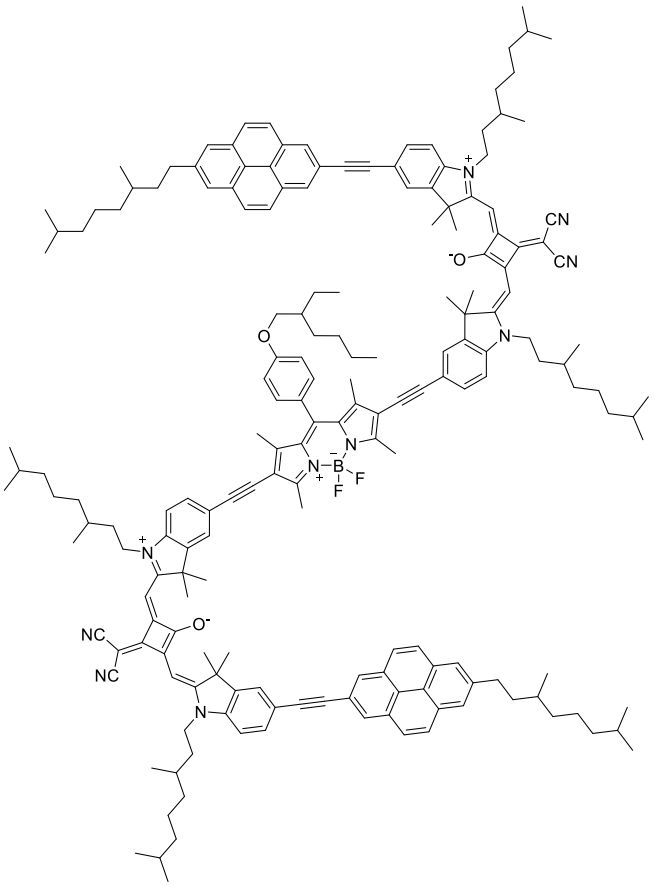

Synthesis according to GPII

$(SQB)_2B$-3 (39.0 mg, 17.7 µmol), $Pd(PPh_3)_4$ (10.3 mg, 8.87 µmol), CuI (1.69 mg, 8.87 µmol), **Py-8** (13.0 mg, 35.5 µmol), toluene (4 ml), TEA (1 ml); stirred for 1 d at 40 °C; purified by GPC in $CHCl_3$.

Yield: 2.65 mg 0.990 µmol 6 % of a blue solid with a purple gleam

$C_{185}H_{215}BF_2N_{10}O_3$ [2675.57]

MALDI-TOF MS (POS, DCTB : $CHCl_3$ = 1:3):

calc. for $C_{185}H_{215}BF_2N_{10}O_3$ [$M^{+\bullet}$]: m/z = 2674.708 found: m/z = 2675.698

^{1}H-NMR (400.0 MHz, CD_2Cl_2):

δ [ppm] = 8.33 (s, 4 H, 4 × CH), 8.09 – 8.04 (-, 12 H, 12 × CH), 7.67 – 7.65 (-, 4 H, 4 × CH), 7.50 – 7.47 (-, 4 H, 4 × CH), 7.23 (AA', 2 H, 2 × CH), 7.12 – 7.08 (-, 4 H, 4 × CH), 7.03 (d, $^3J_{HH}$ = 8.8 Hz, 2 H, 2 × CH), 6.51 (-, 4 H, 4 × =CH), 4.13 – 3.95 (-, 10 H, 4 × NCH_2, OCH_2), 4.13 – 3.95 (m, 4 H, 2 × CH_2), 2.72 (s, 6 H, 2 × CCH_3), 1.90 – 1.14 (-, 69 H, 13 × CH, 28 × CH_2), 1.81 (s, 12 H, 2 × $C(CH_3)_2$) 1.77 (s, 12 H, 2 × $C(CH_3)_2$), 1.65 (s, 6 H, 2 × CCH_3), 1.06 – 0.92 (-, 24 H, 6 × $CHCH_3$, 2 × CH_2CH_3), 0.89 – 0.85 (-, 36 H, 6 × $C(CH_3)_2$).

This compound was not completely purified.

$(PyB)_2$SQA

CA [–]

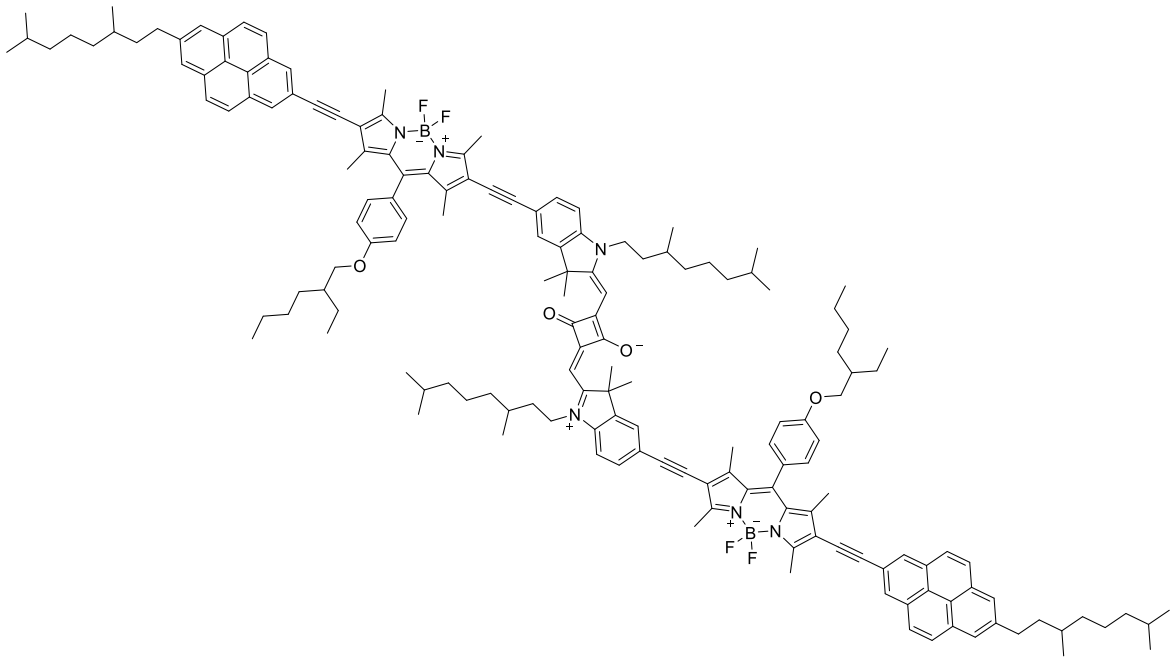

Synthesis according to GPII

SQA-4 (19.2 mg, 20.9 µmol), $Pd(PPh_3)_4$ (1.19 mg, 1.03 µmol), CuI (196 µg, 1.03 µmol), **PyB-3** (40.0 mg, 47.6 µmol), toluene (4 ml), TEA (1 ml); stirred for 3 d at 40 °C; filtered over silica and precipitated from acetone.

Yield: 16.8 mg 7.13 µmol 34 % of a blue solid with a red gleam

$C_{160}H_{186}B_2F_4N_6O_4$ [2354.85]

MALDI-TOF MS (POS, DCTB : $CHCl_3$ = 1:3):

calc. for $C_{160}H_{186}B_2F_4N_6O_4$ [$M^{+\bullet}$]: m/z = 2354.471 found: m/z = 2354.536

^{1}H-NMR (400.0 MHz, $CDCl_3$):

δ [ppm] = 8.22 (s, 4 H, 4 × CH), 8.04 – 7.97 (-, 12 H, 12 × CH), 7.44 – 7.41 (-, 4 H, 4 × CH), 7.21 (AA', 4 H, 4 × CH), 7.09 – 7.07 (BB', 4 H, 4 × CH), 6.91 (d, $^3J_{HH}$ = 8.2 Hz, 2 H, 2 × CH), 6.03 (s, 2 H, 2 × =CH), 4.06 – 3.94 (-, 8 H, 2 × NCH_2, 2 × OCH_2), 3.13 – 2.96 (-, 4 H, 2 × CH_2), 2.83 (s, 6 H, 2 × CCH_3), 2.76 (s, 6 H, 2 × CCH_3), 1.90 – 1.11 (-, 58 H, 10 × CH, 24 × CH_2), 1.78 (s, 12 H, 2 × $C(CH_3)_2$) 1.71 (s, 6 H, 2 × CCH_3), 1.63 (s, 6 H, 2 × CCH_3), 1.05 – 0.93 (-, 24 H, 4 × $CHCH_3$, 4 × CH_2CH_3), 0.87 – 0.86 (-, 24 H, 4 × $C(CH_3)_2$).

This compound was not completely purified.

7.2.8 Bridged Squaraine

SQA_2Anth

CA [–]

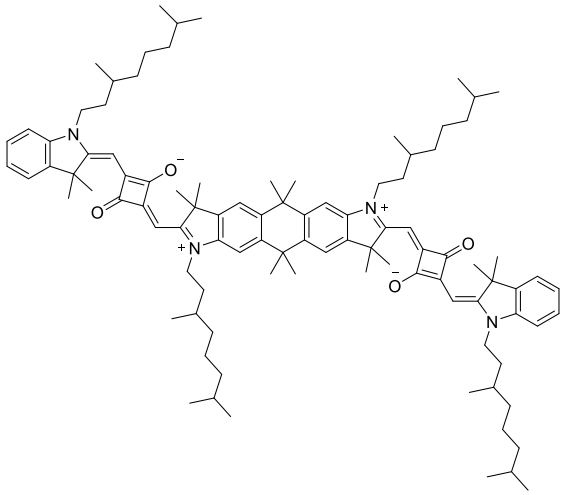

Synthesis according to literature[169]

Ind-6 (392 mg, 991 µmol) and **Ind-8** (400 mg, 428 µmol) were dissolved in toluene/*n*-butanol 1:1 and pyridine (1.88 ml, 23.3 mmol) was added. The mixture was refluxed at a dean-stark-trapp for 21 h. The solvent was removed under reduced pressure. The residue was purified by flash column chromatrogaphy (CH_2Cl_2:methanol = 98:2). The crude product was purified by GPC and finally recrystallised from *n*-hexane.

Yield: 245 mg 171 µmol 40 % of a shinny blue solid

$C_{98}H_{136}N_4O_4$ [1434.16]

HRMS (ESI): $[M^{\bullet}+2H^+]$ = $C_{98}H_{138}N_4O_4$, calc.: 718.0370; found: 718.03771 (Δ = 0.99 ppm)

^{1}H-NMR (400.0 MHz, CD_2Cl_2):

δ [ppm] = 7.48 (s, 2 H, 2 × C<u>H</u>), 7.38 – 7.30 (-, 4 H, 4 × C<u>H</u>), 7.16 – 6.99 (-, 6 H, 6 × C<u>H</u>), 5.91 (-, 4 H, 4 × =C<u>H</u>), 4.04 (-, 8 H, 4 × NC<u>H_2</u>), 1.80 – 1.06 (-, 88 H, 8 × C<u>H</u>, 16 × C<u>H_2</u>, 4 × CHC<u>H_3</u>, 6 × C(C<u>H_3</u>)<u>$_2$</u>), 0.88 – 0.85 (-, 24 H, 4 × CH(C<u>H_3</u>)<u>$_2$</u>).

^{13}C-NMR (151.0 MHz, CD_2Cl_2):

δ [ppm] = 182.1 (2 × C_q), 180.5 (C_q), 180.2 (C_q), 170.2 (C_q), 165.8 (C_q), 142.9 (C_q), 142.6 (C_q), 141.9 (C_q), 141.5 (C_q), 140.9 (C_q), 137.4 (C_q), 128.3 (CH), 123.8 (CH), 122.6 (CH), 120.8 (CH), 109.6 (CH), 107.3 (CH), 86.8 (2 × CH), 49.5 (2 × C_q), 42.4 (2 × CH_2), 39.53 (CH_2), 39.50 (CH_2), 38.5 (C_q), 37.51 (CH_2), 37.48 (CH_2), 35.73 (CH_3), 35.71 (CH_3), 34.1 (2 x CH_2), 31.5 (CH), 31.4 (CH), 28.4 (2 × CH), 27.3 (2 × CH_3), 27.1 (2 × CH_3), 25.10 (CH_2), 25.09 (CH_2), 22.8 (2 × CH_3), 22.7 (2 × CH_3), 19.9 (CH_3), 19.8 (CH_3).

8 Literature

[1] B. Albinsson, M. P. Eng, K. Pettersson, M. U. Winters, *PCCP* **2007**, *9*, 5847-5864.

[2] A. Harriman, *PCCP* **2010**, *12*, 7317-7318.

[3] F. C. Spano, *Acc. Chem. Res.* **2010**, *43*, 429-439.

[4] J. L. Brédas, D. Beljonne, V. Coropceanu, J. Cornil, *Chem. Rev.* **2004**, *104*, 4971-5003.

[5] T. Brixner, R. Hildner, J. Köhler, C. Lambert, F. Würthner, *Adv. Energy Mater.* **2017**, *7*, 1700236/1700231-1700236/1700233.

[6] P. García-Fernández, L. Andjelković, M. Zlatar, M. Gruden-Pavlović, A. Dreuw, *J. Chem. Phys.* **2013**, *139,* 174101.

[7] T. Nelson, S. Fernandez-Alberti, A. E. Roitberg, S. Tretiak, *J. Phys. Chem. Lett.* **2017**, *8*, 3020-3031.

[8] G. D. Scholes, T. Mirkovic, D. B. Turner, F. Fassioli, A. Buchleitner, *Energy & Environmental Science* **2012**, *5*, 9374-9393.

[9] A. Harriman, *Chem. Commun.* **2015**, *51*, 11745-11756.

[10] T. Förster, *Discuss. Faraday Soc.* **1959**, *27*, 7-17.

[11] D. L. Dexter, *J. Chem. Phys.* **1953**, *21*, 836-850.

[12] G. D. Scholes, *Annu. Rev. Phys. Chem.* **2003**, *54*, 57-87.

[13] A. Kimura, T. Kakitani, T. Yamato, *J. Phys. Chem. B* **2000**, *104*, 9276-9287.

[14] J. Frenkel, *Phys. Rev.* **1931**, *37*, 17-44.

[15] E. G. McRae, M. Kasha, in *Physical Processes in Radiation Biology* (Eds.: L. Augenstein, R. Mason, B. Rosenberg), Academic Press, New York, **1964**, pp. 23-42.

[16] G. D. Scholes, G. Rumbles, *Nat. Mater.* **2006**, *5*, 683-696.

[17] C. J. Bardeen, *Annual Review of Physical Chemistry, Vol 65* **2014**, *65*, 127-148.

[18] L. V. Herbert van Amerongen, Rienk van Grondelle, in *Photosynthetic Excitons*, World Scientific, Singapur, **2000**, pp. 47-72.

[19] O. Kuhn, S. Lochbrunner, in *Quantum Efficiency in Complex Systems, Pt Ii: From Molecular Aggregates to Organic Solar Cells, Vol. 85* (Eds.: U. Wurfel, M. Thorwart, E. R. Weber), **2011**, pp. 47-81.

[20] J. Knoester, in *Optical properties of molecular aggregates* (Eds.: e. V. M. Agranovich, G. C. L. Rocca), IOS Press, Amsterdam, **2002**, pp. 149-186.

[21] V. R. Nicolas J. Turro, J. C. Scaiano, in *Modern Molecular Photochemistry of Organic Molecules*, University Science Books, Sausalito, California, **2010**, pp. 383-481.

[22] M. N. B.-S. Bernard Valeur, in *Molecular Fluorescence*, Wiley-VCH, Weinheim, Germany, **2012**, pp. 213-261.

[23] Z. Q. You, C. P. Hsu, *Int. J. Quantum Chem* **2014**, *114*, 102-115.

[24] O. K. Volkhard May, in *Charge and Energy Transfer Dynamics in Molecular Systems, Vol. Third Revised and Enlarged Edition*, Wiley-VCH, Berlin, **2011**, pp. 467-557.

[25] V. May, *Dalton Transactions* **2009**, 10086-10105.

[26] W. W. Parson, in *Modern Optical Spectroscopy*, Springer Verlag Berlin Heidelberg, **2009**, pp. 259-279.

[27] T. Förster, *Naturwiss.* **1946**, *33*, 166-175.

[28] S. H. Lin, *Mol. Phys.* **1971**, *21*, 853-863.

[29] G. W. Robinson, R. P. Frosch, *J. Chem. Phys.* **1962**, *37*, 1962-1973.

[30] S. Speiser, *Chem. Rev.* **1996**, *96*, 1953-1976.

[31] C. Y. Wong, C. Curutchet, S. Tretiak, G. D. Scholes, *J. Chem. Phys.* **2009**, *130*, 081104.

[32] A. Czader, E. R. Bittner, *J. Chem. Phys.* **2008**, *128*, 035101.

[33] G. C. B. Wieb Van Der Meer, S.-Y. Simon Chen, in *Resonance Energy Transfer*, VCH Publishers Inc, Weinheim, **1994**, pp. 5-31.

[34] G. C. B. Wieb Van Der Meer, S.-Y. Simon Chen, in *Resonance Energy Transfer*, VCH Publishers Inc, Weinheim, **1994**, pp. 35-54.

[35] L. Stryer, R. P. Haugland, *Proc. Natl. Acad. Sci. U. S. A.* **1967**, *58*, 719-726.

[36] L. Stryer, *Annu. Rev. Biochem* **1978**, *47*, 819-846.

[37] J. N. Miller, *Analyst* **2005**, *130*, 265-270.

[38] L. M. S. Loura, M. Prieto, *Front. Physiol.* **2011**, *2*, 1-11.

[39] J. R. Winkler, *Science* **2013**, *339*, 1530-1531.

[40] V. Hirschfeld, H. Paulsen, C. G. Hübner, *PCCP* **2013**, *15*, 17664-17671.

[41] J. R. Lakowicz, in *Principles of Fluorescence Spectroscopy, Vol. 3. (corr. at 4. print) edn.* , Third edition ed., Springer, New York, NY, **2010**, pp. 97-155.

[42] F. Laquai, Y. S. Park, J. J. Kim, T. Basche, *Macromol. Rapid Commun.* **2009**, *30*, 1203-1231.

[43] J. R. Lakowicz, in *Principles of Fluorescence Spectroscopy, Vol. 3. (corr. at 4. print) edn.* , Third edition ed., Springer, New York, NY, **2010**, pp. 443-475.

[44] S. Jang, Y. J. Jung, R. J. Silbey, *Chem. Phys.* **2002**, *275*, 319-332.

[45] T. Mirkovic, E. E. Ostroumov, J. M. Anna, R. van Grondelle, Govindjee, G. D. Scholes, *Chem. Rev.* **2017**, *117*, 249-293.

[46] M. Kasha, H. R. Rawls, M. A. El-Bayoumi, *Pure Appl. Chem.* **1965**, *11*, 371-392.

[47] T. Brixner, R. Hildner, J. Köhler, C. Lambert, F. Würthner, *Advanced Energy Materials* **2017**, *7*, 1700236/1–1700236/33.

[48] A. Eisfeld, J. S. Briggs, *Chem. Phys.* **2006**, *324*, 376-384.

[49] E. E. Jelley, *Nature* **1936**, *138*, 1009-1010.

[50] P. O. J. Scherer, S. F. Fischer, *Chem. Phys.* **1984**, *86*, 269-283.

[51] C. Lambert, *Angew. Chem. Int. Ed.* **2005**, *44*, 7337-7339.

[52] M. Steeger, C. Lambert, *Chem. Eur. J.* **2012**, *18*, 11937-11948.

[53] Y. C. Cheng, G. R. Fleming, *Annu. Rev. Phys. Chem.* **2009**, *60*, 241-262.

[54] P. K. Dutta, R. Varghese, J. Nangreave, S. Lin, H. Yan, Y. Liu, *J. Am. Chem. Soc.* **2011**, *133*, 11985-11993.

[55] V. Balzani, G. Bergamini, P. Ceroni, E. Marchi, *New J. Chem.* **2011**, *35*, 1944-1954.

[56] M. Allegra, P. Giorda, *Phys. Rev. E* **2012**, *85*, 051917/051911-051917/051913.

[57] M. Sener, J. Strümpfer, J. Hsin, D. Chandler, S. Scheuring, C. N. Hunter, K. Schulten, *Chemphyschem* **2011**, *12*, 518-531.

[58] T. Förster, *Angew. Chem. Int. Ed.* **1969**, *8*, 333-343.

[59] C. Lambert, J. Ehbets, D. Rausch, M. Steeger, *J. Org. Chem.* **2012**, *77*, 6147-6154.

[60] A. G. Crawford, A. D. Dwyer, Z. Liu, A. Steffen, A. Beeby, L.-O. Pålsson, D. J. Tozer, T. B. Marder, *J. Am. Chem. Soc.* **2011**, *133*, 13349-13362.

[61] M. Kreyenschmidt, M. Baumgarten, N. Tyutyulkov, K. Müllen, *Angew. Chem. Int. Ed. Eng.* **1994**, *33*, 1957-1959.

[62] S.-i. Kawano, C. Yang, M. Ribas, S. Baluschev, M. Baumgarten, K. Müllen, *Macromolecules* **2008**, *41*, 7933-7937.

[63] T. Iwamoto, E. Kayahara, N. Yasuda, T. Suzuki, S. Yamago, *Angew. Chem. Int. Ed.* **2014**, *53*, 6430-6434.

[64] D. Rausch, C. Lambert, *Org. Lett.* **2006**, *8*, 5037-5040.

[65] K. R. J. Thomas, M. Velusamy, J. T. Lin, C. H. Chuen, Y. T. Tao, *J. Mater. Chem.* **2005**, *15*, 4453-4459.

[66] A. Harriman, L. Mallon, R. Ziessel, *Chem. Eur. J.* **2008**, *14*, 11461-11473.

[67] R. Ziessel, C. Goze, G. Ulrich, M. Césario, P. Retailleau, A. Harriman, J. P. Rostron, *Chem. Eur. J.* **2005**, *11*, 7366-7378.

[68] B. Albinsson, J. Mårtensson, *PCCP* **2010**, *12*, 7338-7351.

[69] A. Prodi, C. Chiorboli, F. Scandola, E. Iengo, E. Alessio, *Chemphyschem* **2006**, *7*, 1514-1519.

[70] H. E. Song, C. Kirmaier, J. K. Schwartz, E. Hindin, L. H. Yu, D. F. Bocian, J. S. Lindsey, D. Holten, *J. Phys. Chem. B* **2006**, *110*, 19131-19139.

[71] Y. Nakamura, N. Aratani, A. Osuka, *Chem. Soc. Rev.* **2007**, *36*, 831-845.

[72] R. Ziessel, A. Harriman, *Chem. Commun.* **2011**, *47*, 611-631.

[73] F. Schlosser, J. Sung, P. Kim, D. Kim, F. Würthner, *Chem. Sci.* **2012**, *3*, 2778-2785.

[74] G. Sánchez-Mosteiro, E. van Dijk, J. Hernando, M. Heilemann, P. Tinnefeld, M. Sauer, F. Koberlin, M. Patting, M. Wahl, R. Erdmann, N. F. van Hulst, M. F. García-Parajó, *J. Phys. Chem. B* **2006**, *110*, 26349-26353.

[75] J. K. Hannestad, P. Sandin, B. Albinsson, *J. Am. Chem. Soc.* **2008**, *130*, 15889-15895.

[76] A. L. Stevens, P. G. A. Janssen, A. Ruiz-Carretero, M. Surin, A. Schenning, L. M. Herz, *J. Phys. Chem. C* **2011**, *115*, 10550-10560.

[77] P. Ensslen, H. A. Wagenknecht, *Acc. Chem. Res.* **2015**, *48*, 2724-2733.

[78] R. Varghese, H. A. Wagenknecht, *Chem. Eur. J.* **2009**, *15*, 9307-9310.

[79] P. Ensslen, Y. Fritz, H. A. Wagenknecht, *Organic & Biomolecular Chemistry* **2015**, *13*, 487-492.

[80] K. J. Channon, G. L. Devlin, S. W. Magennis, C. E. Finlayson, A. K. Tickler, C. Silva, C. E. MacPhee, *J. Am. Chem. Soc.* **2008**, *130*, 5487-5491.

[81] K. J. Channon, G. L. Devlin, C. E. MacPhee, *J. Am. Chem. Soc.* **2009**, *131*, 12520-12521.

[82] L. Chen, S. Revel, K. Morris, D. J. Adams, *Chem. Commun.* **2010**, *46*, 4267-4269.

[83] C. Devadoss, P. Bharathi, J. S. Moore, *J. Am. Chem. Soc.* **1996**, *118*, 9635-9644.

[84] J. M. Serin, D. W. Brousmiche, J. M. J. Fréchet, *Chem. Commun.* **2002**, 2605-2607.

[85] T. Goodson, *Annu. Rev. Phys. Chem.* **2005**, *56*, 581-603.

[86] A. Nantalaksakul, D. R. Reddy, C. J. Bardeen, S. Thayumanavan, *Photosynth. Res.* **2006**, *87*, 133-150.

[87] V. Balzani, A. Credi, M. Venturi, *Chemsuschem* **2008**, *1*, 26-58.

[88] F. C. De Schryver, T. Vosch, M. Cotlet, M. Van der Auweraer, K. Müllen, J. Hofkens, *Acc. Chem. Res.* **2005**, *38*, 514-522.

[89] A. Ajayaghosh, V. K. Praveen, C. Vijayakumar, S. J. George, *Angew. Chem. Int. Ed.* **2007**, *46*, 6260-6265.

[90] M. Gilbert, B. Albinsson, *Chem. Soc. Rev.* **2015**, *44*, 845-862.

[91] M. R. Wasielewski, *Acc. Chem. Res.* **2009**, *42*, 1910-1921.

[92] K. T. Wong, D. M. Bassani, *Npg Asia Materials* **2014**, *6,* e116.

[93] F. Würthner, A. Sautter, *Org. Biomol. Chem* **2003**, *1*, 240-243.

[94] K. Kilså, J. Kajanus, J. Mårtensson, B. Albinsson, *J. Phys. Chem. B* **1999**, *103*, 7329-7339.

[95] R. Ziessel, G. Ulrich, A. Haefele, A. Harriman, *J. Am. Chem. Soc.* **2013**, *135*, 11330-11344.

[96] A. Harriman, G. Izzet, R. Ziessel, *J. Am. Chem. Soc.* **2006**, *128*, 10868-10875.

[97] C. Lambert, T. Scherpf, H. Ceymann, A. Schmiedel, M. Holzapfel, *J. Am. Chem. Soc.* **2015**, *137*, 3547-3557.

[98] R. Ziessel, G. Ulrich, A. Harriman, *New J. Chem.* **2007**, *31*, 496-501.

[99] H. C. Chen, Z. Q. You, C. P. Hsu, *J. Chem. Phys.* **2008**, *129*, 084708.

[100] J. Warnan, F. Buchet, Y. Pellegrin, E. Blart, F. Odobel, *Org. Lett.* **2011**, *13*, 3944-3947.

[101] C. Goze, G. Ulrich, R. Ziessel, *Org. Lett.* **2006**, *8*, 4444-4448.

[102] C. Goze, G. Ulrich, R. Ziessel, *J. Org. Chem.* **2007**, *72*, 313-322.

[103] G. Ulrich, S. Goeb, A. De Nicola, P. Retailleau, R. Ziessel, *Synlett* **2007**, 1517-1520.

[104] A. Haefele, G. Ulrich, P. Retailleau, R. Ziessel, *Tetrahedron Lett.* **2008**, *49*, 3716-3721.

[105] L. Bonardi, G. Ulrich, R. Ziessel, *Org. Lett.* **2008**, *10*, 2183-2186.

[106] A. Harriman, L. J. Mallon, S. Goeb, G. Ulrich, R. Ziessel, *Chem. Eur. J.* **2009**, *15*, 4553-4564.

[107] M. A. H. Alamiry, J. P. Hagon, A. Harriman, T. Bura, R. Ziessel, *Chem. Sci.* **2012**, *3*, 1041-1048.

[108] D. Bai, A. C. Benniston, J. Hagon, H. Lemmetyinen, N. V. Tkachenko, R. W. Harrington, *PCCP* **2013**, *15*, 9854-9861.

[109] R. Ziessel, C. Goze, G. Ulrich, *Synthesis-Stuttgart* **2007**, 936-949.

[110] M. Fakis, J. S. Beckwith, K. Seintis, E. Martinou, C. Nancoz, N. Karakostas, I. Petsalakis, G. Pistolis, E. Vauthey, *PCCP* **2018**, *20*, 837-849.

[111] C. W. Wan, A. Burghart, J. Chen, F. Bergstrom, L. B. Å. Johansson, M. F. Wolford, T. G. Kim, M. R. Topp, R. M. Hochstrasser, K. Burgess, *Chem. Eur. J.* **2003**, *9*, 4430-4441.

[112] C. Brüning, E. Welz, A. Heilos, V. Stehr, C. Walter, B. Engels, S. F. Völker, C. Lambert, V. Engel, *J. Phys. Chem. C* **2015**, *119*, 6174-6180.

[113] S. Kuster, T. Geiger, *Dyes and Pigments* **2012**, *95*, 657-670.

[114] S. Kuster, F. Sauvage, M. K. Nazeeruddin, M. Grätzel, F. A. Nüesch, T. Geiger, *Dyes and Pigments* **2010**, *87*, 30-38.

[115] S. Kuster, T. Geiger, *Dyes and Pigments* **2015**, *113*, 110-116.

[116] H. Ceymann, A. Rosspeintner, M. H. Schreck, C. Mützel, A. Stoy, E. Vauthey, C. Lambert, *PCCP* **2016**, *18*, 16404-16413.

[117] A. Nakajima, *Bull. Chem. Soc. Jpn.* **1973**, *46*, 2602-2604.

[118] A. Nakajima, *Bull. Chem. Soc. Jpn.* **1971**, *44*, 3272-3277.

[119] A. Nakajima, *J. Mol. Spectrosc.* **1976**, *61*, 467-469.

[120] J. Ehbets, Diploma thesis, Universität Würzburg **2012**.

[121] J. Merz, J. Fink, A. Friedrich, I. Krummenacher, H. H. Al Mamari, S. Lorenzen, M. Haehnel, A. Eichhorn, M. Moos, M. Holzapfel, H. Braunschweig, C. Lambert, A. Steffen, L. Ji, T. B. Marder, *Chem. Eur. J.* **2017**, *23*, 13164-13180.

[122] S. F. Völker, C. Lambert, *Chem. Mater.* **2012**, *24*, 2541-2553.

[123] U. Mayerhoffer, B. Fimmel, F. Würthner, *Angew. Chem. Int. Ed.* **2012**, *51*, 164-167.

[124] U. Mayerhoffer, M. Gsanger, M. Stolte, B. Fimmel, F. Würthner, *Chem. Eur. J.* **2013**, *19*, 218-232.

[125] M. Raytchev, E. Pandurski, I. Buchvarov, C. Modrakowski, T. Fiebig, *J. Phys. Chem. A* **2003**, *107*, 4592-4600.

[126] N. Krebs, I. Pugliesi, J. Hauer, E. Riedle, *New J. Phys.* **2013**, *15*, 085016/085011-085016/085017.

[127] A. Bessette, G. S. Hanan, *Chem. Soc. Rev.* **2014**, *43*, 3342-3405.

[128] G. Ulrich, R. Ziessel, A. Harriman, *Angew. Chem. Int. Ed.* **2008**, *47*, 1184-1201.

[129] N. Boens, V. Leen, W. Dehaen, *Chem. Soc. Rev.* **2012**, *41*, 1130-1172.

[130] A. Loudet, K. Burgess, *Chem. Rev.* **2007**, *107*, 4891-4932.

[131] S. Sreejith, P. Carol, P. Chithra, A. Ajayaghosh, *J. Mater. Chem.* **2008**, *18*, 264-274.

[132] H. N. S. Yagi, in *Heterocyclic Polymethine Dyes, Vol. 14*, Springer, Berlin Heidelberg, **2008**, pp. 133-181.

[133] L. Beverina, P. Salice, *Eur. J. Org. Chem.* **2010**, 1207-1225.

[134] H. Ceymann, PhD thesis, Universität Würzburg **2016**.

[135] A. G. Crawford, Z. Liu, I. A. I. Mkhalid, M.-H. Thibault, N. Schwarz, G. Alcaraz, A. Steffen, J. C. Collings, A. S. Batsanov, J. A. K. Howard, T. B. Marder, *Chem. Eur. J.* **2012**, *18*, 5022-5035.

[136] N. A. Schopf, Master thesis, Universität Würzburg **2014**.

[137] D. N. Coventry, A. S. Batsanov, A. E. Goeta, J. A. K. Howard, T. B. Marder, R. N. Perutz, *Chem. Commun.* **2005**, 2172-2174.

[138] F. Voegtle, *Chemische Zeitung* **1972**, *96*, 396.

[139] C.-T. Yang, Z.-Q. Zhang, H. Tajuddin, C.-C. Wu, J. Liang, J.-H. Liu, Y. Fu, M. Czyzewska, P. G. Steel, T. B. Marder, L. Liu, *Angew. Chem. Int. Ed.* **2012**, *51*, 528-532.

[140] T. Hundertmark, A. F. Littke, S. L. Buchwald, G. C. Fu, *Org. Lett.* **2000**, *2*, 1729-1731.

[141] X. F. Shen, D. M. Ho, R. A. Pascal, *J. Am. Chem. Soc.* **2004**, *126*, 5798-5805.

[142] G. Durocher, C. Sandorfy, *J. Mol. Spectrosc.* **1966**, *20*, 410-424.

[143] J. S. Ham, *J. Chem. Phys.* **1953**, *21*, 756-758.

[144] F. M. Winnik, *Chem. Rev.* **1993**, *93*, 587-614.

[145] P. Avis, G. Porter, *J. Chem. Soc., Faraday Trans. 2* **1974**, *8*, 1057-1065.

[146] W. G. Herkstroeter, P. A. Martic, S. E. Hartman, J. L. R. Williams, S. Farid, *J. Polym. Sci. Part A: Polym. Chem.* **1983**, *21*, 2473-2490.

[147] M. Kastler, W. Pisula, D. Wasserfallen, T. Pakula, K. Müllen, *J. Am. Chem. Soc.* **2005**, *127*, 4286-4296.

[148] A. S. Shetty, J. S. Zhang, J. S. Moore, *J. Am. Chem. Soc.* **1996**, *118*, 1019-1027.

[149] H. Ceymann, M. Balkenhohl, A. Schmiedel, M. Holzapfel, C. Lambert, *PCCP* **2016**, *18*, 2646-2657.

[150] M. Montalti, A. Credi, L. Prodi, M. T. Gandolfi, Taylor & Francis Group, LLC, **2006**, pp. 1-47.

[151] S. Karuppannan, J. C. Chambron, *Chem. Asian J.* **2011**, *6*, 964-984.

[152] C. Thivierge, J. Han, R. M. Jenkins, K. Burgess, *J. Org. Chem.* **2011**, *76*, 5219-5228.

[153] P. Gautam, B. Dhokale, S. M. Mobin, R. Misra, *Rsc Advances* **2012**, *2*, 12105-12107.

[154] B. C. Popere, A. M. Della Pelle, S. Thayumanavan, *Macromolecules* **2011**, *44*, 4767-4776.

[155] P.-L. E. Chu, L.-Y. Wang, S. Khatua, A. B. Kolomeisky, S. Link, J. M. Tour, *Acs Nano* **2013**, *7*, 35-41.

[156] S. Osati, H. Ali, J. E. van Lier, *Tetrahedron Lett.* **2015**, *56*, 2049-2053.

[157] J. Godoy, G. Vives, J. M. Tour, *Org. Lett.* **2010**, *12*, 1464-1467.

[158] Q. Huaulme, A. Mirloup, P. Retailleau, R. Ziessel, *Org. Lett.* **2015**, *17*, 2246-2249.

[159] R. Chinchilla, C. Najera, *Chem. Rev.* **2007**, *107*, 874-922.

[160] V. P. W. Bohm, W. A. Herrmann, *Eur. J. Org. Chem.* **2000**, 3679-3681.

[161] J. H. Li, Y. Liang, Y. X. Xie, *J. Org. Chem.* **2005**, *70*, 4393-4396.

[162] T. Scherpf, Master thesis, Universität Würzburg **2014**.

[163] T. Ljungdahl, K. Pettersson, B. Albinsson, J. Mårtensson, *J. Org. Chem.* **2006**, *71*, 1677-1687.

[164] V. N. B. R. I. Zubatyuk, A. L. Tatarets, L. D. Patsenker, O. V. Shishkin, *Acta Crystallogr. Sect. E.-Struct Rep. Online* **2004**, *60*, O2252-O2254.

[165] H.-J. Chen, Z.-Y. Lin, M.-Y. Li, R.-J. Lian, Q.-W. Xue, J.-L. Chung, S.-C. Chen, Y.-J. Chen, *Tetrahedron* **2010**, *66*, 7755-7761.

[166] H. Huang, H. Liu, H. Jiang, K. Chen, *J. Org. Chem.* **2008**, *73*, 6037-6040.

[167] S. A. Odom, S. Webster, L. A. Padilha, D. Peceli, H. Hu, G. Nootz, S.-J. Chung, S. Ohira, J. D. Matichak, O. V. Przhonska, A. D. Kachkovski, S. Barlow, J.-L. Brédas, H. L. Anderson, D. J. Hagan, E. W. Van Stryland, S. R. Marder, *J. Am. Chem. Soc.* **2009**, *131*, 7510-7511.

[168] W. V. Moreshead, O. V. Przhonska, M. V. Bondar, A. D. Kachkovski, I. H. Nayyar, A. E. Masunov, A. W. Woodward, K. D. Belfield, *J. Phys. Chem. C* **2013**, *117*, 23133-23147.

[169] S. F. Völker, T. Dellermann, H. Ceymann, M. Holzapfel, C. Lambert, *J. Polym. Sci. Part A: Polym. Chem.* **2014**, *52*, 890-911.

[170] J. Schäfer, M. Holzapfel, B. Mladenova, D. Kattnig, I. Krummenacher, H. Braunschweig, G. Grampp, C. Lambert, *J. Am. Chem. Soc.* **2017**, *139*, 6200-6209.

[171] A. Klapars, S. L. Buchwald, *J. Am. Chem. Soc.* **2002**, *124*, 14844-14845.

[172] S. Thorand, N. Krause, *J. Org. Chem.* **1998**, *63*, 8551-8553.

[173] P. Ehlers, A. Neubauer, S. Lochbrunner, A. Villinger, P. Langer, *Org. Lett.* **2011**, *13*, 1618-1621.

[174] H. L. Kee, C. Kirmaier, L. H. Yu, P. Thamyongkit, W. J. Youngblood, M. E. Calder, L. Ramos, B. C. Noll, D. F. Bocian, W. R. Scheidt, R. R. Birge, J. S. Lindsey, D. Holten, *J. Phys. Chem. B* **2005**, *109*, 20433-20443.

[175] S. F. Völker, PhD thesis, Universität Würzburg **2014**.

[176] J. E. Lewis, M. Maroncelli, *Chem. Phys. Lett.* **1998**, *282*, 197-203.

[177] J. Gierschner, J. Cornil, H. J. Egelhaaf, *Adv. Mater.* **2007**, *19*, 173-191.

[178] J. R. Lakowicz, in *Principles of Fluorescence, Vol. 3. (corr. at 4. print) edn.,* Third edition ed., Springer, New York, NY, **2010**, pp. 353-382.

[179] S. J. Strickler, R. A. Berg, *J. Chem. Phys.* **1962**, *37*, 814-822.

[180] A. V. Deshpande, A. Beidoun, A. Penzkofer, G. Wagenblast, *Chem. Phys.* **1990**, *142*, 123-131.

[181] R. P. Sabatini, T. M. McCormick, T. Lazarides, K. C. Wilson, R. Eisenberg, D. W. McCamant, *J. Phys. Chem. Lett.* **2011**, *2*, 223-227.

[182] R. Englman, J. Jortner, *Mol. Phys.* **1970**, *18*, 145-164.

[183] M. I. S. Röhr, H. Marciniak, J. Hoche, M. H. Schreck, H. Ceymann, R. Mitric, C. Lambert, *J. Phys. Chem. C* **2018**, *122*, 8082-8093.

[184] K. Prabakaran, F. N. Khan, J. S. Jin, *Tetrahedron Lett.* **2011**, *52*, 2566-2570.

[185] A. R. Ballestas-Barrientos, A. W. Woodward, W. V. Moreshead, M. V. Bondar, K. D. Belfield, *J. Phys. Chem. C* **2016**, *120*, 7829-7838.

[186] J.-Y. Hu, X.-L. Ni, X. Feng, M. Era, M. R. J. Elsegood, S. J. Teat, T. Yamato, *Org. Biomol. Chem* **2012**, *10*, 2255-2262.

[187] M. R. an der Heiden, H. Plenio, S. Immel, E. Burello, G. Rothenberg, H. C. J. Hoefsloot, *Chem. Eur. J.* **2008**, *14*, 2857-2866.

[188] P. Nguyen, Y. A. Zheng, L. Agocs, G. Lesley, T. B. Marder, *Inorg. Chim. Acta* **1994**, *220*, 289-296.

[189] S. A. Kovalenko, R. Schanz, V. M. Farztdinov, H. Hennig, N. P. Ernsting, *Chem. Phys. Lett.* **2000**, *323*, 312-322.

[190] T. Kumpulainen, B. Lang, A. Rosspeintner, E. Vauthey, *Chem. Rev.* **2017**, *117*, 10826-10939.

[191] A. Pigliucci, G. Duvanel, L. M. L. Daku, E. Vauthey, *J. Phys. Chem. A* **2007**, *111*, 6135-6145.

[192] M. Berg, *Chem. Phys. Lett.* **1994**, *228*, 317-322.

[193] A. C. Yu, C. A. Tolbert, D. A. Farrow, D. M. Jonas, *J. Phys. Chem. A* **2002**, *106*, 9407-9419.

[194] M. Glasbeek, H. Zhang, *Chem. Rev.* **2004**, *104*, 1929-1954.

[195] S. F. Völker, A. Schmiedel, M. Holzapfel, K. Renziehausen, V. Engel, C. Lambert, *J. Phys. Chem. C* **2014**, *118*, 17467-17482.

[196] K. N. Liang, M. S. Farahat, J. Perlstein, K. Y. Law, D. G. Whitten, *J. Am. Chem. Soc.* **1997**, *119*, 830-831.

[197] R. Kantam, R. Holland, B. P. Khanna, K. D. Revell, *Tetrahedron Lett.* **2011**, *52*, 5083-5085.

[198] T. T. Jun Kamatani, Shinjiro Okada*, Vol. US 2008/0007161 Al*, US 2008/0007161 Al ed., **2008**.

[199] H. Tanida, H. Ishitobi, *Tetrahedron Lett.* **1964**, 807-811.

[200] I. Candiani, G. D'Arasmo, F. Heidempergher, A. Tomasi, *Org. Process Res. Dev.* **2009**, *13*, 456-462.

[201] N. G. White, M. J. MacLachlan, *J. Org. Chem.* **2015**, *80*, 8390-8397.

[202] V. Hrobáriková, P. Hrobárik, P. Gajdoš, I. Fitilis, M. Fakis, P. Persephonis, P. Zahradník, *J. Org. Chem.* **2010**, *75*, 3053-3068.

[203] E. A. T. Leonid D. Patsenker, Irina A. Fedyunyaeva, Olga N. Kolosova, Alexey Klochko*, Vol. US 2007/0281363 A1*, **2007**.

[204] A. Rajca, A. Olankitwanit, S. Rajca, *J. Am. Chem. Soc.* **2011**, *133*, 4750-4753.

[205] X. Zhao, R. S. Wei, L. G. Chen, D. Jin, X. L. Yan, *New J. Chem.* **2014**, *38*, 4791-4798.

[206] M. Alyari, M. M. Baradarani, A. Afghan, J. A. Joule, *J. Heterocycl. Chem.* **2014**, *51*, 854-859.

[207] K. G. Liu, A. J. Robichaud, *Tetrahedron Lett.* **2007**, *48*, 461-463.

[208] N. Barbero, C. Magistris, J. Park, D. Saccone, P. Quagliotto, R. Buscaino, C. Medana, C. Barolo, G. Viscardi, *Org. Lett.* **2015**, *17*, 3306-3309.

[209] R. Borrelli, S. Ellena, C. Barolo, *PCCP* **2014**, *16*, 2390-2398.

[210] M. Kasha, *Discuss. Faraday Soc.* **1950**, 14-19.

[211] J. R. Lakowicz, in *Principles of Fluorescence, Vol. 3. (corr. at 4. print) edn.,* Third edition ed., Springer, New York, NY, **2010**, pp. 383-411.

[212] G. R. Fulmer, A. J. M. Miller, N. H. Sherden, H. E. Gottlieb, A. Nudelman, B. M. Stoltz, J. E. Bercaw, K. I. Goldberg, *Organometallics* **2010**, *29*, 2176-2179.

[213] G. A. Olah, S. C. Narang, B. G. B. Gupta, R. Malhotra, *J. Org. Chem.* **1979**, *44*, 1247-1251.

[214] T. S. Ahn, R. O. Al-Kaysi, A. M. Müller, K. M. Wentz, C. J. Bardeen, *Rev. Sci. Instrum.* **2007**, *78*, 086105.

[215] E. Riedle, M. Beutter, S. Lochbrunner, J. Piel, S. Schenkl, S. Sporlein, W. Zinth, *Appl. Phys. B* **2000**, *71*, 457-465.

[216] I. H. M. van Stokkum, D. S. Larsen, R. van Grondelle, *BBA-Bioenergetics* **2004**, *1658*, 262-262.

[217] J. J. Snellenburg, S. P. Laptenok, R. Seger, K. M. Mullen, I. H. M. van Stokkum, *Journal of Statistical Software* **2012**, *49*, 1-22.

[218] D. V. D. M. A. Shriver, *The manipulation of air-sensitive compounds*, John Wiley & Sons New York, **1968**.

[219] W. C. Still, M. Kahn, A. Mitra, *J. Org. Chem.* **1978**, *43*, 2923-2925.

[220] C. J. Bennett, S. T. Caldwell, D. B. McPhail, P. C. Morrice, G. G. Duthie, R. C. Hartley, *Biorg. Med. Chem.* **2004**, *12*, 2079-2098.

[221] M. V. Reddington, *Bioconjugate Chem.* **2007**, *18*, 2178-2190.

[222] F. Zieschang, M. H. Schreck, A. Schmiedel, M. Holzapfel, J. H. Klein, C. Walter, B. Engels, C. Lambert, *J. Phys. Chem. C* **2014**, *118*, 27698-27714.

[223] J. Schäfer, PhD thesis, Universität Würzburg, **2017**.

9 Table of Formulas

Precursors

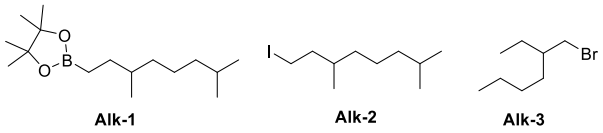

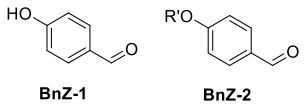

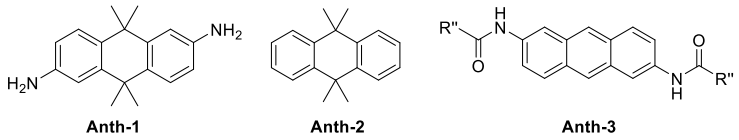

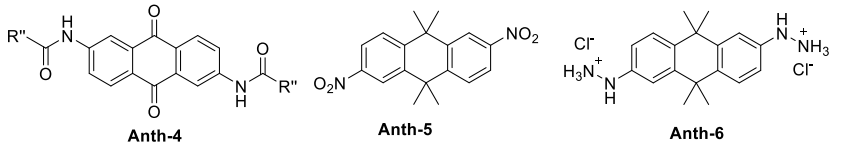

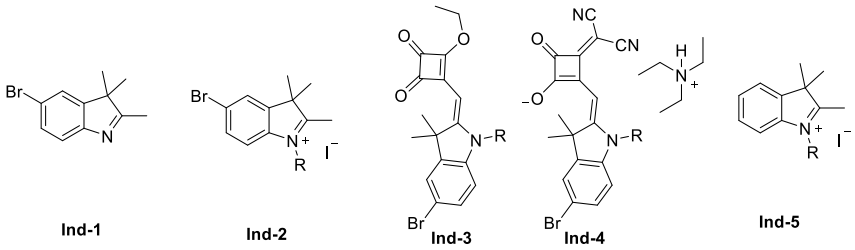

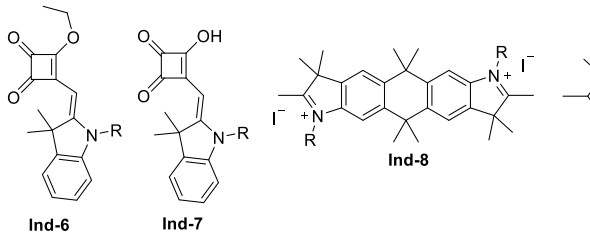

R = 3,7-dimethyloctyl; R' = 2-ethylhexyl; R'' = 1-ethylbutyl

Pyrenes

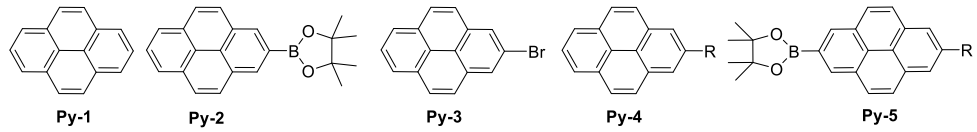

Py-1 Py-2 Py-3 Py-4 Py-5

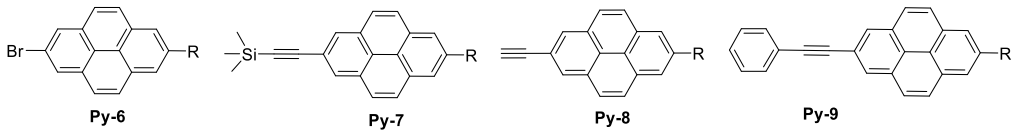

Py-6 Py-7 Py-8 Py-9

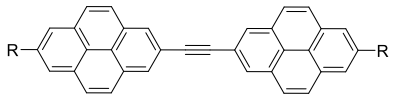

Py-10

R = 3,7-dimethyloctyl

Bodipys

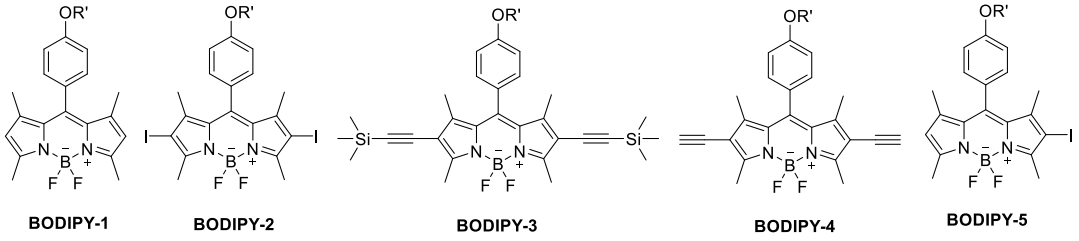

BODIPY-1 BODIPY-2 BODIPY-3 BODIPY-4 BODIPY-5

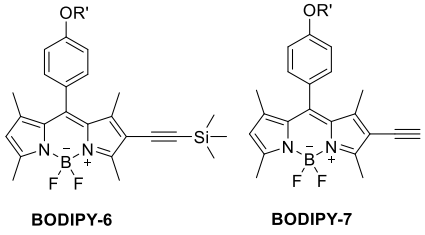

BODIPY-6 BODIPY-7

R' = 2-ethylhexyl

Squaraines

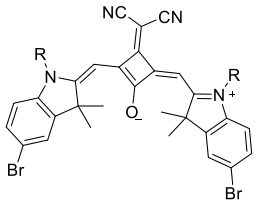

SQB-1

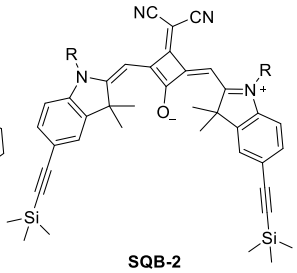

SQB-2

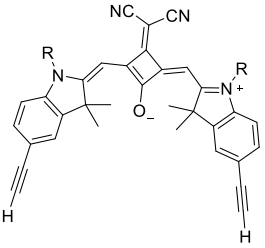

SQB-3

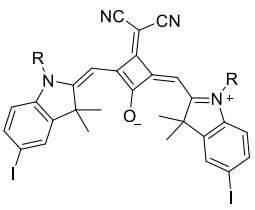

SQB-4

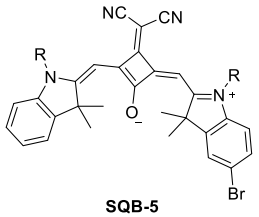

SQB-5

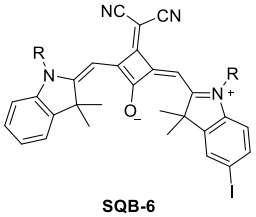

SQB-6

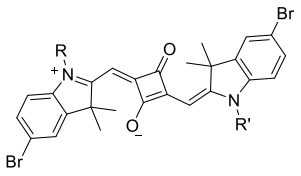

SQA-1

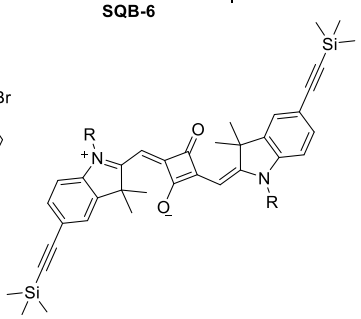

SQA-2

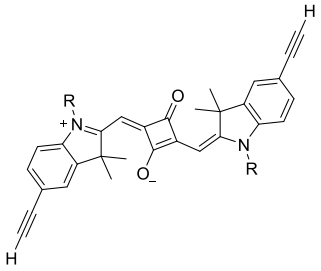

SQA-3

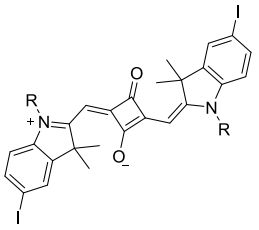

SQA-4

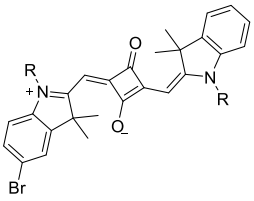

SQA-5

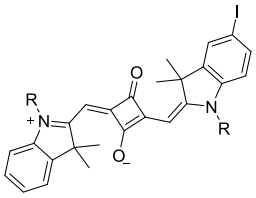

SQA-6

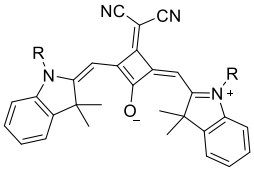

SQB

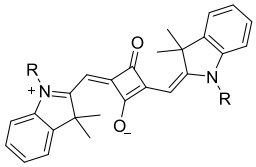

SQA

R = 3,7-dimethyloctyl

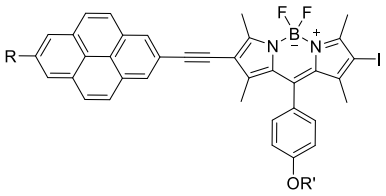

PyB-1

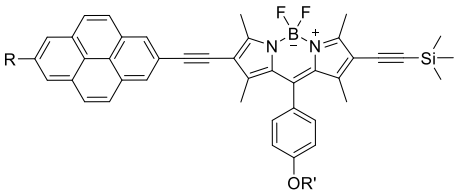

PyB-2

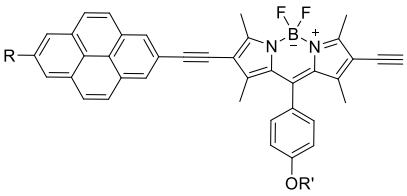

PyB-3

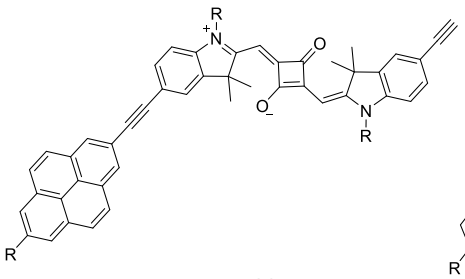

PySQA-1

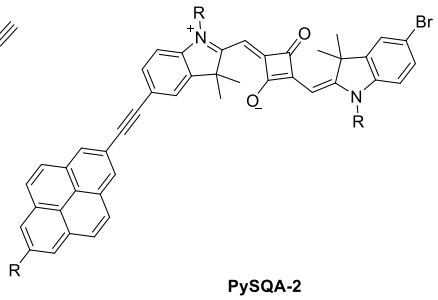

PySQA-2

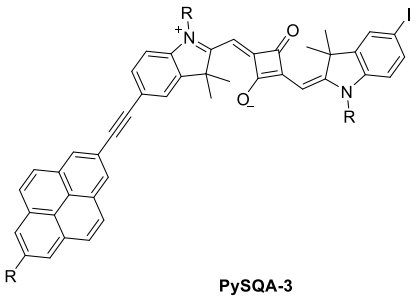

PySQA-3

Diads

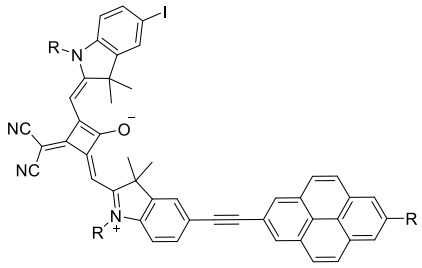

PySQB

R = 3,7-dimethyloctyl; R' = 2-ethylhexyl

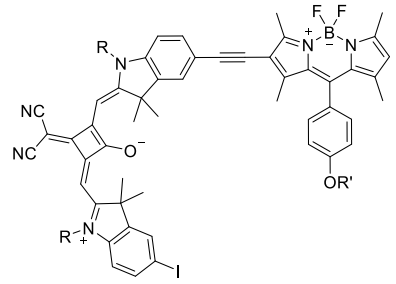

B(SQB)

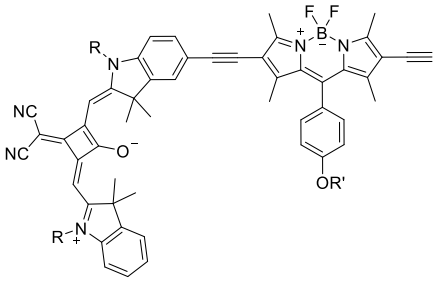

(SQB)B

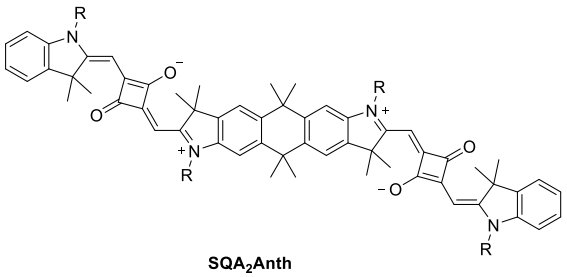

SQA_2Anth

R = 3,7-diemthyloctyl; R' = 2-ethylhexyl

Triads

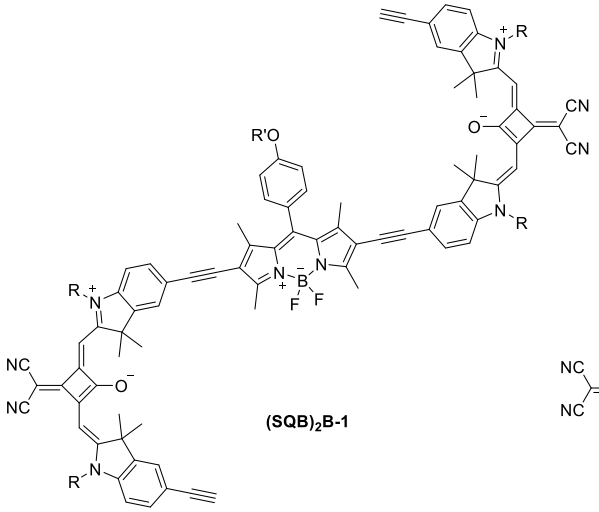

$(SQB)_2B$-1

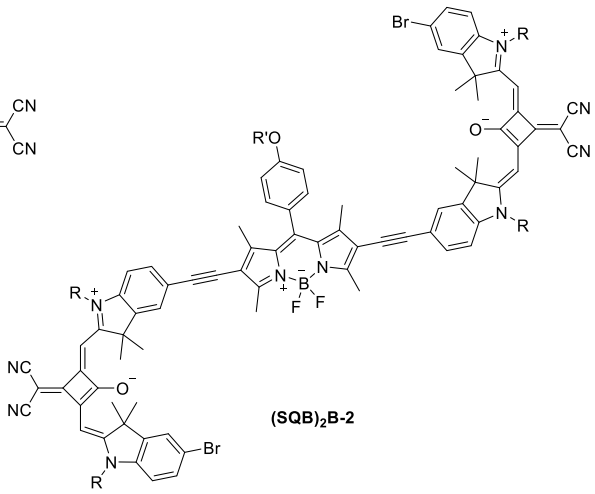

$(SQB)_2B$-2

R = 3,7-dimethyloctyl; R' = 2-etyhlhexyl

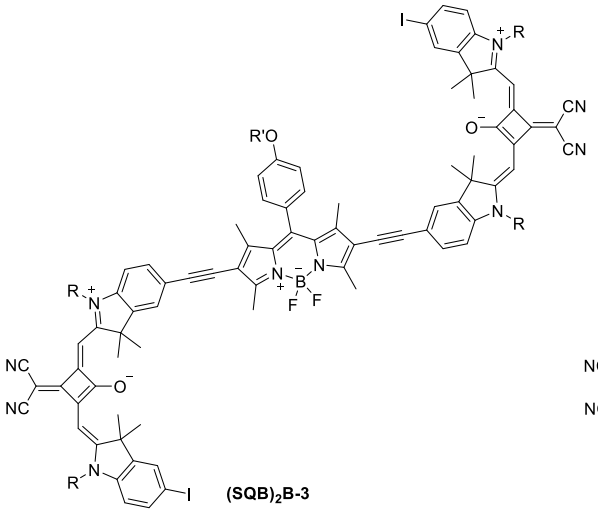

(SQB)$_2$B-3

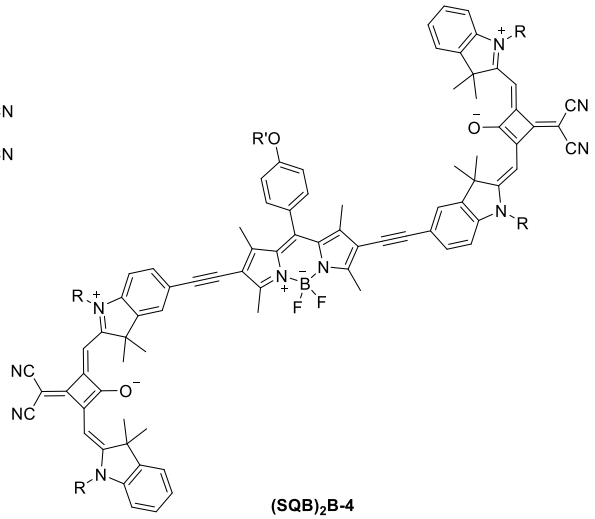

(SQB)$_2$B-4

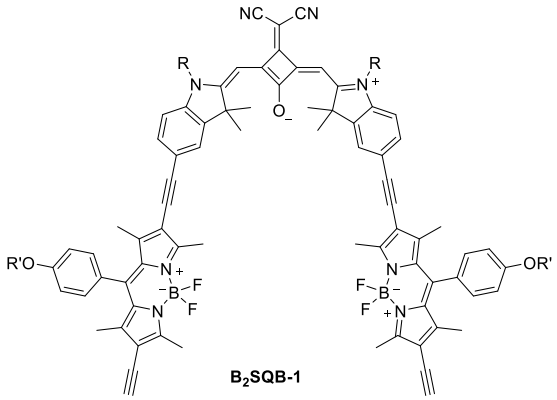

B$_2$SQB-1

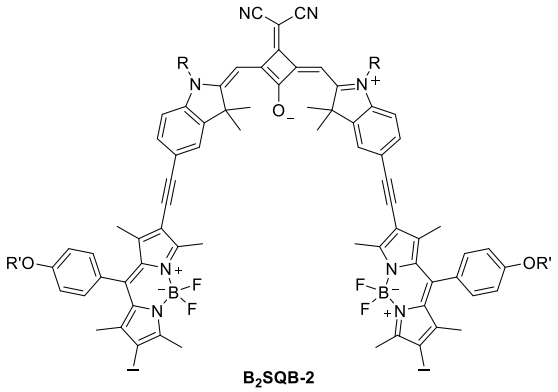

B$_2$SQB-2

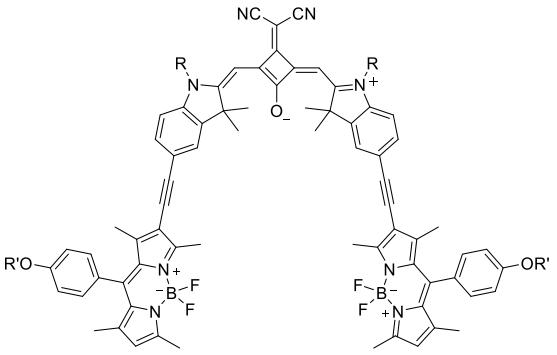

B$_2$SQB-3

R = 3,7-dimethyloctyl; R' = 2-etyhlhexyl

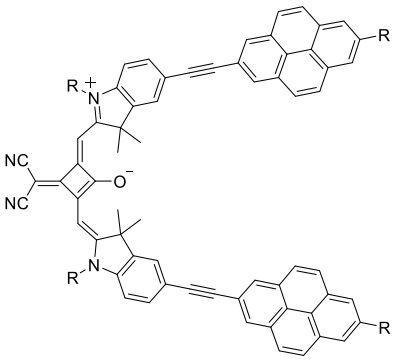

Py_2SQB

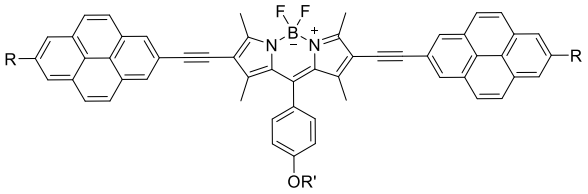

Py_2B

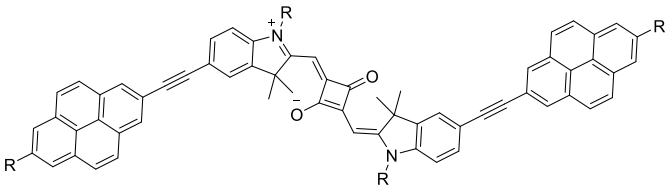

Py_2SQA

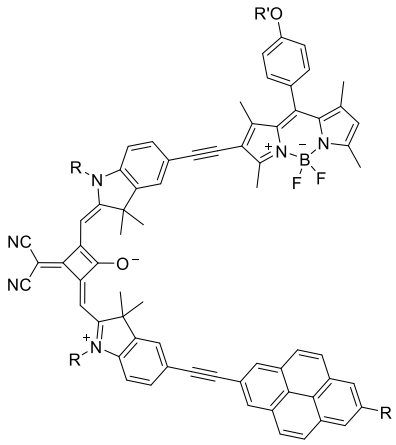

Py(SQB)B

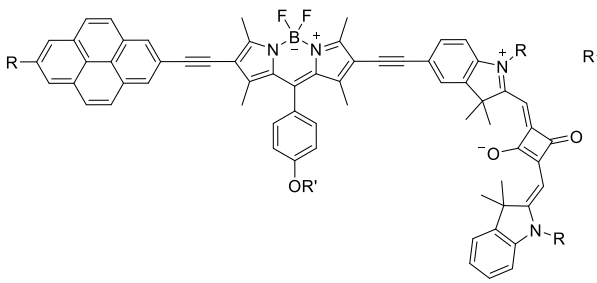

PyB(SQB)

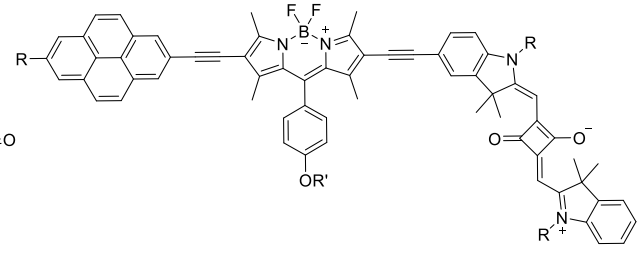

PyB(SQA)

R = 3,7-dimethyloctyl; R' = 2-ethylhexyl

Pentades

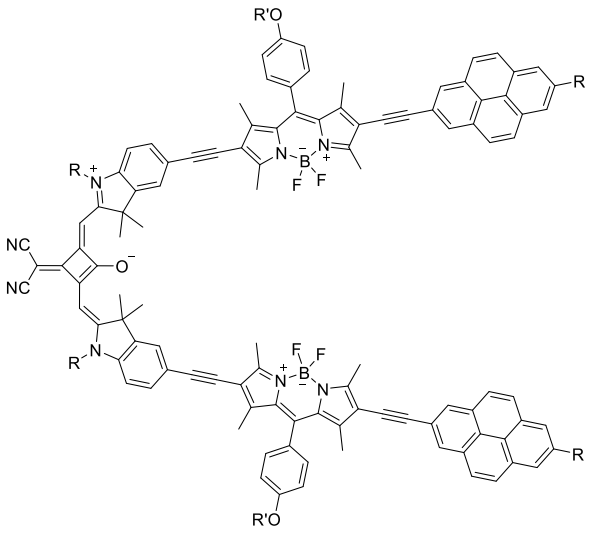

$(PyB)_2SQB$

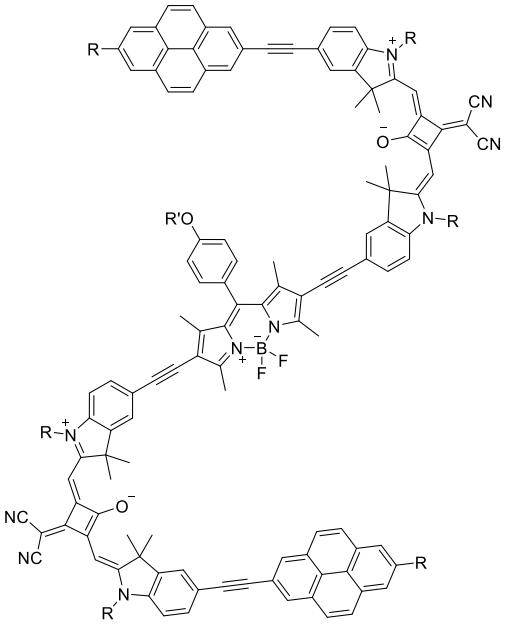

$(PySQB)_2B$

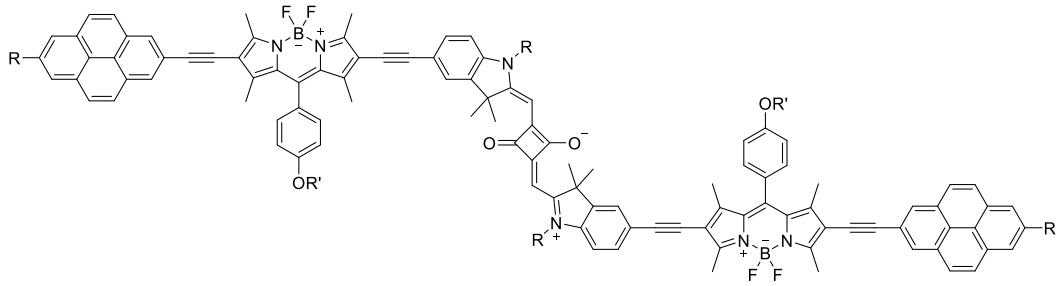

$(PyB)_2SQA$

R = 3,7-dimethyloctyl; R' = 2-ethylhexyl

Hexaarylbenzenes

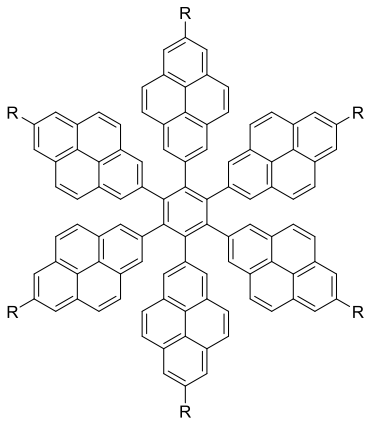

HAB1

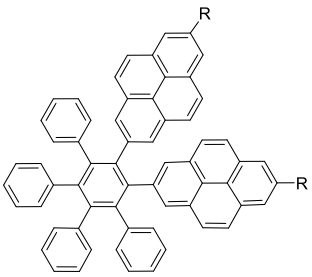

HAB2

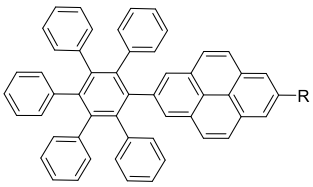

HAB3

R = 3,7-dimethyloctyl

10 Zusammenfassung

Diese Arbeit beschäftigt sich mit der Untersuchung von Energietransfer und Exzitonenkopplung in Farbstoffen. Durch Variation der Verbrückungseinheit und der räumlichen Orientierung der Chromophore relativ zueinander konnte die Kopplungsstärke beeinflußt werden.

Die Synthese von 2,7-substituierten Pyrenverbindungen konnte optimiert werden und schließlich gelang es mittels kobalt-katalisierten Trimerisierung oder *Diels Alder* Reaktionen gute Ausbeuten von **HAB 1** und **HAB 2** sowie geringere Mengen an **HAB 3** zu isolieren. Absorption- und Fluoreszenzspektren deuten auf starke Wechselwirkungen unter den Chromophoren hin, die bereits im Grundzustand deutlich werden. Anregungsspektren bei verschiedenen Wellenzahlen zeigen, dass zwei verschiedene Spezies, wovon eine den Aggregaten die im Grundzustand vorhanden sind ähneln, zu den beobachteten spektralen Eigenschaften beitragen und ein weiteres größere Ähnlichkeit mit dem Pyrenmonomer aufweist. Betrachtet man all diese Eigenschaften im Gesamten kann man schlußfolgern, dass zwei fluoreszierende Zustände für die Desaktivierung verantwortlich sind, was sich auf elektronische Entkopplung im angeregten Zustand zurückführen lässt.

Aufgrund der starken elektronischen Kopplung im Grundzustand und die Ausbildung von intramolekularen Aggregaten war es nicht möglich Energietransfer an diesem System zu studieren, da die sechs Pyreneinheiten nicht getrennt betrachtet werden können.

Im zweiten Teil dieser Arbeit wurden Farbstoffkonjugate verschiedener Größe und Anordnung synthetisiert um die Wechselwirkung der Übergangsdipolmomente zu studieren. Dazu wurde ein systematsiches Reaktionscreening der *Sonogashira*-Kupplung durchgeführt, um Bedingungen zu finden, unter denen sich Dehalogenierung in Grenzen hält, jedoch gute Ausbeuten der gewünschten Endprodukte erzielt werden können. Trotzdem konnten nur die symmetrischen Trimere erfolgreich isoliert, da sich herausstellte, dass sowohl die unsymmetrischen Trimere als auch die Pentamere zu instabil für eine vollständige Aufreinigung sind.

Die pyren-beinhaltenden Triaden **Py_2B** und **Py_2SQB** zeigen geringfügige Wechselwirkungen im Grundzustand, die sich durch eine Rotverschiebung und Verbreiterung der Absorptionsbanden zeigen. Allerding lässt sich diese Kopplung dem sehr schwachen Wechselwirkungsbereich zuordnen, sodass Energietransfer zwischen den Chromophoren möglich ist. Im Gegensatz dazu zeigt sich im TA Spektrum, dass gleichzeitig mehrere Teile der Triade angeregt sind und dass die Anregung nicht auf ein Chromophor lokalisiert ist. Die Frage, ob die Desaktivierung des angeregten Zustands durch Energietransfer oder interne Konversion in einem Superchromophor stattfindet, konnte im Zuge dieser Arbeit nicht geklärt

werden. Aktuell sind zusätzliche Rechnungen (DFT) in Arbeit um ein besseres Verständnis von den ablaufenden, photophysikalischen Prozessen zu bekommen.

Die Farbstoffkonjugate **B_2SQB-3** und **$(SQB)_2$B-4** lassen sich dem Bereich der starken Kopplung zuordnen und können daher mit der Exzitonentheorie beschrieben werden. Die Übergangsdipolmomente zeigen ein Verhalten, dass mehr als additiv ist und nehmen von der Absorption zur Fluoreszenz zu. Das lässt sich durch eine Verstärkung der Kopplung im relaxierten angeregten Zustand in Vergleich zur Absorption in den Franck-Condon Zustand erklären. Der Grund für dieses Phänomen ist eine deutlich schmalere, steilere Energiepotentialfläche im angeregten Zustand.

Im letzten Teil dieser Arbeit wurde die elektronische Kommunikation in einem *trans*-Squaraindimer durch Einfügen einer nicht-konjugierten Brücke untersucht. Während die flexiblen Dimere komplexe Spektren aufgrund unterschiedlicher Konformere aufweisen, enthält **SQA_2Anth** eine starre Brücke, die Rotationen verhindert. Diese Änderung der Flexibilität zeigt sich in den stationären Spektren durch eine Hauptabsorptions- und Fluoreszenzbande, da nur ein exzitonischer Zustand erlaubt ist. Das System weißt einen angeregten Zustand auf, der über das gesamte Molekül delokalisiert ist.

11 Appendix

11.1 Excitation Spectra of HAB 1

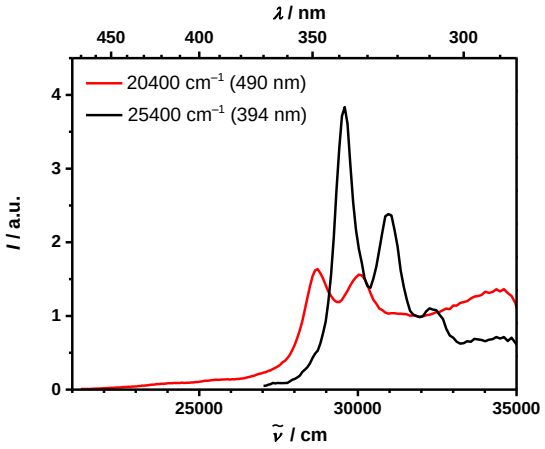

Figure 76 Excitation spectra of **HAB 1** in toluene monitored at different wavelength.

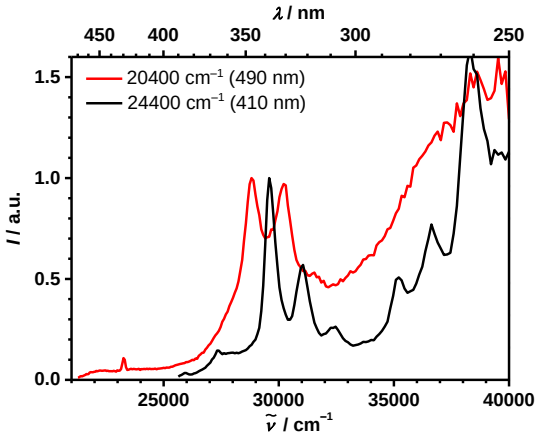

Figure 77 Excitation spectra of **HAB 1** in cyclohexane monitored at different wavelengths.

11.2 Excitation Spectra of Symmetrical Triads and Reference Compounds

Py-7

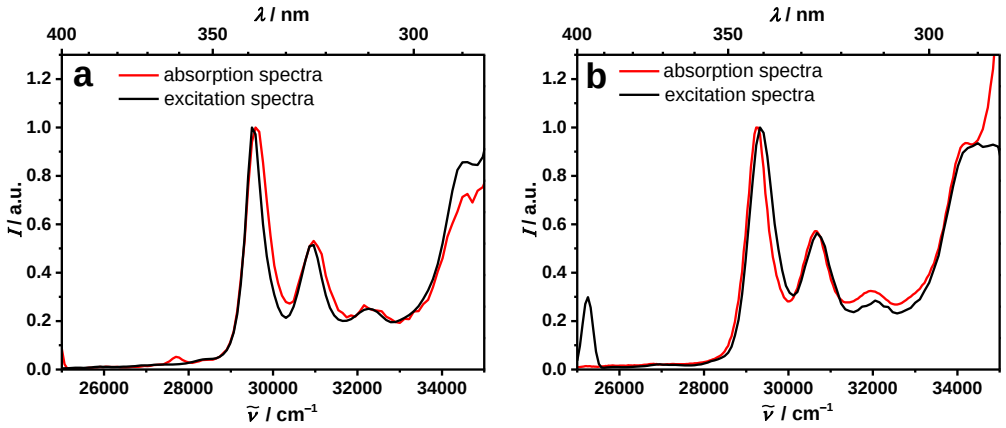

Figure 78 Absorption (red) and excitation spectra (black) of **Py-7** in cyclohexane monitored at 24800 cm^{-1} (404 nm) (**a**) and toluene monitored at 25200 cm^{-1} (399 nm) (**b**).

Py-9

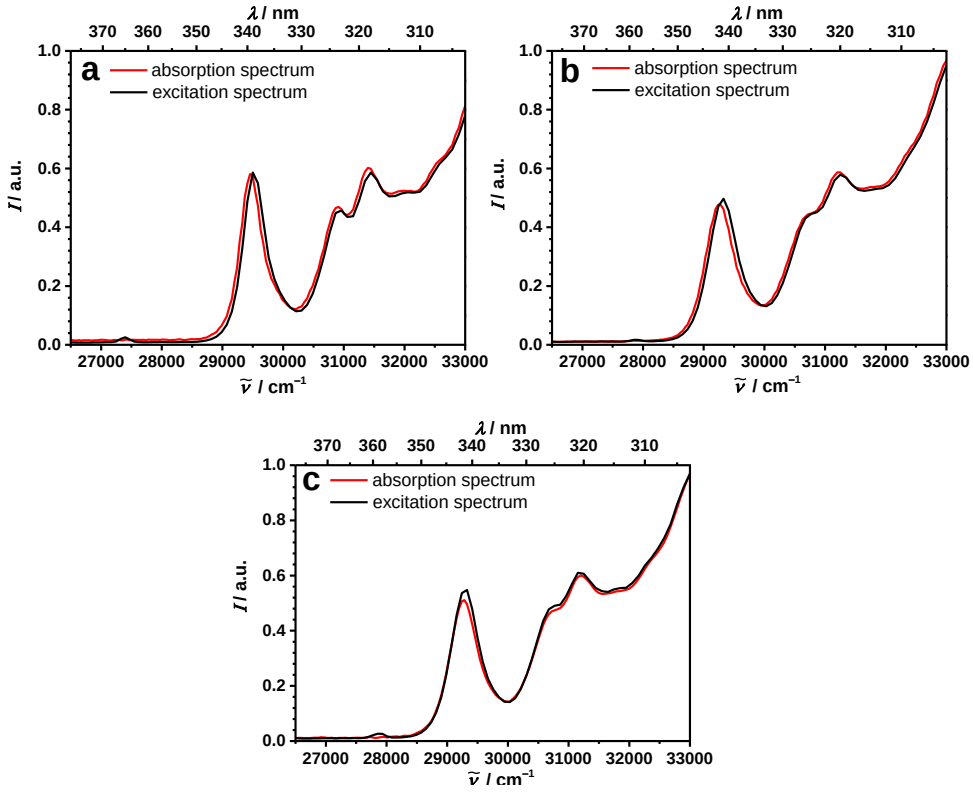

Figure 79 Absorption and excitation spectra of **Py-9** in cyclohexane monitored at 24500 cm^{-1} (408 nm) (**a**), $CHCl_3$ monitored at 24800 cm^{-1} (403 nm) (**b**) and toluene monitored at 24800 cm^{-1} (403 nm) (**c**).

Py_2B

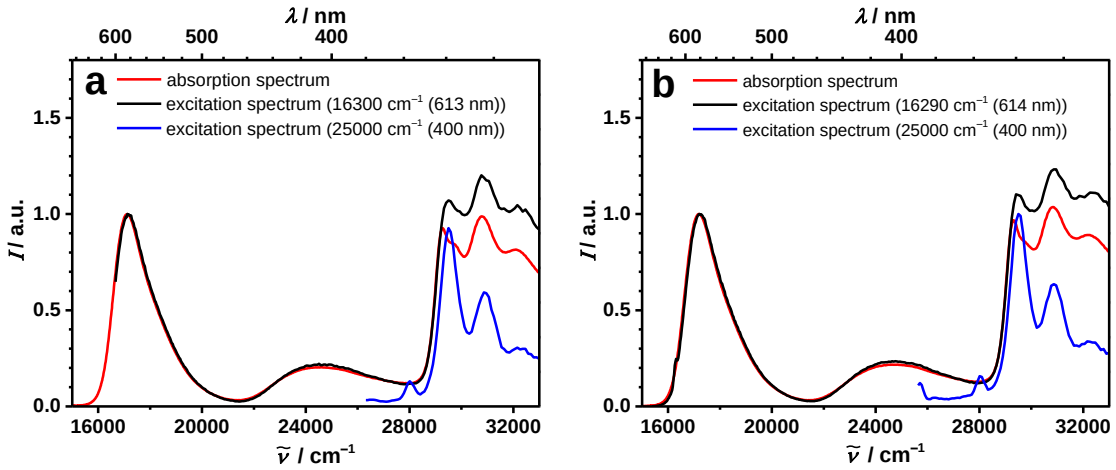

Figure 80 Absorption and excitation spectra of **Py_2B** in toluene (**a**) and $CHCl_3$ (**b**).

Py_2SQB

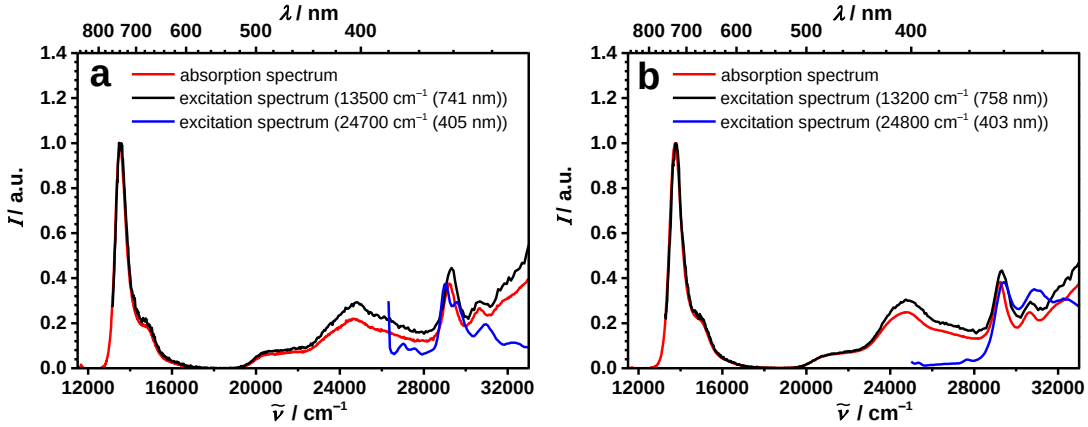

Figure 81 Absorption and excitation spectra of **Py_2SQB** in toluene (**a**) and $CHCl_3$ (**b**).

$(SQB)_2B$-4

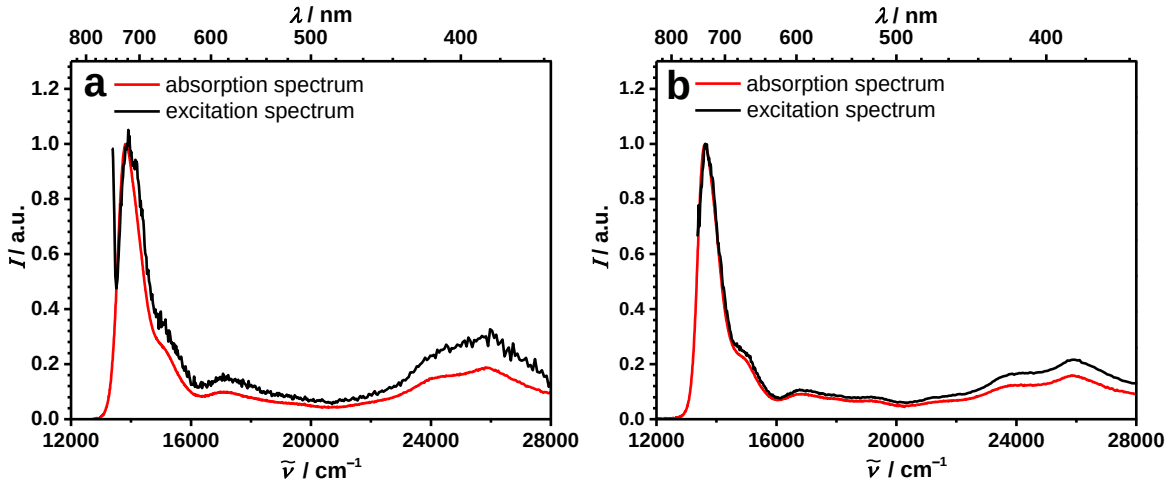

Figure 82 Absorption and excitation spectra of **$(SQB)_2B$-4** monitored at 13300 cm^{-1} (752 nm) in CH_2Cl_2 (**a**) and toluene (**b**).

B_2SQB-3

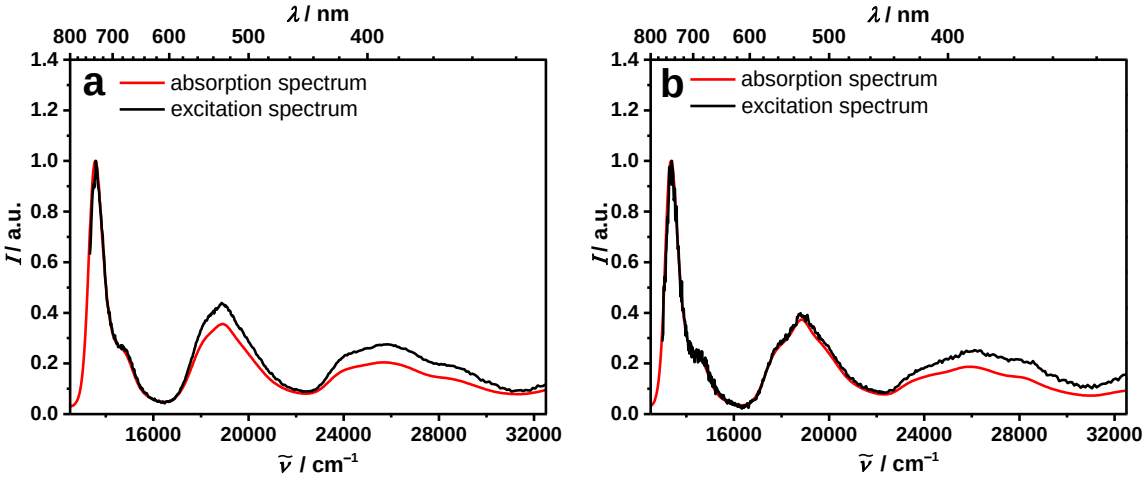

Figure 83 Absorption and excitation spectra of **B_2SQB-3** in CH_2Cl_2 monitored at 13200 cm^{-1} (756 nm) (**a**) and toluene monitored at 12900 cm^{-1} (775 nm) (**b**).

11.3 Geometry Optimised Structures of the Symmetrical Triads

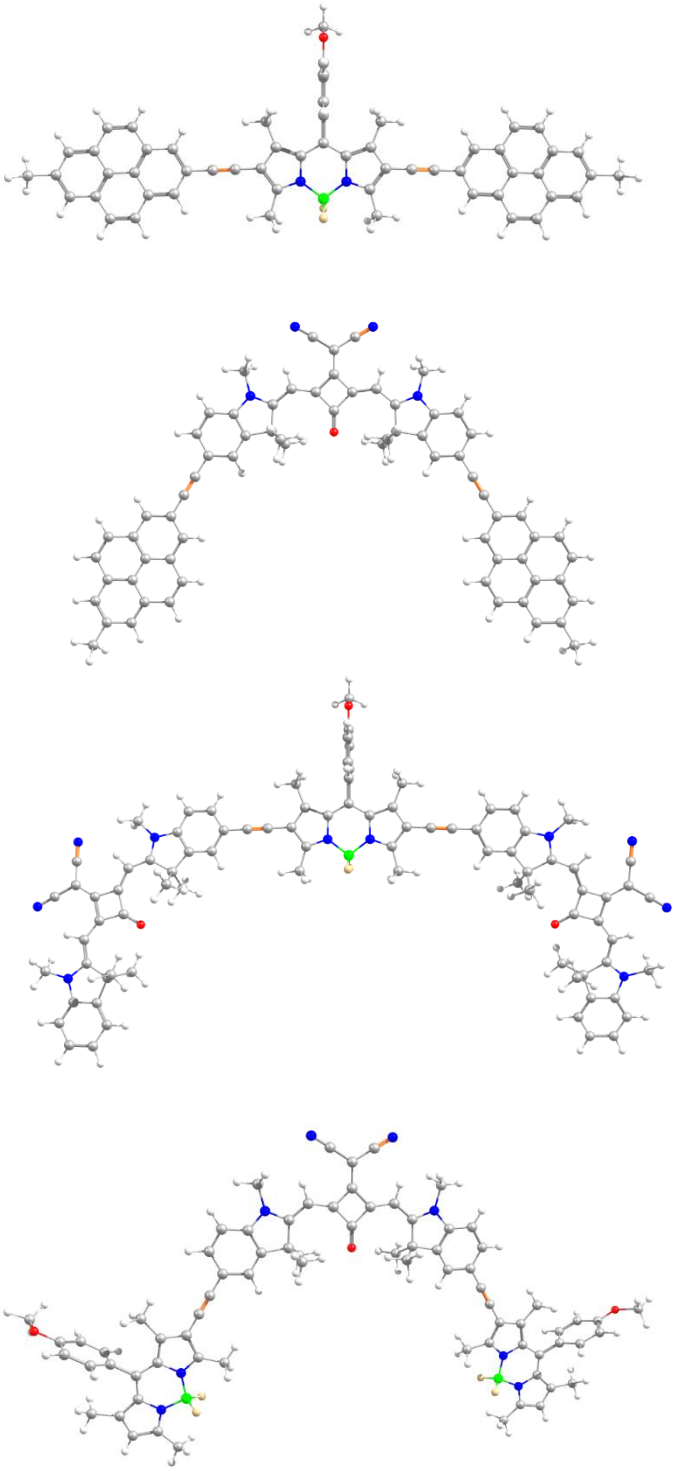

Figure 84 Optimised structures of symmetrical triads **Py_2B** (top left), **Py_2SQB** (top right), **$(SQB)_2B$-4** (bottom left) and **B_2SQB-3** (bottom right) resulting from DFT calculations at B3LYP/6-31G* level of theory.[1]

[1]The DFT calculations were carried out by *Dr. Marco Holzapfel*.

11.4 Transient Absorption Measurements of SQA_2Anth[1]

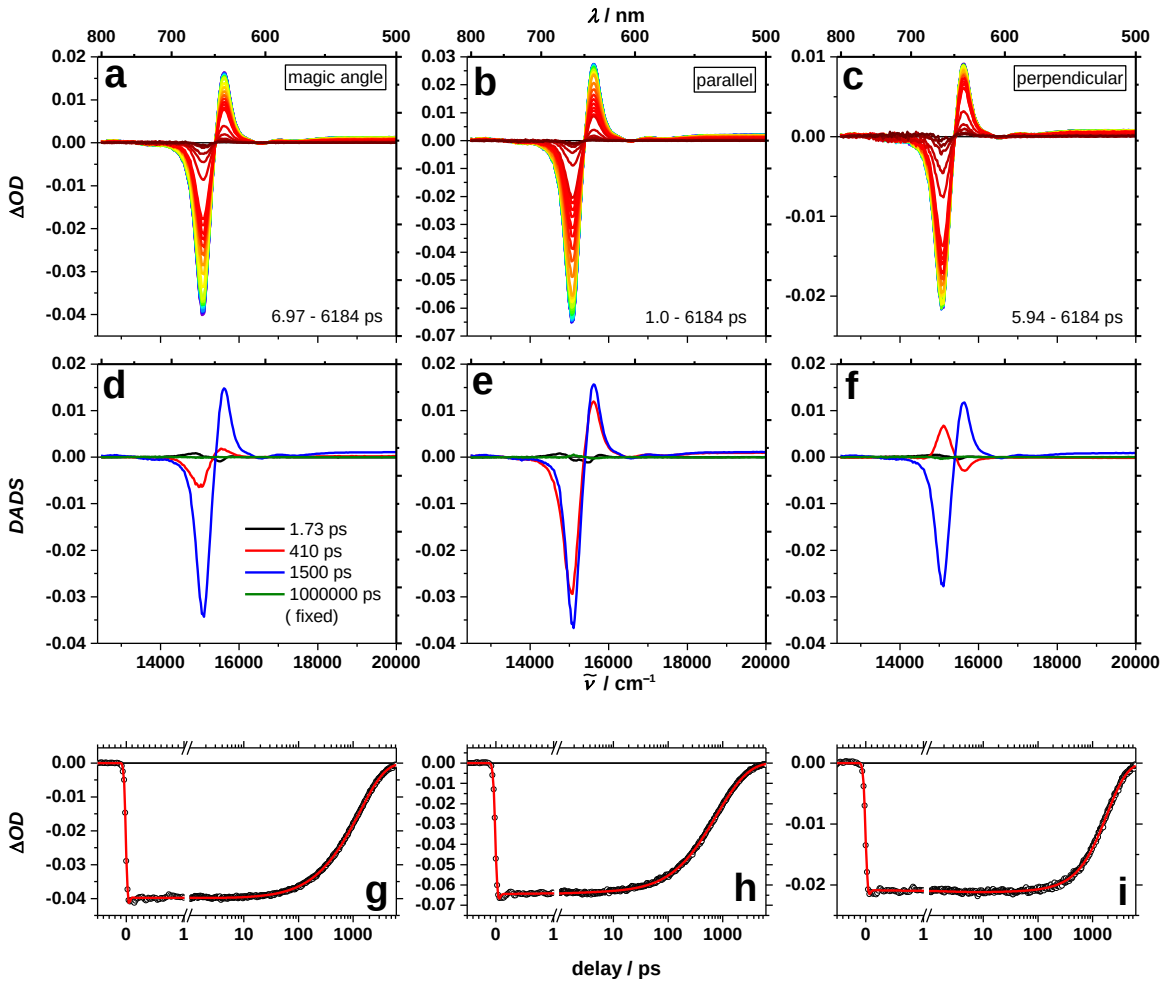

Figure 85 TA spectra of **SAQ_2Anth** after excitation at 15150 cm^{-1} (660 nm) in toluene at rt measured at magic angle (**a**), parallel (**b**) or perpendicular (**c**) orientation of pump and probe pulse. Early spectra are given in blue, later spectra in red. The decay associated difference spectra (**d**-**f**) resulted from a combined fit for all three measurements. Time scans at 15200 cm^{-1} (662 nm) are shown in **g**-**i**. The spectra and time scans were corrected for chirp and scattered light.

[1]The femtosecond spectroscopy measurements were performed and analysed by *Dr. Henning Marciniak.*

11.5 Conference Contributions

1. Oral presentations:

Workshop of the Research Training School 1221 (GRK 1221), September **2014**, Niederstetten, Germany.

2. Posters:

2.1 Conference of the Research Training School (GRK 1221), March **2015**, Würzburg, Germany.

2.2 Workshop of the DFG Forschergruppe 1809, June **2015**, Schöntal, Germany.

2.3 16th International Symposium on Novel Aromatic Compounds (ISNA-16), July **2015**, Madrid, Spain.

2.4 Conjugated Oligomers and Polymers (KOPO 2015), September **2015**, Würzburg, Germany.

2.5 26th IUPAC Symposium on Photochemistry, April **2016**, Osaka Japan

2.6 Conjugated Oligomers and Polymers (KOPO 2017), August **2017**, Bad Honnef, Germany.

11.6 Publication

Exciton Coupling Enhancement in the Relaxed Excited State
N. Auerhammer, A. Schmiedel, M. Holzapfel, C. Lambert
J. Phys. Chem. C. **2018**, DOI**:** 10.1021/acs.jpcc.8b03337.